



UNIVERSITY OF NAPLES FEDERICO II
 PH.D. PROGRAMME IN SEISMIC RISK
 XXV CYCLE

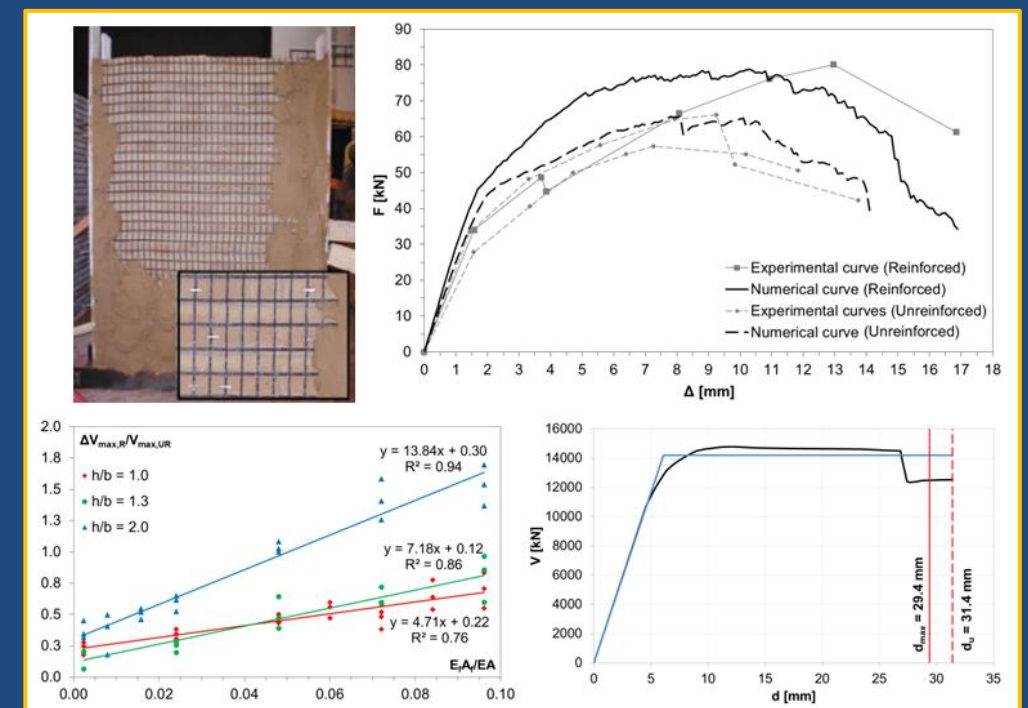
The Application of Composite Materials for the Reduction of the Seismic Vulnerability of Masonry Buildings

Angelo Garofano

2013

Angelo Garofano

The Application of Composite Materials for the Reduction of the Seismic Vulnerability of Masonry Buildings



2013

UNIVERSITY OF NAPLES FEDERICO II

PH.D. PROGRAMME IN SEISMIC RISK
COORDINATOR PROF. ALDO ZOLLO
XXV CYCLE



ANGELO GAROFANO
PH.D. THESIS

THE APPLICATION OF COMPOSITE MATERIALS FOR THE REDUCTION OF THE SEISMIC VULNERABILITY OF MASONRY BUILDINGS

TUTORS: PROF. FRANCESCA CERONI AND PROF. MARIA ROSARIA PECCE

2013

ACKNOWLEDGEMENTS

This thesis closes a three years period of intense and passionate work, but with no doubts full of satisfaction. I would like to express my gratitude to all the people who helped me during this doctorate programme and contributed to the final result.

The highest appreciation goes to my supervisors for their assistance and for thrusting me to work in this field. Special thanks to my overseeing supervisor Prof. Maria Rosaria Pecce for the continuous support, endless patience and encouragement during all these years. I will never forget the excellent and constant guidance and the example she offered to me.

I would also like to express my deep gratitude to Prof. Francesca Ceroni for her time, valuable suggestions and enthusiasm which represented a precious source of help throughout the course of this work.

I would also like to offer my regards and thanks to the Professors that I met during the Ph.D. course in these years, whose lectures I especially appreciated. I have been particularly fascinated by the friendly way of teaching and educating, as well as the scientific rigor for research, of Prof. Pere Roca from the Polytechnic University of Catalonia, Barcelona, whose lessons will be remembered forever.

I would like to acknowledge the Professors of the Institute of Theoretical and Applied Mechanics (ITAM), Prague, for giving me the opportunity to carry out research activities in their Institute. My sincere appreciation goes to Prof. Miloš Drdácák and Prof. Zuzana Slížková, for their advice and guidance during the experimental activity. I am also grateful to Prof. Stanislav Pospíšil for his willingness to help, stimulating scientific conversations and effort in supporting me.

I would also like to mention the precious cooperation and frequent attention provided by Prof. Petr Kabele of the Czech Technical University in Prague. The interesting discussions we had, that offered constructive criticisms, and his valuable suggestions have strongly contributed to my education.

My heartfelt thanks to all the friends and colleagues from the Engineering Department of the University of Sannio. Their friendship is the finest reward of all.

I warmly thank my family for the unconditional support and encouragement throughout these years, during my stay at home and the periods abroad.

Finally, there are no words I can say that would describe, as perfectly as she deserves it, how grateful I feel to my love, Mira. I am glad to have her every day by my side, who is smart, talented, kind, and always makes me happy. I dedicate this work to her.

ABSTRACT

Masonry buildings, whether ordinary or monumental, represent a particular class of buildings characterized by high vulnerability with respect to actions induced by earthquakes. The seismic events recently occurred all over the world constituted a valuable contribution in the direct evaluation of the critical aspect associated to such type of structures, causing widespread damage and loss of serviceability and load bearing capacity. In the last decades several studies have been carried out about the seismic behaviour of masonry buildings, but still many open issue exist regarding assessment methods, strengthening techniques, availability of adequate reinforcement design standards.

The damage experienced by masonry buildings constitutive elements, such as masonry walls, piers and spandrels, has brought to light the necessity to strengthen them with appropriate reinforcing systems in order to achieve the upgrading to the necessary seismic and energy dissipation capacity. Different strengthening systems have been proposed and studied during the last decades, with particular reference to the type of materials, system configuration with respect to the element to be strengthened, difficulties in the application and effectiveness of the reinforcement. Many issues regarding the methods for adequate design of the intervention and the evaluation of the effectiveness of these techniques in the improvement of seismic behaviour of structural members are still open.

The present research focuses on the structural behaviour of unreinforced masonry walls strengthened with composite grid reinforced mortar layers, concerning the assessment of the overall increase of in-plane capacity of the strengthened element. It is studied an innovative reinforcing technique composed by mortar layers incorporating a FRP reinforcement in form of grid. The FRP reinforced mortar layers are externally applied to the wall surfaces in a symmetric fashion, and can also be connected to the wall by means of connection devices.

The characterization of the mechanical behaviour of the masonry in compression by means of finite element modelling by means of micro- and macro-modelling is first carried out, considering the influence of the presence of mortar

joints, as well as the influence of different non-linear parameters on the post-peak behaviour of the material.

The behaviour of masonry walls strengthened by means of the considered technique is then studied and the in-plane shear behaviour is considered, in case of cyclic loading state. The performances of the global strengthened assemblage is thus examined with both experimental and numerical investigation criteria. Also, the overall ductility and energy dissipation capacity of the system, while subjected to horizontal in-plane actions, is studied. The actual mechanical behaviour of the proposed structural solution is investigated through an experimental program with prototypes.

Moreover, the numerical modelling of the masonry walls unreinforced and reinforced by the mortar layers with the composite grids is performed with the aim to define the effectiveness of the strengthening technique in the upgrading and retrofitting of the overall behaviour of masonry walls with respect to the in-plane shear resistance and overall ductility. A macro-modelling technique has been considered and a homogeneous material has been calibrated in which the effect of the characteristics of mortar joints and masonry units are smeared. Afterwards, a wide parametric analysis has been conducted to evaluate the effect of the amount and type of FRP on the stiffness, strength and ductility of the masonry wall. The results show that the most important parameter of the FRP material used for the strengthening is the axial stiffness (EA), while for the mortar the two parameters are the thickness and the strength in compression.

The results provided by the analysis on the panels are employed in the analysis of the model of a masonry building by means of equivalent frame elements through the software Tremuri in order to assess the influence of the reinforcement in the overall seismic capacity of the structure. The analysis evidenced that the increase of ductility was more effective than the increase of strength in terms of global behaviour of the building.

TABLE OF CONTENTS

ACKNOWLEDGMENTS	i
ABSTRACT	iii
LIST OF FIGURES	xiii
LIST OF TABLES	xxvii
1 INTRODUCTION	pag. 1
1.1 MOTIVATIONS	» 2
1.1.1 Why the use of FRP composites for masonry strengthening and retrofitting	» 4
1.1.2 Why the study of bond between FRP and masonry	» 5
1.1.3 Why the use of layers of mortar for FRP embedding	» 6
1.1.4 Why the non-linear modelling of masonry structures	» 7
1.1.5 Why the use of simplified methods for masonry structures	» 9
1.2 AIMS, SCOPE AND LIMITATIONS	» 10
1.3 OBJECTIVES OF THE THESIS	» 11
1.4 THESIS OUTLINE	» 12
2 SEISMIC BEHAVIOUR OF MASONRY BUILDINGS	pag. 15
2.1 SEISMIC VULNERABILITY OF MASONRY BUILDINGS	» 16

2.2	RESPONSE OF MASONRY BUILDINGS SUBJECTED TO SEISMIC ACTIONS	pag. 17
2.2.1	Seismic deficiencies of masonry structures	» 17
2.2.2	Damage mechanisms of masonry structures	» 23
2.2.2.1	<i>In-plane failure mechanisms</i>	» 24
2.2.2.2	<i>Out-of-plane damage mechanisms</i>	» 25
2.2.2.3	<i>Lateral thrust of roofs</i>	» 27
3	REVIEW OF EXPERIMENTAL TESTS ON MASONRY PANELS	pag. 29
3.1	NONLINEAR ANALYSES OF TUFF MASONRY WALLS STRENGTHENED WITH CEMENTITIOUS MATRIX-GRID COMPOSITES	» 29
3.2	SHEAR CAPACITY OF MASONRY WALLS EXTERNALLY STRENGTHENED BY A CEMENT-BASED COMPOSITE MATERIAL: AN EXPERIMENTAL CAMPAIGN	» 34
3.3	VALIDATION OF ANALYTICAL AND CONTINUUM NUMERICAL METHODS FOR ESTIMATING THE COMPRESSIVE STRENGTH OF MASONRY	» 41
3.4	MECHANICAL BEHAVIOUR OF POST-MEDIEVAL TUFF MASONRY OF THE NAPLES AREA	» 49
3.5	METROLOGICAL DEFINITION AND EVALUATION OF SOME MECHANICAL PROPERTIES OF POST-MEDIEVAL NEAPOLITAN YELLOW TUFF MASONRY	» 56
4	STRENGTHENING OF MASONRY WALLS	pag. 61
4.1	TRADITIONAL STRENGTHENING TECHNIQUES FOR UNREINFORCED MASONRY PANELS	» 61
4.1.1	Surface treatments	» 62
4.1.2	Grout and epoxy injection	» 64

4.1.3	External reinforcement	pag.	66
4.1.4	Confinement of URM with R.C. tie columns	»	67
4.1.5	Post-tensioning	»	67
4.1.6	Center core technique	»	69
4.2	GENERAL ASPECTS	»	70
4.3	STRENGTHENING TECHNIQUES FOR IN-PLANE BEHAVIOUR	»	71
4.4	EXTERNALLY APPLIED FRP GRID REINFORCED MORTAR LAYERS	»	75
4.5	MODELLING OF THE BEHAVIOUR OF THE REINFORCED SYSTEM	»	86

5 EXPERIMENTAL TESTS ON REINFORCED MASONRY WALLS

pag. 93

5.1	EXPERIMENTAL SPECIMENS	»	94
5.2	MATERIALS PROPERTIES	»	98
5.3	EXPERIMENTAL EQUIPMENT AND TEST SET-UP	»	101
5.4	EXPERIMENTAL RESULTS	»	105
5.4.1	Adobe brick walls	»	106
5.4.2	Damaged adobe brick wall retrofitted with reinforced mortar plaster	»	118
5.4.3	Dry clay brick walls	»	124
5.4.4	Solid clay brick walls	»	125
5.5	EVALUATION METHODS	»	126
5.5.1	Method for the evaluation of the bilinear curve	»	126
5.5.2	Method for the evaluation of the energy dissipation	»	130
5.6	ANALYSIS AND COMPARISON OF RESULTS	»	131
5.6.1	Deformation capacity	»	131
	5.6.1.1 Adobe brick walls	»	131
	5.6.1.2 Dry clay brick walls	»	133
	5.6.1.3 Solid clay brick walls	»	133

5.6.2	Energy dissipation	pag. 135
	5.6.2.1 <i>Adobe brick walls</i>	» 135
	5.6.2.2 <i>Dry clay brick walls</i>	» 136
	5.6.2.3 <i>Solid clay brick walls</i>	» 137
5.7	MECHANICAL TESTS ON UNREINFORCED AND REINFORCED MORTAR SPECIMENS	» 138
5.7.1	Experimental specimens preparation	» 139
5.7.2	Tensile tests	» 145
5.7.3	Compressive tests	» 146
5.7.4	Shear tests	» 148
5.7.5	Summary of results	» 150
5.8	CONCLUSIONS	» 151
6	BOND BEHAVIOUR OF FRP REINFORCEMENT ON MASONRY	pag. 153
6.1	THE ROLE OF BOND BETWEEN MASONRY AND FRP	» 153
6.2	EXPERIMENTAL SET-UP FOR BOND TESTS	» 155
6.3	EXPERIMENTAL PROGRAMME	» 157
	6.3.1 Asymmetrical pull-push test set-up and properties of the masonry supports	» 157
	6.3.2 Failure modes and loads	» 158
	6.3.3 Strain distributions and load-displacement curves	» 162
	6.3.4 Shear stress distribution	» 167
6.4	CONCLUSIVE REMARKS	» 169
7	BEHAVIOUR AND MODELLING OF MASONRY	pag. 171
7.1	MECHANICAL CHARACTERIZATION OF MASONRY AND ITS CONSTITUTIVE MATERIALS	» 173
	7.1.1 Uniaxial compressive behaviour	» 175
	7.1.2 Uniaxial tensile behaviour	» 176

7.1.3	Biaxial behaviour	pag. 177
7.2	MICRO-MODELLING	» 179
7.3	MACRO-MODELLING AND HOMOGENIZATION TECHNIQUES	» 184
7.3.1	Elasto-plastic homogenization of layered materials	» 186
7.3.2	Anisotropic continuous models	» 189
7.4	CRACKING MODELS	» 193
7.4.1	Discrete cracking models	» 196
7.4.2	Smeared cracking models	» 197
	7.4.2.1 <i>Fixed single crack approach</i>	» 199
	7.4.2.2 <i>Fixed multi-directional crack approach</i>	» 203
	7.4.2.3 <i>Rotating crack approach</i>	» 204
8	ANALYSIS AND ASSESSMENT METHODS FOR MASONRY STRUCTURES	pag. 205
8.1	ANALYSIS AND ASSESSMENT METHODS	» 205
8.2	NON-LINEAR RESPONSE OF URM WALLS	» 206
	8.2.1 Failure modes of URM walls	» 207
	8.2.2 Softening behaviour of URM walls	» 209
8.3	NON-LINEAR MODELLING OF MASONRY BUILDINGS	» 212
	8.3.1 Macro-elements modelling technique	» 212
	8.3.2 Equivalent Frame Modelling	» 213
	8.3.3 Limit analysis	» 219
9	NUMERICAL MODELLING OF MASONRY UNDER COMPRESSIVE LOADING	pag. 221
9.1	EXPERIMENTAL DATA	» 221
9.2	THREE-DIMENSIONAL FINITE ELEMENTS MICRO-MODELLING OF MASONRY PANELS	» 228
	9.2.1 Adopted finite elements	» 229

9.2.2	Adopted non-linear material model	pag. 230
9.2.3	Geometry definition and meshing	» 234
9.3	RESULTS AND COMPARISONS WITH EXPERIMENTAL CURVES	» 238
9.4	EQUIVALENT BI-DIMENSIONAL FINITE ELEMENTS MACRO-MODELLING OF MASONRY PANELS	» 243
10	MODELLING OF SHEAR PANELS TESTED AT THE ITAM AND EFFECT OF THE FRP REINFORCED MORTAR LAYER	pag. 247
10.1	MODELLING OF THE UNREINFORCED MASONRY PANEL	» 248
10.1.1	Adopted finite elements	» 248
10.1.2	Adopted non-linear material model	» 249
10.1.3	Geometry definition and meshing	» 251
10.2	RESULTS AND COMPARISONS WITH EXPERIMENTAL TESTS	» 252
10.3	MODELLING OF THE REINFORCED MASONRY PANEL	» 260
10.3.1	Modelling of the reinforcement system	» 262
10.4	EFFECT OF THE COMPOSITE GRID	» 266
10.5	PARAMETRIC ANALYSIS ON THE EFFECT OF FRP ON SHEAR MASONRY WALLS	» 269
11	MODELLING OF A REINFORCED MASONRY BUILDING	pag. 287
11.1	DESCRIPTION OF THE BUILDING	» 287
11.2	GEOMETRY AND STRUCTURAL ARRANGEMENT	» 289
11.3	INSPECTION AND MATERIAL CHARACTERIZATION	» 293
11.3.1	Analytical materials survey	» 294
11.3.2	In-situ tests	» 295
11.3.3	Foundations excavations	» 297

11.4	MODELLING OF THE BUILDING IN THE SOFTWARE TREMURI	pag. 298
11.5	SEISMIC HAZARD ASSESSMENT	» 303
11.6	PUSH-OVER ANALYSIS	» 304
	11.6.1 Unreinforced building	» 304
	11.6.2 Reinforced building	» 307
12	CONCLUSIONS AND FUTURE DEVELOPMENTS	pag. 311
	REFERENCES	pag. 319
	APPENDIX	pag. 333

LIST OF FIGURES

Figure 2.1. Masonry building under horizontal seismic action: loosely connected walls with flexible floor (a); well connected walls with flexible floor (b); connected walls with rigid floor.	18
Figure 2.2. Key requirements for ensuring box action in a masonry building.	19
Figure 2.3. Role of wall connections in the box-like action of a building: walls A (loaded in the strong direction) support walls B (loaded in the weak direction).	20
Figure 2.4. Effect of inadequate wall-to-roof connection.	21
Figure 2.5. Delamination of masonry walls: (a) two-whythe stone wall with a rubble core; (b) stones displacement due to vibrations; (c) internal lateral pressure due to rubble fill increases and (d) wall collapse (Meyer et al., 2007) [2].	22
Figure 2.6. Various types of failures observed in unreinforced masonry buildings under seismic actions.	24
Figure 2.7. In-plane failure modes of a laterally loaded URM wall: (a) two-whythe stone wall with a rubble core; (b) stones displacement due to vibrations; (c) internal lateral pressure due to rubble fill increases	25
Figure 2.8. Out-of-plane collapse mechanisms with and without ties.	26
Figure 2.9. Overturning mechanism without wall connection, with good wall connection, in presence of ties.	27
Figure 3.1. Numerical and experimental comparison for unreinforced panels [5].	32
Figure 3.2. Numerical and experimental comparison for panels reinforced with one layer of CMG [5].	32
Figure 3.3. Numerical and experimental comparison for panels reinforced with two layers of CMG [5].	33
Figure 3.4. Parametric analysis of strength and shear modulus for different degrees of joint filling [5].	34
Figure 3.5. Diagonal compression test [6].	37
Figure 3.6. Load-displacement diagram, Specimen 1 [6].	38

Figure 3.7. Load-displacement diagram, Specimen 9 [6].	38
Figure 3.8. Comparison between experimental and theoretical results from different formulations [6].	40
Figure 3.9. Test set-up and positions of LVDTs [7].	42
Figure 3.10. Definition of the base cell used in the analyses [7].	43
Figure 3.11. Numerical and experimental stress-strain diagram [7].	44
Figure 3.12. Comparison between the stress-strain diagram obtained using an adjusted value of the modulus of elasticity of the mortar [7].	46
Figure 3.13. Plots of the strain versus the load for different cross-section of the element: S1 (a), S2 (b), S3 (c) [7].	47
Figure 3.14. Front side and cross-section of the wall in ‘cantieri’ style [11].	50
Figure 3.15. Front side and cross-section of the wall in ‘bozzette’ style [11].	50
Figure 3.16. Front side and cross-section of the wall in ‘a sacco’ style [11].	51
Figure 3.17. Constitutive law for tuff and mortar specimens [11].	52
Figure 3.18. Constitutive law for three typology of walls analysed [11].	53
Figure 3.19. Moment – curvature diagram for three typologies of walls analysed [11].	54
Figure 3.20. Comparison between the constitutive laws of mortar and tuff employed for construction of the ‘bozzette’ panel and curve from its analysis [11].	55
Figure 3.21. Built panels: ‘bozzette’ (a), ‘cantieri’ (b), blocchetti (c) [12].	57
Figure 3.22. Compressive tests results for ‘bozzette’ walls [12].	59
Figure 4.1. Surface treatments: samples of reinforcement used in ferrocement (a); typical layout of reinforced plaster (b); application of shotcrete (c) [13].	63
Figure 4.2. Overview of injection holes distribution.	65
Figure 4.3. External reinforcement using vertical and diagonal bracing (a) or creating infill panel (b) [13].	66
Figure 4.4. Different in-plane test configurations to investigate the shear response of FRP reinforced brick masonry elements: (a) (Valluzzi et al., 2002) [22], (b) (ElGawady et al., 2005) [23], (c) (Eshani and Saadatmanesh, 1997) [34], (d) (Triantafillou, 1998) [31]. [21].	72

Figure 4.5. Textile-reinforced mortar (TRM) strengthening of a masonry panel: phases of application [42].	76
Figure 4.6. Carbon fiber reinforcement mesh texture (a) and application of the TRM layer [43].	78
Figure 4.7. Bi-directional alkali resistant AR glass coated open grid, SRG 45 [4].	80
Figure 4.8. CMG system: reinforcing grid installation (a) and troweling of final mortar layer (b) [4].	81
Figure 4.9. Coated AR-glass grid employed by (Aldea et al., 2006) [45].	83
Figure 4.10. Different FRP reinforcement configurations investigated by (Aldea et al., 2006) [45].	84
Figure 4.11. Example of a typical Horizontal Force – Displacement curve for CMG strengthened wall compared with URM wall [45].	85
Figure 4.12. Geometry of the masonry walls (a) and Finite Element micro-model (b) [3].	87
Figure 4.13. Assumed non-linear material models for units and mortar [5].	88
Figure 4.14. Comparison between numerical and experimental crack patterns for as-built panel (a) and strengthened panel (b) [5].	89
Figure 4.15. Different configuration of the strengthening system for masonry panels [48].	90
Figure 5.1. Dimensions of the fundamental element used in the masonry specimens.	94
Figure 5.2. Overall dimensions of the masonry specimens and bricks arrangement (a) and position of the reinforcement grid (b).	95
Figure 5.3. Unreinforced masonry walls: (a) adobe, (b) burned clay bricks, (c) unburned clay bricks.	96
Figure 5.4. Geo-nets employed for strengthening of masonry walls: polyester (a) and polypropylene (b) grids.	96
Figure 5.5. Masonry walls strengthened with polymeric nets: (a) solid brick wall; (b) adobe brick wall.	97
Figure 5.6. Adobe brick wall reinforced by means of X-shaped wire ropes (a) and detail of the anchoring system for wire ropes (b).	98
Figure 5.7. Testing rig and reaction wall for testing.	102

Figure 5.8. Scheme of the testing system.	102
Figure 5.9. Servo-hydraulic actuator for horizontal loads.	103
Figure 5.10. Loading pattern for each step of application of the horizontal force.	104
Figure 5.11. Examples of location of sensors.	104
Figure 5.12. Crack pattern at failure of the plain masonry control wall under a combination of vertical compression and cyclic shear.	106
Figure 5.13. Crack pattern at failure of the adobe wall strengthened with reinforced mortar layers under a combination of vertical compression and cyclic shear	107
Figure 5.14. Evidence of the detachment of the plaster from the wall surface.	108
Figure 5.15. Assumed non-linear material models for units and mortar [5].	109
Figure 5.16. Details of the large damage at the wall's base.	109
Figure 5.17. Detail of the damage due to the out-of-plane of the wire ropes reinforcement.	110
Figure 5.18. Cyclic curves for different steps of loading – Unreinforced adobe wall.	111
Figure 5.19. Cyclic curves for different steps of loading – Wall strengthened with reinforced mortar plaster.	112
Figure 5.20. Cyclic curves for different steps of loading – Wall strengthened with wire ropes.	113
Figure 5.21. Cyclic curve for unreinforced adobe wall.	114
Figure 5.22. Cyclic curve for wall strengthened with reinforced mortar plaster.	114
Figure 5.23. Cyclic curve for wall strengthened with wire ropes.	115
Figure 5.24. Envelope curves for unreinforced adobe wall.	115
Figure 5.25. Envelope curves for wall strengthened with reinforced mortar plaster.	116
Figure 5.26. Envelope curves for wall strengthened with wire ropes.	116
Figure 5.27. Behaviour of the wall strengthened with reinforced mortar plaster compared to the unreinforced wall.	117
Figure 5.28. Behaviour of the wall strengthened with wire ropes compared to the unreinforced wall.	118

Figure 5.29. Crack pattern at failure of the retrofitted adobe wall under a combination of vertical compression and cyclic shear	119
Figure 5.30. Damage at the base of the wall: detachment of the mortar layer (a) and large vertical crack in the wall thickness	120
Figure 5.31. Cyclic curves for different steps of loading – Retrofitted adobe wall.	121
Figure 5.32. Cyclic curve for retrofitted adobe wall.	122
Figure 5.33. Envelope curves for retrofitted adobe wall.	122
Figure 5.34. Behaviour of the retrofitted adobe wall to the unreinforced wall.	123
Figure 5.35. Comparison between undamaged wall strengthened with reinforced mortar layers and retrofitted wall.	123
Figure 5.36. Crack pattern at failure of the plain masonry control wall under a combination of vertical compression and cyclic shear: DBW-1 (a); DBW-3 (b); SBW-1 (c).	125
Figure 5.37. Hysteresis envelope and its bilinear idealization.	126
Figure 5.38. Evaluation of the bilinear curve from the six bilinear curves of the tested walls.	128
Figure 5.39. Elastic drift of adobe bricks walls.	132
Figure 5.40. Ultimate drift of adobe bricks walls.	132
Figure 5.41. Ultimate ductility of adobe bricks walls.	132
Figure 5.42. Elastic drift of dry clay bricks walls.	134
Figure 5.43. Ultimate drift of dry clay bricks walls.	134
Figure 5.44. Ultimate ductility of dry clay bricks walls.	134
Figure 5.45. Comparison of the energy dissipation between adobe bricks walls.	136
Figure 5.46. Comparison of the energy dissipation between dry clay bricks walls.	137
Figure 5.47. Comparison of the energy dissipation between solid clay bricks walls.	138
Figure 5.48. Outline of the wooden frame constructed for the casting of reinforced mortar specimens (dimensions in mm).	139
Figure 5.49. Geo-net employed for reinforced mortar specimens.	140
Figure 5.50. Preparation of the reinforcing mesh and orientation in the mortar specimens.	141
Figure 5.51. Phases of preparation of the mortar samples and positioning of the net.	142

Figure 5.52. Specimens casted in the wooden moulds: clay mortar (a) and lime mortar (b).	142
Figure 5.53. Climate chamber (a) and thermo-hygrometric conditions (b).	142
Figure 5.54. Reinforced mortar specimens in the climate chamber: clay mortar (a) and lime mortar (b).	143
Figure 5.55. Reinforced mortar specimens for tensile tests: clay mortar (a) and lime mortar (b).	144
Figure 5.56. Reinforced mortar specimens for three-points bending tests: clay mortar (a) and lime mortar (b).	144
Figure 5.57. Reinforced mortar specimens for compression tests: clay mortar (a) and lime mortar (b).	144
Figure 5.58. Force – displacement curves for unreinforced and reinforced mortar specimens under tensile load: clay mortar (a) and lime mortar (b).	145
Figure 5.59. Tested reinforced mortar specimens under tensile load: clay mortar specimen (a) and detail of crack in lime mortar specimen (b).	146
Figure 5.60. Force – displacement curves for unreinforced and reinforced mortar specimens under compression load: clay mortar (a) and lime mortar (b).	147
Figure 5.61. Tested reinforced mortar specimens under compression load: clay mortar (a) and lime mortar (b) specimens.	148
Figure 5.62. Force – deflection curves for unreinforced and reinforced mortar specimens under shear load: clay mortar (a) and lime mortar (b).	149
Figure 5.63. Tested reinforced mortar specimens under shear load: clay mortar specimen (a) and detail of crack in lime mortar specimen (b).	149
Figure 6.1. Experimental arrangements for pull-push set-up: (a) symmetrical scheme inside a tensile machine (Aiello and Sciolti, 2008) [56]; (b) asymmetrical scheme with a hydraulic jack (Mazzotti et al.,2009) [67].	156
Figure 6.2. Set-up for pull-push bond tests.	157
Figure 6.3. Examples of failure modes: (a) Diagonal crack at the free end of the FRP reinforcement; (b) Superficial debonding at the loaded end; (c) Debonding in specimens with plastering; (d) Edge effects in the tuff block at the loaded end.	161

Figure 6.4. Strain profiles in pull-push bond tests in specimens made of tuff T1 with: (a) Glass fibers for $L_b = 200$ mm and $L_b = 300$ mm with plaster; (b) Carbon fibers for $L_b = 200$ mm and $L_b = 300$ mm with plaster; (c) Carbon and glass fibers for $L_b = 300$ mm with plaster; (d) Linen and carbon fibers for $L_b = 300$ mm without plaster.	163
Figure 6.5. Effect of plastering in pull-push bond tests: (a) strain distributions for specimens made of T1 with carbon fibers; (b) strain distributions in specimens made of tuff T2 with carbon fibers; (c) global load-displacement curves for specimens made of T2 with carbon, glass and basalt fibers with and without plaster.	165
Figure 6.6. Effect of tuff strength (T1 and T2) on the strain distribution in pull-push bond tests with carbon and glass fibers: (a) strain profiles for specimens with carbon fibers; (b) global load-displacement curves for specimens with carbon, glass and linen.	166
Figure 6.7. Shear stress distributions: (a) specimen made of tuff T2 with CFRP and plaster; (b) specimen made of tuff T2 with BFRP.	167
Figure 6.8. Shear stress distributions: (a) Effect of plastering in specimens made of tuff T2 and bonded with glass fibres; (b) Effect of tuff strength (T1 and T2) in specimens bonded with glass fibres and without plastering.	168
Figure 7.1. Modelling techniques for masonry: masonry element (a); detailed micro-modelling (b); simplified micro modelling (c); macro-modelling (d) [71].	172
Figure 7.2. Specimen for RILEM test and compressive constitutive diagram.	175
Figure 7.3. Set-up for tensile test on masonry.	176
Figure 7.4. Load-displacement curve from tensile test on masonry.	177
Figure 7.5. Biaxial strength of clay brick masonry.	178
Figure 7.6. Composite interface model.	179
Figure 7.7. Masonry failure mechanism: joint cracking (a); joint sliding (b); unit vertical cracking (c); unit diagonal cracking (d); masonry crushing (e).	180
Figure 7.8. Interface model and position of interfaces.	181
Figure 7.9. Layered composite material with periodical characteristics.	187

Figure 7.10. Two-steps homogenization procedure usually adopted for masonry structures.	188
Figure 7.11. Comparison between the yielding domain according to Hoffman and the experimental data.	191
Figure 7.12. Continuous yielding criterion for different level of tangential stress.	192
Figure 7.13. Yielding criteria according to Tresca and Von Mises.	195
Figure 7.14. Multi-directional cracking model.	198
Figure 7.15. Definition of model parameters.	201
Figure 8.1. Hysteretic response of masonry walls: a) flexure dominated response, b) shear dominated response (Magenes and Calvi, 1997) [96].	207
Figure 8.2. Failure Modes of In-plane Masonry Walls (Tian Yi et al., 2006) [97].	208
Figure 8.3. Evolution of damage and structural degradation in confined masonry walls failing under diagonal tension (Ruiz-García and Alcocer, 1998) [101].	209
Figure 8.4. Stiffness degradation function for different levels of vertical load, proposed by (Tomazevic et al., 1996) [103].	211
Figure 8.5. Stiffness degradation vs. shear stresses for different levels of precompression (Bosiljkov et al., 2005) [104].	211
Figure 8.6. Structural components modelling techniques for masonry wall system (a): lumped masses (b); equivalent frame (c); panel system (d) [71].	213
Figure 8.7. Modified wide column model for push-over analysis (Gilmore at al., 2009) [109].	214
Figure 8.8. Idealized backbone curve for confined masonry walls (Gilmore at al., 2009) [109].	215
Figure 8.9. Modelling Details for Piers in the Computer Program (Salonikios et al., 2003) [111].	216
Figure 8.10. Spread Nonlinearity Approach in EFM (Belmouden and Lestuzzi, 2007) [114].	218
Figure 8.11. Limit analysis model for perforated URM wall; a) wall, b) failure mechanism (Orduña, 2003) [120].	220

Figure 9.1. Specimen under uniaxial compressive load along the direction orthogonal to bed joints.	222
Figure 9.2. Results of the compressive tests along the direction orthogonal to bed joints.	223
Figure 9.3. Interval of confidence of the mean curve.	224
Figure 9.4. Results of the compressive tests along the direction parallel to bed joints.	225
Figure 9.5. Comparison between mean curves from experiments and analytical constitutive model for compressive lading orthogonal (a) and parallel (b) to bed joints.	228
Figure 9.6. Finite Element (CHX60) used for 3-D model of masonry panels.	229
Figure 9.7. Material model adopted for mortar and bricks.	230
Figure 9.8. Tensile cut-off criterion.	230
Figure 9.9. Linear tension softening.	231
Figure 9.10. Constant shear retention.	232
Figure 9.11. Parabolic compressive behaviour.	232
Figure 9.12. Parabolic compressive behaviour.	233
Figure 9.13. Three-dimensional geometry definition for the masonry panel.	235
Figure 9.14. Three-dimensional mesh division for the masonry panel.	236
Figure 9.15. Material assignment for the masonry panel.	237
Figure 9.16. Three-dimensional modelling of the masonry panel: geometry definition (a), meshing (b) and material assignment (c).	238
Figure 9.17. Comparison between the numerical curves obtained for $G_{fc,b} = 6.0$ N/mm and the experimental results.	240
Figure 9.18. Comparison between the numerical curves obtained for $G_{fc,b} = 3.2$ N/mm and the experimental results.	241
Figure 9.19. Comparison between the numerical curve obtained for $G_{fc,j} = 1.5$ N/mm and $G_{fc,b} = 4.5$ N/mm and the experimental results.	242
Figure 9.20. Flat plane stress element.	243
Figure 9.21. Finite Element (CQ16M) used for 2-D model of masonry panels.	244

Figure 9.22. Two-dimensional geometry definition (a) and meshing (b) for the masonry panel.	244
Figure 9.23. Comparison between bi-dimensional homogeneous model and detailed three-dimensional model.	246
Figure 10.1. Finite Element (CQ16M) used for 2-D model of masonry panels.	249
Figure 10.2. Rankine/Von Mises plasticity model used for brick masonry panels.	250
Figure 10.3. Adopted non-linear laws: exponential tensile softening (a) and parabolic compressive law (b).	250
Figure 10.4. FE model of adobe masonry panel: geometry definition (a), mesh and constraints assignment (b) and loading conditions (c).	251
Figure 10.5. Comparison between numerical curves obtained for different values of compressive fracture energy ($G_{ft} = 0.01$ N/mm).	254
Figure 10.6. Comparison between numerical curves obtained for different values of tensile fracture energy ($G_{fc} = 3.0$ N/mm).	255
Figure 10.7. Comparison between numerical curves obtained for three sets of fracture energy (G_{ft} , G_{fc}) values.	256
Figure 10.8. Comparison between the numerical curve obtained for $G_{ft} = 0.011$ N/mm, $G_{fc} = 2.8$ N/mm and the experimental envelope curves for the unreinforced adobe brick wall.	257
Figure 10.9. Constitutive laws for the homogeneous adobe masonry material: tension (a) and compression (b).	257
Figure 10.10. Vectors for principal stresses at different load level: horizontal displacement of 3 mm (a), 6 mm (b), 10 mm and (c) and 14 mm (d).	258
Figure 10.11. Vertical strain ϵ_{yy} different load level: horizontal displacement of 3 mm (a), 6 mm (b), 10 mm and (c) and 14 mm (d).	259
Figure 10.12. Crack pattern at different load level: horizontal displacement of 3 mm (a), 6 mm (b), 10 mm and (c) and 14 mm (d).	259
Figure 10.13. FE model of reinforced adobe masonry panel: reinforcement layer (a), mesh and constraints assignment (b) and loading conditions (c).	261

Figure 10.14. Grid reinforcement: particle in 2-D (a); particle in solid (b); stresses (c).	263
Figure 10.15. Grid reinforcement in plane stress element.	264
Figure 10.16. Equivalent thickness of the reinforcement grid.	265
Figure 10.17. Comparison between the numerical curve and the experimental envelope curve for the reinforced adobe brick wall.	267
Figure 10.18. Comparison between the numerical curve and the experimental envelope curves for the unreinforced and reinforced adobe brick wall.	267
Figure 10.19. Comparison between the numerical curve for the case with and without polymeric grid.	268
Figure 10.20. Comparison between the numerical curve for the wall reinforced with polyester grid and GFRP grid.	269
Figure 10.21. Definition of mechanical parameters from the nonlinear shear – displacement curve (a) and construction of the equivalent bilinear curve (b).	270
Figure 10.22. Outline of the reinforced masonry wall.	271
Figure 10.23. Effect of FRP grid axial stiffness: numerical curves for adobe and tuff masonry for mortar layer thickness $t_p = 30$ mm and shape factor $h/d = 1.0$.	277
Figure 10.24. Effect of FRP grid axial stiffness: numerical curves for adobe and tuff masonry for mortar layer thickness $t_p = 30$ mm and shape factor $h/d = 2.0$.	277
Figure 10.25. Tangent elastic stiffness increment due to reinforcement for adobe (a) and tuff (b) masonry walls with shape factor $h/b = 1.0$.	278
Figure 10.26. Maximum horizontal force increment due to reinforcement for adobe (a) and tuff (b) masonry walls with shape factor $h/b = 1.0$.	280
Figure 10.27. Maximum horizontal force increment due to reinforcement for adobe (a) and tuff (b) masonry walls with shape factor $h/b = 1.3$.	280
Figure 10.28. Maximum horizontal force increment due to reinforcement for adobe (a) and tuff (b) masonry walls with shape factor $h/b = 2.0$.	280

Figure 10.29. Drift increment due to reinforcement for adobe (a) and tuff (b) masonry walls with shape factor $h/b = 1.0$.	281
Figure 10.30. Drift increment due to reinforcement for adobe (a) and tuff (b) masonry walls with shape factor $h/b = 1.3$.	282
Figure 10.31. Drift increment due to reinforcement for adobe (a) and tuff (b) masonry walls with shape factor $h/b = 2.0$.	282
Figure 10.32. Strength increments and regression for adobe masonry walls for $h/b = 1.0, 1.3$ and 2.0 .	283
Figure 10.33. Strength increments and regression for tuff masonry walls for $h/b = 1.0, 1.3$ and 2.0 .	283
Figure 10.34. Non-linear curves of adobe (a) and tuff (b) panels with $h/b = 1.0$ for different reinforcement configurations providing similar strength increment.	284
Figure 10.35. Maximum horizontal force increment due to reinforcement for adobe (a) and tuff (b) masonry walls with shape factor $h/b = 1.0$ versus $f_{pc}A_i / f_cA$.	285
Figure 10.36. Maximum horizontal force increment due to reinforcement for adobe (a) and tuff (b) masonry walls with shape factor $h/b = 1.3$ versus $f_{pc}A_i / f_cA$.	285
Figure 10.37. Maximum horizontal force increment due to reinforcement for adobe (a) and tuff (b) masonry walls with shape factor $h/b = 2.0$ versus $f_{pc}A_i / f_cA$.	285
Figure 11.1. Palazzo Bevere-Gambacorta in the historic centre of the city of Ariano Irpino.	288
Figure 11.2. Historical photo of Palazzo Bevere-Gambacorta.	288
Figure 11.3. Floor plans of Palazzo Bevere-Gambacorta: ground floor (a) and first floor (b).	290
Figure 11.4. Cross-sections of Palazzo Bevere-Gambacorta along the short (a) and long side (b).	291
Figure 11.5. Example of slab with steel profiles.	292
Figure 11.6. Example of original wooden slab.	292
Figure 11.7. Pictures of the considered type of masonry (PI).	295

Figure 11.8. Position of the single and double flat-jack tests execution: ground floor (a) and first floor (b).	296
Figure 11.9. Position of the foundation excavations.	297
Figure 11.10. Particular of the foundation structures.	298
Figure 11.11. Macro-element modelling of a masonry wall (a); 3-D building model assembling (b) [128].	299
Figure 11.12. Non-linear beam degrading behaviour [128].	300
Figure 11.13. Position of walls, slabs and vaults in the model of the building: ground floor (a) and first floor (b).	301
Figure 11.14. Orientation of slabs in the model of the building: basement level (a), ground floor (b) and first floor (c).	302
Figure 11.15. Three-dimensional views of the model of the building.	303
Figure 11.16. Pushover curve for +X direction for force distribution proportional to masses.	310
Figure 11.17. Pushover curve for +Y direction for force distribution proportional to masses.	310
Figure A.1. Adobe brick masonry wall with aspect ratio $h/b = 1.0$: relative variation of $\Delta k_{el,s,R}/k_{el,s,UR}$ (a), $\Delta V_{u,R}/V_{u,UR}$ (b), $\Delta \mu_R/\mu_{UR}$ (c), $\Delta k_{el,s,R}/k_{el,s,UR}$ (d), $\Delta V_{max,R}/V_{max,UR}$ (e), d_r (f) with respect to the axial stiffness $E_f A_f/EA$, for different levels of compressive strength $2t_p \cdot f_{pc}/t \cdot f_c$.	336
Figure A.2. Adobe brick masonry wall with aspect ratio $h/b = 1.3$: relative variation of $\Delta k_{el,s,R}/k_{el,s,UR}$ (a), $\Delta V_{u,R}/V_{u,UR}$ (b), $\Delta \mu_R/\mu_{UR}$ (c), $\Delta k_{el,s,R}/k_{el,s,UR}$ (d), $\Delta V_{max,R}/V_{max,UR}$ (e), d_r (f) with respect to the axial stiffness $E_f A_f/EA$, for different levels of compressive strength $2t_p \cdot f_{pc}/t \cdot f_c$.	338
Figure A.3. Adobe brick masonry wall with aspect ratio $h/b = 2.0$: relative variation of $\Delta k_{el,s,R}/k_{el,s,UR}$ (a), $\Delta V_{u,R}/V_{u,UR}$ (b), $\Delta \mu_R/\mu_{UR}$ (c), $\Delta k_{el,s,R}/k_{el,s,UR}$ (d), $\Delta V_{max,R}/V_{max,UR}$ (e), d_r (f) with respect to the axial stiffness $E_f A_f/EA$, for different levels of compressive strength $2t_p \cdot f_{pc}/t \cdot f_c$.	340
Figure A.4. Tuff block masonry wall with aspect ratio $h/b = 1.0$: relative variation of $\Delta k_{el,s,R}/k_{el,s,UR}$ (a), $\Delta V_{u,R}/V_{u,UR}$ (b), $\Delta \mu_R/\mu_{UR}$ (c), $\Delta k_{el,s,R}/k_{el,s,UR}$ (d), $\Delta V_{max,R}/V_{max,UR}$ (e), d_r (f) with respect to the axial stiffness $E_f A_f/EA$, for different levels of compressive strength $2t_p \cdot f_{pc}/t \cdot f_c$.	342

- Figure A.5.** Tuff block masonry wall with aspect ratio $h/b = 1.3$: relative variation of $\Delta k_{el,s,R}/k_{el,s,UR}$ (a), $\Delta V_{u,R}/V_{u,UR}$ (b), $\Delta \mu_R/\mu_{UR}$ (c), $\Delta k_{el,s,R}/k_{el,s,UR}$ (d), $\Delta V_{max,R}/V_{max,UR}$ (e), d_r (f) with respect to the axial stiffness $E_r A_f/EA$, for different levels of compressive strength $2t_p \cdot f_{pc}/t \cdot f_c$. 344
- Figure A.6.** Tuff block masonry wall with aspect ratio $h/b = 2.0$: relative variation of $\Delta k_{el,s,R}/k_{el,s,UR}$ (a), $\Delta V_{u,R}/V_{u,UR}$ (b), $\Delta \mu_R/\mu_{UR}$ (c), $\Delta k_{el,s,R}/k_{el,s,UR}$ (d), $\Delta V_{max,R}/V_{max,UR}$ (e), d_r (f) with respect to the axial stiffness $E_r A_f/EA$, for different levels of compressive strength $2t_p \cdot f_{pc}/t \cdot f_c$. 346
- Figure A.7.** Adobe brick masonry wall with aspect ratio $h/b = 1.0$: relative variation of $\Delta k_{el,s,R}/k_{el,s,UR}$ (a), $\Delta V_{u,R}/V_{u,UR}$ (b), $\Delta \mu_R/\mu_{UR}$ (c), $\Delta k_{el,s,R}/k_{el,s,UR}$ (d), $\Delta V_{max,R}/V_{max,UR}$ (e), d_r (f) with respect to the relative equivalent strength $f_{pc} A_f/f_c A$ of the reinforcement. 348
- Figure A.8.** Adobe brick masonry wall with aspect ratio $h/b = 1.3$: relative variation of $\Delta k_{el,s,R}/k_{el,s,UR}$ (a), $\Delta V_{u,R}/V_{u,UR}$ (b), $\Delta \mu_R/\mu_{UR}$ (c), $\Delta k_{el,s,R}/k_{el,s,UR}$ (d), $\Delta V_{max,R}/V_{max,UR}$ (e), d_r (f) with respect to the relative equivalent strength $f_{pc} A_f/f_c A$ of the reinforcement. 350
- Figure A.9.** Adobe brick masonry wall with aspect ratio $h/b = 2.0$: relative variation of $\Delta k_{el,s,R}/k_{el,s,UR}$ (a), $\Delta V_{u,R}/V_{u,UR}$ (b), $\Delta \mu_R/\mu_{UR}$ (c), $\Delta k_{el,s,R}/k_{el,s,UR}$ (d), $\Delta V_{max,R}/V_{max,UR}$ (e), d_r (f) with respect to the relative equivalent strength $f_{pc} A_f/f_c A$ of the reinforcement. 352
- Figure A.10.** Tuff block masonry wall with aspect ratio $h/b = 1.0$: relative variation of $\Delta k_{el,s,R}/k_{el,s,UR}$ (a), $\Delta V_{u,R}/V_{u,UR}$ (b), $\Delta \mu_R/\mu_{UR}$ (c), $\Delta k_{el,s,R}/k_{el,s,UR}$ (d), $\Delta V_{max,R}/V_{max,UR}$ (e), d_r (f) with respect to the relative equivalent strength $f_{pc} A_f/f_c A$ of the reinforcement. 354
- Figure A.11.** Tuff block masonry wall with aspect ratio $h/b = 1.3$: relative variation of $\Delta k_{el,s,R}/k_{el,s,UR}$ (a), $\Delta V_{u,R}/V_{u,UR}$ (b), $\Delta \mu_R/\mu_{UR}$ (c), $\Delta k_{el,s,R}/k_{el,s,UR}$ (d), $\Delta V_{max,R}/V_{max,UR}$ (e), d_r (f) with respect to the relative equivalent strength $f_{pc} A_f/f_c A$ of the reinforcement. 356
- Figure A.12.** Tuff block masonry wall with aspect ratio $h/b = 2.0$: relative variation of $\Delta k_{el,s,R}/k_{el,s,UR}$ (a), $\Delta V_{u,R}/V_{u,UR}$ (b), $\Delta \mu_R/\mu_{UR}$ (c), $\Delta k_{el,s,R}/k_{el,s,UR}$ (d), $\Delta V_{max,R}/V_{max,UR}$ (e), d_r (f) with respect to the relative equivalent strength $f_{pc} A_f/f_c A$ of the reinforcement. 358

LIST OF TABLES

Table 3.1. Mechanical properties of materials [5].	30
Table 3.2. Tested panels and geometrical properties adopted in the models [5].	31
Table 3.3. Compressive tests on tuff specimens [6].	35
Table 3.4. Three-points bending tests on tuff specimens [6].	35
Table 3.5. Compressive tests on mortar specimens [6].	35
Table 3.6. Three-points bending tests on mortar specimens [6].	36
Table 3.7. Mechanical characteristics of carbon fiber net and mortar [6].	36
Table 3.8. Geometrical characteristics of tested panels [6].	37
Table 3.9. Mechanical properties of employed materials [7].	42
Table 3.10. Mechanical properties of panels [7].	42
Table 3.11. Inelastic properties of materials [7].	44
Table 3.12. Comparison between analytical and experimental strength [7].	48
Table 3.13. Mechanical characteristics of materials constituting masonry [11].	52
Table 3.14. Comparison between strength from experiment and from code regulations [11].	55
Table 3.15. Components and dimensional characteristics of panels [12].	58
Table 3.16. Mechanical characteristics of masonry components [12].	58
Table 3.17. Mechanical characteristics of masonry components [12].	59
Table 5.1. Overview of the experimental campaign on masonry walls.	95
Table 5.2. Results of compressive tests on adobe bricks.	99
Table 5.3. Results of bending tests on adobe bricks.	99
Table 5.4. Adobe bricks specifications.	99
Table 5.5. Bricks and mortars specifications by the producer.	100
Table 5.6. Steel wire ropes and geo-nets specifications by the producer.	100
Table 5.7. Summary of results from experimental tests on masonry walls.	105
Table 5.8. Results of tensile tests on mortar specimens.	145
Table 5.9. Results of compression tests on mortar specimens.	147
Table 5.10. Results of shear tests on mortar specimens.	149

Table 5.11. Results of mechanical tests on unreinforced and reinforced mortar specimens.	150
Table 6.1. Geometrical properties of specimens and experimental results.	159
Table 9.1. Results from compressive tests along the direction orthogonal to bed joints.	225
Table 9.2. Results from compressive tests along the direction parallel to bed joints.	226
Table 9.3. Mechanical properties for tuff units and mortar joints (Parisi et al., 2012) [123].	239
Table 9.4. Mechanical properties for tuff units and mortar joints assumed in the model.	239
Table 9.5. Compressive fracture energy for tuff units and mortar joints assumed in the model.	240
Table 9.6. Compressive fracture energy for tuff units and mortar joints assumed in the model.	241
Table 9.7. Compressive fracture energy for tuff units and mortar joints assumed in the model.	242
Table 9.8. Mechanical properties for the homogeneous material assumed in the model.	245
Table 10.1. Mechanical properties for the equivalent material assumed in the model of unreinforced masonry wall.	253
Table 10.2. Cases of fracture energies for $G_{ft} = 0.01$.	253
Table 10.3. Cases of fracture energies for $G_{fc} = 3.0$ N/mm.	255
Table 10.4. Combination of tensile and compressive fracture energies assumed in the model.	256
Table 10.5. Mechanical properties for the equivalent material adopted for adobe brick masonry.	261
Table 10.6. Mechanical properties for the polymeric grid adopted in the model.	265
Table 10.7. Mechanical properties for the mortar layers adopted in the model.	265
Table 10.8. Cases of fracture energies for the mortar layers.	266
Table 10.9. Values for the mechanical parameters for adobe and tuff reinforced masonry walls assumed in the parametric analysis.	272

Table 10.10. Values for the geometrical and mechanical parameters assumed in the parametric analysis.	272
Table 10.11. Cases of analysis for the adobe brick masonry wall.	275
Table 10.12. Cases of analysis for the tuff block masonry wall.	276
Table 11.1. Seismic hazard parameters for Ariano Irpino, Italy.	304
Table 11.2. Parameters of the elastic spectra for every limit state.	304
Table 11.3. Mechanical properties of the considered material.	305
Table 11.4. Results of the pushover analysis for the unreinforced building.	306
Table 11.5. Mechanical parameters considered for the different cases of analysis.	308
Table 11.6. Results of the pushover analysis for the reinforced building (Increment of strength).	309
Table 11.7. Results of the pushover analysis for the reinforced building (Increment of strength and ductility).	308

1 INTRODUCTION

A large portion of the worldwide built heritage and most of the constructions currently present in European countries consist of existing buildings which recurring constructive typology is represented by structural masonry walls. The experience has shown that these classes of buildings are characterized by a high vulnerability when subjected to earthquakes. The seismic events occurred during the last years have revealed, in fact, that unreinforced masonry buildings (URM) exhibit poor capacities to withstand horizontal actions and are prone to suffer high damage.

The failure of URM walls produces loss of resistance capacity against actions induced by earthquake and, when occurring unevenly throughout the building, it is also cause of reduction in the energy dissipation capacity of the whole structure. The most widespread collapsing mechanisms commonly encountered in URM buildings subjected to seismic forces involve both the out-of-plane and in-plane failure modes. Since unreinforced masonry walls are the resistant system, or contribute to the lateral seismic resistance of the building, the first possible failure mode is due to in-plane shear failure. The other type of failure is represented by the out-of-plane flexural failure due to the orthogonal inertial forces induced by the earthquake. In addition, the excessive out-of-plane bending is also a major reason for the reduction in the vertical load carrying capacity of unreinforced masonry walls.

Composites materials, in particular Fiber Reinforced Polymers (FRP), offer an attractive strengthening possibility for existing and historical unreinforced masonry structures. In the past few decades, composites have successfully been used in different construction applications including strengthening of reinforced concrete, steel and timber structures. Lately, several studies have been conducted for evaluating the use of FRP for repairing and strengthening of both unreinforced and

reinforced masonry walls subjected to seismic actions, wind and lateral earth pressure. In most cases, both in-plane shear and out-of-plane flexural strengthening are required to upgrade the seismic performance of old and historical unreinforced masonry structures. In order to fulfil these demands, multidirectional composite systems are required (e.g. cross-ply, angle-ply or quasi-isotropic lamination) to achieve optimum retrofit design.

1.1 MOTIVATIONS

The high vulnerability and the extensive damaging suffered by particular classes of structures, including unreinforced masonry buildings, in case of seismic event, threatening their serviceability and safety, have brought to light the necessity to strengthen them appropriately in order to achieve an upgrading to the required seismic capacity in terms of resistance and ductility. The choice of the strengthening system should be calibrated in order to prevent the failure mechanisms of unreinforced masonry walls and in function of the way the structure is required to behave. If the seismic behaviour is taken into account, the structure should be retrofitted through the implementation of measures to prevent the previously described failure mechanisms and able to improve the overall ductility and energy dissipation capacity.

Masonry elements have been reinforced throughout the years by traditional methods involving, for example, filling of cracks or voids by grouting, stitching of large cracks or other weak areas with metallic elements or concrete, application of reinforced grouted perforations to improve the cohesion and tensile strength of masonry, post-tensioning with steel ties, single- or double-sided jacketing by steel mesh reinforced concrete. All the previously reported traditional technique are affected by some disadvantages that have more and more restricted their application and prompted researchers to seek better solutions. In order to overcome the drawbacks commonly encountered when facing with traditional techniques, the use of composite Fibre-Reinforced Polymers (FRP) has been thus successfully proposed.

Different strengthening methods based on the employment of FRP have been proposed and experimentally/numerically studied during the last decades have been conducted. All the developed techniques take advantage of the well-known benefits proper of these materials including, above all, excellent mechanical properties, high strength-to-weight ratio, high resistance to corrosion in comparison to similar metallic strengthening systems, ease of application, preservation of the geometrical and architectural detail of the walls. The more common systems make use of FRP reinforcement in form of laminates or sheets externally bonded to the surface of the element to be strengthened (FRP-EBR) with different configurations and type of reinforcing or bonding materials. Other techniques recently studied involve the use of FRP rods mounted near the surface (NSM) of the wall in epoxy-filled grooves, that can also follow the bed and head joints of masonry. It is noted that the NSM technique can be more attractive since it does not require the installation of anchoring devices as in some cases is necessary for the externally applied FRP laminates and for aesthetic requirements. Also, it has been showed that NSM retrofitted elements exhibit no worse performances than the case of strengthening with externally bonded FRP.

Alternative possibilities to strengthen URM walls subjected to out-of-plane and in-plane loadings continue to be proposed. One of them is represented by the use of textile-reinforced mortar (TRM) in substitution to the classical FRP overlays. In more recent applications the textile reinforcement is replaced by commercial FRP bi-directional grids, and the polymeric bonding resins substituted by cement- or lime-based mortars.

The present study is focused on the investigation of the mechanical behaviour of a particular strengthening system for unreinforced masonry walls retrofitting. The reinforcing system for this purpose is realized by mortar layers embedding a FRP reinforcement in form of grid. It is intended to externally strengthen the masonry walls applying the FRP reinforced mortar layers on its surfaces. The main interest in the study of this strengthening technique is related to the promising possibility it offers in the upgrading of the out-of-plane flexural behaviour and in-plane shear behaviour of the system to which it can be applied. Moreover, the performances of the whole assemblage need to be investigated for monotonic loading

state as well as for cycling loading conditions. Another important issue to address is also the assessment of the effectiveness of the considered strengthening system in the improvement of the overall ductility of reinforced elements.

It is finally noted that in the last decades different aspect related to the field of retrofitting of URM have been explored by experimental campaigns and numerical studies. The previous researches have been focused on the investigation of the behaviour of retrofitted URM walls regarding the in-plane actions, the out-of-plane bending and, in some cases, the cyclic behaviour has been considered. In particular, the various possible strengthening technique have been studied with respect to the type of materials and reinforcing configuration. Nevertheless, many issues regarding the evaluation of the actual behaviour of these techniques, and the effectiveness of some of them in the improvement of the overall behaviour of structural members to which they are applied, remain still open.

1.1.1 Why the use of FRP composites for masonry strengthening and retrofitting

A significant motivation for the structural strengthening of masonry buildings is given by the necessity to repair the damages produced by the earthquakes and, particularly, to provide an appropriate safety level in case of new seismic event. In this framework, the use of fiber-reinforced composite materials represents an important innovation, which is finding more and more employment from the practical applications point of view. The technique of bonding fibre reinforced polymer (FRP) materials is a consolidated technology in the application on reinforced concrete structures and it is in constant development also in the application on unreinforced masonry buildings. FRPs materials are composite materials consisting of high strength fibres (in tension) that are embedded in a matrix. The fibres are typically carbon, glass, or aramid and the resin is usually epoxy. In last application, the use of an inorganic matrix, such as cement or lime mortar, is developing.

From the analysis of experimental tests on reinforced panels some advantages due to the use of FRP composites for strengthening of masonry

structures come to light. One of the advantages lies in the high mechanical characteristics of composites materials, which allow to reach important strength levels, with no relevant increment of static loads on the structure. The employment of FRP materials in form of strips or grids does not produce significant increase of mass and stiffness of the structure, which may be responsible of modifications in the dynamic response of the building against seismic actions. Moreover, the results of the studies carried out in the last decades showed an increment of the in-plane resistance and ductility of strengthened panels. Also, compared to other traditional strengthening methods, FRP composites materials do not affect the aesthetic aspect of buildings' façades and, since they have limited thickness, do not invade usable spaces of the building. Finally, the application is fast and easy reducing the time of suspending the functionality of the building. It is evident that the use of FRP composites can be an effective alternative for the improvement of the in-plane and out-of-plane strength and for the displacement capacity of masonry walls.

1.1.2 Why the study of bond between FRP and masonry

The FRP reinforcement is designed to provide tensile strength to a masonry wall. This increases the strength and ductility of the masonry wall, which in turn improves the behaviour of the wall during an extreme loading event.

Common FRP composites are completely elastic until failure, even though some attempts have been made recently to introduce some ductility into the composite material by using a combination of different modulus fibres.

The main disadvantage with using FRP materials for reinforcement is that they have brittle failure modes. FRP materials may fail by rupturing or, if no mechanical anchorage is provided, by debonding from the substrate material. Tensile force in the FRP is transferred through the adhesive to the masonry via shear. When the shear strength of the adhesive or the superficial layer of brick is exceeded, debonding occurs. Debonding may also occur along the interface between the brick and adhesive or the interface between the adhesive and FRP. Both rupture and debonding failure modes are brittle in nature, potentially leading to non-ductile

behaviour and catastrophic collapse. However, because a masonry wall is inherently brittle itself, the addition of FRP reinforcement may not only increase the strength but also increase the ductility, even though the FRP may eventually break or debond.

Moreover, when inorganic matrixes are used, in place of common polymeric adhesives, the debonding surface is no longer localized in the superficial layer of the support material, but rather inside the matrix, which represents the weaker element. Therefore, one of the limitation in the application of reinforcement in inorganic matrixes is related to the actual debonding strength, that represents one of the fundamental collapse mechanisms of the strengthening system.

1.1.3 Why the use of layers of mortar for FRP embedding

Alongside of traditional strengthening systems made by the use of fiber-reinforced composites with polymeric matrix, in last decades a new composite system developed featuring the use of high strength fibers immersed into an inorganic mortar matrix. Such an inorganic matrix has the purpose to provide the bond between the fibers and the support material. Even though mortars are less effective than resins as adhesive materials, they can offer many advantages in terms of cost and application modality, as well as they are characterized by transpirability and resistance against fire. Moreover, they are particularly suitable for interventions of strengthening of masonry elements, where it is not possible to take completely advantage of the superior mechanical properties of traditional FRP materials, because of the different strength of the masonry material.

In the last years, the employment of reinforcement made by high strength fibers into inorganic matrixes has been successfully tested. This kind of matrix is compatible with the masonry substrate from the chemical, physical and mechanical point of view, and it offers several advantages if compared with traditional polymeric resins:

- It has a fire resistance comparable to the support material (concrete or masonry) to which it is applied, showing high performances and protecting the fibers from the direct exposure to high temperatures. Unlike the polymers,

whose mechanical properties decay significantly when a temperature of 60°C to 80°C is exceeded.

- It has a permeability comparable to that of masonry, allowing heat and humidity transfer towards the external environment, and thus a good transpirability of the strengthened element. This is a very important aspect particularly for heritage buildings in which are present decoration and frescos to be protected.
- It permits the reinforcement system to be applied also on wet or moist supports, unlike the traditional FRP systems, where the resins (polymeric or epoxy) do not catalyse in presence of water.
- It makes easier the application of the reinforcement onto irregular and rough surfaces. It is the mortar itself that is able to fill the irregularities of the surface (considering the thickness of the system) and without necessity of previous levelling or plastering.
- It is characterized by ease of application, being the mortar a commonly used material, which does not require particular caution or high specialized workmanship.

In the literature there are still few contribution regarding the experimental behaviour of strengthening systems with mortar matrix. Among the application on structural elements, this kind of strengthening systems have been applied onto the surfaces of masonry walls in order to improve the capacity of the panels through a tensile stress redistribution over a wider surface. Further experimental research is needed in order to get more information about the improvement in terms of in-plane and out-of-plane strength and ductility of the reinforced elements.

1.1.4 Why the non-linear modelling of masonry structures

Masonry represents a composite material made by units and joint, with or without mortar, and different bond arrangements. The issues associated with modelling of ancient and modern masonry structures are very different due to the high

variability in the physical and mechanical characteristics of the material, which is defined by a three-dimensional internal arrangement and which exhibits distinct directional properties due to the presence of mortar joints, which act as planes of weakness.

A common feature of quasi-brittle materials, like clay brick, mortar, ceramics, rock or concrete, which fail due to a process of progressive internal crack growth, is a non-linear behaviour for low levels of load. This high non-linear behaviour is due to the internal heterogeneity of the material, due to the presence of different phases and defects. In addition, both mortar and bricks may include micro-cracks due to shrinkage even before application of loads

Advanced non-linear structural modelling (using numerical techniques) is necessary for understanding the behaviour and damage of complex masonry constructions, understanding experimental testing programmes and to assist in the development of design rules. This is also the case for masonry structures that are reinforced with FRP materials. The structural behaviour of masonry elements is characterized by phenomena, such as strain localization, damage, and friction, which need to be modelled at fine scale. Fine-scale modelling represents a significant challenge with regards to numerical simulations, due to its computational expensiveness and hard manageability. Generally, it requires also sophisticated solution strategies which cannot be effortlessly used in engineering software for structural analysis and design.

Furthermore, masonry is a material which exhibits a non-linear behaviour for early stages of loading and low level of stresses. The post-peak behaviour of the material is characterized by a gradual decrease of mechanical resistance under a continuous increase of deformation, namely a softening behaviour.

Accurate modelling requires a thorough experimental description of the material, able to reproduce comprehensively all the possible failure mechanisms of the material. Bond between unit and mortar is often the weakest link in masonry assemblages. The non-linear response of the joints, which is then controlled by the unit-mortar interface, is one of the most relevant features of masonry behaviour. Two different phenomena occur in the unit-mortar interface, one associated with tensile failure (mode I) and the other associated with shear failure (mode II).

The non-linear finite element method is the most common numerical technique used to model the behaviour of masonry structures (with and without FRP reinforcement) and allow to take into account the materials behaviour but also the bond relationship at the interface with the FRP system.

Other numerical approaches such as limit analysis and the discrete element method have also been used. To accurately model the behaviour of an FRP strengthened masonry wall, the structural response and failure modes of the masonry, FRP reinforcement and the interface between them (bond) need to be considered.

1.1.5 Why the use of simplified methods for masonry structures

The analysis of masonry structures by means of detailed modelling strategies can only be feasible for limited portions or sub assemblages, or can be used in order to study local phenomena involving well defined elements. If the analysis concerns the whole structural system, computational time and numerical issues make necessary to follow different approaches for the study of masonry buildings. Different methods for the simplified non-linear analysis of unreinforced masonry buildings have been presented over the year. Particularly these methods are based on the idealization of the structure by means of an equivalent frame describing multi-storey walls subjected to in-plane loads. The formulation of such model conceptually simple and makes use of simple strength and ductility formulations for piers and spandrels. An important issue concerns the non-linear behaviour to be assumed for the behaviour of such elements and their displacement capacity, as well as the study of the influence of the spandrel beam element on the global behaviour of the walls.

The simplicity of the geometric model allows increased complexity on the loading side and in the non-linear dynamic response. A model based on the equivalent frame approximates the actual structural geometry more accurately by using beams and joints as structural components. This approach allows the assessment of the system behaviour in more detail. In particular, it is possible to

determine the sequential formation of local, predefined failure mechanisms and overall collapse, both statically and dynamically.

1.2 AIMS, SCOPE AND LIMITATIONS

The main issues investigated in the present programme are related to the study of the structural behaviour and the definition of simplified strategies for global modelling of masonry buildings. The effect of strengthening of masonry walls by means of FRP grid reinforced mortar layers is investigated. In particular, the strengthening technique taken into account in the research is represented by externally applied mortar panels embedding a FRP reinforcement in form of bi-directional grid. The mortar encloses the reinforcement passing through the grid's openings allowing an effective mechanical interlocking that assure a composite behaviour of the system. In addition, the use of lime- or cement-based mortar allows the development of a better bonding between the strengthening system and the surface of the masonry panel. The effectiveness of the collaboration between reinforcement and substrate will be also investigated in the course of the research programme.

The described FRP reinforced mortar panels are applied on the surfaces of the unreinforced masonry wall in a symmetric configuration, and can be also connected to the substrate by means of an adequate anchoring system. The effectiveness of the reinforcing system will be explored in case of cyclic loading conditions. The research aims to assess the effectiveness in the upgrading of the overall behaviour of the strengthened URM walls. The retrofitting of masonry elements through FRP grid reinforced mortar layer is expected to increase the in-plane shear resistance, provide the system an enhanced ductility, assure a higher integrity and reduce the damage of the panels in order to contain serviceability problems. Thus, the performances of the URM walls strengthened by means of this reinforcing system will be investigated. An experimental programme on prototypes as well as the FEM modelling of the system will be carried out in order to replicate the structural behaviour of the assemblage.

The study is firstly focused on the characterization of the mechanical behaviour of the masonry in compression by means of finite element modelling. For this purpose, the influence of the presence of mortar joints, as well as the influence of different non-linear parameters on the post-peak behaviour of the material is investigated. The numerical modelling of the unreinforced and reinforced masonry panels tested at the structural laboratory of the Institute of Theoretical and Applied Mechanics in Prague is performed, and the calibration of non-linear mechanical parameters of the involved materials, namely the masonry, as well as the properties of the reinforced layers' mortar, is carried out. On the basis of the previous results, the influence of the reinforcement on the global behaviour of the masonry walls, in terms of stiffness, strength and displacement capacity, is investigated by means of a parametric analysis. Different types of materials have been considered for the walls, and different values of mortar thickness and reinforcement grid stiffness have been considered for the analyses. Finally, a case study masonry building is modelled by means of the equivalent frame method in order to evaluate the global effect of the reinforcement system.

1.3 OBJECTIVES OF THE THESIS

The main objectives of the present research can be, finally, summarized as follows:

- Numerical study of masonry panels subjected to compressive loading at different levels of detail. Finite element models reproducing the actual geometry of units and mortar joints and homogenized models are used to investigate the influence of mechanical characteristics of masonry.
- Experimental study of the bond behaviour of masonry blocks externally bonded with different kinds of FRP materials.
- Experimental study the experimental in-plane cyclic behaviour of both unreinforced and reinforced masonry walls by means of mortar layers reinforced with polymeric grids. In particular, the objective is to evidence the critical aspects

of such reinforcement system in terms of failure modes, increments of in-plane resistance and displacement capacity.

- Assessment of the effectiveness of the FRP grid reinforced mortar layer in the upgrading and retrofitting of the overall behaviour of masonry walls with respect to the in-plane shear resistance and overall ductility;
- Numerical modelling of masonry walls reinforced by means of polymeric grids embedded in mortar layers subjected to in-plane loading, in order to determine the effectiveness of the technique, the fundamental shear mechanisms and the ductility of masonry panels. The results from the representative finite element model can be used as an instrument able to replicate the structural behaviour of the global system.
- Investigation of the influence of the reinforcement stiffness and strength on the global behaviour of the masonry walls. Two types of masonry materials have been considered, characterized by different values of compressive strength and elastic stiffness. Parameters like the thickness of the reinforced mortar layers and the axial stiffness of the reinforcement have been varied in the analysis, in order to quantitatively evaluate the effect on the strength and displacement capacity of the reinforced panels.
- Analysis of a case study historical masonry building and study of the influence of the reinforcement system on the enhancement of its seismic capacity.

1.4 THESIS OUTLINE

The present thesis has been organized in twelve chapters, including an introductory part (*Chapter 1*) in which an overall outline of the thesis motivation, scopes and organisation is given.

In *Chapter 2* a description of the main issues related to the behaviour of masonry building under seismic action is given. The structural arrangement and behaviour of masonry structures is described and the main failure mechanisms of masonry walls are explained.

In *Chapter 3* a review of different experimental campaigns carried out on masonry panels subjected to vertical and in-plane loadings available in the technical literature is presented.

In *Chapter 4* a brief overview in relation to the traditional strengthening techniques for masonry walls used in the past decades is illustrated. The same chapter provides a comprehensive study of the relevant literature in the same field related to the strengthening of masonry walls. Experimental and theoretical studies are reviewed, with reference to the available existing strengthening techniques for masonry walls, the use of Fibre Reinforced Polymers (FRP) with different arrangements, the evaluation of the contribution of these techniques to the improvement of the mechanical capacity of strengthened elements. Particular attention is paid to the studies concerning the employed of mortar layers reinforced with FRP.

In *Chapter 5* the experimental tests on masonry walls carried out in the ITAM Structural Laboratory are described, reporting information about the specimens, in terms of geometry and employed materials, the strengthening systems and the test set-up. The experiments consist of in-plane shear tests on masonry brick walls strengthened with different techniques and subjected to a combination of compression and cyclic shear loading. Furthermore, the mechanical tests campaign on unreinforced and reinforced mortar specimens and bricks is also described. In particular, the employed material, namely mortars and reinforcement, and the preparation of specimens is reported and the results of the characterization tests are presented.

In *Chapter 6* the results of bond tests on tuff blocks externally bonded with various types of FRP systems and carried out at University of Sannio are reported.

Chapter 7 describes the behaviour of masonry at the material level and presents a review of all the possible modelling, with reference to their level of complexity and capability in the description of the actual behaviour of the material. Particular attention is given to modelling of cracks formation in quasi-brittle materials and different cracking concepts, since the choice of modelling strategy represents one of the most relevant issue when studying a masonry structure or element.

In *Chapter 8* the main aspects related to the methods of analysis and assessment of the global behaviour of masonry structures are analysed. The response of masonry walls is described with respect to the different sources of non-linearity, failure mechanisms and softening behaviour.

The numerical modelling through finite elements techniques of masonry panels subjected to compressive loading under control of displacement is carried out in *Chapter 9*. The non-linear behaviour of masonry is investigated through models characterized by different levels of complexity and considering a micro-modelling technique or a homogenized equivalent material.

In *Chapter 10* the numerical modelling of the masonry walls in the ITAM Structural Laboratory, described in Chapter 5, is carried out in order to produce an instrument to replicate the structural behaviour of the whole system. Both unreinforced and reinforced panels have been considered and modelled through macro-modelling approach and using a non-linear equivalent material. The chapter presents also the results of a parametric analysis, in order to study the influence of the reinforcement on the global behaviour of the masonry walls, in terms of stiffness, strength and displacement capacity, considering different types of materials and varying the reinforcement grid stiffness.

In *Chapter 11* is presented a case study masonry building. The structure is modelled by means of the equivalent frame method in order to evaluate the global effect of the reinforcement system.

In the final *Chapter 12* the major conclusions of the study are provided, together with a discussion and suggestions for future researches.

2 SEISMIC BEHAVIOUR OF MASONRY BUILDINGS

Masonry is a traditional form of construction that has been practiced for centuries in regions where stone and earthen materials are locally available. Masonry has been used for the construction of some of the most important monuments and structures around the world. Buildings of this type range from cultural and historical landmarks, often built by highly skilled stonemasons, to simple dwellings built by their owners in developing countries where stone or clay for brick elements are affordable and cost-effective building materials for housing construction. Masonry buildings can be found in many earthquake-prone regions and countries including Mediterranean Europe, North Africa, the Middle East, and Southeast Asia.

Houses of this construction type are found in urban and rural areas around the world. There are broad variations in construction materials and technology, shape, and the number of stories. Houses in rural areas are generally smaller in size and have smaller sized openings since they are typically used by a single family. Multi-family residential buildings in urban areas are often of mixed use - with a commercial ground floor and a residential area above. Houses in rural areas and suburbs of urban centres are built as detached structures, while housing units in urban centres often share a common wall. In hilly Mediterranean areas the number of stories varies from two (in rural areas) to five (in urban centres). These buildings have often experienced several interior and exterior repairs and renovations over the course of their useful lives. Typically, masonry houses are built by building owners themselves or by local builders without any formal training. The quality of construction in urban areas is generally superior to that found in rural areas.

2.1 SEISMIC VULNERABILITY OF MASONRY BUILDINGS

Masonry buildings are brittle in nature and one of the most vulnerable among the different types of structural buildings under strong earthquake shaking. Horizontal loads, induced by earthquake causes severe in-plane and out of plane forces in wall. A wall topples down easily if pushed horizontally at the top in a direction perpendicular to its plane (out-of-plane), but offers much greater resistance if pushed along its length (in-plane). The lateral load resistance of masonry buildings is mainly due to in-plane shear resistance of the masonry elements/piers.

Therefore detailed investigation on the in-plane shear behaviour of masonry thus becomes necessary. Earthquake performance of a masonry wall is very sensitive to the properties of its constituents, namely masonry units and mortar. The shear strength of masonry mainly depends upon the bond or adhesion at the contact surface between the masonry unit and the mortar. Thus, it is very important to improve the shear behaviour of masonry buildings. The primary gap identified through literature review was the lack of experimental research that addressed the response of masonry shear walls.

Unreinforced masonry structures are normally designed for vertical loads and since masonry has adequate compressive strength, the structures behave well as long as the loads are vertical. When such a masonry structure is subjected to lateral inertial loads during an earthquake, the walls develop shear and flexural stresses. The strength of masonry under these conditions often depends on the bond between brick and mortar (or stone and mortar), which is quite poor. This bond is also often very poor when lime mortars or mud mortars are used. A masonry wall can also undergo in-plane shear stresses if the inertial forces are in the plane of the wall. Shear failure in the form of diagonal cracks is observed due to this. However, catastrophic collapses take place when the wall experiences out-of-plane flexure. This can bring down a roof and cause more damage. Masonry buildings with light roofs such as tiled roofs are more vulnerable to out-of-plane vibrations since the top edge can undergo large deformations.

It is always useful to investigate the behaviour of masonry buildings after an earthquake, so as to identify any inadequacies in earthquake resistant design.

Studying types of masonry construction, their performance and failure patterns helps in improving the design and detailing aspects.

2.2 RESPONSE OF MASONRY BUILDINGS SUBJECTED TO SEISMIC ACTIONS

Masonry buildings differ from other types of buildings by the arrangement and relative stiffness of lateral load resisting elements. In case of masonry buildings, these structural elements are, normally, interconnected orthogonally to each other with relatively flexible diaphragms.

The resisting mechanism of a masonry building depends on the degree of connection of the structural parts. The horizontal forces are transferred from foundations to the in-plane walls during a seismic activity, which are the stiffest components of the building. The in-plane walls, if properly connected to diaphragm, transfer these forces to diaphragm, which ultimately transfer the forces to the attached walls in the out-of-plane direction. The diaphragm acts as a deep beam, simply-supported at the ends.

The diaphragm deflects, under the action of transmitted inertial forces, in an amount which depends upon the in- plane stiffness of the diaphragm. In case of a wooden diaphragm, the flexibility of the diaphragm can result in excessive deflection, causing damage to the walls connected to the diaphragm in the out-of-plane direction.

Separation of the walls transverse to the in-plane walls can also occur in the absence of proper connection between the diaphragm and the connecting walls. In such a case, the out-of-plane walls vibrate independently, thus increasing the vulnerability of the out-of-plane bending failure.

2.2.1 Seismic deficiencies of masonry structures

Masonry buildings are vulnerable to the effects of even moderate earthquakes. The significant thickness of vertical walls, often compounded by heavy

floors or roof, accounts for the heavy weight of these buildings, thus resulting in significant inertia forces being developed during an earthquake. As a building material, masonry usually has a significant strength when subjected to compression, and in particular stone is usually stronger than most other conventional masonry units (bricks and concrete blocks). However, when masonry is characterised by poor quality, due for example to the presence of round, unshaped stones or low-strength mortar and artisan skills are at a low level, the resulting structures are extremely vulnerable.

The seismic performance of an unreinforced masonry building depends on how well the walls are tied together and anchored to the floor and the roof (Tomažević, 1999) [1]. Considering a simple building as shown in Figure 2.1, when the walls are not connected at the intersections, each wall is expected to vibrate on its own when subjected to earthquake ground shaking (see Figure 2.1(a)). In this situation, the walls perpendicular to the direction of the shaking (transverse walls) are going to experience out-of-plane vibrations and are prone to instability, and possibly collapse when anchorage to the roof and transverse walls is not adequate. Walls parallel to the direction of the shaking (shear walls) are also susceptible to damage.

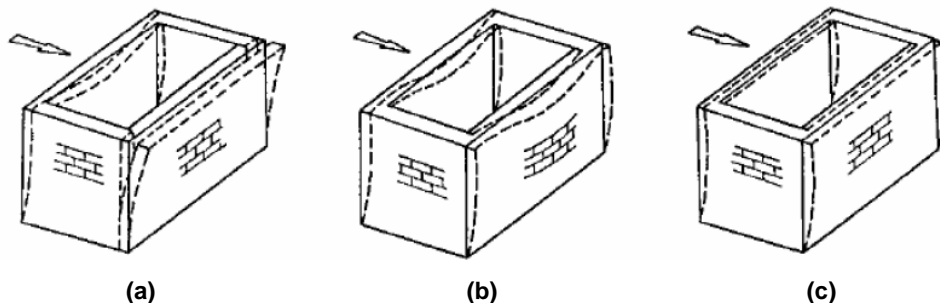


Figure 2.1. Masonry building under horizontal seismic action: loosely connected walls with flexible floor (a); well connected walls with flexible floor (b); connected walls with rigid floor.

When the walls are well connected, but there is still a flexible floor, the walls of the structure behave in a more compact way, but the walls placed in the direction of the seismic action cannot produce a proper bracing effect on the transversal walls,

which are subjected to high horizontal bending effect (see Figure 2.1(b)). It should be noted that a masonry building with a flexible roof may show good seismic performance provided that the walls are well connected and the roof maintains its integrity. When the walls are well connected, there is a rigid roof, and a horizontal ring beam (band) at the lintel level acts like a belt, the building vibrates as a monolithic box; that is a satisfactory seismic performance (see Figure 2.1(b)).

Past earthquakes have shown that damage to unreinforced masonry buildings is significantly reduced when building components are well connected and the building vibrates like a monolithic box. In many cases, unreinforced masonry buildings have flexible floors (in-plane), so there is a need to provide additional elements to tie the walls together and ensure acceptable seismic performance. Structural integrity of a building can be achieved by developing a box action by ensuring good connections between all building components-foundations, walls, floors, and roof. Key requirements for the structural integrity in a masonry building are illustrated in Figure 2.2. A ring beam (band) at lintel level is one of the critical provisions for ensuring structural integrity.

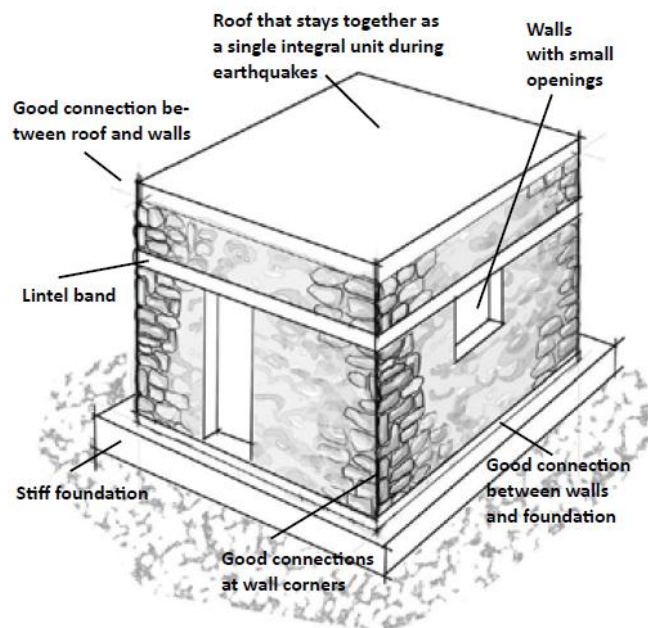


Figure 2.2. Key requirements for ensuring box action in a masonry building.

A lack of integrity is characterized by the following damage patterns:

- Damage and/or separation of walls at intersections;
- Floor and/or roof collapse from inadequate wall-to-floor (or wall-to-roof) anchorage.

Wall intersections are particularly vulnerable to earthquake effects due to significant tensile and shear stresses developed when seismic forces are transferred from walls B (transverse walls) to walls A (shear walls), as illustrated in Figure 2.3. When wall connections are inadequate or absent, vertical cracks may develop or separation may take place at wall intersections.

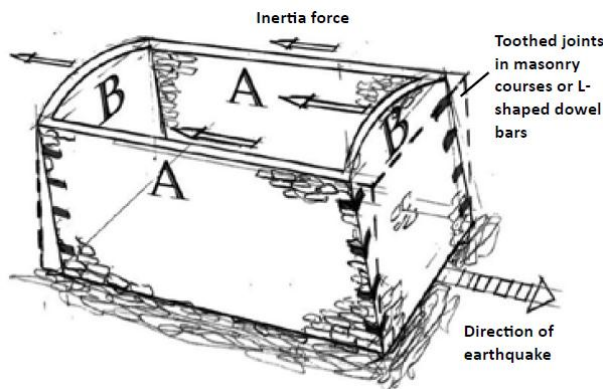


Figure 2.3. Role of wall connections in the box-like action of a building: walls A (loaded in the strong direction) support walls B (loaded in the weak direction).

Adequate connections between intersecting walls are critical for ensuring the satisfactory seismic performance of a building as a whole. However, evidence from past earthquakes has shown that the presence of ring beams/bands (or alternative provisions such as ties or bandages) is very effective in enhancing structural integrity.

Evidences of damages from many past earthquakes have confirmed that wall-to-floor and wall-to-roof anchorages are critical for ensuring the integrity of a building and preventing floor and roof collapse. When an anchorage is not adequate, the walls perpendicular to the direction of the earthquake shaking move away from the floors and roof, and might topple; this is known as 'out-of-plane' collapse (illustrated in Figure 2.4).

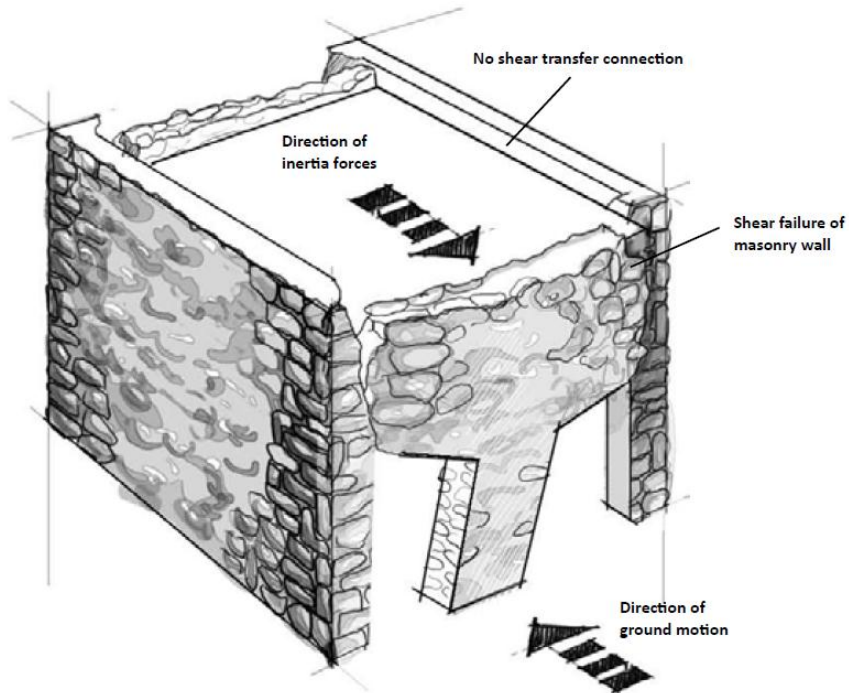


Figure 2.4. Effect of inadequate wall-to-roof connection.

Roof collapse is one of the major causes of fatalities in masonry buildings during earthquakes, and it can take place when either the walls lose the ability to resist gravity loads and collapse, or when the roof structure collapses (e.g. timber post-and-beam construction). Roof collapse is often caused by inadequate wall-to-roof anchorage. The roof structure can simply ‘walk away’ from the walls and cave into the building. Roof collapse can also be caused by the collapse of supporting walls. Some masonry buildings have heavy roofs that contribute to their seismic vulnerability. In the earthquake, heavy roof mass can cause lateral swaying of the frames, pushing the stone walls outward and causing their collapse.

Furthermore, masonry walls constructed of two exterior wythes are prone to delamination. The space between the wythes is usually filled with small stones and pieces of rubble bonded together with mud mortar. These wythes are usually constructed using large stone boulders (either round stones or partially dressed stones). The large wall thickness is required to ensure the thermal comfort and/or

personal security of the inhabitants. Delamination takes place when vertical wall layers (wythes) bulge and collapse outward due to earthquake ground shaking. One of the causes of delamination is the absence of through-stones (long stones which tie the wythes together). Other factors influencing delamination include intensity of ground shaking, shape of blocks (round, irregular, or regular), and the magnitude of the gravity load.

A detailed experimental and analytical research study on the delamination of stone masonry walls was performed by (Meyer et al., 2007) [2]. According to the study, delamination is triggered by high-frequency vibrations that cause inter-stone vibrations. This results in a reduction of frictional forces that hold the stones together, particularly when wedge-shaped stones are used. Another possible cause of delamination is an increase in internal lateral pressure from the soil or rubble core of the wall, which pushes the wall wythes outward. The delamination process observed during the testing is illustrated in Figure 2.5.

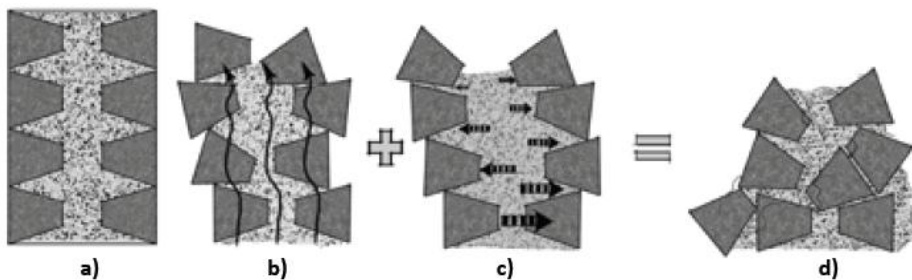


Figure 2.5. Delamination of masonry walls: (a) two-wythe stone wall with a rubble core; (b) stones displacement due to vibrations; (c) internal lateral pressure due to rubble fill increases and (d) wall collapse (Meyer et al., 2007) [2].

Delamination is usually initiated in the upper portion of the wall, where the lack of overburden weight allows the masonry to vibrate apart, and the appearance of the damaged wall is as if the exterior wythe has been peeled off. The stability of the wall can be most at risk when the masonry units vary in size and are laid with a minimum of horizontal bedding. The chances of delamination can be considerably reduced if wall wythes are stitched by means of through-stones (also known as 'bond

stones' or 'headers'), which are effective in enhancing the out-of-plane seismic performance of stone walls.

2.2.2 Damage mechanisms of masonry structures

Structural damage, based on observation and on correlation with past experience, can be classified according to the possible inferred causes. The in-plane wall failure modes are usually related to an overall global response. Such type of failure can be distinguished from local collapse mechanism, which can occur due to intrinsic vulnerability of the material or unsuitable structural details. Structures with proper connections between the orthogonal walls as well as between the walls and the floors can exploit the in-plane resistance of walls, allowing the building to resist the seismic action as a whole, and the damage associated to this kind of response is generally related to the in-plane response of the masonry walls. Depending on the geometry and position of the walls and on the distribution of the openings, these damage tend to be located in specific portions of masonry such as masonry piers and spandrel beams.

In the presence of low-quality construction and inadequate structural details, the response of the masonry building tends to be governed by local phenomena and damage mechanisms. In poor quality masonry walls, made of two leaves of irregular stones and no transverse connection offered by the through elements, a typical collapse is the out-of-plane crumbling of the external veneer. Similarly, absence of good connections between floors and walls or roofs and walls, and absence of the out-of-plane restraints such as the ties or the ring beams give rise to out-of-plane overturning of single walls. In the following sections, different types of damage and failure modes observed in masonry structures are described. Some of the typical damage in URM buildings is summarized in Figure 2.6.

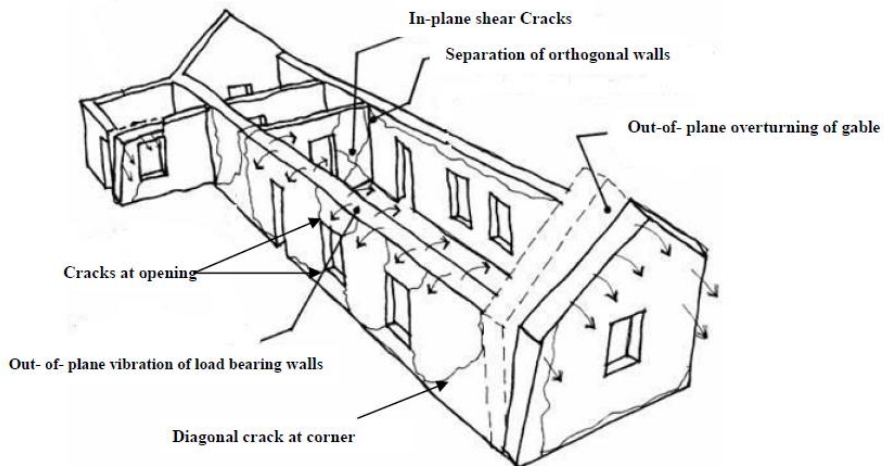


Figure 2.6. Various types of failures observed in unreinforced masonry buildings under seismic actions.

2.2.2.1 In-plane failure mechanisms

The main structural elements that resist earthquakes in masonry buildings are the unreinforced masonry walls which are designed to resist mainly gravity loads. Under seismic loading, the principle in-plane failure mechanisms of unreinforced masonry walls can be summarized as shown in Figure 2.7. These failure modes are as follows (ElGawady et al., 2007) [3]:

Shear failure: Walls with low aspect ratios and high axial loads tend to develop a diagonal cracking failure. Diagonal cracks developed in the wall either follow the path of the bed and head joints for relatively strong bricks and weak mortars or may go through the masonry units in case of relatively weak bricks and strong mortars, or both. Depending on the level of drift demand, the damage can be moderate and easily repairable, or severe to the extent that the buildings are usually unfit for further use. However, the consequences of such failures to the residents using the buildings are significantly less serious than in the case of the out-of-plane wall overturning.

Sliding failure: In the case of low vertical loads and/or low friction coefficient, which may be due to poor quality mortar, horizontal cracks in the bed joints can form a

sliding plane extending along the wall length. This causes the upper part of the wall to slide on the lower part of the wall.

Rocking and toe crushing failure: In the case of high moment/shear ratio or improved shear resistance the wall may be set into rocking motion or toe crushing depending on the level of the applied normal force. Numerous conventional techniques (e.g., ferrocement, shotcrete, grout injection, external reinforcement, posttensioning, center core, etc.) are available for retrofitting of existing masonry structures. Pier flexural-rocking failure cracks are produced in case of slender piers (portion of the wall between two openings). Failure initiates with large flexural cracks developing at the bottom and the top of the pier. As the displacement increases, the pier deforms as a 'rigid body' rotating about the compressed toe. Rocking may occur in piers having relatively higher aspect ratios (i.e., height-to-length ratio) with lower magnitudes of compressive stresses acting over piers.

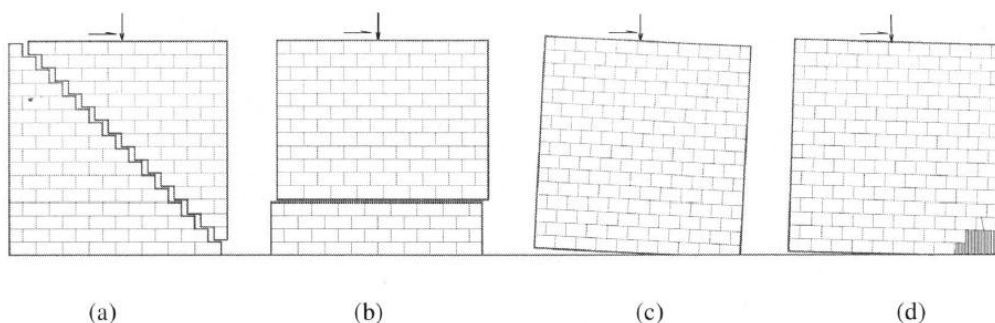


Figure 2.7. In-plane failure modes of a laterally loaded URM wall: (a) two-whythe stone wall with a rubble core; (b) stones displacement due to vibrations; (c) internal lateral pressure due to rubble fill increases.

2.2.2.2 Out-of-plane damage mechanisms

Out-of-plane wall collapse is one of the major causes of damage in masonry buildings, particularly in presence of flexible floors and roofs. As previously discussed, the overall building integrity is critical for the satisfactory seismic performance of

masonry buildings and the connections between structural components are crucial for maintaining building integrity. Integrity is absent or inadequate when the walls are not connected at their intersections and there are no ties or ring beams at the floor and roof levels. As a result, each wall vibrates on its own when subjected to earthquake ground shaking and is therefore likely to collapse. In multi-story buildings, this type of collapse usually takes place at the top floor level due to the significant earthquake accelerations there.

Depending on the intensity of earthquake ground shaking, this failure mechanism is characterized either by vertical cracks developed at the wall intersections, or by tilting and collapse of an entire wall.

When cross walls parallel to the direction of earthquake shaking are far apart, the central areas of long walls are subjected to significant out-of-plane vibrations and may collapse (Figure 2.8). The inadequacy of connections between the cross walls and long walls is one of the key factors influencing out-of-plane wall collapse. When connections are inadequate, long walls are more susceptible to the effects of out-of-plane vibrations and the chances of collapse are higher (Figure 2.9).

Furthermore, out-of-plane wall collapse is common in buildings with flexible roofs and floors, and where wall-to-roof connections are inadequate. Buildings with pitched roofs have gable walls. These are taller than other walls and tend to vibrate as freestanding cantilevers during earthquakes, unless they are tied to the roof structure. These walls are often inadequately connected to the roof.

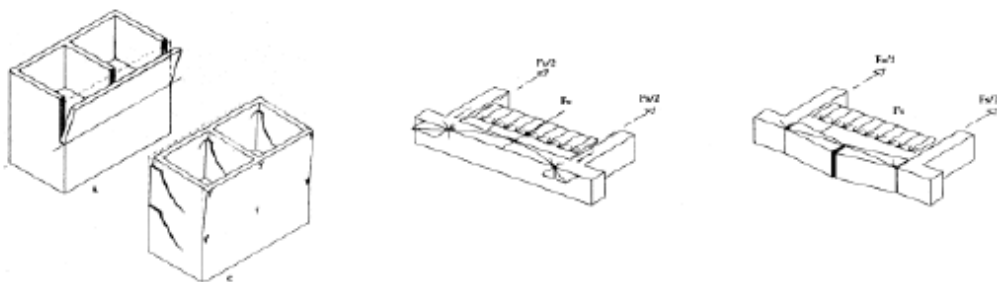


Figure 2.8. Out-of-plane collapse mechanisms with and without ties.

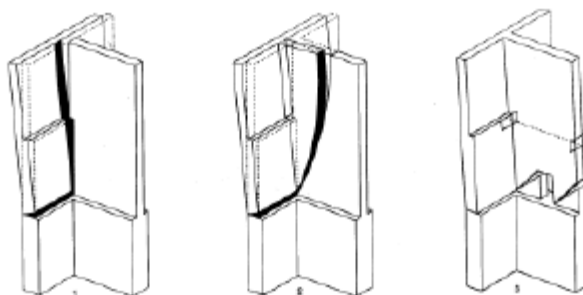


Figure 2.9. Overturning mechanism without wall connection, with good wall connection, in presence of ties.

2.2.2.3 Lateral thrust from roofs

Out-of-plane lateral thrust at roof level due to inclined roofs, added to inertial forces, can become a significant cause of collapse of masonry structures. In addition to the roof lateral thrust, another observed reason for out-of-plane failures is the lack of connection between the walls and the supporting roof, as often observed when wooden roof trusses are just resting on the walls, thus providing no out-of-plane restraint. The supporting walls thus fail in the out-of-plane bending as the building is unable to develop ‘box action’ against the lateral vibrations induced by the earthquake.

Also, the wedge separation at top of the wall junctions due to lateral thrust from the supporting roof truss can be observed. Such types of localized failures normally occur in the masonry walls supporting roofs inclined in the both horizontal directions. Masonry gets separated in the form of wedges below the roof level due to thrust from roof purlins, added to the inertial forces. Such failure mechanisms are mostly observed in case of openings close to the corner.

Regarding the wall-to-roof connections, it was observed that such type of damage occurs as a result of the forces transmitted between the walls and roof, mostly due to out-of plane horizontal excitation of the walls but also due to vertical ground accelerations, which could be very high in localities very close to the fault

rupture. The top of the wall may slip out from underneath the roof and/or crush under the dynamic loading. Such types of failure particularly occur in the case of poor quality masonry (rubble stone) and relatively heavy and rigid roofs, not connected properly to the supporting walls. Also, in the case of light roofs, the friction under the roof bearing may not be sufficient to avoid slippage.

3 REVIEW OF EXPERIMENTAL TESTS ON MASONRY PANELS

In this chapter are presented the main results from different experimental campaigns carried out on masonry panels tested under in-plane loading conditions. Both plane masonry walls and reinforced walls have been considered, in order to put in evidence the improvement in terms of strength and displacement capacity given by the reinforcement. The reinforcement system is represented by the use of Fiber-Reinforced materials in form of grid embedded in a layer of mortar applied onto the external surfaces of the wall, while different types of masonry have been considered, in terms of blocks and mortar materials, shape of blocks and structural arrangement.

3.1 NONLINEAR ANALYSES OF TUFF MASONRY WALLS STRENGTHENED WITH CEMENTITIOUS MATRIX-GRID COMPOSITES

In case of seismic event, masonry panels of a building are generally subjected to in-plane cyclic actions, causing three types of collapse mechanisms: diagonal cracking, when the principal tensile stress developed into the wall due to the combination of seismic and vertical loads exceeds the material's strength; shear sliding, when a reduced vertical load and poor quality of mortar cause the sliding of a portion of the wall with respect to the other along a horizontal mortar joint; flexural rupture, in presence of a good shear resistance and crushing occurs in the compressed zones of the wall.

The aim of the research has been the analysis of the influence of the use of reinforcement in a cement matrix (CMG, cementitious matrix-grids) on masonry panels subjected to shear loads. To this purpose, a comparison between the experimental results obtained from experimental compression tests and those from numerical finite elements model was made.

A wide experimental campaign on 8 masonry panels was carried out by (Prota et al., 2006) [4]. The panels are made by yellow tuff stones and mortar with average mechanical characteristics. The characteristics of employed materials, obtained from experimental tests, are reported in Table 3.1.

Material	Tensile strength f_t [N/mm ²]	Compressive strength f_c [N/mm ²]	Young's modulus E [kN/mm ²]	Tensile energy G_t [Nmm/mm ²]	Compressive energy G_c [Nmm/mm ²]
Tuff	0.21	2	2	0.0025	12
Mortar	1.31	5	1.8	0.012	19
CMG system matrix	4.58	24.1	3	0.061	45
CMG system grid	1276	—	72	Brittle	—

Table 3.1. Mechanical properties of materials [5].

Diagonal compression tests were carried out both on unreinforced and reinforced masonry panels, on one side or both sides of the wall, according to ASTM 519 provisions, in displacement control, in a way to catch the post-elastic behaviour of panels. The tests include:

- 4 unreinforced panels;
- 4 panels reinforced by means of a CMG applied on both sides;
- 4 panels reinforced by means of a CMG with two layers of grid applied on one side.

In no case was registered the premature detachment of the reinforcement layer, confirming the good compatibility between the CMG technology and the tuff masonry substrate.

The numerical simulation by means of FEM models of masonry panels was carried out through the TNO DIANA 9.1 code. The analysis was based on the bi-dimensional micro-modelling of specimens, that is the reproduction in the model of both the tuff

blocks and the mortar joints. The bi-dimensional model was preferred over a three-dimensional one in order to reduce the computational effort, mainly due to a very refined discretization of the model. Cementitious matrix used for the reinforcement was modelled as the mortar for used for masonry, while the composite material grid was considered as linear-elastic up to brittle failure in tension, with zero strength in compression. Angular steel plates used during the tests were modelled as well through triangular elements featuring three nodes. The tested panels and the correspondent geometrical properties adopted for the models are summarized in Table 3.2.

Numerical panel code	Mortar joints width [mm]	CMG system ply thickness [mm]	
		Matrix	Grid
W1 [as-built]	125	—	—
W2 [as-built]	185	—	—
W3 [as-built]	240	—	—
W1P1 [1 ply × 2 sides]	125	16	0.0705
W2P1 [1 ply × 2 sides]	185	16	0.0705
W3P1 [1 ply × 2 sides]	240	16	0.0705
W1P2 [2 plies × 2 sides]	125	24	0.1410
W2P2 [2 plies × 2 sides]	185	24	0.1410
W3P2 [2 plies × 2 sides]	240	24	0.1410

Table 3.2. Tested panels and geometrical properties adopted in the models [5].

It is noticed that possible construction defects are also taken into account in the numerical models by means of mortar joints filling only partially wall's thickness.

In Figure 3.1 the comparison between the experimental and numerical results is reported, showing a good agreement also in the non-linear field.

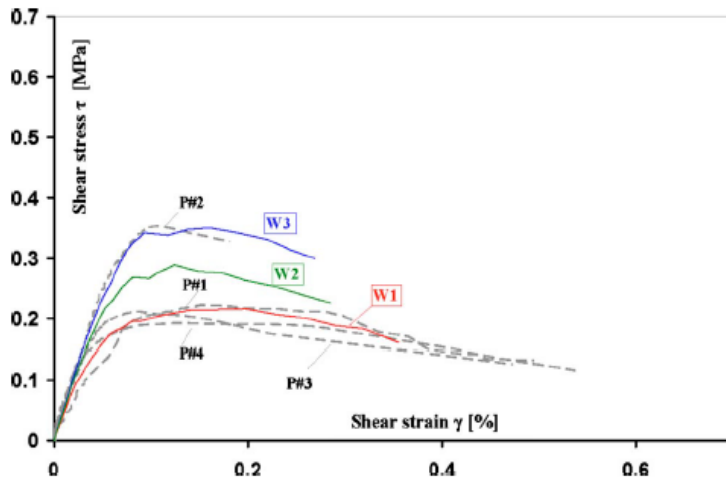


Figure 3.1. Numerical and experimental comparison for unreinforced panels [5].

In general, the numeric analysis evidences that the working defects, simulated through the partial filling of joints, might significantly influence the global response of unreinforced panels, unlike what happens for reinforced specimens, as it is shown in the following.

In Figure 3.2 and 3.3 the comparison is shown for reinforced panels with one or two layers of CMG.

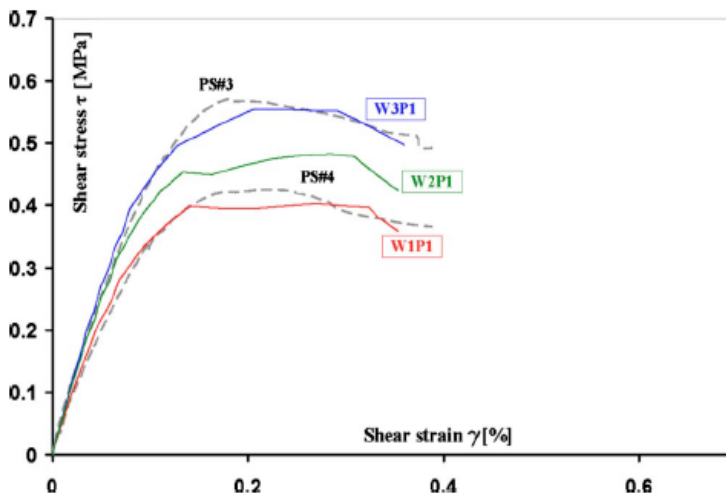


Figure 3.2. Numerical and experimental comparison for panels reinforced with one layer of CMG [5].

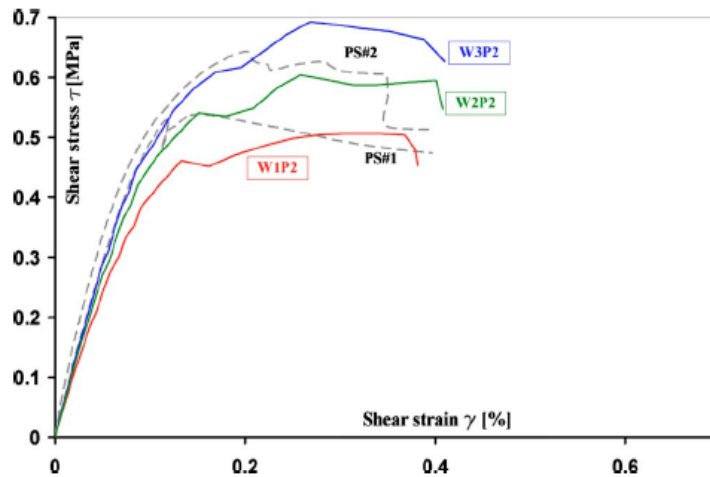


Figure 3.3. Numerical and experimental comparison for panels reinforced with two layers of CMG [5].

The maximum increment in terms of strength is 90% and 143%, for panels with the reinforcement on one or both sides, respectively. From experimental tests it can be noticed that the application of two layers of reinforcement the strength is limited by the crisis at the corners of the panels. Such kind of rupture depends on the high difference in terms of resistance between tuff and steel angular plates employed for the application of the diagonal load. Moreover, the panels reinforced at both sides show a better plastic response in terms of ductility.

In Figure 3.4 the numerical results in terms of normalised strength and shear modulus, varying the degree of filling of mortar joints, is reported.

It is possible to find out how the strengthening made with a mortar layer reinforced with frp grid produces an increment in terms of strength, and how the variability due to working defects influences this strength. It is underlined that the variation in terms of stiffness due to the presence of the reinforcement is negligible, and the limited impact of its employment on existing buildings.

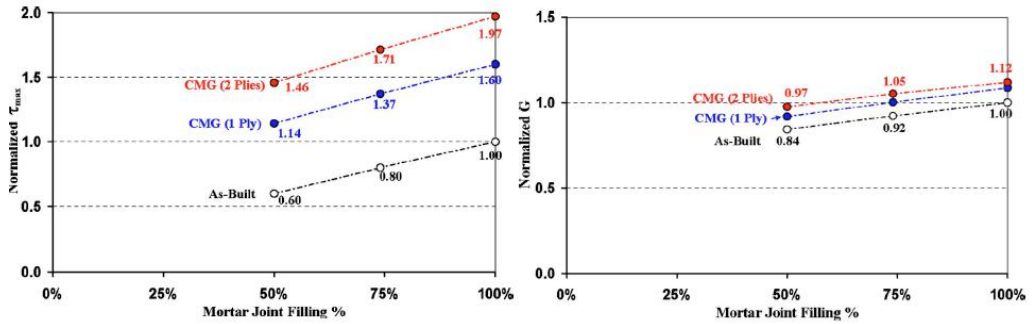


Figure 3.4. Parametric analysis of strength and shear modulus for different degrees of joint filling [5].

3.2 SHEAR CAPACITY OF MASONRY WALLS EXTERNALLY STRENGTHENED BY A CEMENT-BASED COMPOSITE MATERIAL: AN EXPERIMENTAL CAMPAIGN

The seismic behaviour of masonry can be reproduced and studied by means of the diagonal compression tests, regulated by the ASTM 519 standard. The study by (Faella et al., 2010) [6] presents the results of an experimental campaign carried out at the Structural Laboratory of the University of Salerno, on panels made by Neapolitan yellow tuff. In particular, 9 specimens were tested; among them 3 were unreinforced and 6 were reinforced on both sides by means of a layer of FRCM (fiber-reinforced cement matrix). This type of strengthening system is characterized by the use of a cement matrix, in place of the more common epoxy resin, in order to incorporate the composite material reinforcement. Standard dimensions defined by ASTM for the panels are 120 x 120 x 40 cm. The reinforcement is represented by a carbon fiber mesh embedded in between two layers of mortar. In order to evaluate the strength of each material, some compressive and flexural tests were carried out on specimens made of the same mortar and tuff employed for the construction of reinforced panels. The results obtained from tests are summarized in the following tables.

Specimen (#)	P_{max} (N)	f_b (MPa)
01	33,800	3.419
02	45,780	4.643
03	37,200	3.737
04	38,560	3.899
05	45,320	4.566
06	45,160	4.573
07	37,820	3.820
08	41,280	4.195
09	37,240	3.786
10	38,980	3.941

Table 3.3. Compressive tests on tuff specimens [6].

Specimen (#)	b (mm)	h (mm)	L (mm)	F_{max} (N)	$f_{b,t}$ (MPa)
TU01	36	41	162	436	0.811
TU02	39	36	165	454	1.011
TU03	37	38	163	369	0.778
TU04	36	42	166	495	0.877
TU05	40	40	162	456	0.801
TU06	36	40	163	390	0.761

Table 3.4. Three-points bending tests on tuff specimens [6].

Specimen (#)	$f_{m,c}$ (MPa)	Specimen (#)	$f_{m,c}$ (MPa)
M01-A	0.879	M01-B	0.846
M02-A	0.709	M02-B	0.834
M03-A	1.210	M03-B	1.117
M04-A	1.295	M04-B	1.115
M05-A	1.086	M05-B	0.914
M06-A	1.296	M06-B	–
M07-A	1.073	M07-B	0.983

Table 3.5. Compressive tests on mortar specimens [6].

Specimen (#)	<i>b</i> (mm)	<i>h</i> (mm)	<i>L</i> (mm)	<i>F</i> _{max} (N)	<i>f</i> _{m,t} (MPa)
MA 01	39	39	159	270	0.513
MA 02	48	40	160	242	0.355
MA 03	51	38	162	250	0.382
MA 04	50	40	165	238	0.334
MA 05	43	41	162	222	0.345
MA 06	48	40	159	192	0.281
MA 07	47	39	158	254	0.399

Table 3.6. Three-points bending tests on mortar specimens [6].

Furthermore, a compressive test on a 40 cm³ specimens cut out from a masonry panels was performed in order to evaluate the strength of the composite material tuff-mortar, obtaining a compressive strength of 1.31 MPa. The Eurocode 6 gives the following formula for the calculation of the same parameter using a combination of the strength of materials composing the masonry:

$$f_w = k \cdot f_b^{0.7} \cdot f_m^{0.3} = 1.21 \text{ MPa}$$

which gives a value very close to the experimental one.

Table 3.7 summarizes the mechanical characteristics of the strengthening system.

Mesh	Mineral mortar		
Mesh weight (g/m ²)	168	Compression strength (MPa)	38
Nominal thickness (mm)	0.047	Bending strength (MPa)	7.5
Strength (for a width of 1 cm) (N/cm)	1600	Young modulus (GPa)	15.0
Tensile strength (MPa)	4800		
Young modulus (GPa)	240		
Fiber density (g/cm ³)	1.78		
Ultimate strain (%)	1.8		

Table 3.7. Mechanical characteristics of carbon fiber net and mortar [6].

Figure 3.5 shows one panels tested with the diagonal compressive machine, while the characteristics of all the tested panels are reported in Table 3.8.



Figure 3.5. Diagonal compression test [6].

	<i>B</i> (mm)	<i>L</i> (mm)	<i>t</i> (mm)	Reinforcement type
1	1207	1148	388	Unreinforced
2	1197	1153	388	Unreinforced
3	1201	1145	390	Unreinforced
4	1220	1140	400	Double side reinforced
5	1200	1200	400	Double side reinforced
6	1207	1148	388	Double side reinforced
7	1210	1153	405	Double side reinforced
8	1206	1155	393	Double side reinforced
9	1197	1153	388	Double side reinforced

Table 3.8. Geometrical characteristics of tested panels [6].

Tests results are reported in terms of load-displacement diagram. In Figure 5.6 the result of the test on a unreinforced panel is reported. This typology of specimens featured a shear sliding rupture along a diagonal direction developing by the whole length of the panel at the interface between tuff and mortar. The collapse was attained at a value of load between 30 and 45 kN. In Figure 5.7 is shown the behaviour of a reinforced panel. In such case the collapse was attained for a value of the applied load from 4 to 6 times bigger than in the case of the unreinforced panel. In some cases a sudden change in the slope of the load-displacement curve, at a value near to the one corresponding to the collapse load of unreinforced panels, when the

crack forms inside the panel without having the possibility to develop due to the presence of the reinforcement applied on the specimen's surfaces.

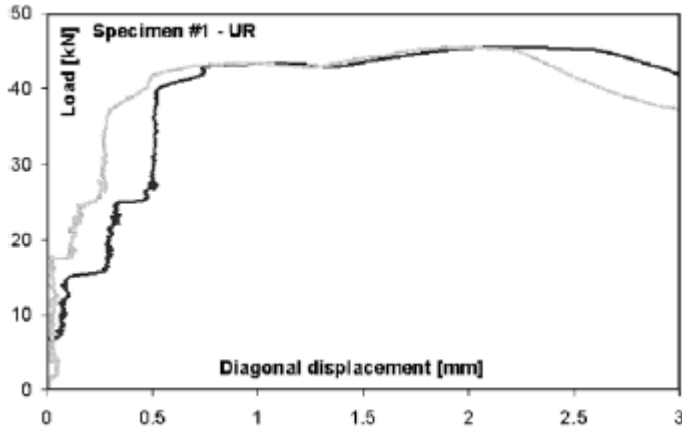


Figure 3.6. Load-displacement diagram, Specimen 1 [6].

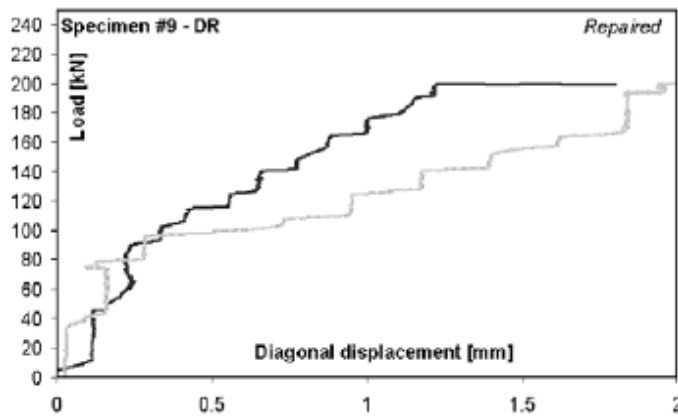


Figure 3.7. Load-displacement diagram, Specimen 9 [6].

The results from experiments were also compared to the theoretical ones, obtained by means of different formulations found in the literature. The shear strength of the tested specimens can be obtained from the ultimate compressive load by means of the formulas given by the ASTM E519:

$$f_v = \frac{0.707 P_u}{A_n}$$

$$A_n = \left(\frac{B + L}{2} \right) \cdot t \cdot n$$

where A_n is the net area of the transversal cross-section of the specimens, depending on the dimensions of the panel and on the percentage of gross area n .

The formulations available in the literature consider the shear strength of reinforced panels as the sum of resistance of the unreinforced masonry panel and the contribution due to the strengthening system. For example, the Eurocode 6 considers the following formulation:

$$f_{v,EC6} = f_{v0} + \rho_f \cdot 0.9 \cdot f_{fu}$$

where:

f_{v0} is the shear strength of the unreinforced panel;

ρ_f is the ratio between the cross-section of reinforcement and the cross-section of the panel;

f_{fu} is the tensile strength of reinforcing fibers employed for the strengthening.

Since it has been experimentally observed that the collapse occurs with the detachment of the strengthening system always before reaching the ultimate tensile strength of fibers, the formulation of the Eurocode 6 tends to overestimate the strength of the reinforced system. Thus it can be useful to calculate the value of the strength, based on the effective deformation that the fibers reach in correspondence of the ultimate load of the panel during the test ($\epsilon_{f,eff}$):

$$f_v = f_{v0} + \rho_f \cdot E_f \cdot \epsilon_{f,eff} .$$

In the following different formulations for calculation of $\epsilon_{f,eff}$ used in the comparison are reported:

$$\varepsilon_{f,eff} = 0.004 \leq 0.75 \varepsilon_{f,u}$$

I.C.B.O.-AC125

$$\varepsilon_{f,eff} = 0.4 \varepsilon_{f,u}$$

Tomažević et al.

$$\varepsilon_{f,eff} = 0.0119 - 0.0205 \cdot \rho_f \cdot E_f + 0.0104 \cdot (\rho_f \cdot E_f)^2$$

Triantafillou

$$\varepsilon_{f,eff} = 0.00065 \cdot \left(\frac{\sqrt[3]{f_m^2}}{\rho_f \cdot E_f} \right)^{0.56}$$

Triantafillou and Antonopoulos

$$\varepsilon_{f,eff} = \sqrt{\frac{2\Gamma_F}{E_f t_f}} \quad \text{dove } \Gamma_F = c_1 \cdot \sqrt{f_{mk} \cdot f_{mtm}} \quad \text{con } c_1=0.015 \quad \text{CNR-DT 200/2004}$$

In Figure 3.8 is reported a diagram with the comparison between the obtained results.

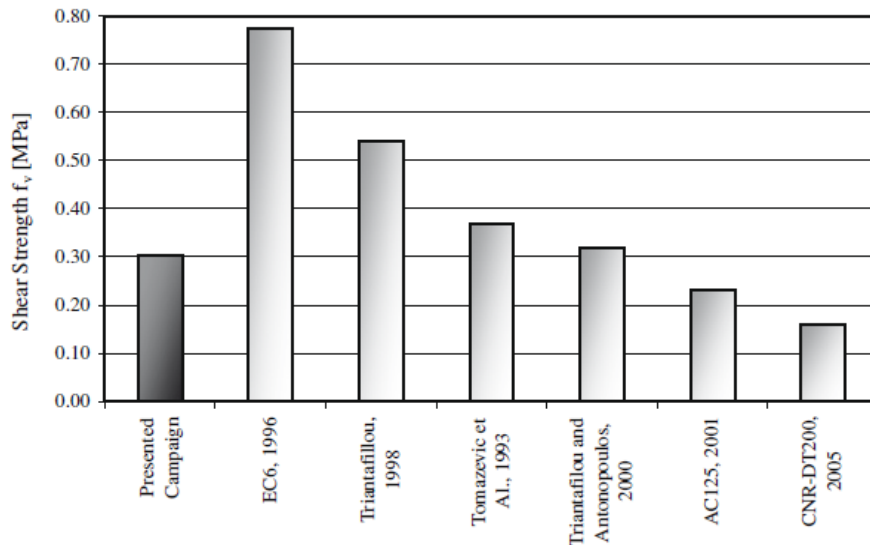


Figure 3.8. Comparison between experimental and theoretical results from different formulations [6].

As previously described, the formulation of the Eurocode 6 significantly overestimates the shear strength of reinforced masonry panels, since it is not able to catch the detachment of the strengthening system from the surface of the panel, but takes into account the strength of carbon fibers. It is noted how the formulations of both Triantafillou and Tomažević overestimate the strength of panels, even if not so much as the Eurocode 6, since they are obtained experimentally from tests carried out on clay brick masonry panels with better mechanical properties of tuff employed in this case. On the contrary, the formulation proposed by Triantafillou and Antonopoulos is able to catch the actual value of the shear strength also found in the experiments since it takes into account also the mechanical properties of the substrate material. Finally, the formulations of ACI-125 and CNR-DT 200 underestimate the experimental results, because the former one has a simplified formulation of $\varepsilon_{t,eff}$, while the latter one would require a better calibration of coefficient C_1 .

3.3 VALIDATION OF ANALYTICAL AND CONTINUUM NUMERICAL METHODS FOR ESTIMATING THE COMPRESSIVE STRENGTH OF MASONRY

The present research work, carried out by (Lourenço and Piña Henriques, 2006) [7], analyses the capability of numerical models to reproduce the experimental behaviour of masonry subjected to compression loads. The experimental campaign is presented (Binda et al., 1988) [8], performing compressive tests, in displacement control, on 9 masonry panels composed by 9 layers of clay blocks connected by means of 10 mm thick mortar bed joints. The dimensions of single blocks are 250 x 120 x 55 mm, used to construct masonry prisms with dimensions of 600 x 500 x 250 mm. Three types of mortar were used (M1, M2 and M3), and each of them was employed to build 3 panels. In Figure 3.9 the test set-up and the position of LVDTs is reported.

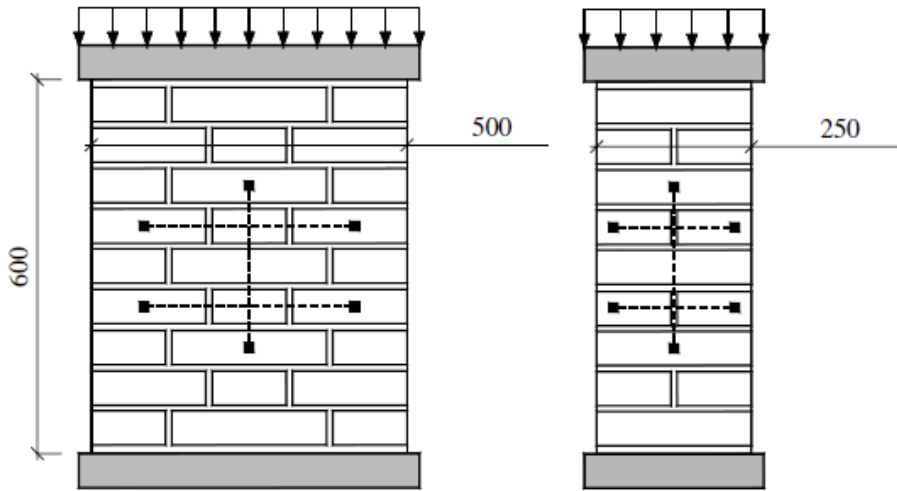


Figure 3.9. Test set-up and positions of LVDTs [7].

Vertical deformations of masonry panels and elastic modulus were calculated on the basis of data read from transducers. In Table 3.9 the mechanical characteristics of employed materials are reported, in terms of compressive strength f_c , tensile strength f_t , Young modulus E and Poisson's coefficient ν ; while in Table 3.10 the results obtained from panels P1, P2 and P3, made with M1, M2 and M3 mortar respectively, are reported.

Component	E [N/mm ²]	ν [-]	f_c [N/mm ²]	f_t [N/mm ²]
Unit	4865	0.09	26.9	4.9
Mortar M1	1180	0.06	3.2	0.9
Mortar M2	5650	0.09	12.7	3.9
Mortar M3	17,760	0.12	95.0	15.7

Table 3.9. Mechanical properties of employed materials [7].

Prism type	Mortar type	E [N/mm ²]	f_c [N/mm ²]
P1	M1	1110	11.0
P2	M2	2210	14.5
P3	M3	2920	17.8

Table 3.10. Mechanical properties of panels [7].

In order to reduce the computational effort for the analyses, only a part of the specimens was modelled, as it is shown in Figure 3.10. The model is represented by a portion of the wall, which is identically repeated in the panel, and giving to it appropriate boundary conditions in order to reproduce the actual behaviour of the whole specimen.

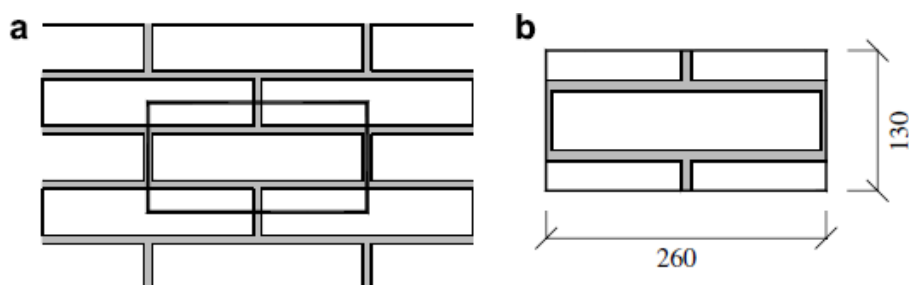


Figure 3.10. Definition of the base cell used in the analyses [7].

The previously described assumptions assumed for modelling do not allow to carry out a comparison of numerical results with experimental collapse modalities due to non-symmetric conditions, stress or strain localization, or effect of constraints. Moreover, since the combination of such elements lead almost totally the post-elastic behaviour of the test, it is not possible to analyse the plastic behaviour of panels.

In order to investigate the out-of-plane of the panels, different numerical approaches were adopted: plane stress state (PS) using bidimensional finite elements, plane strain state (PE), and an intermediate approach, namely an 'enhanced-plane strain state' (EPE) using three-dimensional finite elements constrained to have the same displacement on two opposite faces of the panel. In the plane stress state the out-of-plane stresses are null, thus the specimen is free to deform in this direction. In the plane strain state, out-of-plane strains are null. The last case simulate an interesting behaviour between the two considered formerly. The code employed for the analysis was TNO Diana, and the non-linear parameter are reported in Table 3.11.

Component	c [N/mm ²]	f_t [N/mm ²]	$\sin \phi$ [-]	$\sin \psi$ [-]	Gf_t [N/mm]	Gf_c [N/mm]
Unit	11.3	3.7	0.17	0.09	0.190	12.5
Mortar <i>M1</i>	1.3	0.7	0.17	0.09	0.350	2.7
Mortar <i>M2</i>	5.3	3.0	0.17	0.09	0.150	10.0
Mortar <i>M3</i>	39.9	12.0	0.17	0.09	0.600	23.0

Table 3.11. Inelastic properties of materials [7].

Despite of the effort made in the research in last decades, information for a correct evaluation of materials parameter, such as the friction angle ϕ , the dilatancy angle ψ , and particularly the fracture energy in compression G_{fc} , and in tension G_{ft} , are still lacking. In particular, the values assumed for last two properties are based on experimental evidences (Lourenço, 1996) [9] and on the necessity to assume a satisfactory value in order to reach numeric convergence of the model.

In Figure 3.11 it is shown the comparison of numerical results with the experimental ones, with reference to the P2 specimen, in terms of stress-strain diagram.

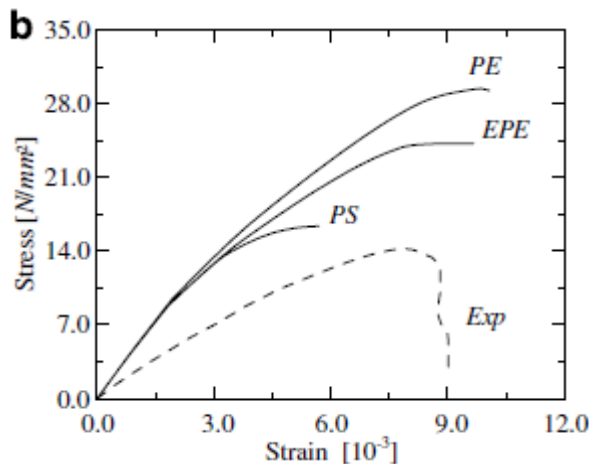


Figure 3.11. Numerical and experimental stress-strain diagram [7].

It is noticed that the response obtained from the EPE model is intermediate compared to the ones obtained from the PS and PE models. The numerical strength

of the specimen significantly overestimate the experimental one, even if the value of strain corresponding to the peak stress is very close to the experimental one. Another important difference is in the values of stiffness, much higher than the numerical ones. This can be explained because the stiffness used to simulate the numerical behaviour of the mortar was taken from experimental tests on prisms with different dimensions, constraint conditions and manufacture from the one employed in the composite model of the panel. The difficulties in the evaluation of stiffness of the mortar used in the panel represents an important disadvantage of micro-modelling strategy. Such a deficiency can be overcome by means of an inverse parametric adaptation. Considering the vertical displacement of the panel (Δy_M) composed by the sum of the contribution given by the mortar (Δy_m) and the contribution given by the blocks (Δy_u) can be written:

$$\Delta y_M = \Delta y_u + \Delta y_m$$

that by means of some calculations can be rewritten as:

$$E_{adj} = \frac{h_m E_M E_u}{E_u (h_m + h_u) - h_u E_M}$$

where:

E_{adj} is the correct modulus of elasticity of the mortar;

E_u is the modulus of elasticity of the masonry unit;

E_M is the elasticity modulus of the composite panel;

h_m is the thickness of the mortar joint;

h_u is the height of the panel.

In the Figure 3.12 are reported the results obtained correcting the values of the modulus of elasticity of the mortar.

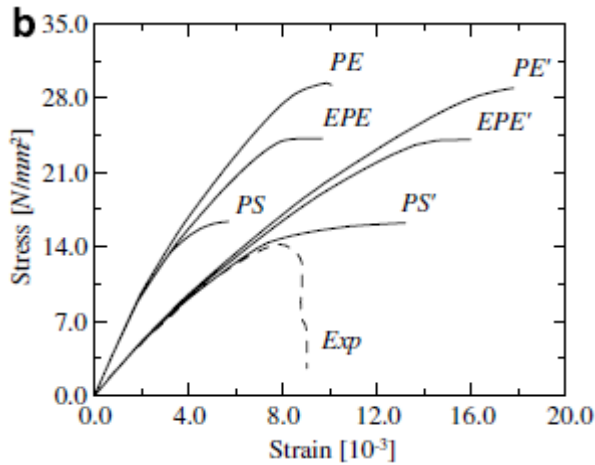


Figure 3.12. Comparison between the stress-strain diagram obtained using an adjusted value of the modulus of elasticity of the mortar [7].

It is noticed that, compared to the case of previous analysis, even though similar values of strength were obtained, they are reached in correspondence to higher values of strain. Nevertheless, the possibility to adjust also the values of the peak strain was not considered in this work.

Failure mechanism obtained from the analysis depend, of course, from the adopted modelling strategy, but even if they are numerically correct, they do not reflect the actual physical behaviour of the element.

In Figure 3.13 is reported the behaviour of the strains along different cross-section of the element. Three level of load were considered, and each of them is representative of a particular branch of the stress-strain diagram. The specimen P1 was considered, since it is composed by a weaker mortar compared to blocks, and it represent better the conditions of ancient buildings.

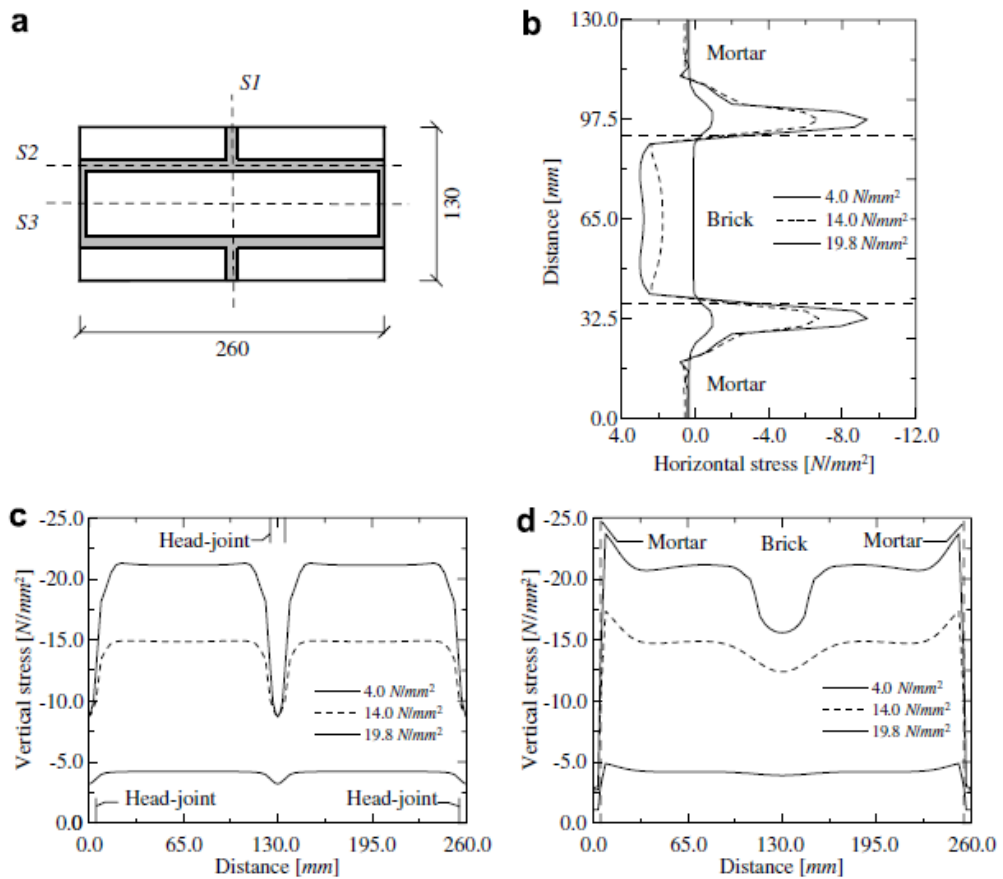


Figure 3.13. Plots of the strain versus the load for different cross-section of the element: S1 (a), S2 (b), S3 (c) [7].

As can be seen from the figure, the mortar is in a three-axial compression state, while the blocks are subjected to bi-axial compression-tension. A reduction of vertical compression can be observed in proximity to head joints due to the low stiffness of mortar. This unloading effect is bigger in proximity to the failure point because of the inelastic behaviour of head joints. Moreover, it is possible to observe a stress concentration at the external borders when the load increases, causing the crisis of head joints.

Furthermore, it was performed a comparison between the experimental data and results given by formulations from the literature, in terms of compressive strength. The following equations were used:

1.
$$f_c = \frac{1}{1 + \frac{\alpha\varphi(\beta\nu_m - \nu_u)}{\beta(1 - \nu_m)}} \cdot f_{c,u}$$
 Francis et al.
2.
$$A f_c^3 + B f_c^2 + C f_c + D = 0$$
 Khoo and Hendry
3.
$$f_c = f_{c,m} + \frac{s f_{c,u} - f_{c,m}}{1 + \frac{t h_{m f c,u}}{m h_{u f t,u}}}$$
 Ohler
4.
$$f_{c,k} = K f_{c,u}^{0.7} f_{c,m}^{0.3}$$
 Eurocode 6
5.
$$f'_m = A(400 + B f_{c,u})$$
 ACI Specification for masonry units

The obtained results are summarized in Table 3.12.

Prism	Exp. [17]	Francis et al. [13] ^a	Khoo and Hendry [11]	Ohler [12]	EC 6 [8]	ACI [9]	Numerical simulations <i>EPE</i> ^a
P1	11.0	25.0 (225%)	15.2 (140%)	14.8 (135%)	7.5 (70%)	9.4 (85%)	18.2 (165%)
P2	14.5	24.2 (165%)	20.2 (140%)	19.0 (130%)	11.3 (80%)	11.0 (75%)	24.1 (165%)
P3	17.8	23.4 (130%)	–	–	13.0 (75%)	11.0 (60%)	30.0 (170%)

Table 3.12. Comparison between analytical and experimental strength [7].

The first three equations were obtained from equilibrium methods, under the hypothesis that the blocks are subjected to uniaxial compression and biaxial tension, while the mortar joints are subjected to triaxial compression. It is evident that these formulas overestimate the actual strength of specimens, while the empirical formulas of Eurocode 6 and ACI conservatively evaluate the experimental results. It is also important to notice that the formulation by (Francis et al., 1971) [10] reduces the value of strength when the mortar stiffness is incremented. This is mainly due to the high sensibility of such formulation to the Poisson's coefficient. This represents an important disadvantage for this method because of the objective difficulties in the

evaluation of this value. Finally, as a result, it can be said that the continuous finite elements modelling, based on plasticity and cracking, cannot be used to adequately describe masonry failure mechanisms or for assessment of strength of masonry starting from mechanical characteristics of its constitutive materials. In order to progress in this direction it is thus necessary to look for alternative models for the representation of the microstructure of masonry panels, and carry out deep experimentations for characterization of mechanical behaviour of mortar present in masonry elements joints.

3.4 MECHANICAL BEHAVIOUR OF POST-MEDIEVAL TUFF MASONRY OF THE NAPLES AREA

The work carried out by the authors (Calderoni et al., 2009) [11] has the aim to realize and test some real scale models of historic post-medieval masonry present in the Neapolitan region of Southern Italy. Displacement controlled compressive tests were carried out in order to get the constitutive law of masonry, including the softening branch.

From the first half of XVI century to the first half of XX century, the Neapolitan masonry, mostly built with mortar and tuff, can be divided into three main categories, depending on the year of construction and on the morphologic and geometric aspects. The first typology, namely the 'cantieri', was used to be realized during the rule of 'Viceré di Spagna' (XVI – XVII century) and it was made of stone elements randomly distributed with thin mortar layers. It was generally used a cement mortar, or a lime mortar mixed with small rubble stones. In the XVIII century, stones called 'bozzette' were used, having every face worked, excepted from the ones in the interior part of the wall. This type of stone was used for the external part of the walls, while the internal mass was made by roughly worked stones. At the age of Bourbons, instead, stones were used to be cut by means of a particular tool called 'mannara', lately placing such stones in rows separate by mortar joints with variable thickness. It is easy to distinguish on to the external surfaces of this type of walls, commonly called 'a sacco', the presence of stones with a very variable height to width ratio.

For each typology of historic masonry, two scaled models were constructed. Yellow tuff blocks employed for the walls were extracted from a quarry placed under the ancient church in the neighbourhood 'Vergini di Napoli', while in order to reproduce the masonry 'a sacco' were used some blocks obtained from demolition of a wall in the complex of San Lorenzo in Aversa. In Figure 3.14, 3.15 and 3.16 it is reported a picture for every masonry typology.

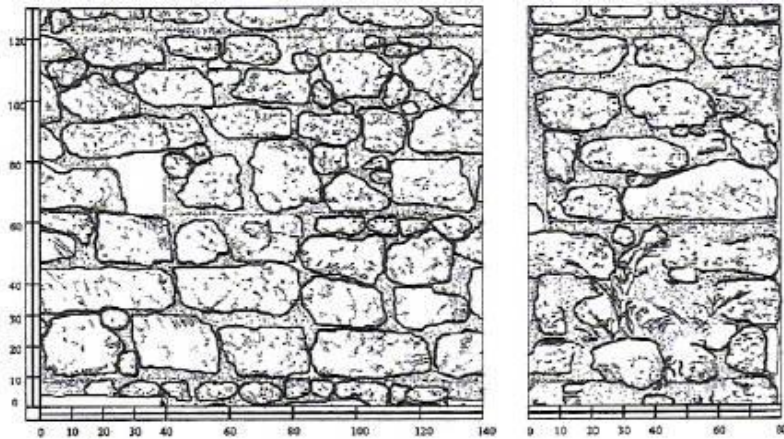


Figure 3.14. Front side and cross-section of the wall in 'cantieri' style [11].

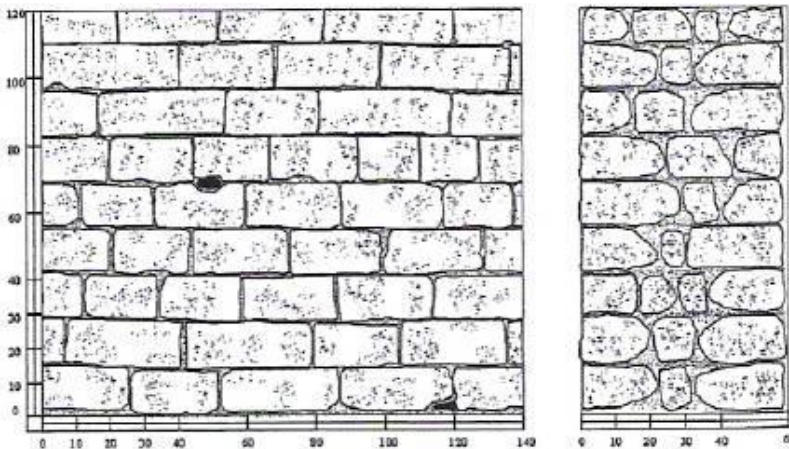


Figure 3.15. Front side and cross-section of the wall in 'bozzette' style [11].

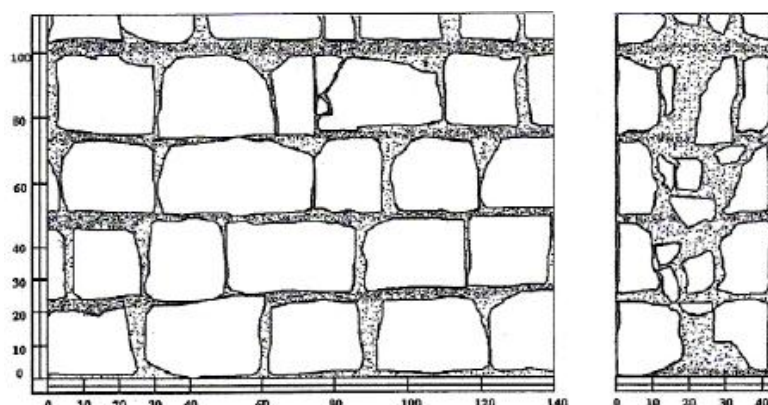


Figure 3.16. Front side and cross-section of the wall in 'a sacco' style [11].

Since the mechanical behaviour of masonry is strictly dependent on constitutive materials, some tests on single materials were carried out, in order to obtain their constitutive law and some important characteristics. Compression tests on tuff blocks were performed according the UNI EN 772-1, which prescribes that the tests must be carried out in control of load, applied at a prescribed velocity, and that the maximum load must be reached within one minute. Since the softening part of the constitutive law had to be caught, tests on tuff were carried out in control of displacement, applying the load at a certain velocity in order to be in a limit set by the standard UNI EN 772-1. A total number of fourteen specimens (70 mm^3) was tested, eight of which extracted from the quarry of Virgins and six from the complex in Aversa.

In order to test the mortar, the prescriptions of the UNI EN 1015-11 were considered. A total number of seven specimens ($40 \times 40 \times 160 \text{ mm}$) for each type of mortar were tested in a three-points bending test, and in a compressive test on the resulting portions of the specimens from previous test. The obtained results are summarized in Table 3.13, where σ_{\max} is the strength, ϵ_p is the strain corresponding to the maximum stress and $\epsilon_{(\sigma_{\max}/2)}$ is the strain on the softening branch when the load reaches half of the strength.

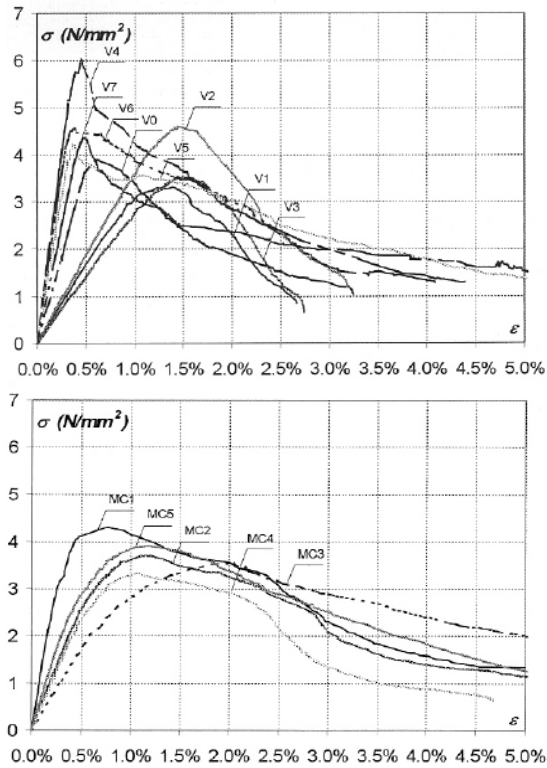


Figure 3.17. Constitutive law for tuff and mortar specimens [11].

Sample	σ_{max} (N/mm^2)	ϵ_p	$\epsilon_{(\sigma_{max}/2)}$
Vergini tuff	4.30	0.84%	2.38%
Aversa tuff	3.49	0.51%	3.31%
MB mortar	1.56	2.29%	5.00%
MC mortar	3.76	1.24%	3.86%

Table 3.13. Mechanical characteristics of materials constituting masonry [11].

The values reported in the table are obtained as the average of results from different specimens. No shape factor was used since all the tested specimens have a cubic shape.

The masonry panels were tested in control of displacement by means of a compressive machine with a capability of 3000 kN. In order to overcome problems of eccentricity and non-uniform stress distribution a levelling mortar was applied on top

of the panels, a stiff beam was used. Between such beam and the hydraulic jack was placed a spherical hinge. Displacement and deformations are measured by means of inductive and resistive transducers. All the tests were characterized by the formation of a vertical crack when the strength of the panel was attained. When the load was incremented, also diagonal cracks formed, causing the detachment of the more external face of specimens. However, no important detachment between mortar and tuff was observed, indicating a good homogeneity of the masonry.

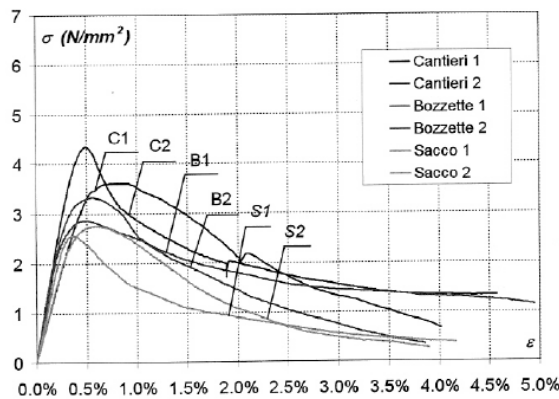


Figure 3.18. Constitutive law for three typology of walls analysed [11].

Constitutive $\sigma - \epsilon$ diagrams resulting from the tests (Figure 3.18) on panels show a first elastic part, becoming non-linear right after attaining the strength of the system, followed by a softening branch until the collapse of the panel. The ultimate strain is quite high, showing an unexpected plastic capacity of the material.

Starting from the results obtained from tests on panels, two relations were proposed for the description of the whole non-linear behaviour of specimens:

$$\sigma = \left[\frac{k \cdot \mu - \mu^2}{[1 + (k-2) \cdot \mu]} \right] \cdot \sigma_{max} \quad \text{for } \mu = \frac{\epsilon}{\epsilon_p} \leq 1.2$$

$$\sigma = \sigma_{max} [a \cdot \ln(\mu) + b] \quad \text{for } \mu = \frac{\epsilon}{\epsilon_p} > 1.2$$

It can be noticed a correspondence between the experimental results and the curve obtained from previous expressions.

A realistic evaluation of the behaviour of a masonry structure, or some of its constitutive element, subjected to seismic loads needs a detailed non-linear analysis. To this end, starting from the $\sigma - \epsilon$ diagram, taking into account the tensile strength of material and assuming a linear stress distribution, the $M - \chi$ diagram was obtained with respect to a transversal cross-section at the base of the panels (Figure 3.19).

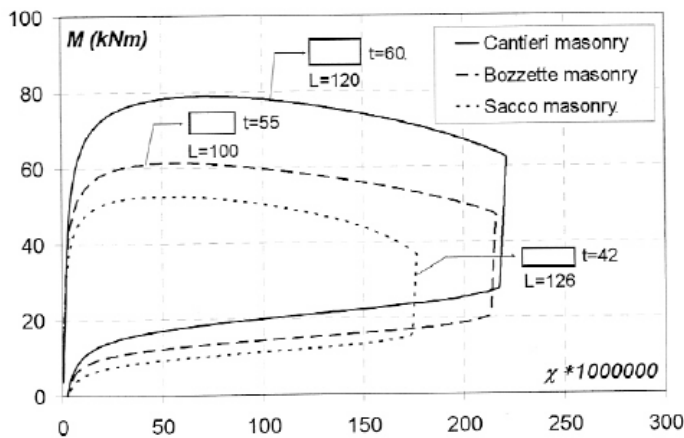


Figure 3.19. Moment – curvature diagram for three typologies of walls analysed [11].

The diagram shows also an unloading branch, obtained in the hypothesis of linear $\sigma - \epsilon$ diagram during the unloading phase. The shape of this curve is characterized by an unexpected dissipative and ductile behaviour of the masonry element, which might be the reason why such structures can stand seismic events.

A further comparison was made between the strength showed by the elements during the experimental tests and the one calculated by means of analytical expressions given by the codes, such as the D.M. '87 or the Eurocode 6. The results are summarized in Table 3.14.

Masonry	Resistance to mean compression (f_m) (N/mm ²)		
	Experimental values	Prescribed values	
		DM '87	EC6
<i>Cantieri</i>	3.97	2.9	2.1
<i>Bozzette</i>	3.09	–	1.6
<i>Sacco</i>	2.65	–	1.4

Table 3.14. Comparison between strength from experiment and from code regulations [11].

It can be noticed that the D.M. '87 underestimate the actual strength of specimens, probably because such formulation is calibrated for new types of masonry and is not valid also for historic masonry as the one that was tested.

Another comparison was done considering the curve obtained using the formulations calibrated for the description of panels behaviour and the constitutive behaviour of materials used for their construction. An example is reported in Figure 3.20.

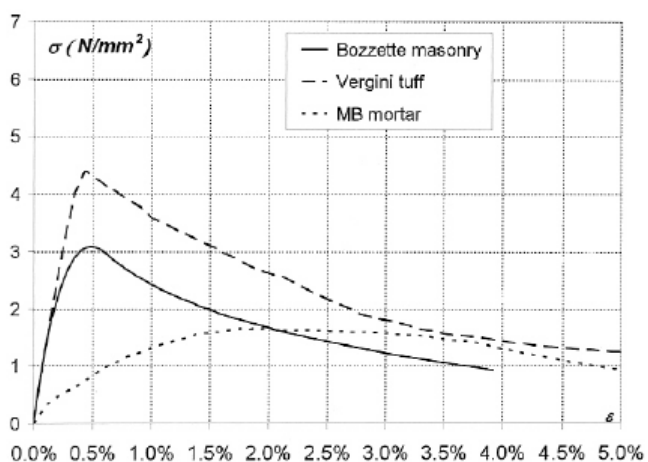


Figure 3.20. Comparison between the constitutive laws of mortar and tuff employed for construction of the 'bozzette' panel and curve from its analysis [11].

It can be noticed that the curve of the panel initially follows the behaviour and stiffness of tuff and only in correspondence of $\frac{1}{2}$ of the peak resistance it starts to move and position in between the curves of two constitutive materials of the wall. In terms of strength the panel is closer to the tuff strength rather than the mortar strength.

It can be concluded that the good compressive strength of specimens confirms what is already known for the historic masonry, the fact that such typologies show a very good dissipative capacity even against horizontal loads. The knowledge of the constitutive law of the material is then very important in order to study the post-elastic behaviour and the seismic performance of masonry structures.

3.5 METROLOGICAL DEFINITION AND EVALUATION OF SOME MECHANICAL PROPERTIES OF POST-MEDIEVAL NEAPOLITAN YELLOW TUFF MASONRY

Metrological researches carried out on Neapolitan yellow tuff masonry have identified three different constructive typologies, depending on chronology, morphology and geometric parameters:

- 'cantieri' masonry, widely used between the XVI and the XVII century;
- 'bozzette' masonry, used around the XVIII century;
- 'blocchetti a filari' masonry, used in the XIX century and in the first half of XX century.

A large presence of such masonry typologies in the Neapolitan area permits a deep knowledge of geometric and constructive characteristics diffused at that time. The 'cantieri' masonry was widely used in the Spanish Quarters, in the suburban area next to the city walls during the period of Spanish Viceré, and often used also for the construction of foundations of important buildings. Such type of masonry are made mainly with roughly cut stones by means of manual tools, joined with irregular courses of mortar. These stones are usually called 'spacca atoni', 'spaccate' or 'spaccatelle', depending on size and shape. After the seismic event of 1688, in the last quarter of XVII century, a new constructive technology started to develop and walls were made with 'bozzette' stones, vertically worked onto the external faces and roughly cut on the internal ones. Masonry was used to be built with such stones in rows of 13 cm of height ('mezzo palmo'). Starting from the Napoleonic period, 'blocchetti' masonry walls were used, made with smaller blocks, easily recognizable due to different dimension ratio. Also, thinner and variable bed joints were commonly

used in this type of masonry. In past years, the authors of the present study carried out an experimental research on scaled columns 1:10 made by the same masonry typologies previously described, obtaining a non-linear σ - ϵ diagram from which the M - χ curve of the transversal cross-section of the panel was obtained together with the theoretical F - δ diagram. The study carried out by (Calderoni et al., 2009) [12] is an extension of previous work on real scale walls. It is important to underline that the mechanical characteristics of tuff are not subject to high deterioration with time; in fact, the wind, only in the case it insists on the material for long time, can lead to erosion of material, while the rain and the moisture only temporarily reduce the mechanical characteristics of stones. This permitted to employ stones from the original time of constructive typologies for the constructions of models, taken from old quarries already used at that time or from the rests of buildings aggregates present in the Neapolitan area.

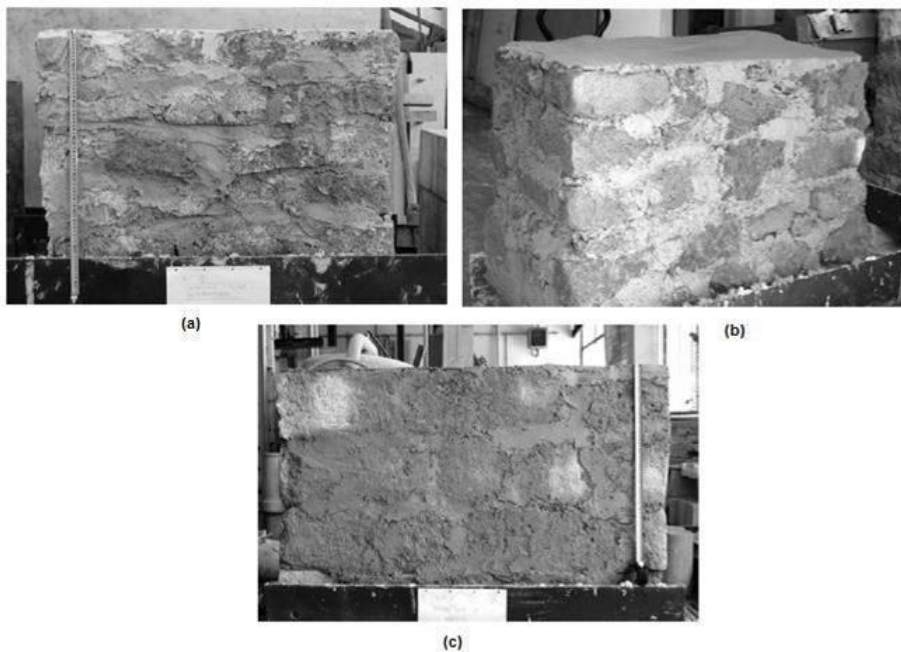


Figure 3.21. Built panels: 'bozzette' (a), 'cantieri' (b), blocchetti (c) [12].

In order to reproduce the mortar employed for the construction of the elements and to know the mix, the type of binder and aggregates used at that time, some documents from literature were analysed and some physical and chemical tests were carried out. In Figure 3.21 it is reported a picture for the panels build according different typology, while in Table 3.15 the dimensions of every panel are summarized.

Sample	Typology	Dimensions (cm)			Components	
		L	t	H	Tuff	Mortar
C1	<i>Cantieri</i>	125	67	90	<i>Vergini</i>	MC
C2	<i>Cantieri</i>	120	65	95	<i>Vergini</i>	MC
B1	<i>Bozzette</i>	100	55	82	<i>Vergini</i>	MB
B2	<i>Bozzette</i>	100	55	82	<i>Vergini</i>	MB
S1	<i>Blocchetti</i>	133	42	91	<i>Aversa</i>	MB
S2	<i>Blocchetti</i>	120	42	88	<i>Aversa</i>	MB

Table 3.15. Components and dimensional characteristics of panels [12].

The experimental campaign concerned a first part for the characterization tests on tuff specimens and mortar specimens. In particular, the UNI EN 771-6 for tuff specimens, and the UNI EN 1015-11 for mortar specimens were followed for test execution. In Table 3.16 are summarized the values of mechanical characteristics of masonry components.

Sample	σ_{\max} (N/mm ²)	ε_p (%)	ε ($\sigma_{\max}/2$) (%)
Vergini tuff	4.30	0.84	2.38
Aversa tuff	3.49	0.51	3.31
MB mortar	1.73	2.29	5.00
MC mortar	3.76	1.24	3.86

Table 3.16. Mechanical characteristics of masonry components [12].

During compressive tests on whole masonry panels, in order to avoid the possibility of localized rupture of masonry or eccentric loads, on top of panels was applied a self-levelling mortar in contact with a steel profile through which the load was applied. Between the steel profile and the hydraulic jack a spherical hinge was placed. Deformation were read by means of LVDT. In total, six real scale panels were

tested according to the following procedure: a first phase where a 0.1 N/mm^2 load was applied in order to let the specimen settle; a second phase where a 0.5 mm/s displacement was imposed with breaks of 10 seconds.

The tests give load – displacements diagrams from which $\sigma - \epsilon$ curves were obtained. In Figure 3.22 the results are reported for the 'bozzette' walls.

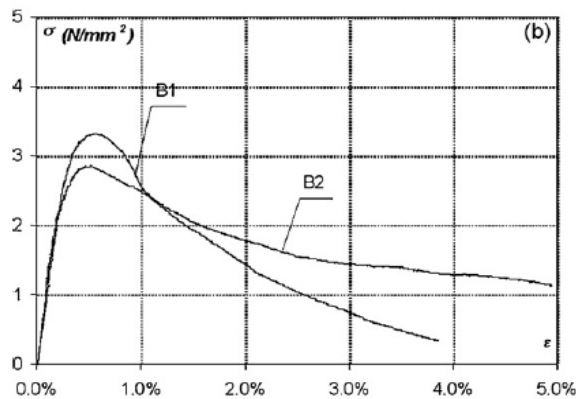


Figure 3.22. Compressive tests results for 'bozzette' walls [12].

During the loading process, the first damage was attained when the peak strength was reached, and a vertical crack appeared. Afterwards, there was the formation of further cracking surfaces, inclined by an angle of 45° , demonstrating a good bond between tuff and mortar. The maximum strength was reached for an interval between 2.55 N/mm^2 and 4.34 N/mm^2 , corresponding to a strain ranging from 0.4% to 0.8%. The interval related to the ultimate strain goes from 3.2% to 5%. The diagram shows a first elastic behaviour, with a curve starting to bend right after the strength was reached, followed by a softening branch till the ultimate strain was reached, showing a good plastic capacity.

Moreover, a comparison in terms of ultimate strength was done, between the tested models and the formulation given by the Eurocode 6. The results are reported in Table 3.17, showing that the code underestimate the strength since it is calibrated in modern constructive typologies, resulting in a not so good formulation for prediction of strength of ancient masonry walls.

Masonry	Mean value of compressive resistance (N/mm ²)	
	Experimental values	EC6
<i>Cantieri</i>	3.97	2.1
<i>Bozzette</i>	3.09	1.6
<i>Blocchetti</i>	2.65	1.4

Table 3.17. Mechanical characteristics of masonry components [12].

In the behaviour of different masonry typologies some differences can be found due to the employed mortar and to the arrangement of the blocks. The low peak strength of the ‘bozzette’ wall and the ‘blocchetti’ wall is due to the low quality of mortar, in the first case, and to the low mechanical capacity of tuff used in the second case. For the behaviour of the softening branch, very important is the bond behaviour between mortar and blocks and the interlocking created by the mutual arrangement of both elements. Finally, the historic masonry showed a very good behaviour in compression and good plastic capacity, which seems to be due both to the blocks arrangement and to the mortar type.

4 STRENGTHENING OF MASONRY WALLS

In the following sections a review of the main aspects related to the strengthening of masonry walls is presented. Some of the most relevant previous studies carried out by different authors in the recent years are examined. In particular, the state of previous knowledge and the information so far obtained through experimental and theoretical studies are investigated with reference to the available existing strengthening techniques for masonry walls, the use of Fibre Reinforced Polymers (FRP) with different arrangements, the evaluation of the contribution of these techniques to the improvement of the overall mechanical capacity of the strengthened element, in terms of shear capacity and energy dissipation. Furthermore, the last development regarding the upgrading of structural masonry walls in terms of seismic behaviour will be outlined and the last innovative reinforcing methodologies proposed during the last years will be reviewed. In addition, the new issues requiring further investigations in terms of experimental studies and numerical modelling are outlined and described in the framework of the present work.

4.1 TRADITIONAL STRENGTHENING TECHNIQUES FOR UNREINFORCED MASONRY PANELS

Existing unreinforced masonry (URM) buildings, many of which have historical and cultural importance, constitute a significant portion of existing buildings around the world. Recent earthquakes have repeatedly shown the vulnerability of URM buildings. This brought to light the urgent need to improve and develop better methods of retrofitting for existing seismically inadequate URM buildings.

In many seismically active regions of the world there are large numbers of masonry buildings. Most of these buildings have not been designed for seismic loads. Recent earthquakes have shown that many of such buildings are seismically vulnerable and should be considered for retrofitting. Different conventional retrofitting techniques are available to increase the strength and/or ductility of unreinforced masonry walls. In the following sections a review on some seismic retrofitting techniques for masonry walls is presented.

Although a variety of technical solutions have been implemented for seismic retrofitting, there exists little information or technical guidelines with which an engineer can judge the relative merits of these methods. Furthermore, no reliable analytical techniques are available to evaluate the seismic resistance of retrofitted masonry structures.

Several conventional techniques are available to improve the seismic performance of existing URM walls and are briefly reviewed in the following sections. Surface treatments (ferrocement, shotcrete, etc.), grout injections, external reinforcement, and center core are examples of such conventional techniques. Several researchers (ElGawady et al., 2004) [13] have discussed the disadvantages of these techniques: available space reduction, architecture impact, heavy mass, corrosion potential, etc. Modern fiber reinforced polymers FRP offer promising retrofitting possibilities for masonry buildings and present several well-known advantages over existing conventional techniques. Studies on shear retrofitting of URM using FRP are limited and a review of the most recent of them will be carried out in the following chapter.

4.1.1 Surface treatments

Surface treatment is a common method, which has largely developed through experience. Surface treatment incorporates different techniques such as ferrocement, reinforced plaster, and shotcrete. By nature this treatment covers the masonry exterior and affects the architectural or historical appearance of the structure.

Ferrocement consists of a thin cement mortar laid over wire mesh (Figure 4.1(a)), which acts as a reinforcement. It is relatively cheap, strong and durable, and the basic technique is easily acquired. Although ferrocement is not strictly a 'sustainable' technology as it uses cement and steel, it nevertheless employs them in a highly efficient and cost-effective manner. The mechanical properties of ferrocement depend on mesh properties. Ferrocement is ideal for low cost housing since it is cheap and can be done with unskilled workers. It improves both in-plane and out-of-plane behaviour. The mesh helps to confine the masonry units after cracking and thus improves in-plane inelastic deformation capacity. This retrofitting technique increases the in-plane lateral resistance and improves wall out-of-plane stability and arching action since it increases the wall height-to-thickness ratio.

Another technique is represented by the application of a reinforced plaster to the wall. A thin layer of cement plaster applied over high strength steel reinforcement can be used for retrofitting. The steel can be arranged as diagonal bars or as a vertical and horizontal mesh. A reinforced plaster can be applied as shown in Figure 4.1(b). In diagonal tension test and static cyclic tests, the technique was able to improve the in-plane resistance by a factor of 1.25-3. The improvement in strength depends on the strengthening layer thickness, the cement mortar strength, the reinforcement quantity and the means of its bonding with the retrofitted wall, and the degree of masonry damage.

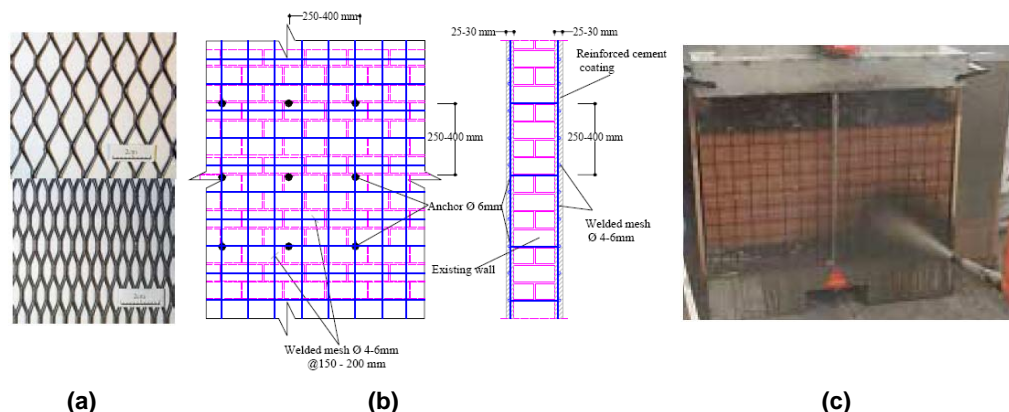


Figure 4.1. Surface treatments: samples of reinforcement used in ferrocement (a); typical layout of reinforced plaster (b); application of shotcrete (c) [13].

Shotcrete represents an alternative solution. Shotcrete overlays can be sprayed onto the surface of a masonry wall over a mesh of reinforcing bars (Figure 4.1(c)). Shotcrete is more convenient and less costly than casting-situ jackets. The thickness of the shotcrete can be adapted to the seismic demand. In general, the overlay thickness is at least 60 mm. In order to transfer the shear stress across shotcrete-masonry interface, shear dowels are fixed using epoxy or cement grout into holes drilled into the masonry wall.

Many of the physical properties of sound shotcrete are comparable or superior to those of conventional concrete or mortar having the same composition. Improperly applied shotcrete may create conditions much worse than the untreated condition. Shotcrete is used in lieu of conventional concrete, in most instances, for reasons of cost or convenience. Shotcrete is advantageous in situations when formwork is cost prohibitive or impractical and where forms can be reduced or eliminated, access to the work area is difficult, thin layers or variable thicknesses are required, or normal casting techniques cannot be employed. Additional savings are possible because shotcrete requires only a small, portable plant for manufacture and placement. Shotcreting operations can often be accomplished in areas of limited access to make repairs to structures. The selection of shotcrete for a particular application should be based on knowledge, experience, and a careful study of required and achievable material performance. Retrofitting using shotcrete significantly increases the ultimate load of the retrofitted walls. This retrofitting technique dissipates high-energy due to successive elongation and yield of reinforcement in tension.

4.1.2 Grout and epoxy injection

Grout injection is a popular strengthening technique, as it does not alter the aesthetic and architectural features of the existing buildings. The main purpose of injections is to restore the original integrity of the retrofitted wall and to fill the voids and cracks, which are present in the masonry due to physical and chemical deterioration and/or mechanical actions. For multi-leaves masonry walls, injecting

grout into empty collar joint enhances composite action between adjacent leaves. The success of a retrofit by injection depends on the injectability of the mix used, and on the injection technique adopted. The injectability of the mix influences by mix's mechanical properties and its physical chemical compatibility with the masonry to be retrofitted.

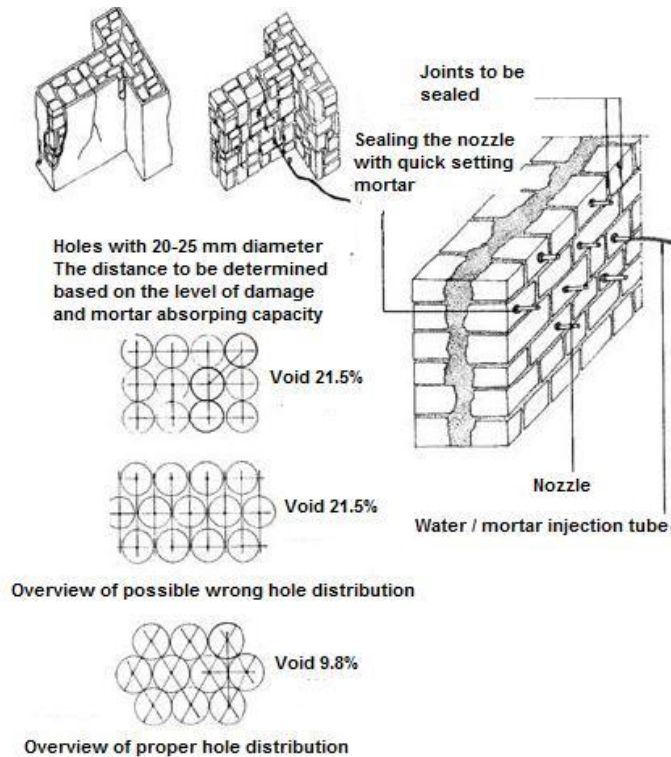


Figure 4.2. Overview of injection holes distribution.

The retrofit of walls by cement grouting can be carried out as follows:

- Placement of injection ports and sealing of the cracked areas in the basic wall as well as around injection ports.
- Washing of cracks and holes with water. Inject of water (soak of the bricks), from the bottom to the top of the wall, to check which tubes are active.

- Injection of grout (Figure 4.2), with injection pressure of less than 0.1 MPa, through each port in succession. Begin injection at the lower-most port. After filling all large voids, a second grout mix (cement-based or epoxy) is used for fine cracks.

This retrofitting technique improves the overall behaviour of the retrofitted URM and is effective at restoring the initial stiffness and strength of masonry.

4.1.3 External reinforcement

Steel plates or tubes can be used as external reinforcement for existing URM buildings. Steel system is attached directly to the existing diaphragm and wall (Figure 4.3(a)). The relative rigidities of the unretrofitted structure and the new steel bracing are an important factor that should be taken into consideration. In an earthquake, cracking in the original masonry structure is expected and after sufficient cracking has occurred, the new steel system will have comparable stiffness and be effective. The vertical and diagonal bracing improves the lateral in-plane resistance of the retrofitted wall.

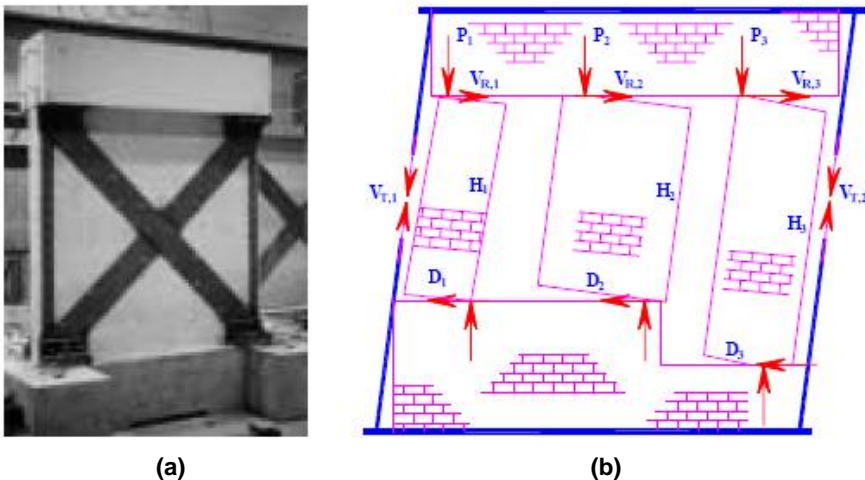


Figure 4.3. External reinforcement using vertical and diagonal bracing (a) or creating infill panel (b) [13].

The increment in the lateral resistance is limited by crushing of the masonry at ends (toes) followed by vertical strips global buckling. In the case of creating infill panel, the rocking motion of the pier is associated with a vertical movement of its corner butting against the support masonries and the steel verticals resist the motion by restringing this vertical movement. This mechanism put both vertical members under tension forces (Figure 4.3(b)). The system increased the in-plane lateral resistance of the retrofitted wall and, in addition, the external steel system provides an effective energy dissipation mechanism.

4.1.4 Confinement of URM with R.C. tie columns

Confined masonry with R.C. weak frame represents one of the most widely used masonry construction system in Asia and Latin America. In China, they used such confinement in new masonry buildings as well as it is used as retrofitting for existing URM buildings. However, it is not easy to construct such confinement in existing masonry buildings. The basic feature of confined masonry structures is the vertical R.C. or reinforced masonry tie columns, which confine the walls at all corners and wall intersections as well as the vertical borders of doors and windows openings. In order to be effective, tie columns should connect with a tie beam along the walls at floors levels.

The confinement prevents disintegration and improves ductility and energy dissipation of URM buildings, but has limited effect on the ultimate load resistance. The amount of reinforcement and concrete dimensions for this system is determined on the basis of experience, and depends on the height and size of the building.

4.1.5 Post-tensioning

Post-tensioning involves a compressive force applied to masonry wall; this force counteracts the tensile stresses resulting from lateral loads. There has been little application of this technique; post-tensioning is mainly used to retrofit structures

characterized as monuments. This is due in part to lack of knowledge about the behaviour of post-tensioning masonry. In addition, the codification of post-tensioning masonry has only begun recently. Post-tensioning tendons are usually in the form of alloy steel thread bars, although mono-strand tendons are not uncommon. Bars typically show higher relaxation losses (2-3 times strand losses) and much lower strength/weight ratio; in addition, a major drawback for using of steel bars is corrosion. However, fiber reinforced plastic presents a promising solution for this problem.

Tendons are placed inside steel tube (duct) either within holes drilled along the midplane of the wall or along grooves symmetrically cut on both surfaces of the wall. Holes are cement grouted and external grooves are filled with shotcrete. In this case, the tendons are fully restrained (i.e. it is not free to move in the holes). This is true even if the tendon is unbonded, i.e. no grout is injected between the duct and the tendons. However, the holes can be left un-grouted (unguided unrestrained). This simplifies the strengthening procedure and allows future surveillance, re-tensioning, or even removal of the post-tensioning bars. It is also important for un-bonded bars to continue the protection of the bar inside the foundation to avoid differential oxidation.

Anchorage of post-tensioning in masonry is more complicated than in R.C. as masonry has a relatively low compressive strength. The self-activating dead end can be encasing to continuous and heavy R.C. foundation beams, constructed on either side of the wall bottom and connected well with it. At the top, post-tensioning is anchored in the existing R.C. elements or in a new precast R.C. special beam or specially stiffened steel plates. Anchorage devices and plates are usually placed in a recess of the surface, and covered later on with shotcrete or cement mortar. The requirement for bottom anchorage penalizes considerably this retrofitting technique. Vertical post-tensioning resulting in substantial improvement in wall ultimate behaviour for both in-plane and out-of-plane; in addition, it improves both cracking load and distribution.

For bonded grouted post-tensioning the ultimate tendon force may be determined assuming rigid bond and plane sections similar to design of R.C. post-tensioning. Thus, the tendon will reach their yield force. For un-bonded post-tensioning the tendon force will increase from service up to ultimate load depending

on the deformations. This increment in the tendon force may be estimated by applying rigid mechanisms. For short time behaviour and under the same post-tensioning force, strand configuration and amount has insignificant effect on wall behaviour.

4.1.6 Center core technique

The center core system consists of a reinforced, grouted core placed in the center of an existing URM wall. A continuous vertical hole is drilled from the top of the wall into its basement wall. The core achieved by this oil-well drilling technique may be 50-125 mm in diameter, depending on the thickness of the URM wall and the retrofitting required. After placing the reinforcement in the center of the hole, a filler material is pumped from the top of the wall to the bottom such that the core is filled from the bottom under pressure controlled by the height of the grout.

The placement of the grout under pressure provided by the height of the core provides a beneficial migration of the grout into all voids adjacent to the core shaft. The strong bonding of the grout to the inner and outer wythes of brick provides a homogeneous structural element much larger than the core itself. This reinforced homogeneous vertical beam provides strength to the wall with a capacity to resist both in-plane and out-of-plane loading. Wall anchors for lateral ties to the roof and floors are placed at the core location to make a positive connection to the wall. The filler material itself consists of a binder material (e.g. epoxy, cement, and polyester) and a filler material (e.g. sand). For cement-based grout, the volume proportions of the components play an essential role in the shear resistance.

This technique is successfully used to enhance the resistance of URM wall under cyclic actions, and lateral maximum lateral displacement, even if the energy dissipated is not so high. However, the system has several advantages: it will not alter the appearance of wall surface as well as the function of the building will not be impaired since the drilling and reinforcing operation can be done externally from the roof. The main disadvantage is this technique tends to create zones with widely varying stiffness and strength properties.

4.2 GENERAL ASPECTS

The high vulnerability of buildings based on systems of structural masonry walls to the actions induced by earthquakes, and the increased serviceability and safety requirements imposed by the new codes, make clear the necessity of such existing buildings to be upgraded. In fact, it is necessary to strengthen this particular class of structures with appropriate reinforcing systems, in order to achieve the required upgrading of their seismic and energy dissipation performances. Furthermore, the damage patterns experienced by two-dimensional elements in masonry structures observed after the stroke during seismic events require development of new types of strengthening techniques and systems, effectiveness of which has to be quantitatively evaluated through experimental and numerical analyses.

The reinforcement of two-dimensional masonry elements has been carried out during the last years by means of different strengthening methods. Some of the most used traditional methods in order to upgrade structural elements in masonry buildings are represented by: (a) filling of cracks and voids by grouting; (b) stitching of large cracks and other weak areas with metallic or brick elements or concrete zones; (c) application of reinforced grouted perforations to improve the cohesion and tensile strength of masonry; (d) external or internal post-tensioning with steel ties, joining structural elements together into an integrated three dimensional system; and (e) single or double sided jacketing by shotcrete or by cast-in-situ concrete, in combination with steel reinforcement (e.g. in the form of two-directional welded mesh). It has been seen that these traditional strengthening techniques are affected by many problems and drawbacks; thus sundry new methods based on the use of innovative materials, such as the Fibre Reinforced Polymers (FRP), have been developed in the last decades (Triantafillou, 1998) [14]. All the last developed techniques take advantage of the well-known benefits proper to the FRP materials including, above all, a light weight, resistance to corrosive environment, excellent mechanical properties such as stiffness and strength, and simplicity to put in place.

One of the early studies on the use of non-metallic reinforcement for strengthening of masonry walls was that by (Crocì et al., 1987) [15], in which it is

presented a campaign of tests carried out on shear walls with vertical or inclined reinforcement realized by low modulus polypropylene braids. Furthermore, detailed concepts and analytical results on the applicability and effectiveness of FRP tendons used to apply circumferential pre-stressing to historic masonry structures are given by (Triantafillou and Fardis, 1997, 1993) [16, 17]. In the work of (Schwegler, 1994) [18] the use of carbon laminates (CFRP) as non-seismic strengthening elements of masonry structures was investigated. The laminates used as tensile reinforcement were bonded to the masonry surface by means of epoxy resin. The tests carried out in order to clarify the effectiveness of this technique were conducted on full-scale, both in-plane and out-of-plane, cyclic testing of one-story masonry walls, and was developed an analytical model for the in-plane behaviour of CFRP-strengthened walls within the framework of stress fields theory. Also, the studies by (Saadatmanesh, 1994) [19] and (Ehsani, 1995) [20] focused on experimental investigations, involving monotonic static tests of unreinforced masonry specimens strengthened with epoxy-bonded glass fabrics. The results obtained from these studies led to the conclusion that for the sake of both economy and mechanical response, unidirectional FRP reinforcement in the form of laminates or fabric strips is preferable to two-dimensional fabrics which cover the whole surface of masonry walls.

4.3 STRENGTHENING TECHNIQUES FOR IN-PLANE BEHAVIOUR

As previously outlined, during the years the researchers developed different strengthening techniques based on the use of Fibre Reinforced Polymers (FRP) externally bonded to the surfaces of the element to be reinforced. These techniques can be described in terms of the FRP typology, reinforcement arrangement, connection system to the substrate. In general, the strengthening techniques can be devoted to the improvement of the out-of-plane flexural capacity, the in-plane shear resistance and the ductility of the system to which the reinforcement is applied.

Several experimental or analytical research works have been carried out on the in-plane response of walls strengthened with FRP sheets or laminates. In (Roca and Araiza, 2010) [21] a review of some in-plane tests configurations used to study

the shear response of reinforced elements is reported (Figure 4.4). In these cases the strengthening strategy is represented by an externally chemically bonded Fibre Reinforced Polymers in form of sheets or laminates. It is noted that such externally chemical bonded reinforcement involves complex mechanical phenomena such as the peeling off of the substrate bricks surface or the influence of friction and dilatancy in the brick-mortar interface on the response of the strengthening itself.

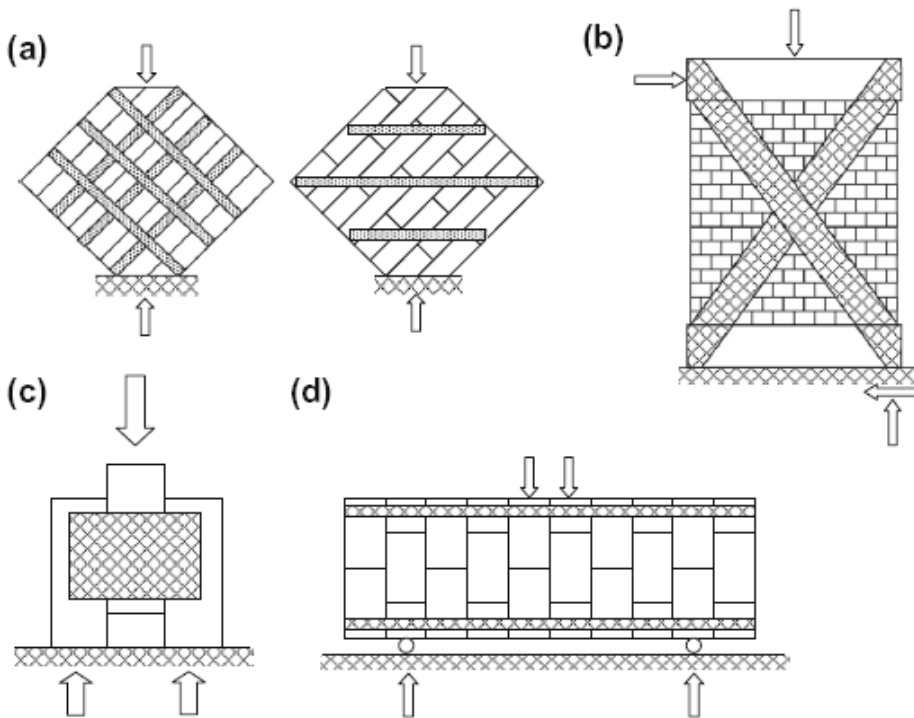


Figure 4.4. Different in-plane test configurations to investigate the shear response of FRP reinforced brick masonry elements: (a) (Valluzzi et al., 2002) [22], (b) (ElGawady et al., 2005) [23], (c) (Eshani and Saadatmanesh, 1997) [34], (d) (Triantafillou, 1998) [31]. [21].

In particular, (Valluzzi et al., 2002) [22] used the classical diagonal compressive tests (Figure 4.4(a)) to explore the in-plane shear response of brick masonry panels strengthened with FRP laminates and compared the experimental results with the predictions yielded by different analytical models. In the cited study the difference in the effectiveness of the reinforcement has been investigated for both

side (symmetric) or for one side (non-symmetric) strengthening configurations. In (ElGawady et al., 2005) [23] and (Avramidou et al., 1999) [24] the effectiveness of FRP strengthening is evaluated through tests on masonry walls reinforced with externally bonded laminates applied diagonally to the joints, as shown in Figure 4.4(b). Moreover, in (ElGawady et al., 2007) [3] the cyclic behaviour of masonry shear walls, employing specimens similar to those in Figure 4.4(b), is investigated by the authors. Also, similar experimental campaigns have been carried out, for example, by (Santa Maria et al., 2006) [25] using CFRP, and by (Fam et al., 2008) [26], (Al-Salloum and Almusallam, 2005) [27], (Wang et al., 2006) [28], (Stratford et al., 2004) [29] using GFRP, (Marcari et al., 2007) [30] considering CFRP and GFRP strips arranged according to cross- and grid-pattern. In particular, in (Fam et al., 2008) [26] has been studied the effect of the combination of two repair techniques for damaged walls, namely grout injection of mortar and application of GFRP sheets, showing that it is possible to fully recover and even upgrade the capacity of the walls.

As previously outlined, (Valluzzi et al., 2002) [22] performed a study in order to investigate the efficiency of the strengthening system considering different configurations, namely strips with grid arrangement or diagonal strips, and the influence of the eccentricity of the reinforcement, strengthening the panels on both sides or only at one side. It is noted that, first of all, the asymmetrical application of the reinforcement is associated to a limited effectiveness in the improvement of the shear resistance of masonry panels. Moreover, it is shown that the diagonal configuration can be more efficient concerning the enhancement of the shear capacity, while the configuration of strips as a grid allows a better stress redistribution producing a less brittle failure due to crack spreading (Valluzzi et al., 2002) [22], (Santa Maria et al., 2006) [25], (Luccioni and Rougier, 2010) [32]. In general, for masonry panels externally reinforced with FRP and subjected to diagonal compression it is observed an increase of strength between 15 and 70%.

(ElGawady et al., 2005, 2007) [23, 3] and (Santa Maria et al., 2006) [25] studied the response of half scale masonry panels strengthened with FRP laminates applied diagonally to the joints subjected to both static and cyclic loading. The tests showed that the increase of lateral strength was proportional to the FRP axial rigidity and, also, using high amount of FRP brittle failure occurred.

A number of researches have been performed in order to study the seismic strengthening of unreinforced masonry walls with FRP. Some results have shown that the reinforcement improves significantly the lateral stability of the walls, increases the shear strength, the maximum displacement before the failure, and the displacement and load at first crack (ElGawady et al., 2005) [22], (Santa Maria et al., 2006) [25], (Chuang et al., 2003) [33].

Finally, some studies have been carried out on elementary shear masonry assemblages, such as that represented in Figure 4.4(c), rather than entire masonry walls or panels, in order to identify and study the elementary mechanisms involved in the strength response of reinforced masonry instead of the evaluation of the overall efficiency of the strengthening (Roca and Araiza, 2010) [21]. Moreover, in such studies the difference with respect to some previous research works lays on the consideration of strengthening strips applied perpendicular to the mortar joints, considered important not only regarding the brick cracking but also for the sliding mode failure of elements. A similar approach, also using simple shear assemblages strengthened by means of overlay reinforcement placed through the mortar joints, has been previously considered by (Eshani and Saadatmanesh, 1997) [34] (Figure 4.4(c)). In (Haroun et al., 2003) [35] shear tests on small wall strengthened transversely to the mortar joints have been also carried out.

A number of experimental procedures and numerical models have been proposed for the study of the bond performances between FRP sheets and bricks. An example is the test procedure described in (Aiello and Sciolti, 2006) [36], allowing the evaluation of bond stress-slip relationship. Another example of investigation of the bond behaviour of the FRP reinforcement on clay bricks is in (Liu et al., 2005) [37], (Willis et al., 2009) [38]. Also some numerical models for the masonry-FRP interface have been recently proposed (Grande et al., 2010) [39].

It is further noted that this technique may lead to some problems that can limit more or less considerably its application for all cases, requiring additional studies. Since the reinforcement is made by continuous strips or sheets externally applied on the surface of masonry wall, this may create a water-proof barrier and produce difficulties for the natural transpiration of stone or ceramic material. In addition, some problems may arise regarding the fire resistance of the strengthening systems that,

especially when used in combination with epoxy-based matrix or bonding material, can be particularly vulnerable.

4.4 EXTERNALLY APPLIED FRP GRID REINFORCED MORTAR LAYERS

An alternative strengthening method to previously described ones has been recently proposed by (Papanicolaou et al., 2007, 2008, 2011) [40, 41, 42] for strengthening of unreinforced masonry walls subjected to in-plane and out-of-plane cyclic loadings. As already described, numerous techniques have been developed in order to rehabilitate and strengthen URM structures; these may be roughly categorized as 'conventional' and as 'modern'. The former include surface treatments (such as shotcrete or ferrocement overlays), grout injections and internal or external prestressing with steel ties. The latter include the use of metallic or polymer-based grid-reinforced surface coatings, externally bonded fiber-reinforced polymers (FRP, such as epoxy-bonded strips or in situ impregnated fabrics) and near-surface mounted (NSM) FRP reinforcement.

In the cited case, a technique that combines the benefits of both types of interventions, conventional and modern, is the one in which the reinforcement consists of a textile reinforced mortar (TRM) in substitution of the FRP used as overlays or near surface mounted reinforcement. The researchers introduced the TRM in the strengthening of unreinforced masonry walls in order to address the numerous drawbacks related to the use of FRP externally bonded to element surface and mainly associated to the employment of organic binders.

These drawbacks are attributed mainly to the use of organic binders (resins) and can be summarized as follows:

- (a) poor behaviour of resins at temperatures above the glass transition temperature;
- (b) relatively high cost of epoxies;
- (c) potential hazards for the manual worker;
- (d) difficulty to apply FRPs on wet surfaces or at low temperatures;

- (e) lack of vapour permeability;
- (f) incompatibility of epoxy resins and some substrate materials (e.g. clay);
- (g) difficulty to conduct post-earthquake assessment of the damage suffered by the masonry behind the FRP.

In addition, certain properties of clay masonry, such as the porosity and surface unevenness and/or roughness, which affect the epoxy-brick bond behaviour, as well as restrictions related to intervention strategies for historic masonry buildings (e.g. requirements for reversibility), may possibly inhibit the success of FRP application (Papanicolaou et al., 2007) [40].

In Figure 4.5 a snapshot of the TRM strengthening is shown, considering the different phases of the application of the reinforcement system. The benefits of this technique have been compared to the classical application of FRP in forms of strips, considering both the in-plane shear and out-of-plane flexural increase of strength for the cases of monotonic and cyclic loading conditions.



Figure 4.5. Textile-reinforced mortar (TRM) strengthening of a masonry panel: phases of application [42].

The specimens used by the authors in this study are represented by medium-scale clay brick shear walls, beam-column type walls and beam type walls subjected

to cyclic out-of-plane or in-plane loading. On the basis of the experimental results, it has been noted that the textile-reinforced mortar system lead to an increase of the load carrying capacity and deformability of unreinforced masonry walls. Furthermore, for the case of out-of-plane loading the TRM overlays perform even better than the ordinary FRP reinforcement in terms of maximum load and displacement at failure, in the cases in which tensile fracture of textile reinforcement does not occur. For the case of in-plane loading, TRM results in reduced effectiveness for strength (but not more than 30%), if compared with FRP-EBR strengthening. In terms of deformation capacity, representing a fundamental characteristic in seismic retrofitting of masonry structural elements, TRM reinforcement is found to be more effective than FRP, up to about 15–30% in shear walls. In addition, the strength generally increases with the number of layers and the axial load, at the expense of deformation capacity (Papanicolaou et al., 2011) [42].

The experimental study highlighted the effectiveness of the TRM jacketing technique as a solution for strengthening of unreinforced masonry walls subjected to either out-of-plane or in-plane loading. The authors also suggest further investigation in order to expand the amount of experimental data and to optimize this technique for the seismic retrofitting.

In (Faella et al., 2010) [43] a similar technique has been employed in order to strengthen yellow-tuff-masonry walls, which are rather common in the South of Italy as well as in the Mediterranean basin. The composite material utilized for strengthening is made out of a carbon fiber mesh, arranged according the configuration shown in Figure 4.6(a), placed within two layers of mortar, according to the usual procedure currently carried out for spreading a plaster layer upon the wall faces: in particular, two mortar layers have to be placed for embedding carbon fibers and developing composite interaction between fibers and matrix (Figure 4.6(b)).

The experimental campaign carried out on these reinforced elements showed that strengthened walls did not fail for the characteristic diagonal sliding fracture at the mortar-to-brick interface, that generally develops in unreinforced masonry walls. In fact, the strengthening layer restrain the possible formation of such diagonal crack, as indicated by the change in stiffness which can be observed on the load–displacement curves. Consequently, the ultimate load in diagonal compression, and

the corresponding shear strength, for strengthened walls was found to be between four and six times greater than the one observed for bare walls.

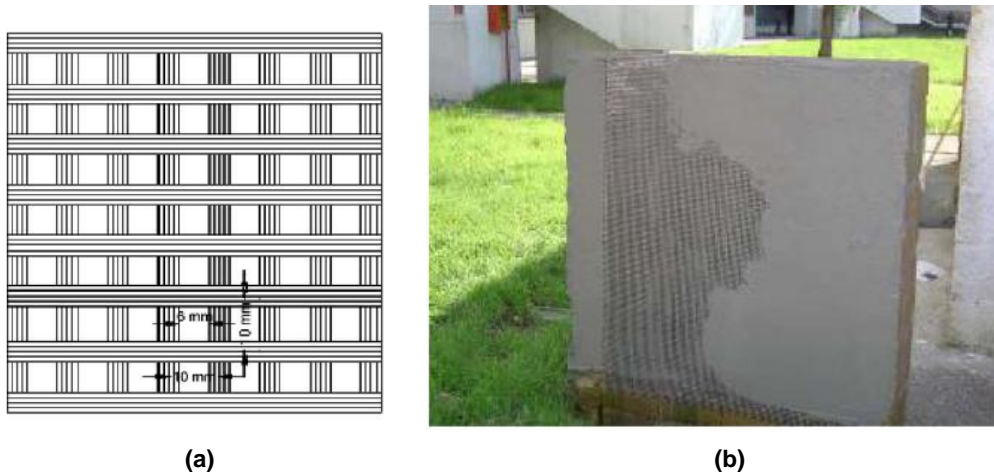


Figure 4.6. Carbon fiber reinforcement mesh texture (a) and application of the TRM layer [43].

Furthermore, no fiber tearing failure has been observed, but failure usually occurs prematurely after loss of adhesion between the strengthening layer and the masonry substrate. Due to this evidence, the same increase in shear strength would have been observed even if a less resistant layer would be employed; in particular, based on characteristics compatible with mechanical properties of masonry substrate, namely strength and stiffness.

In any case, the system examined represents a reliable solution for enhancing shear strength on tuff-masonry, confirmed in its effectiveness by the significant increment in shear resistance observed in strengthened walls compared to the non-strengthened ones.

Another innovative strengthening method developed in the last years features, on the basis of the previous described technique, that the textile reinforcement is replaced by commercial grids made of long fibre rovings, usually made of carbon, glass or aramid, arranged in two orthogonal directions. In addition, the polymer resins are substituted by cement- or lime-based mortars. The composite action is achieved in this case through mechanical interlock of the grid structure and the mortar passing through the grid's openings. An important aspect to be remarked

is represented by the fact that the use of an inorganic material as a binder rather than an organic resin can be more advantageous and can solve some problems, such as poor behaviour at high temperatures, vapour impermeability, incompatibility with masonry substrate (Prota et al., 2006) [4].

The specimen employed by (Prota et al., 2006) [4] are represented by tuff masonry walls reinforced by a cementitious matrix–grid (CMG) system externally applied to the masonry wall surface. Yellow tuff stone represents the main volcanic product widely spread particularly in Southern Italy where seismic hazard is relevant and represents a crucial aspect in the preservation process of historical constructions. Due to high porosity and low abrasion resistance, tuff surfaces need to be pre-treated by using proper coating primers in order to consolidate the support and improve the adhesion of strengthening FRP materials. High compatibility and reversibility are concepts of particular relevance for application on historical buildings, and are also required when selecting the strengthening methods using FRP.

The grid used for the strengthening system, as shown in Figure 4.7, was a bi-directional alkali resistant AR glass coated open grid, SRG 45, consisting of machine and cross direction strands connected perpendicularly at about 25.4 mm spacing, while the matrix was a polymer modified AR-glass fiber reinforced mortar. The choice of such cementitious composite material was due to some advantages, mainly due to its highly compatibility in terms of physical and mechanical properties with the tuff substrate. Among the advantages of the CMG strengthening system, the following can be mentioned:

- (a) ease of installation;
- (b) no need for any surface preparation or high levels of workmanship;
- (c) fire resistance;
- (d) excellent bond with the substrate;
- (e) breathability of the system which allows transport of air and moisture through the matrix, and reversibility.

Moreover, as already stated, for strengthened walls exposed to high temperature or environmental effects, the application of a thick layer of cementitious mortar substantially ensures a protection for the reinforcing grid and improves the long-term behaviour of the strengthening system. Due to these key advantages and unique

properties, this system is a potential alternative to the traditional strengthening techniques used for masonry structures.

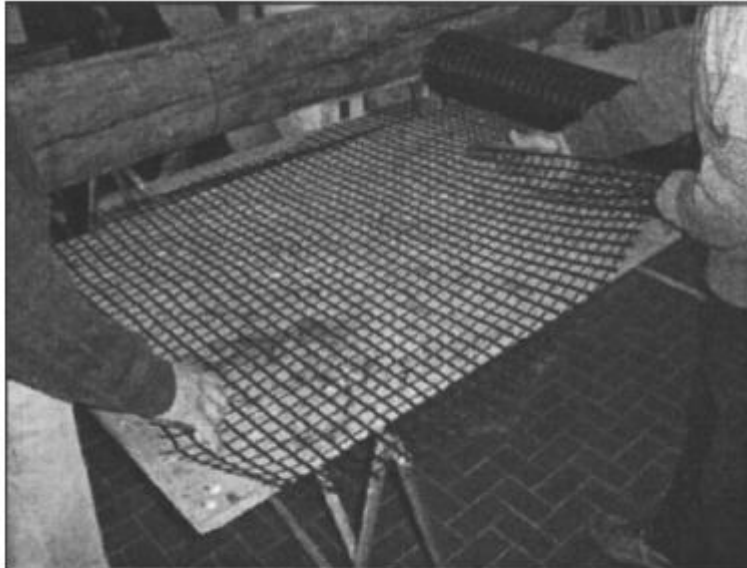


Figure 4.7. Bi-directional alkali resistant AR glass coated open grid, SRG 45 [4].

The installation of the strengthening system on the masonry substrate has been done considering controlled procedure. First of all the wall was properly pre-wetted and the mortar, previously mixed with water and an acrylic hardener, was then trowelled onto the wall in a 5 mm thick layer. The first 900 mm² fabric sheet was firmly hand pressed into the wet binder to ensure its adequate embedding to the support wall. The first ply was laid up with the primary fibers aligned horizontally to the bottom of the wall (Figure 4.8(a)). Then, a second layer of mortar was applied by trowelling an additional 5 mm thick layer. Finally, the second ply was applied with the primary fibers aligned vertically. A 15 mm offset of the second ply with respect to the first was ensured in order to avoid that any fracture plane could originate from the overlap. The second ply was covered by a relatively smooth surface, and the resulting CMG system nominal thickness was of about 10 mm (Figure 4.8(b)). In the cited tests, the installation of the CMG system involved one or both sides of tuff masonry walls.

The experimental campaign carried out by the authors allows to recognize that the CMG system reduces the high anisotropy of the as-built panels; the engineered composite masonry–CMG wall is made of two components: the CMG system that ensures the required shear strength to the mortar–stone interface, and the stone blocks providing the compressive strength. The obtained results indicate that relevant increases of shear strength can be obtained using the CMG reinforcement, especially when a double layer of CMG is applied on both sides of the panel. This configuration also provides a better post-peak response and a significant increase in ductility (Prota et al., 2006) [4].

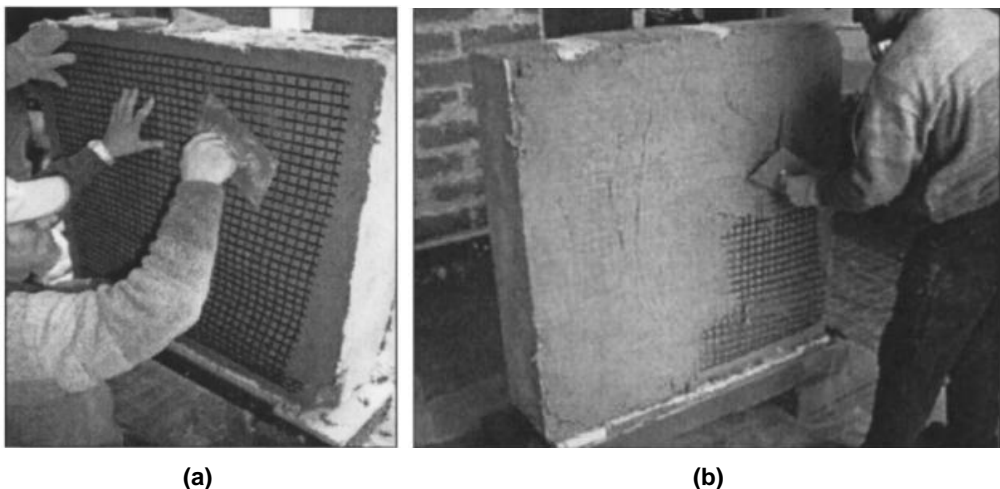


Figure 4.8. CMG system: reinforcing grid installation (a) and troweling of final mortar layer (b) [4].

It can be finally observed that the CMG system satisfies basic design requirements such as compatibility with the support, high bond properties, and reversibility of the intervention. Significant improvements of strength and ductility of panels were achieved installing different layouts of the CMG grid, while there is a negligible influence on the initial stiffness of the strengthened walls. Moreover, the impact of the intervention on the existing structure is very low and compatible with conservation requirements. The comparison of results provided by different reinforcement layouts gives important, even though not comprehensive, information

for the design of in-plane strengthening of masonry walls. Further research is needed to assess the effectiveness of the proposed strengthening solution when applied to different brickworks and structural layouts and further experimental investigations are necessary as well in order to assess the performance under cyclic actions of masonry elements strengthened with the CMG system.

In (Drdáček and Lesák, 2009) [44] a test campaign on masonry walls strengthened by different techniques has been carried out, including also the use of geo-net reinforced plaster layers applied to the specimen surface. For the masonry walls strengthened with geo-nets, three different cases were considered by varying geometrical and mechanical characteristics. The rendering used to embed the geo-net reinforced consisted in lime mortar containing a small percentage of Portland cement. Some of the specimen tested by the authors were represented by damaged specimen used in previous test under the application of a horizontal load, repaired with the same system. The test were carried out applying a cyclic load with a stepwise increase in the maximum cyclic limits.

The tested specimens presented a particular crack pattern, that is different from the one that can be found in specimens reinforced with X-shaped FRP strips. In fact, the cracks visible on the surface represent a combination of two sets of damages: masonry cracks, and cracks which occur in the plaster only and originate from the differential movement of a plastic mesh. In general geo-nets have a better ratio of strength to the strength of brick, if compared with FRP laminate reinforcement, and it is advisable to apply them on masonry substrates.

Systems similar to the previous ones have started to be studied using again cement-based matrix grid systems to strengthen unreinforced masonry walls. In (Aldea et al., 2006) [45] a composite system consisting of a sequence of layers of cement-based matrix and alkali resistant glass coated reinforcing grid has been used (Figure 4.9). The characterization of the considered strengthened systems has been carried out and the assessment of its effectiveness for improving unreinforced masonry walls seismic performance has been investigated by the authors. The experimental campaign resulted in the evidence of the ability of the cement-based system to strengthen the walls and showed a better performance compared to other FRP reinforcement alternatives.

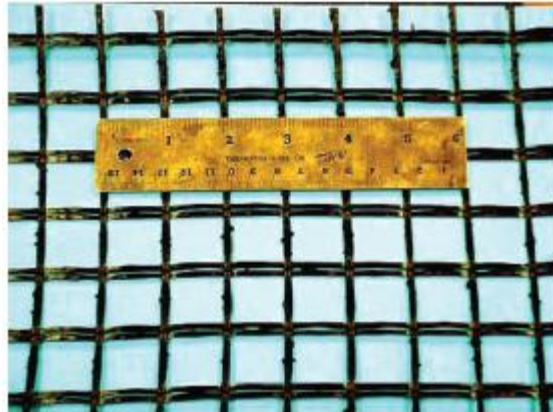


Figure 4.9. Coated AR-glass grid employed by (Aldea et al., 2006) [45].

The tests have been carried out on lightly reinforced single-wythe masonry walls to simulate typical piers between windows of a building. The concrete masonry full scale walls were tested under in-plane shear loading in order to simulate seismic action. In the experimental campaign carried out by the authors, as illustrated in Figure 4.10, different commercially available FRP systems using E-glass fabrics applied in various reinforcement configurations and the CMG system were considered. In particular, CMG system application was full coverage, on one side of the wall only.

X-cracking was the failure mode observed for all the walls strengthened with CMG system. The bond between the strengthening system and the substrate plays a critical role in providing adequate load carrying capacity to the structural element strengthened. Multiple cracking of CMG system surface was observed during the tests, which suggests stress distribution and energy absorption provided by the reinforcing grid.

Since in this study, the reinforcement was placed on only one side of the walls, it can be observed the difference between the reinforced face and the unreinforced back at failure: in particular, the reinforced face of the wall held the masonry wall together at failure, whereas the material was spalled away from the back. In all tests the structural integrity of the walls at failure was ensured by CMG

system. This suggests that its use may be able to prevent the collapse of unstrengthened walls, which is a major source of hazard during earthquakes.

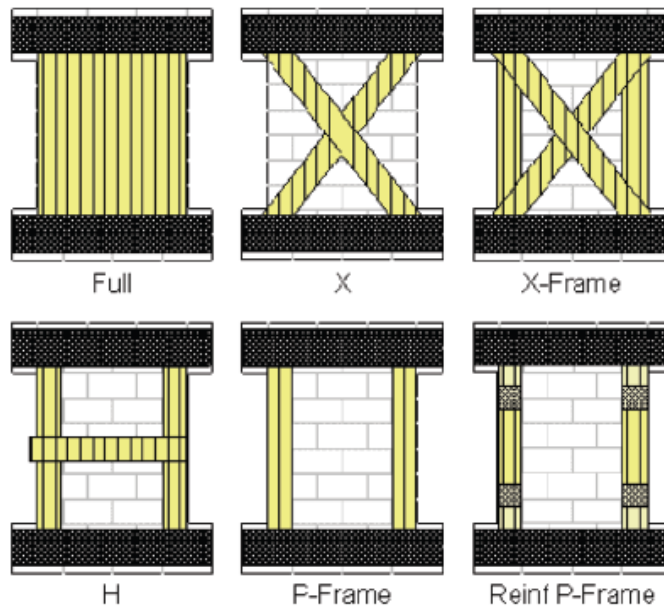


Figure 4.10. Different FRP reinforcement configurations investigated by (Aldea et al., 2006) [45].

Finally, in Figure 4.11, typical horizontal force - displacement curves for a reference and a strengthened wall using CGM system are presented. It can be observed that the addition of the strengthening system significantly improves the performance of the wall, both in terms of strength and ductility. In all cases the engineered load improved for the strengthened walls tested compared to reference.

In conclusion, as already described, the strengthening of masonry walls by means of fibre reinforced polymer grid embedded in a cement- or lime-based mortars, constituting also the bonding material on the substrate to which it is applied, is an effective strengthening technique for both in-plane and out-of-plane actions. Also, this reinforcing methodology allows to overcome some of the main disadvantages characterizing the employment of the externally bonded FRP in forms of strips or sheets and the FRP elements applied via the near-surface mounted (NSM) technique.

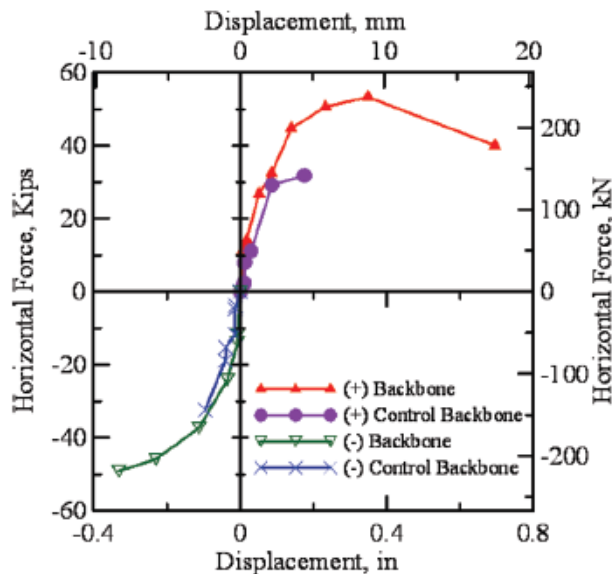


Figure 4.11. Example of a typical Horizontal Force – Displacement curve for CMG strengthened wall compared with URM wall [45].

In the present thesis the strengthening technique that will be considered is represented by mortar layers embedding a FRP reinforcement in form of a grid. The FRP-Reinforced Mortar Layers are symmetrically externally applied to the walls surfaces. This technique is characterized by a number of advantages if compared to other possible FRP-based strengthening methods; particularly, a superior resistance to fire action has to be remarked, a good compatibility and bond with the substrate material, particularly in the case of masonry, vapour permeability. The main interest in the study of this strengthening technique is related to the promising possibility it offers in the upgrading in-plane shear behaviour of the system to which it is applied. The performances of the whole assemblage need to be investigated for monotonic loading state as well as for cycling loading conditions. Another important issue to address is also the assessment of the effectiveness of the considered strengthening system in the improvement of the overall ductility of reinforced elements.

4.5 MODELLING OF THE BEHAVIOUR OF THE REINFORCED SYSTEM

Some numerical analysis have been also carried out on masonry panels strengthened with cementitious matrix grid composites with the aim of investigate the scattered results due to workmanship defects through FEM parametric analyses (Lignola et al., 2009) [5]. In addition, it has been shown that the presence of the external reinforcement reduces the anisotropy of the as-built panels leading to a better redistribution of the stresses and a more uniform and diffused crack pattern, allowing for higher shear strength and deformability. For that reason, strengthened panels are less sensitive to the workmanship defects. Moreover, it has been observed that the strengthening also provides a good post-peak response and a better ductility for the panels.

In order to conduct the analyses, finite-element method (FEM) models of the elements have been compared by the authors. Experimental data obtained through a past test campaign carried out by (Prota et al., 2006) [4] can represent the database of results about how fiber density and layout could influence the strength and ductility performance of strengthened panels. Moreover, in a previous work conducted by (Lignola et al., 2007) [47], a parametric analysis was carried out on a geometrical ideal panel focusing mainly on the variability of mortar and tuff properties. The experimental data were compared to numerical model. Regarding the numerical modelling strategy of the elements, a micro-modelling approach was adopted to fully understand the contribution of basic constitutive materials, namely mortar and tuff blocks, and to quantify the effect of the eventual workmanship defects on the masonry behaviour by means of many parametric analyses on the numerical model. At the micro level, the interaction between mortar joints and brick units is analyzed by means of a detailed analysis involving discrete nonlinear models of single elements layered according to predefined patterns.

The details of the specimen geometry are given in Figure 4.12(a). The overall dimensions of the panels tested by the authors were: 1030 mm height, 1030 mm length, and 250 mm width, with an aspect height-to-length ratio of 1, commonly found in multi-storey buildings.

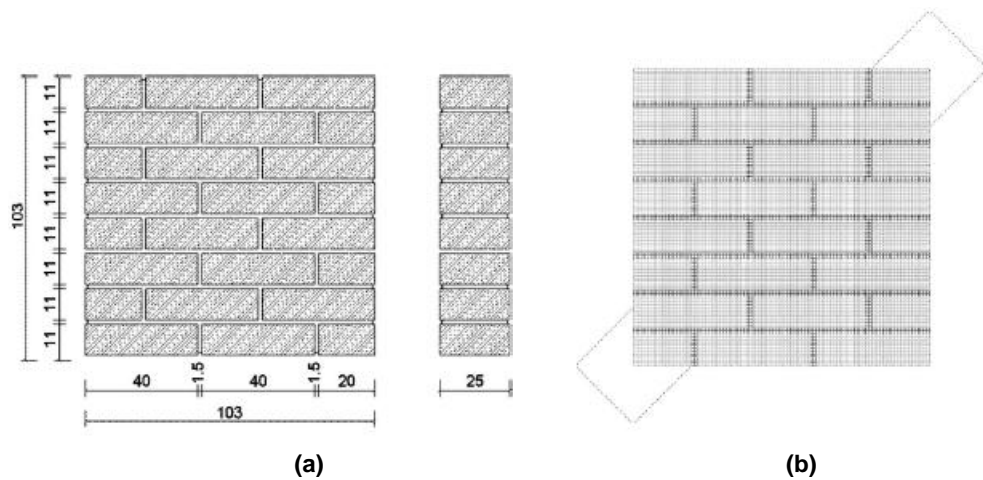


Figure 4.12. Geometry of the masonry walls (a) and Finite Element micro-model (b) [3].

The panels were modelled by eight-node quadrilateral isoparametric plane stress elements; the resulting finite element model is shown in Figure 4.12(b). These elements are based on quadratic interpolation and Gauss integration. At the micro level the tuff and the mortar are modelled independently, without frictional interfaces between them, according to a smeared-crack approach with exponential strain softening in tension and plasticity in compression by means of a parabolic curve formulation both based on tensile and compressive fracture energy Figure 4.13. The biaxial stress state in the two materials has been modelled by a combination of the yield conditions of Rankine and Von Mises. The former is adopted to describe the tensile regime, the latter to describe the compressive regime. This combined yield surface is especially applicable in plane stress situations. CMG is modelled as an additional material bonded to the masonry panel. The cement based mortar, representing the matrix, is modelled like the mortar of the masonry substrate, while the composite grid material is linear elastic up to failure (brittle) in tension and no strength is considered in compression. In all the experimental tests, the wall structural integrity at failure was ensured by the CMG strengthening system, revealing the high bond performance between CMG and the support even without any mechanical anchorage (Prota et al., 2006) [4]. This suggests that the strengthening system can be perfectly bonded to the masonry panel in the FEM simulations. Thus, in the model

it was simulated with eight-node quadrilateral elements over the first masonry substrate mesh, connecting the same nodes, but with their own properties.

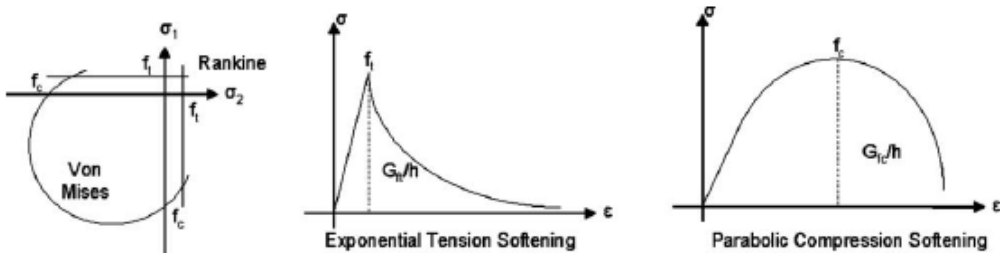


Figure 4.13. Assumed non-linear material models for units and mortar [5].

The response of the reference, as-built, panels was characterized by the development of early cracks through the diagonal mortar joints starting at the middle of the diagonal of the wall (example is shown in Figure 4.14(a)). The composite fibers led to a better redistribution of the stresses in the panel, and a more uniform and diffused crack pattern was achieved, instead of few localized cracks allowing for higher shear strength and deformations. The CMG system reduces the anisotropy of the as-built panels; the strengthened wall is then made of two components: the CMG system that ensures the required tensile strength and the masonry substrate providing the compressive strength. The load applied to the panel passed through the matrix and induced tension forces in the composite grid. Figure 4.14(b) shows multiple and spread cracking of the panel after the CMG system application, which confirms the better stress distribution and, consequently energy absorption, provided by the reinforcing grid. This means also that once the composite action is ensured between masonry and strengthening system, doubling the number of plies does not produce a proportional performance improvement, but smaller strength increases are expected to be achieved.

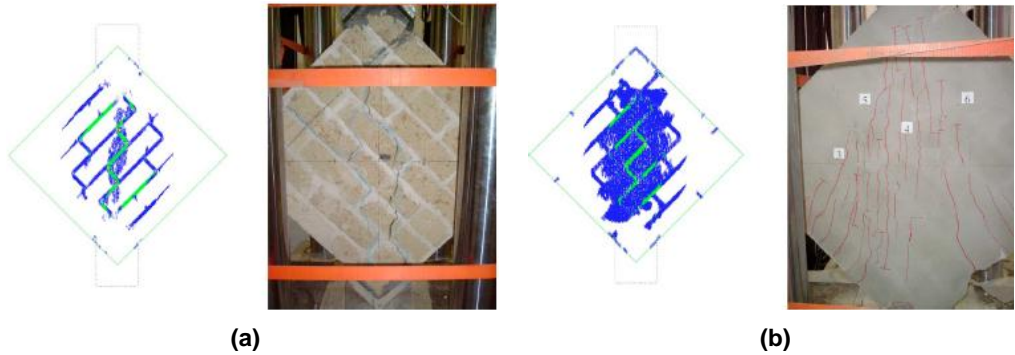


Figure 4.14. Comparison between numerical and experimental crack patterns for as-built panel (a) and strengthened panel (b) [5].

In (Gabor et al., 2007) [48] are presented different finite element modelling approaches for the analysis of the behaviour of unreinforced and FRP strengthened masonry walls when they are subjected to a predominant shear load. Three models have been analysed, having different complexity levels, and used for the simulation of diagonal compression tests on masonry panels.

The models have different complexity levels:

- (a) Detailed modelling, which considers the real configuration of the masonry panels (constituted from bricks and mortar) and the composite reinforcement.
- (b) Simplified modelling, considering the experimentally measured global mechanical parameters of the masonry panels.
- (c) Simplified modelling, based on homogenization theory, where bricks and mortar are replaced by an equivalent continuum.

As illustrated in Figure 4.15, three types of FRP composites are employed: a unidirectional glass fiber, a unidirectional carbon fiber and a bidirectional glass fiber. The mechanical properties of the composites have been determined in tension on coupons. The composite coupons are manufactured in the same conditions as they are overlayed on the walls: embedding the composite fibers in the epoxy resin.

Firstly, the authors considered a detailed micro-modelling of the unreinforced masonry. This approach considers the detailed structure of the masonry: it is built as a regular inclusion of bricks into a matrix of mortar. The mortar is considered as a net which perfectly bonds to bricks. The geometrical configuration and the boundary

conditions are identical to the real ones. The bricks are fully elastic and the mortar joint is characterized by an appropriate elasto-plastic model; thus, the non-linearity of the brick/mortar interface is transposed onto the behaviour of the mortar joint. A plane stress modelling is carried out using four node standard elements having two degrees of freedom per nodes, four Gauss integration points and Lagrangian polynomials as shape functions. This model is found to give a relatively good prediction of the behaviour of the unreinforced masonry panel.

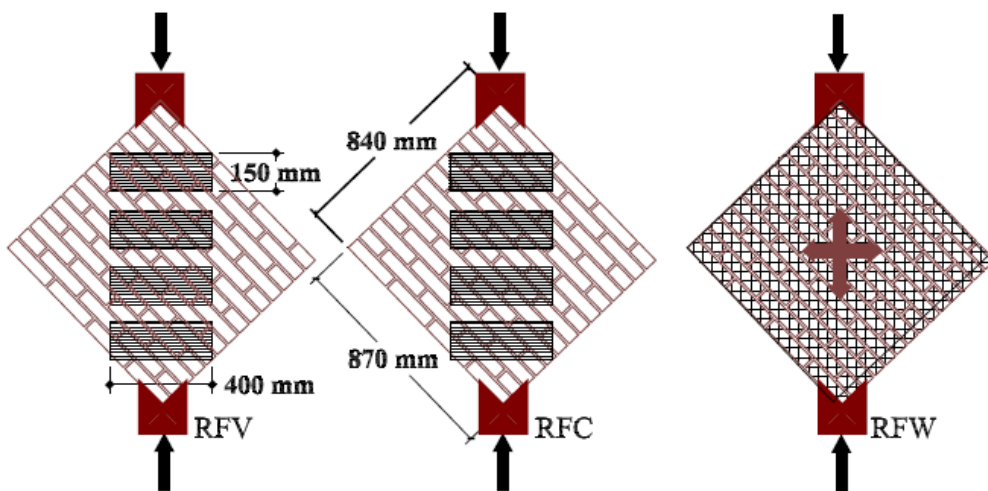


Figure 4.15. Different configuration of the strengthening system for masonry panels [48].

It is noted that the detailed modelling of the geometrical structure of the masonry requires important computational resources and renders the modelling quite laborious. Thus, if the goal of the modelling is to obtain an approximation of the average behaviour of the masonry in terms of loads and strains, it is conceivable to build an equivalent material model without considering the internal geometry of the masonry. In addition, in this case the model parameters are considered independent: the elastic modulus does not act on the global resistance as well as the shear strength does not modify the global stiffness of the masonry. In these conditions, an equivalent material having the global elastic properties of the masonry panel and the plastic parameters of the joint/brick interface can be considered.

Another approach followed by the authors is the modelling of panels using homogenized medium. Through the homogenization is possible to obtain the mechanical parameters of an equivalent material, based on the establishment of average stresses and strains on a representative volume element.

For the simulation of the behaviour of the reinforced masonry panels the detailed modelling, considering separately the bricks, the mortar and the composite reinforcement, have been only used. Even if the homogenized model for the unreinforced masonry gives a quite accurate response of the structure, it needs some improvements for taking into account the composite reinforcement. The elements used in the model allow membrane stiffness and tension-only option for the composite layers. The elements are standard tri-dimensional element having three degrees of freedom at each node. The behaviour law of the composite sheets is considered as elastic, and the real thicknesses of the composite reinforcements were considered. The model of the reinforced masonry panel is obtained by coupling the nodes of the elements of the masonry with those of composite strips. This corresponds to a perfect bonding between the masonry constituents and the composite strips.

Finally, the parametrical study carried out by the authors based on the finite element modelling underlined again the effectiveness of bi-directional composites applied on the entire surface, since the increase of the thickness of composite strips that are applied in strips does not induce a proportional increase of the strength or of the deformation capability.

5 EXPERIMENTAL TESTS ON REINFORCED MASONRY WALLS

In the present chapter the experimental tests on masonry walls carried out in the ITAM Structural Laboratory will be described. In particular, the description of the specimens, in terms of geometry and employed materials, the strengthening systems and the test set-up will be outlined. Finally, the results obtained from the test campaign will be presented and some comparisons and evaluations will be performed between the different cases. The tests carried out can be successively used in order to verify the numerical model described in the following chapter in order to assess the accuracy of the theoretical approach.

The laboratory tests consist of in-plane shear tests on masonry walls strengthened with different techniques and subjected to a combination of compression and cyclic shear loading. A total of twelve specimens was tested, in which the masonry was made with bricks of different materials. In particular, adobe bricks, solid burned clay bricks and dry unburned clay bricks were used according to the same arrangement. For the reinforcing systems, a first strengthening method polyester geo-nets and polypropylene geo-nets externally applied on both surfaces of the wall. Another strengthening method is represented by the use of steel rods mechanically fastened to the wall and disposed according to an X shape, inserted into grooves parallel to each diagonal and fastened to the wall. For all the specimens the configuration of the reinforcement was done in a symmetric fashion, namely on both surfaces of the masonry wall.

The experimental campaign presented in this work represents a continuation of previous researches carried out by (Avramidou et al., 1999) [24], (Drdácký and Lesák, 2001) [49] and (Drdácký and Lesák, 2009) [44] on brick walls strengthened by

fibre reinforced plastics strips with an epoxy resin matrix. The experimental evidences in that case led to the conclusion that even though the strips increased the load carrying capacity of brick walls and might be effectively used for repair of damaged walls after earthquake, the method is very costly, labour consuming and require the use material of a very high quality non-comparable to the co-operating bricks. Other important issues are also related to the possible fire protection of the reinforcement system, that is questionable in practical applications in interior of buildings. The experimentation is thus continued in order to investigate brick walls strengthened with plastic nets with rectangular grids. The effectiveness of nets was tested also on brick walls severely damaged during previous cyclic tests. New as well as damaged walls were strengthened with geo-nets.

5.1 EXPERIMENTAL SPECIMENS

In the ITAM Laboratory for Experimental Mechanics, twelve test specimens have been prepared for the experimental campaign presented in this thesis. The overall dimensions of the walls are 240 mm in thickness, 1050 mm in width and 1367 mm in height. The specimens have been walled up on steel-supported channels with fixtures that enabled the specimens to be lifted by a crane and positioned into the testing rig. Three types of bricks have been used to wall up the masonry panels: adobe bricks, solid burned clay bricks and dry unburned clays bricks were used according to the same arrangement. The dimensions of the fundamental element employed to construct the panels are reported in Figure 5.1.

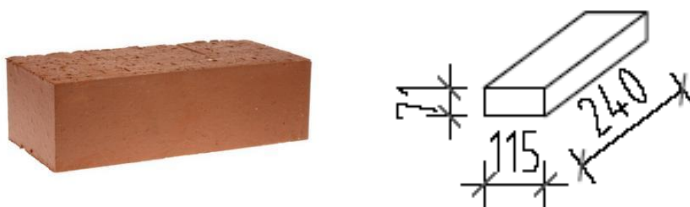


Figure 5.1. Dimensions of the fundamental element used in the masonry specimens.

In Figure 5.2(a) the overall arrangement of the walls is presented, while in Figure 5.2(b) the position of the reinforcement net is illustrated. The overview of all tested specimens with their description is given in Table 5.1.

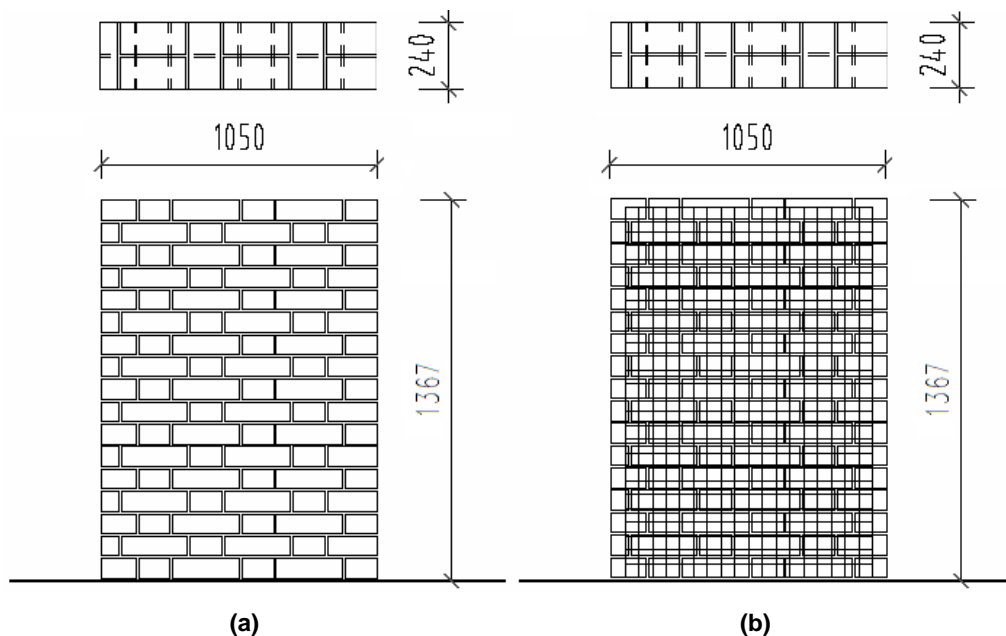


Figure 5.2. Overall dimensions of the masonry specimens and bricks arrangement (a) and position of the reinforcement grid (b).

Material	Type of specimen	Description
Adobe brick	ABW-1	Unstrengthened
Adobe brick	ABW-2	Strengthened with the wire ropes
Adobe brick	ABW-3	Strengthened with the geo - nets polyester
Adobe brick	ABW-4	Strengthened with the geo - nets polyester (Retrofitted ABW-1)
Adobe brick	ABW-5	Strengthened with the geo - nets polypropylene
Dry brick	DBW-1	Unstrengthened
Dry brick	DBW-2	Strengthened with the geo - nets polypropylene
Dry brick	DBW-3	Strengthened with the geo - nets polyester
Dry brick	DBW-4	Strengthened with the wire ropes
Solid brick	SBW-1	Unstrengthened
Solid brick	SBW-2	Strengthened with the wire ropes
Solid brick	SBW-3	Strengthened with the geo - nets polyester

Table 5.1. Overview of the experimental campaign on masonry walls.

In a previous experimental campaign, test specimens without reinforcement were prepared, and they were tested to failure, when pronounced cracks occurred. At the beginning, the deformation characteristics of the plain masonry were measured (compressive deformation modulus). In Figure 5.3 some of the unreinforced masonry panels that have been prepared are shown, for three types of bricks considered in this study.

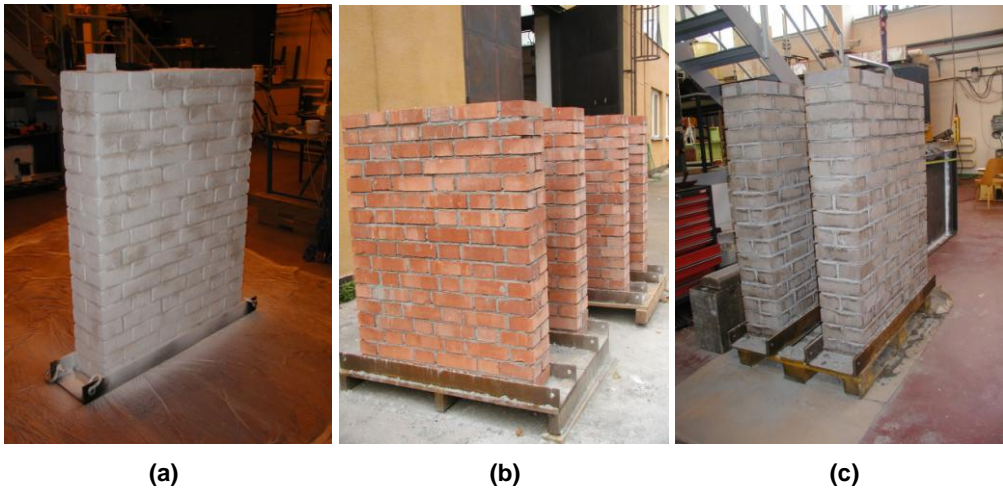


Figure 5.3. Unreinforced masonry walls: (a) adobe, (b) burned clay bricks, (c) unburned clay bricks.

For the reinforced specimens, a first strengthening method is represented by the use of polyester TENCATE geo-nets and polypropylene TENAX geo-nets externally applied onto the wall surfaces (Figure 5.4).



Figure 5.4. Geo-nets employed for strengthening of masonry walls: polyester (a) and polypropylene (b) grids.

The nets were attached to both surfaces of the masonry panels by means of steel staples shot by pneumatic pistol. After they have been mechanically fastened to the surfaces, the walls were rendered with about 2 cm thick plaster, made with lime mortar containing a small percentage of Portland cement. In Figure 5.5 are shown two examples of masonry walls onto which the reinforcement net was applied, and the plastering was made.

For the experimental programme was also prepared a specimen severely damaged in a previous test, which has been repaired using the same system of geo-nets, after removing the remains of the composite strips previously applied, and tested again. The cracks have been only plastered with a thin cement mortar in order to smooth the surface for fixation of geo-nets.

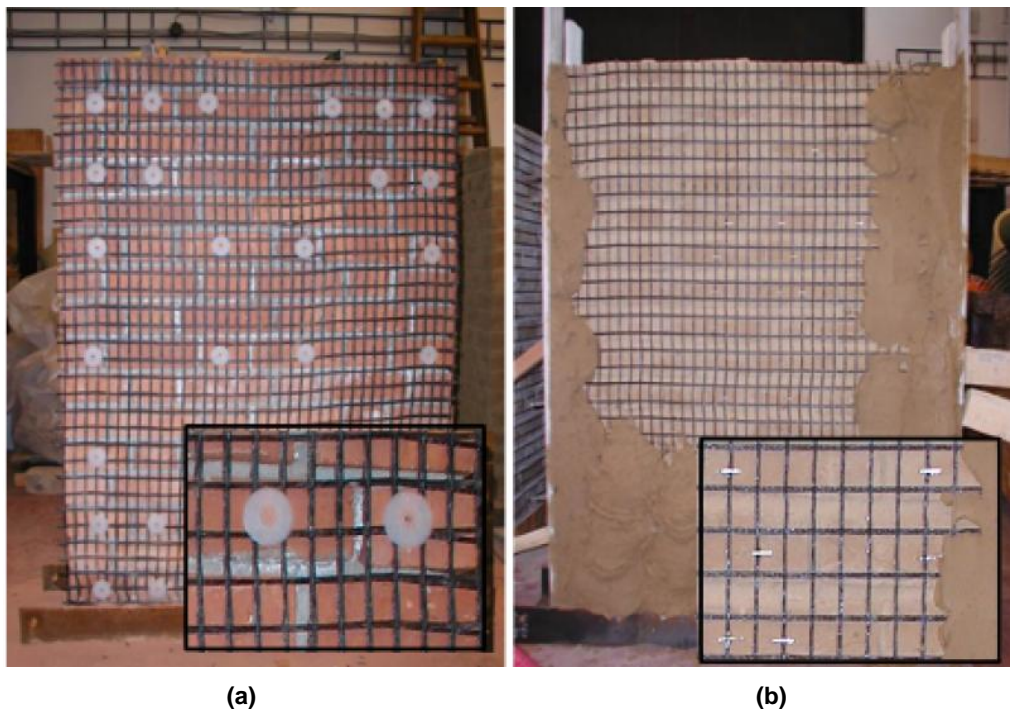


Figure 5.5. Masonry walls strengthened with polymeric nets: (a) solid brick wall; (b) adobe brick wall.

A second strengthening method considered in the experimental campaign concerned one of the adobe brick walls. The reinforcing elements used in this case

are represented by steel wire ropes placed diagonally and in two direction on the wall surfaces. In Figure 5.6(a) the overall arrangement of the reinforced is shown. A total of eight wire ropes were installed in three grooves per direction previously produced on the surface of the wall, parallel to its diagonals, and adequately anchored at their ends by means of screws. A detail of the anchoring system is illustrated in Figure 5.6(b).

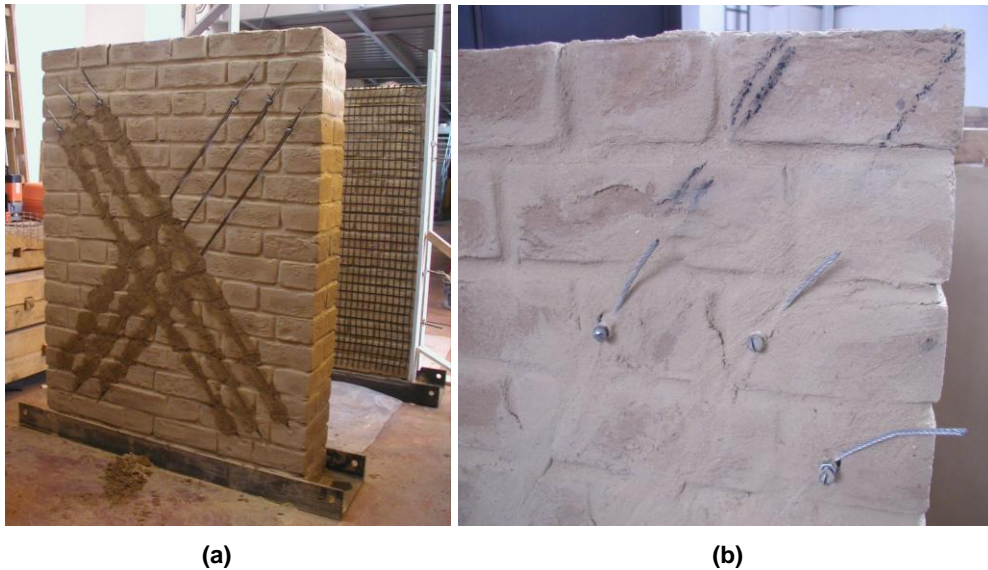


Figure 5.6. Adobe brick wall reinforced by means of X-shaped wire ropes (a) and detail of the anchoring system for wire ropes (b).

5.2 MATERIAL PROPERTIES

The specification of employed materials and physical properties of the geonets and the steel wire ropes, which were used for the strengthening of the walls, are summarized in the following tables. Values from the ongoing tests in other laboratories were considered. In the laboratory of the ITAM only tests for determination of Young's modulus of adobe have been carried out. Regarding the adobe bricks, tests for determination of compressive and tensile strength were carried

out at the University of Sannio, providing the results reported in Table 5.2 and 5.3. The mechanical properties of adobe bricks are summarized in Table 5.4.

Compressive Test								
	a	b	c	Weight	Unit weight	Loading Area	P	σ_c
	[mm]	[mm]	[mm]	[g]	[kN/m ³]	[mm ²]	[N]	[MPa]
SM_C_01	54	51	54	264	17.75	2754	6585	2.39
SM_C_02	55	53	55	271	16.90	2915	7347	2.52
SM_C_03	54	51	53	256	17.54	2754	7352	2.67
SM_C_04	50	52	50	242	18.62	2600	8459	3.25
SM_C_05	50	52	53	248	18.00	2600	6354	2.44
SM_C_06	54	54	52	272	17.94	2916	10940	3.75
SM_C_07	53	51	51	265	19.22	2703	8921	3.30
SM_C_08	49	55	53	257	17.99	2695	7755	2.88
Mean Value					18.00			2.90
St. Dev.					0.65			0.46

Table 5.2. Results of compressive tests on adobe bricks.

Bending Test								
	h	b	l	Weight	Unit weight	l_{app}	P	σ_f
	[mm]	[mm]	[mm]	[g]	[kN/m ³]	[mm]	[N]	[MPa]
SM_B_01	40	60	240	1087	18.87	200	550	1.72
SM_B_02	43	60	240	1151	18.59	200	602	1.63
SM_B_03	40	63	241	1105	18.19	200	552	1.64
Mean Value					18.55			1.66
St. Dev.					0.28			0.04

Table 5.3. Results of bending tests on adobe bricks.

Title	Density	Tension strength	Friction coefficient	Elastic modulus	Compression strength
	ρ [kgm ⁻³]	f_t [MPa]	μ [-]	E [GPa]	f_c [MPa]
Adobe brick (Claytec)	1800	1.66	0.35	3.5	2.9

Table 5.4. Adobe bricks specifications.

An adobe mortar with similar material and physical properties as adobe bricks was used for adobe walls, as it is shown in Table 5.5. In the case of the walls made by dry and solid bricks, a cement mortar was applied, as shown in Table 5.6. The SAK-RET mortar, which belongs to HM group II of mortars, according to DIN 1053. It has a minimum nominal compressive strength of 5 N/mm² and a minimum adhesion and shear strength of 0.2 N/mm². The material characteristics of the mortar were checked on standard specimens made during production of the testing walls.

Title	Density ρ [kgm ⁻³]	Tension strength f_t [MPa]	Friction coefficient μ [-]	Elastic modulus E [GPa]	Compression strength f_c [MPa]
Dry brick	1900	0	0.25	1.0 - 4.0	5.0 - 10.0
Solid brick	1850	2.6	0.3	12.0	27.0
Mortar - Adobe	1900	0.2	-	3.5	1.5
Mortar cement (Weber)	2100	0.5	0.15	27.0	5.0

Table 5.5. Bricks and mortars specifications by the producer.

Title	Tensile strength f_t [kN/m]	Mesh sizes l x b [mm]
Geo nets polypropylene (Tenax)	9.3/17	30x45
Geo nets polyester - Miragrid GX 35/35 (Tencate)	35/35	25x25

Title	Elastic modulus E [GPa]	Diameter ϕ [mm]	Tensile strength f_t [MPa]
Wire ropes	210	4	1770

Table 5.6. Steel wire ropes and geo-nets specifications by the producer.

For the determination of the elastic modulus and static load capacity of adobe bricks, bending tests on four specimens were performed. All the tested blocks had length of 200 mm. The rectangular cross sections of blocks had various widths and heights, varying from 28 mm to 42 mm. The loading speed of the bending tests was chosen as 0.15 mm/min. The tests ended in the total collapses of the blocks. The vertical force F was measured by dynamometer LUCAS 500N and the deflections y of the specimen by LVDT HBM sensor.

The equivalent elastic modulus E was determined from the chosen time interval in which the behaviour of material was almost elastic. The typical length of time interval was from 110 to 300s. The region characterized by non linear behaviour before cracking and the region with cracks were excluded from calculations. For selected time increment Δt (10s) the values of the Young's modulus of elasticity E were computed by means of the relation:

$$E = \frac{\Delta F \cdot l^3}{48 \cdot I \cdot \Delta y}$$

where:

ΔF is the increment of the loading force with time increment Δt ;

Δy is the increment of the deflection with time increment Δt .

An average value of elastic modulus $E = 3.5$ GPa from measurements of all tested specimens was determined.

Material properties of other materials (steel, polyester, polypropylene) were intended by their manufacturer and were determined in their laboratories. The specifications and physical properties of materials are summarized in Table 5.5 and Table 5.6.

5.3 EXPERIMENTAL EQUIPMENT AND TEST SET-UP

The test specimens were mounted into a special testing rig that enabled simultaneous uniform compression and cyclic horizontal loading on the top of the tested specimen. The outline of the experimental equipment is illustrated in Figure 5.7, while in Figure 5.8 the scheme of the specimen placed in the testing system is shown.

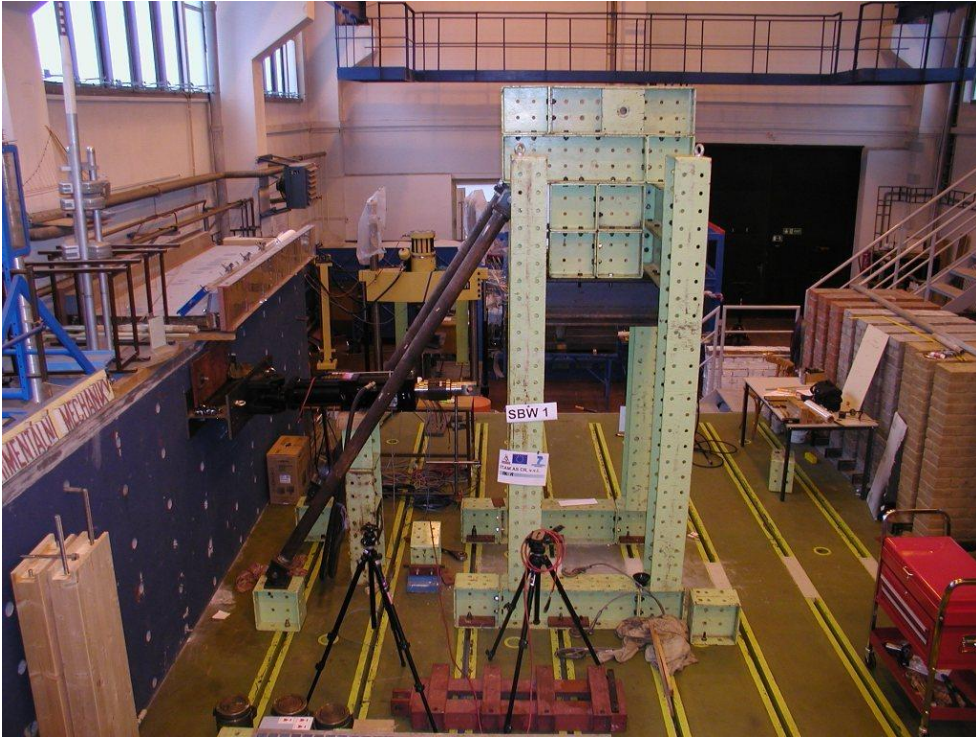


Figure 5.7. Testing rig and reaction wall for testing.

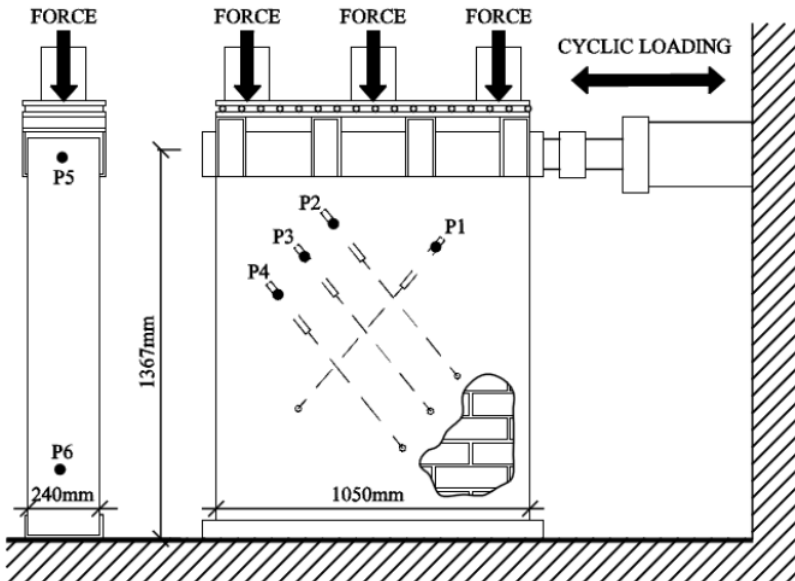


Figure 5.8. Scheme of the testing system.

Three hydraulic jacks were used to generate the vertical load, which was transmitted to the wall by a steel ‘hat’ on the top of the wall. A horizontal displacement (force) on the top of the wall was introduced using a servo-hydraulic MTS actuator of 250 kN capacity, illustrated in Figure 5.9.



Figure 5.9. Servo-hydraulic actuator for horizontal loads.

In the experimental campaign carried out, the following loading conditions have been considered. First, the above-mentioned compressive loading was applied only, and was increased continuously up to a value of 80 kN, evenly distributed across the top cross-section of the wall. Then, the vertical compressive prestress load was combined with the cyclic horizontal loading mode with a stepwise increase in the maximum cycling limits.

During the first loading combination, with static vertical loading only, the deformation characteristics of the masonry wall were obtained. The horizontal displacement on the top of the wall and the deformations orthogonal to the shear diagonals of the panels were measured during combined loading.

The application of the horizontal load follows the sinusoidal pattern illustrated in Figure 5.10. In particular, for each step of loading defined by a maximum value of the amplitude (starting from 2.5 mm and with increments of 2.5 mm) of the displacement imposed by the actuator, three cycles were performed. For each step of loading, the frequency of application of the horizontal force is kept constant and equal to 0.1 Hz.

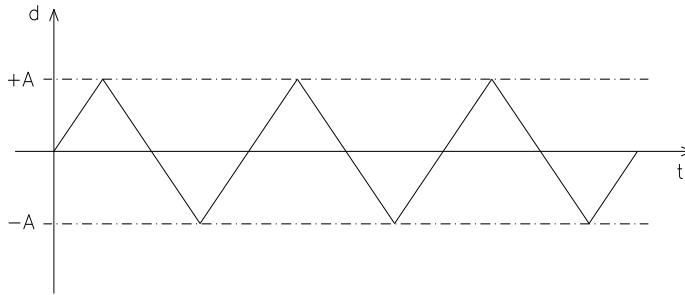


Figure 5.10. Loading pattern for each step of application of the horizontal force.

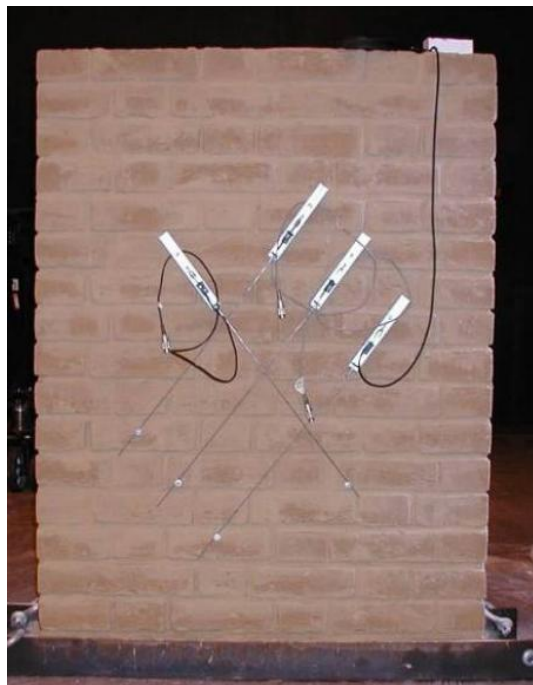


Figure 5.11. Examples of location of sensors.

During the test the forces on the vertical hydraulic jacks as well as on the horizontal actuator were recorded. Furthermore, horizontal displacements at the bottom and top of the wall and diagonal deformations of four lines on both surfaces were measured. Location of sensors is shown in Figure 5.11. The sequence of initiation and development of cracks on both surfaces were recorded in all loading

steps using different colours and by photography. Loading was terminated in a moment when the force started to decrease at the controlled deformation.

5.4 EXPERIMENTAL RESULTS

In Table 5.7 a summary of the results obtained from the tests on all the masonry typologies are reported with reference to strength and displacement capacity measured from the experimental non-linear curves. In particular, in the table the maximum horizontal force, the maximum displacement and the drift of the walls are reported, along with their variation with respect to the unreinforced panels. The most effective technique is represented by the use of geo-net (polyester), also considering the reduced cost. Geo-nets (polyester and polypropylene) have also a better ratio of strength to the strength of brick and. The wall strengthened by means of steel wire ropes behaves in a quite compact manner since the wire ropes play a very effective role in sewing up the cracks.

Material	Specimen	F_{max} [kN]	$\Delta F/F_{UR}$ [-]	d_{max} [mm]	$\Delta d/d_{UR}$ [-]	d_r [%]	$\Delta d_r/d_{r,UR}$ [-]
Adobe brick masonry	ABW-1	66.11	–	13.75	–	1.01	–
	ABW-2	113.11	0.71	23.10	0.68	1.69	0.68
	ABW-3	80.21	0.21	16.85	0.23	1.23	0.23
	ABW-4	53.50	-0.19	12.93	-0.06	0.95	-0.06
	ABW-5	86.04	0.30	25.15	0.83	1.84	0.83
Dry brick masonry	DBW-1	78.60	–	10.65	–	0.78	–
	DBW-2	98.58	0.25	15.90	0.49	1.16	0.49
	DBW-3	75.59	-0.04	17.57	0.65	1.29	0.65
	DBW-4	Failed due to bad anchoring					
Solid brick masonry	SBW-1	212.21	–	10.80	–	0.79	–
	SBW-2	Failed due to actuator limitation					
	SBW-3	Failed due to actuator limitation					

Table 5.7. Summary of results from experimental tests on masonry walls.

5.4.1 Adobe brick walls

The results presented in the following section are related to the tests carried out on walls made by adobe bricks. Three types of tests are considered, namely the ones related to the unreinforced wall used as control specimen, to the specimen reinforced with geo-nets and mortar layers onto the wall surfaces and to the specimen reinforced with X-shaped wire ropes.

Typical failure cracking of a plain masonry wall loaded by combined uniformly distributed vertical static stress and a horizontal cyclic load is shown in Figure 5.12.



Figure 5.12. Crack pattern at failure of the plain masonry control wall under a combination of vertical compression and cyclic shear.

Figure 5.13 presents the crack pattern at failure registered for the wall strengthened with reinforced mortar layers. It is, thus, evidenced the typical behaviour of walls strengthened by means of this technique. It is noticed that the cracks visible on the surface represent a combination of two sets of damages: masonry cracks, and

cracks which occur in the plaster only and originate from the differential movement of the FRP mesh.

It is observed that compared to the typical crack pattern usually found in plane masonry walls, the case of the wall strengthened with reinforced mortar layer present a more widespread and diffused crack pattern. In fact, when unreinforced masonry wall is subjected to a combination of vertical pre-stress and horizontal cyclic load cracks are localized in the two diagonal lines of the walls evidencing the typical X-shaped pattern. The application of the reinforced mortar layers reinforced with a FRP grid to the surfaces of the wall has also the effect to redistribute the stresses originated upon loading along the two diagonal lines of the wall and, thus, to spread the pattern over a wider area of the wall surface.

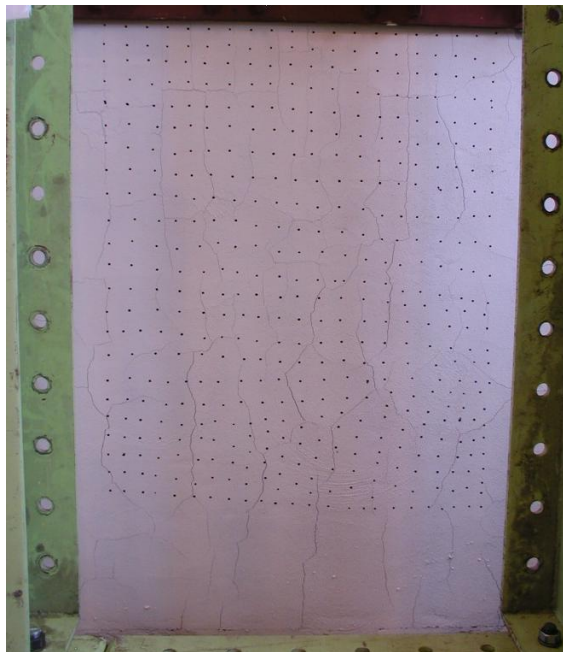


Figure 5.13. Crack pattern at failure of the adobe wall strengthened with reinforced mortar layers under a combination of vertical compression and cyclic shear.

An important aspect to be taken into account in the evaluation of the effectiveness of this kind of reinforcement is the interface behaviour between the external reinforcement and the masonry substrate to which it is applied represented

by the wall. Since the reinforced mortar layer applied on the wall surfaces is slightly thin ($1.5 \div 2.0$ cm), and due to the different stiffness compared to the substrate, it can be subjected to out-of-plane forces that may cause its detachment. The experimental evidence of the detachment of this layer is much more evident when the difference in stiffness is larger. This happens particularly in the cases of application to this kind of reinforcement to clay bricks walls, while in case of adobe walls it is not so evident since the plaster has been made of the same material of the bricks. In Figure 5.14 it is shown a detail of the detachment of the plaster from the surface of the masonry wall; in this case, the polymeric grid is still anchored to the substrate and the detachment involved only the thin layer of plaster.



Figure 5.14. Evidence of the detachment of the plaster from the wall surface.

The adobe brick wall reinforced by means of steel wire ropes has been also tested. In Figure 5.15 the crack pattern upon failure of the specimen is shown. In case this kind of reinforcement is adopted an important improvement in terms of resistance can be attained. The wall strengthened by means of this technique behaves in a quite compact manner since the wire ropes play a very effective role in sewing up the cracks and keeping the masonry blocks together. Some cracks can appear along the

mortar joints in the surroundings of the reinforcement and, in general, there is a good redistribution of the stresses and a more widespread crack pattern compared to the unreinforced wall. The failure of the wall feature the formation of large damage in the wall at the level of the toe over the anchorage of the ropes, in the area where the reinforcement is not present. In Figure 5.16 it is shown the damage at the toe of the wall, with the formation of a plastic hinge at the base.



Figure 5.15. Crack pattern at failure of the adobe wall strengthened with wire ropes under a combination of vertical compression and cyclic shear.



Figure 5.16. Details of the large damage at the wall's base.

Another important aspect brought to light by the experiments is related to the damage due to the possible out-of-plane of the reinforcement. In particular, the wire ropes are placed quite superficially in grooves made on the wall faces and just plastered with mortar. Since during the application of cyclic horizontal loading, or during the shake imposed by a seismic event, both direction of reinforcement can be subjected alternatively to compression, causing the tendency to the ropes to go out of the grooves, hitting the small filling of mortar. However, since the reinforcement is made by steel wire, during tension phase they can easily be able to continue to be effective, involving only superficial damage of the wall, as shown in Figure 5.17.



Figure 5.17. Detail of the damage due to the out-of-plane of the wire ropes reinforcement.

In the following the results of the three tests presented in this section are reported in terms of cyclic curves horizontal force versus displacement of the wall top. In particular in the graphs of Figure 5.18, 5.19 and 5.20, the cyclic curves for each step of loading are presented for the unreinforced wall, for the wall reinforced with grid and for the wall reinforced with wire ropes, respectively. The tests have been carried out considering fixed the frequency of the sinusoidal load and equal to 0.1 Hz, and incrementing the maximum displacement imposed in the actuator, starting from 2.5 mm and with increment of 2.5 mm.

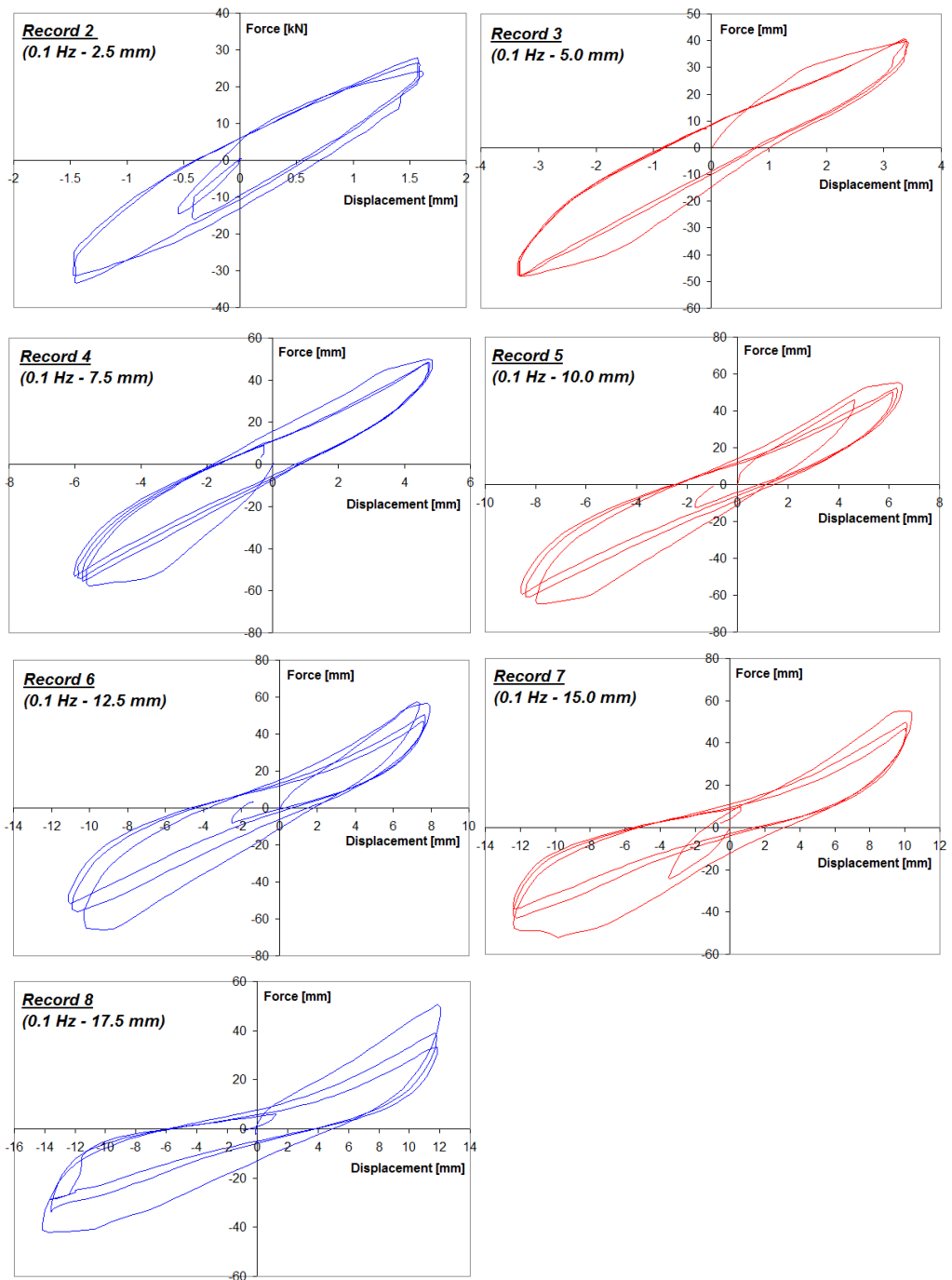


Figure 5.18. Cyclic curves for different steps of loading – Unreinforced adobe wall.

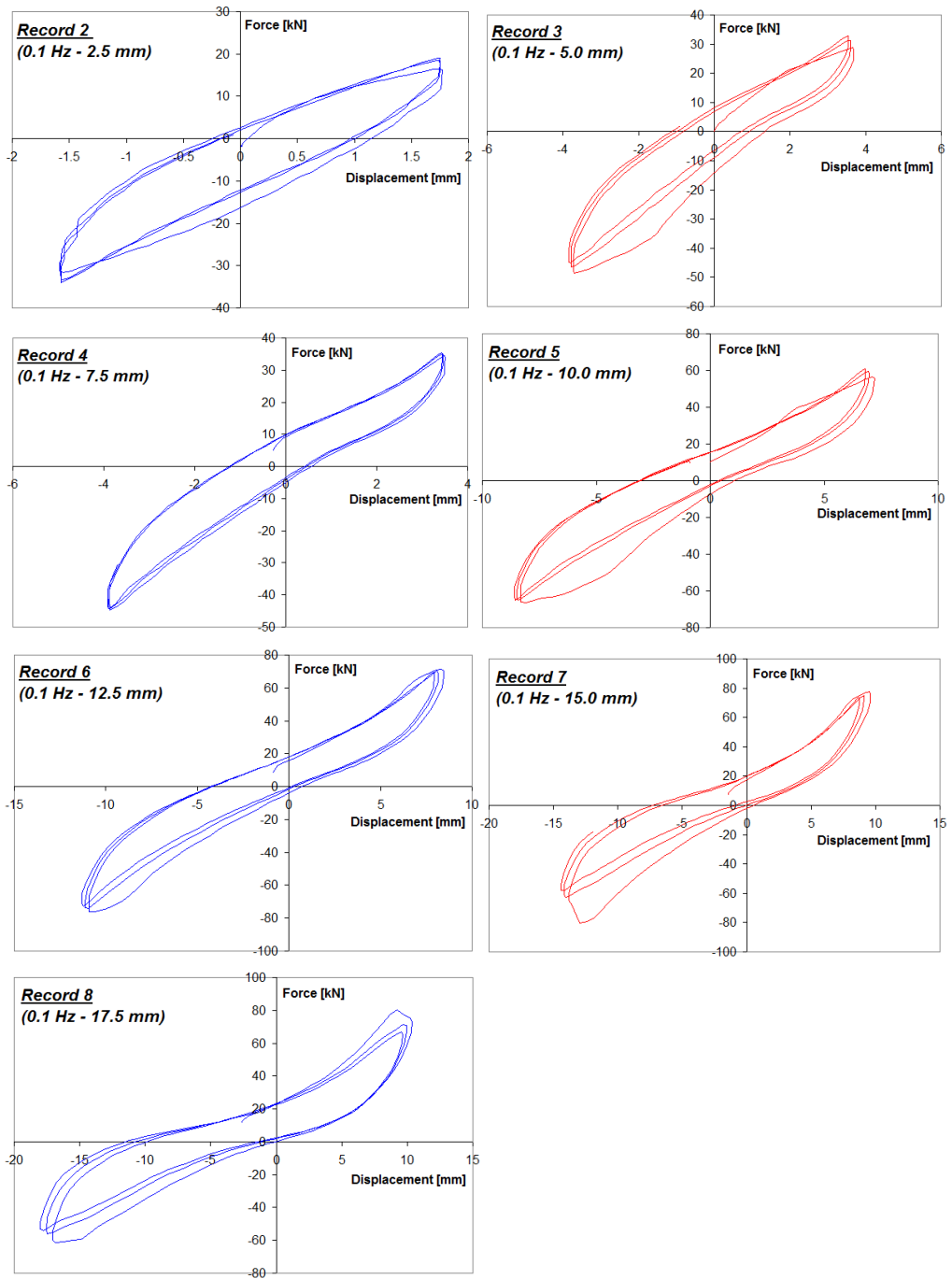


Figure 5.19. Cyclic curves for different steps of loading – Wall strengthened with reinforced mortar plaster.

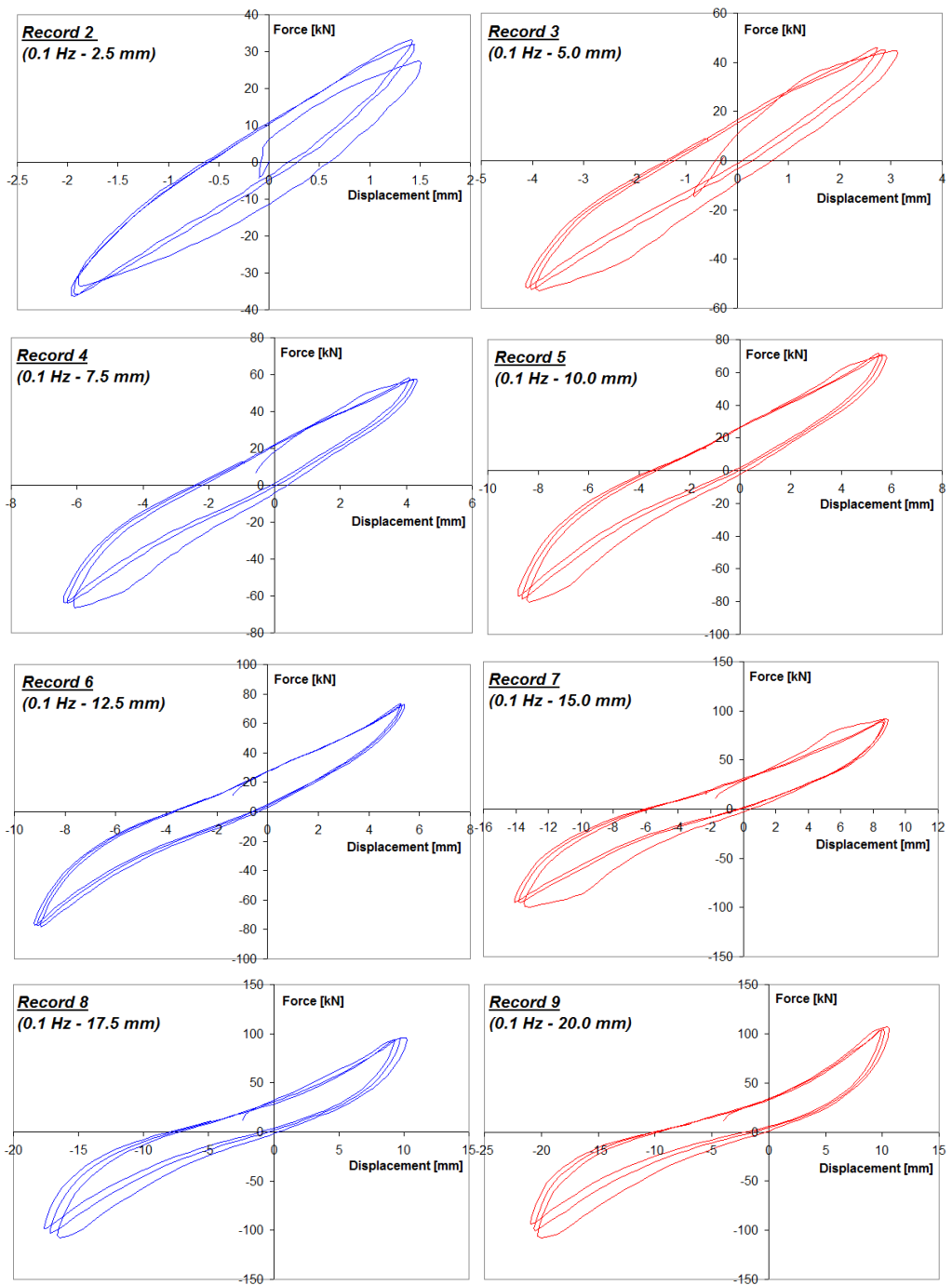


Figure 5.20. Cyclic curves for different steps of loading – Wall strengthened with wire ropes.

In the following graphs the overall cyclic curves for the three different walls are presented. In particular Figure 5.21 is referred to the unreinforced masonry wall, Figure 5.22 to the wall reinforced with FRP grid, Figure 5.23 to the wall reinforced with wire ropes.

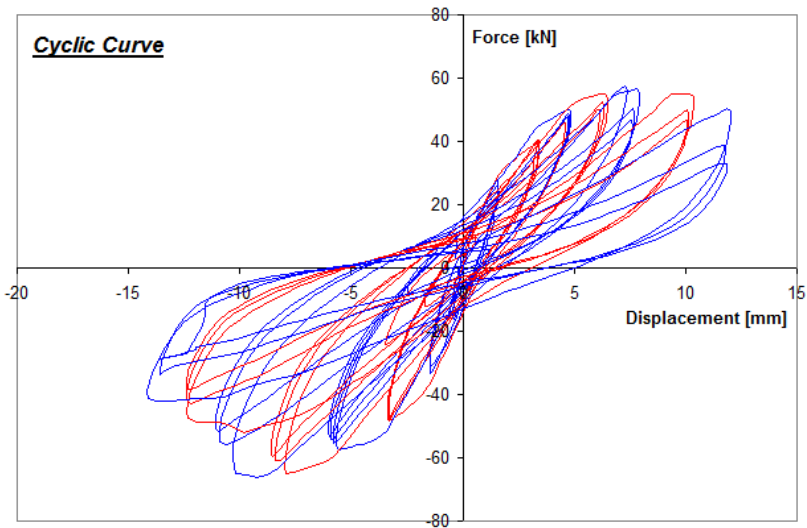


Figure 5.21. Cyclic curve for unreinforced adobe wall.

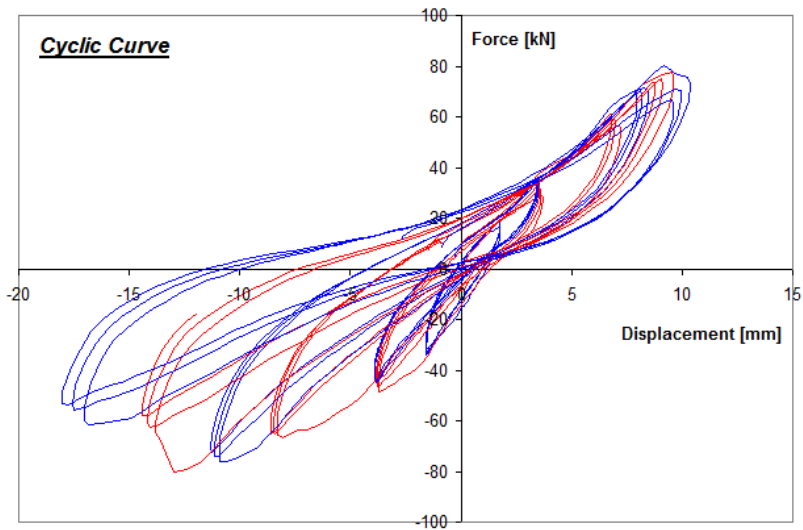


Figure 5.22. Cyclic curve for wall strengthened with reinforced mortar plaster.

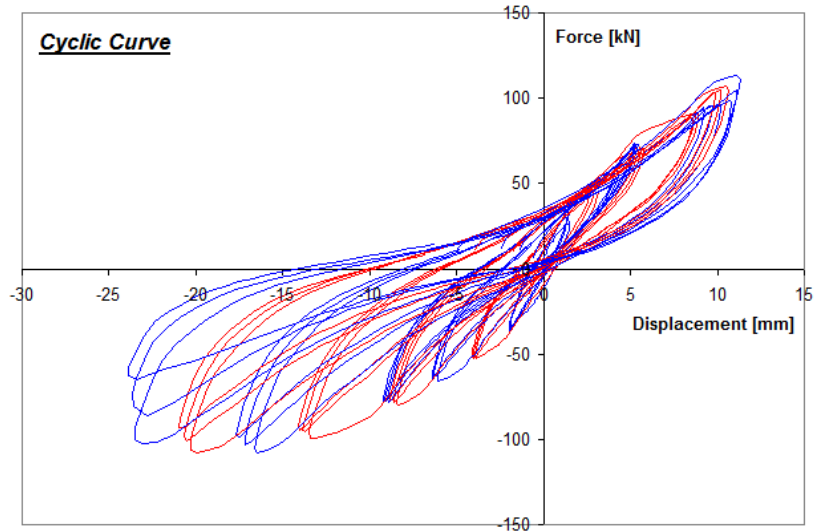


Figure 5.23. Cyclic curve for wall strengthened with wire ropes.

Finally, for each of the tested walls the envelope curves obtained from the cyclic curves are plotted. In particular both the extension side and the compression side of the cyclic curves are obtained, considering the maximum horizontal force and the correspondent displacement at each step of loading, and presented in Figure 5.24, 5.25 and 5.26 for the three cases.

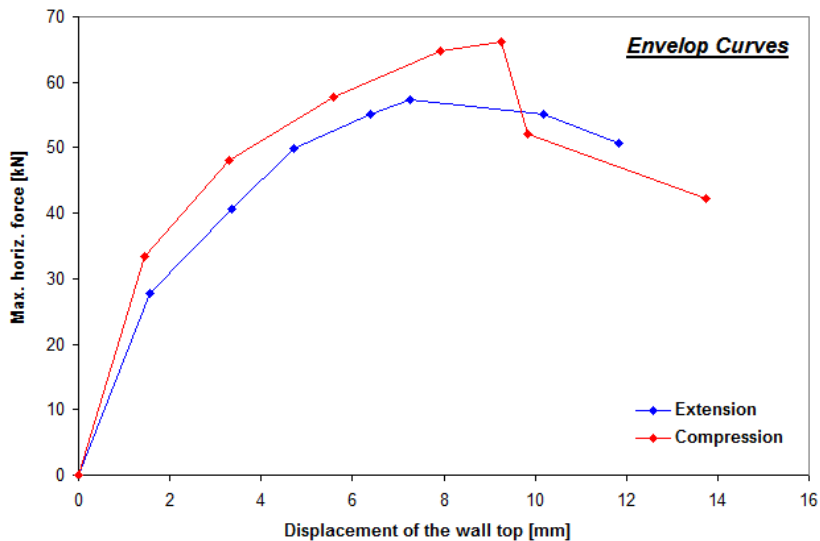


Figure 5.24. Envelope curves for unreinforced adobe wall.

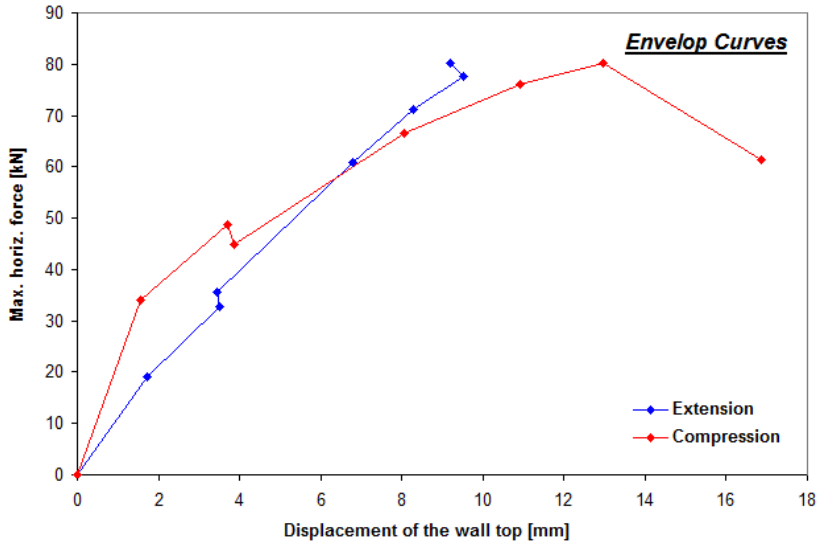


Figure 5.25. Envelope curves for wall strengthened with reinforced mortar plaster.

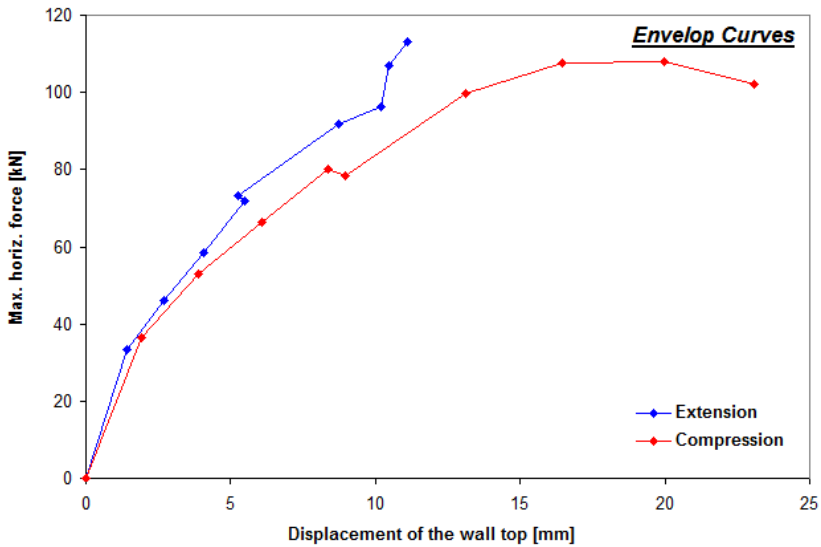


Figure 5.26. Envelope curves for wall strengthened with wire ropes.

In the following figures, some comparisons between the behaviour of the reinforced specimens with respect to the unreinforced control panel are reported. In Figure 5.27 the force-displacement curves for the unreinforced wall and for the wall

reinforced with geo-net are plotted in the same graph. It is observed that the application of the reinforced mortar layers onto the wall's surfaces allows the specimen to reach a higher value of strength, with an increment of about 20%. Moreover, an increment in terms of ductility is also registered.

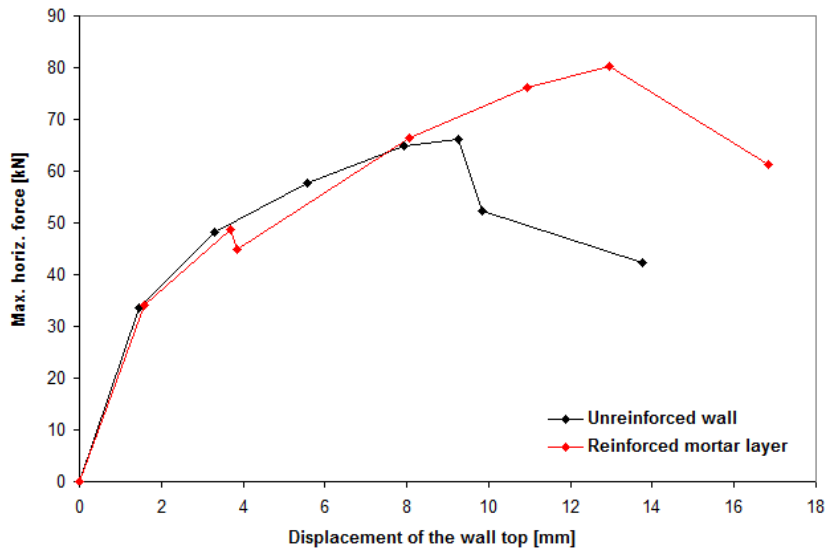


Figure 5.27. Behaviour of the wall strengthened with reinforced mortar plaster compared to the unreinforced wall.

When considering the comparison between the behaviour of the wall reinforced with wire ropes and the unreinforced wall, reported in Figure 5.28, it is observed that the strengthening system is more effective leading to an increment of strength of about 60%. The effectiveness of the system is evident also in terms of increment of the displacement capacity of the wall.

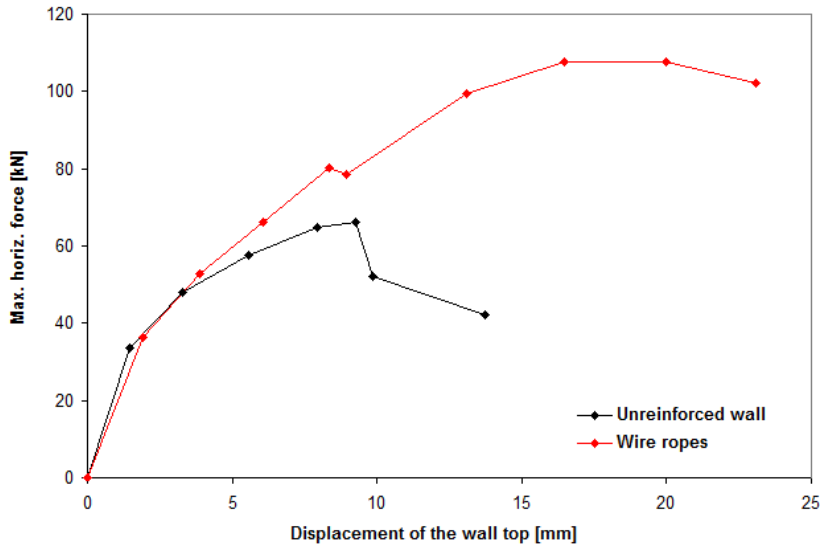


Figure 5.28. Behaviour of the wall strengthened with wire ropes compared to the unreinforced wall.

5.4.2 Damaged adobe brick wall retrofitted with reinforced mortar plaster

The experimental campaign carried out features also a test on a retrofitted wall. It is the case of an adobe brick wall severely damaged under cyclic loading conditions in a test carried out in a previous study at the ITAM. The damaged specimen has been repaired employing the same strengthening technique of the other walls, using geo-nets and plastering the surface with about 2 cm thick layer of mortar. In particular, the retrofitting intervention has been materialized after removing the remains of composite strips previously applied and properly cleaning the surface of the wall for the correct application of new materials.

The retrofitted wall has been, thus, tested again under combination of vertical prestressing load and cyclic horizontal load. In Figure 5.29 the crack pattern at failure registered on the wall surface; it can be observed a diffusion of cracking in the central area of the panel, with detachment of mortar plaster, and a concentration of damage at the base corners of the specimen.

Also in this case, as already observed in the case of the undamaged wall strengthened with reinforced mortar layers, the wall experienced the detachment of the mortar in the central area of the specimen and, for higher values of the top displacement, the out-of-plane of the plaster in the lower part of the wall close to the corners (Figure 5.30(a)). Moreover, due to a very high stress concentration in that area, a significant crack appeared and spread in the wall thickness, as reported in Figure 5.30(b).

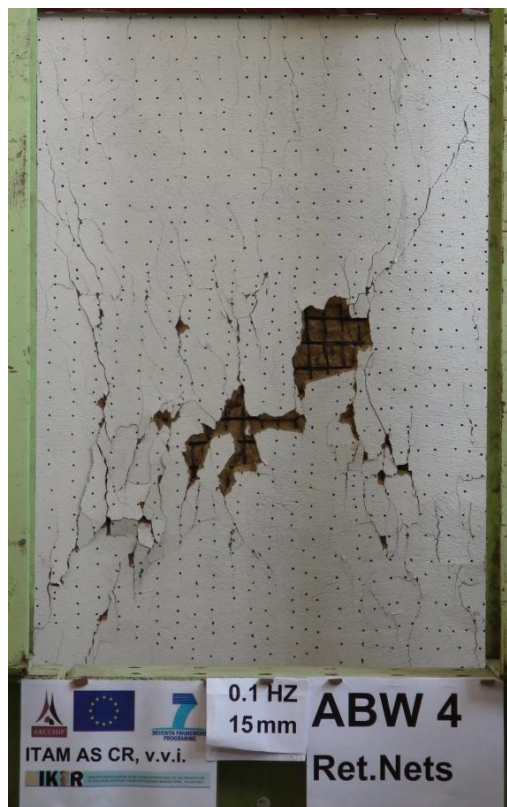


Figure 5.29. Crack pattern at failure of the retrofitted adobe wall under a combination of vertical compression and cyclic shear.

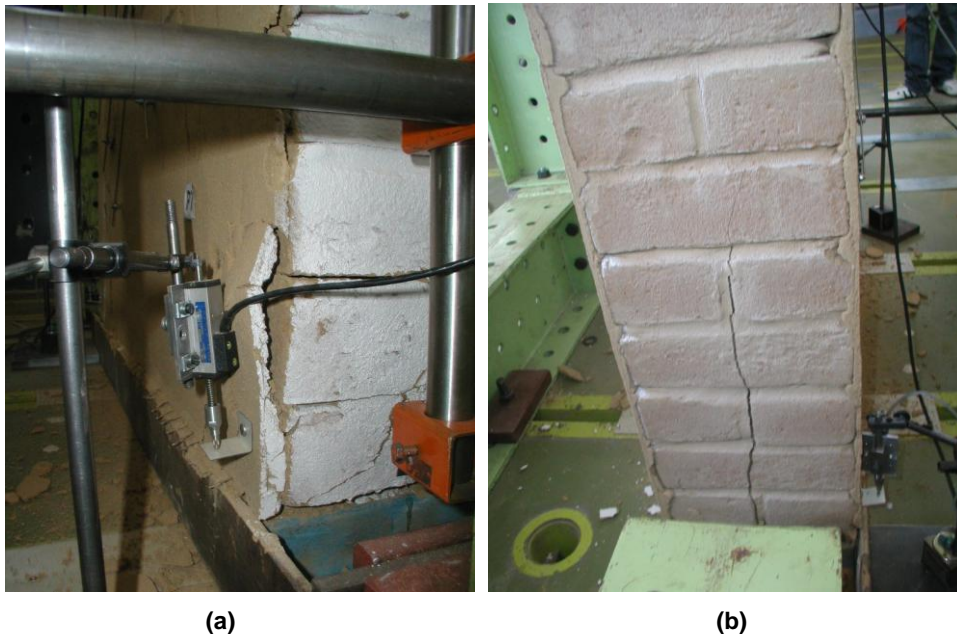


Figure 5.30. Damage at the base of the wall: detachment of the mortar layer (a) and large vertical crack in the wall thickness.

In the following the results of the tests presented in this section are reported in terms of cyclic curves horizontal force versus displacement of the wall top. In particular, in the graphs of Figure 5.31 the cyclic curves for each step of loading are presented, while in Figure 5.32 the global cyclic curve is shown.

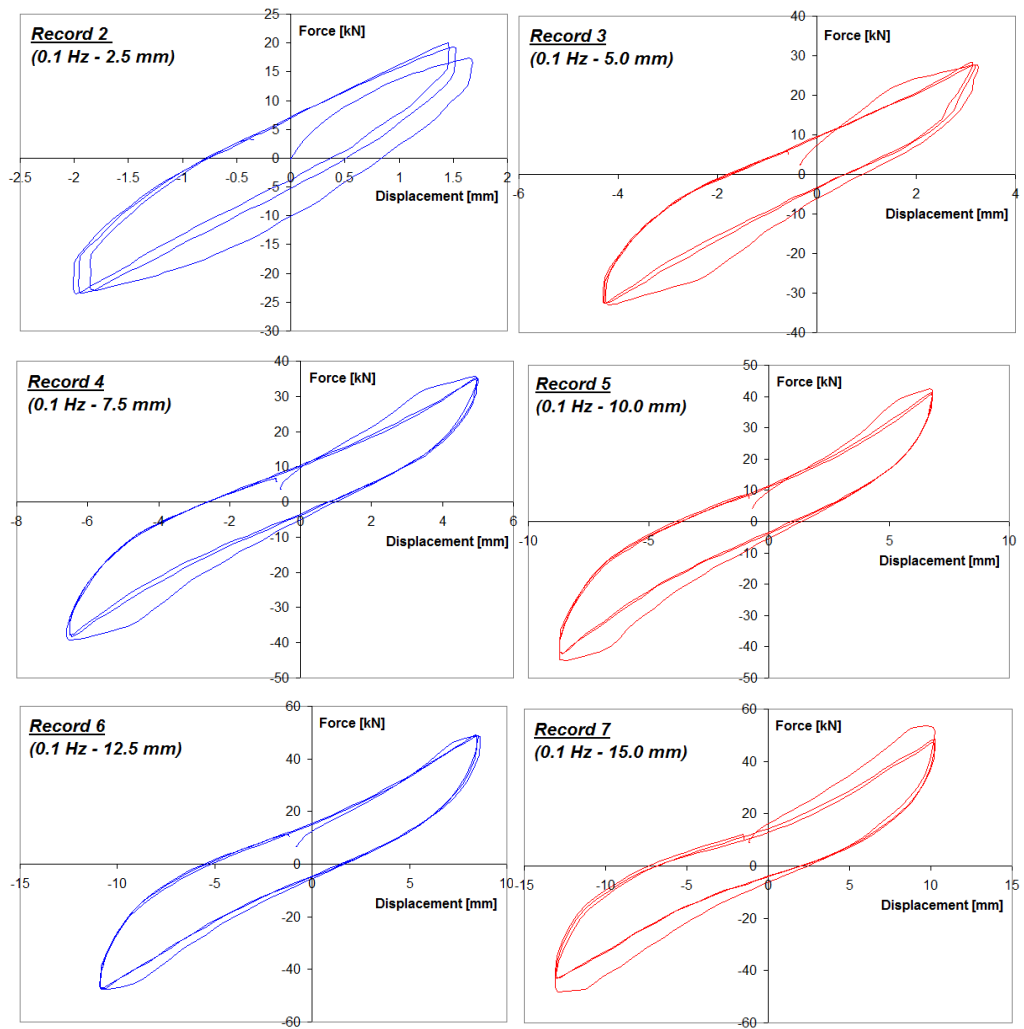


Figure 5.31. Cyclic curves for different steps of loading – Retrofitted adobe wall.

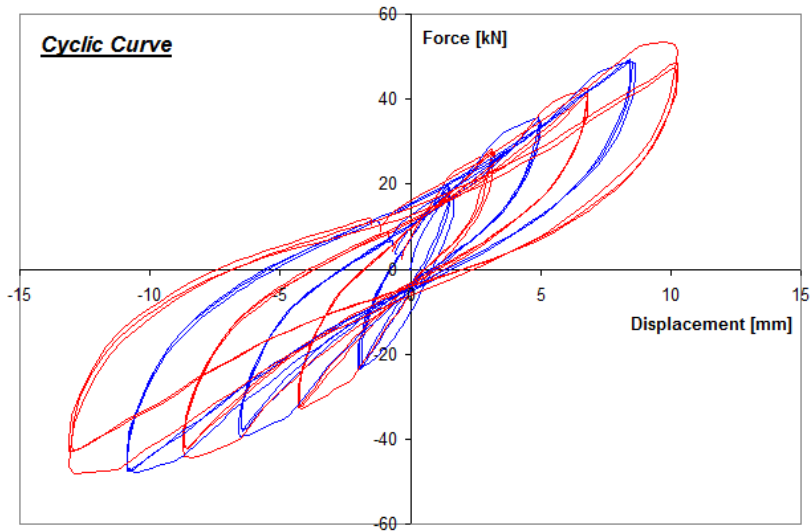


Figure 5.32. Cyclic curve for retrofitted adobe wall.

In Figure 5.33, the envelope curves obtained from the cyclic curves are plotted for both the extension side and the compression side of the cyclic curve.

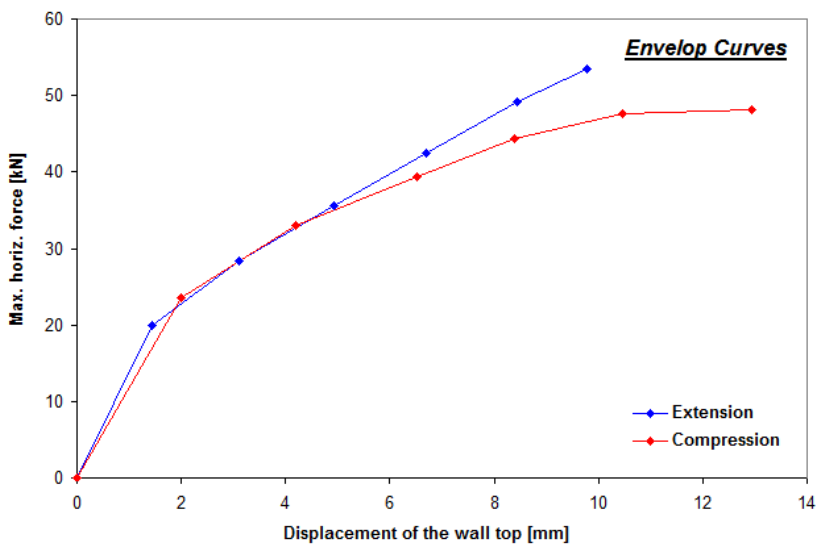


Figure 5.33. Envelope curves for retrofitted adobe wall.

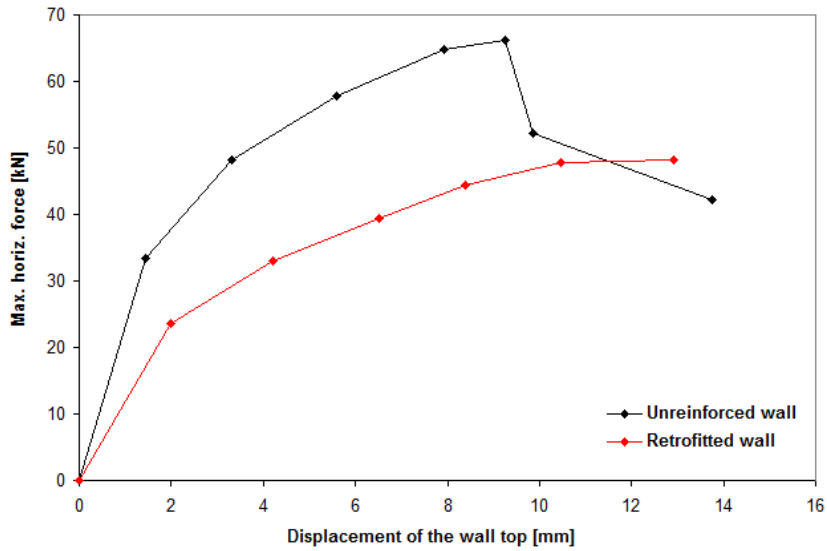


Figure 5.34. Behaviour of the retrofitted adobe wall to the unreinforced wall.

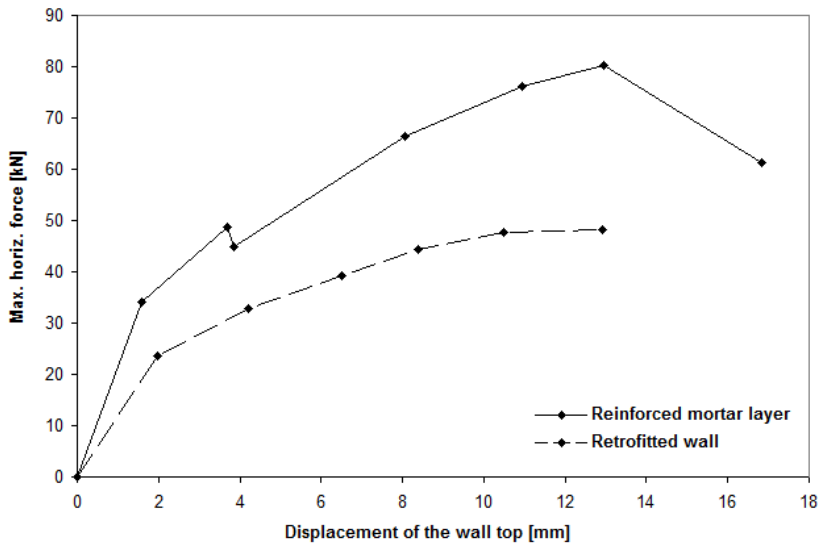


Figure 5.35. Comparison between undamaged wall strengthened with reinforced mortar layers and retrofitted wall.

Comparing the force-displacement curve of the retrofitted wall with the unreinforced adobe brick wall (Figure 5.34) it can be observed that the strengthening with mortar reinforced with geo-net allow the specimen to reach a strength of about

70% of the original situation. However, the stiffness of the retrofitted wall is lower than the stiffness of the control wall, even after the intervention. Finally, in Figure 5.35, it is reported a comparison between the behaviour of two adobe brick walls reinforced with the same technique, represented by the application of geo-nets and plastering, in case of application on undamaged or damaged wall.

5.4.3 Dry clay brick walls

The same loading model as in the cases of adobe walls has been applied also in the case of dry clay brick walls. Four types of tests were considered, namely the ones related to the unstrengthened wall used as control specimen, to the specimen strengthened with geo-nets (polyester and polypropylene) and mortar layers onto the wall surfaces and to the specimen strengthened with X shaped wire ropes. Geo-nets (polyester and polypropylene) and steel wire ropes were fastened to the specimen by the same method used in case of adobe walls. Strengthening systems used in these cases are characterized by the same benefits and shortcomings as for the adobe brick walls.

In Figure 5.36 the specimens after the test are shown. In the first case (a) of unstrengthened specimen cracks are localized in two diagonal lines of the walls evidencing the typical X shaped pattern. From second case (b) is evident that the cracks visible on the surface represent a combination of two sets of damages as well as in the case of adobe: masonry cracks and cracks which occur in the plaster only and originate from the differential movement of the geo-nets mesh. On the surface are shown only vertical cracks of the specimen that formed in the plaster.

Geo-nets have also a better strength ratio compared to the strength of brick and, therefore, it is favourable to apply them. Unlike in the case of steel wire ropes, there is not such a danger of pulling out the strengthening in the out-of-plane. The wall strengthened by means of steel wire ropes behaves in a quite compact manner since the wire ropes play a very effective role in sewing up the cracks and keeping the masonry blocks together. Some cracks can appear along the mortar joints in the

surroundings of the strengthening and, in general, there is a good redistribution of the stresses and a more widespread crack pattern compared to the unstrengthened wall.

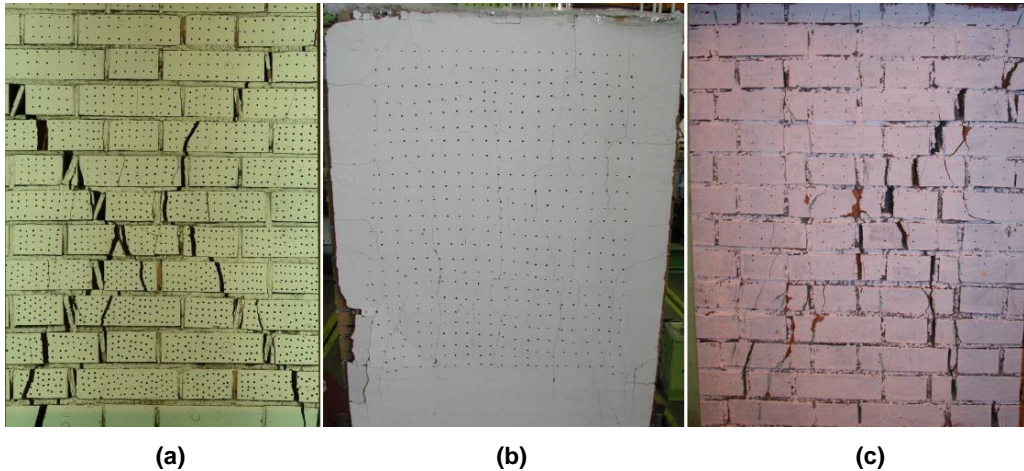


Figure 5.36. Crack pattern at failure of the plain masonry control wall under a combination of vertical compression and cyclic shear: DBW-1 (a); DBW-3 (b); SBW-1 (c).

5.4.4 Solid clay brick walls

The same loading model as in the cases of previous walls has been applied also on case of the solid clay brick walls. Three types of tests were considered, namely the ones related to the unstrengthened wall used as control specimen, to the specimen strengthened with geo-nets (only polyester in this type of wall) and mortar layers onto the wall surfaces and to the specimen strengthened with totally eight X shaped wire ropes. Geo-nets and steel wire ropes were fastened to the specimen by the same method as by the adobe and dry brick masonry. Final shear failure of the wall with visible pattern of the cracks is presented in Figure 5.36(c).

The wall strengthened by means of steel wire ropes behaves in a quite compact manner since the wire ropes play a very effective role in keeping the masonry blocks together. No important damage was found out for commonly used vertical compression (80 kN) and the tests for a potential exceeding of the maximum available force of the actuator were terminated. Only a detachment of two lowest rows

of the bricks and thus a horizontal crack in a bed joint were visible. The detachment and crack corresponded to the horizontal level of the fastening of lower ends of ropes. Due to this phenomenon could not be further addressed the ductile behaviour of wall because it was not reached of plastic deformation. On the other hand the geo-nets provide compactness of the material of the wall even after the partial damage.

5.5 EVALUATION METHODS

5.5.1 Method for the evaluation of the bilinear curve

In order to make the calculation simple, the actual hysteresis behaviour of a masonry wall, subjected to a combination of a constant vertical load and a sequence of lateral load reversals can be represented by the bilinear envelope as indicated in (Magenes and Morandi, 2008) [50], see Figure 5.37.

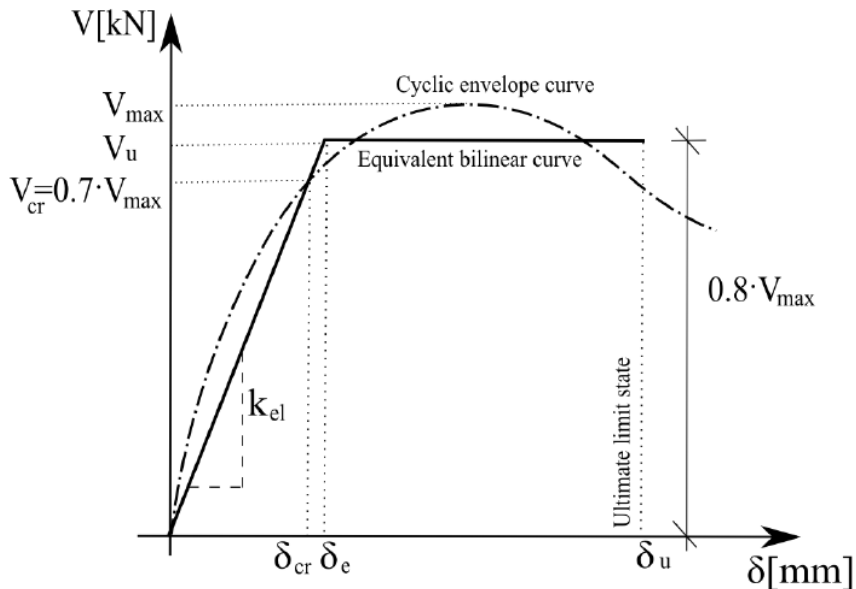


Figure 5.37. Hysteresis envelope and its bilinear idealization.

The first step in the evaluation of the bilinear curve is the construction of a cyclic envelope of the hysteresis loops. In particular, the loading cycles were considered in order to evaluate the maximum lateral force and its degradation.

The second step is the evaluation of the elastic stiffness. The elastic stiffness k_{el} is obtained by drawing the secant to the experimental envelope at $0.7 \cdot V_{max}$, where V_{max} is the maximum shear of the envelope curve:

$$\begin{cases} k_{el} = \frac{V_{cr}}{\delta_{cr}} \\ V_{cr} = 0.7 \cdot V_{max} \end{cases}$$

The third step consists of the estimation of the ultimate displacement (δ_u). The ultimate displacement on the envelope curve is evaluated as the displacement corresponding to a strength degradation equal to 20% of V_{max} . The value of the shear V_u corresponding to the horizontal branch of the bilinear curve has been found by ensuring that the areas below the cyclic envelope curve (evaluated numerically as a sum of discrete areas A_i) and below the equivalent bilinear curve are equal.

$$\begin{cases} A_{envelope} = \sum A_i \\ A_{bilinear} = V_u \cdot \delta_u - \frac{V_u^2}{2 \cdot k_{el}} \end{cases}$$

$$V_u = k_{el} \left[\delta_u - \sqrt{\delta_u^2 - \frac{2 \cdot A_{envelope}}{k_{el}}} \right]$$

Knowing the elastic stiffness k_{el} and the value of V_u , it is possible to evaluate the elastic displacement δ_e . Thus:

$$\delta_e = \frac{V_u}{k_{el}}$$

The ultimate ductility μ_u is defined as:

$$\mu_u = \frac{\delta_u}{\delta_e}$$

At this point, it is important to remind that the horizontal load was applied in the form of programmed displacements, cyclically imposed in both directions, with stepwise increased amplitudes up to the collapse of the specimens. At each displacement amplitude, the loading was repeated three times. During the tests, forces acting on the walls and displacements were measured and, for each wall, the hysteresis loops had been recorded.

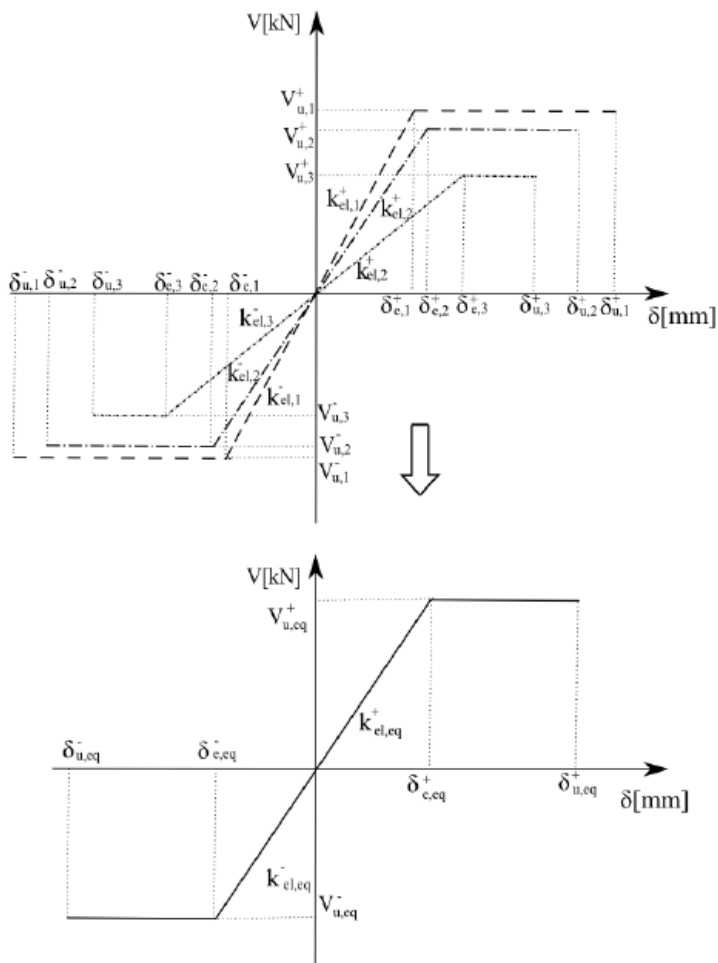


Figure 5.38. Evaluation of the bilinear curve from the six bilinear curves of the tested walls.

Therefore, for each specimen, three loading/unloading cycles were carried out and three positive and three negative envelope curves are obtained. The envelope of the first, the second and the third cycle is the curve that envelopes all the first, the second or the third cycles respectively corresponding to each increasing target displacement.

In order to get only one equivalent bilinear curve for each tested wall, the following procedure has been carried out. The procedure is graphically illustrated in Figure 5.38.

The ultimate displacement is assumed as the lowest of the ultimate displacements in each of the 3rd positive ($\delta_{u,i}^+$) and 3rd negative ($\delta_{u,i}^-$) cycles computed as described similarly to the procedure in (Frumento et al., 2009) [51]:

$$\delta_{u,eq} = \min (|\delta_{u,1}^+|; |\delta_{u,2}^+|; |\delta_{u,3}^+|; |\delta_{u,1}^-|; |\delta_{u,2}^-|; |\delta_{u,3}^-|)$$

The elastic displacement δ_e is instead assumed as the mean value of the elastic displacement for each of the 3rd positive ($\delta_{e,i}^+$) and 3rd negative ($\delta_{e,i}^-$) cycles computed:

$$\delta_{e,eq} = \min (|\delta_{e,1}^+|; |\delta_{e,2}^+|; |\delta_{e,3}^+|; |\delta_{e,1}^-|; |\delta_{e,2}^-|; |\delta_{e,3}^-|)$$

The ultimate ductility is equal to the ratio between the ultimate displacement and the elastic displacement:

$$\mu_u = \frac{\delta_{u,eq}}{\delta_{e,eq}}$$

The equivalent value of V_u has been assumed as the mean value of the V_u for each of the 3rd positive ($V_{u,i}^+$) and 3rd negative ($V_{u,i}^-$) cycles computed:

$$V_{u,eq} = \min (|V_{u,1}^+|; |V_{u,2}^+|; |V_{u,3}^+|; |V_{u,1}^-|; |V_{u,2}^-|; |V_{u,3}^-|)$$

The value of the equivalent elastic stiffness is therefore computed with the following expression:

$$k_{el,eq} = \frac{V_{u,eq}}{\delta_{e,eq}}$$

Another useful parameter is the ratio between V_u and V_{max} . In this case an equivalent value of this ratio $(V_u/V_{max})_{eq}$ has been estimated through the following expression:

$$\left(\frac{V_u}{V_{max}} \right)_{eq} = mean \left(\frac{|V_{u,i}^+|}{|V_{max,i}^+|}; \frac{|V_{u,i}^-|}{|V_{max,i}^-|} \right)$$

5.5.2 Method for the evaluation of the energy dissipation

One of the most important factors which influences the seismic resistance of the structure is its property of energy dissipation, which is the result of irreversible processes taking place in inhomogeneous systems.

The effective dissipation of energy of a structural element could significantly reduce the level of the vibration of the whole structure and decrease the internal forces. The dissipative properties of the investigated brick walls could be described by an area of hysteresis loop. In the present case the hysteresis loop represents a dependence of a horizontal force (force of the actuator) on a displacement of the wall for one cycle of the loading. Energy dissipation was calculated from the area of a hysteresis loop. The area was determined from one cycle in a given step. As default hysteresis curve, the curve of the potentiometer no. 5 was used, see Figure 5.8.

5.6 ANALYSIS AND COMPARISON OF RESULTS

5.6.1 Deformation capacity

In the following paragraphs, the results and the interpretation of the experimental tests on masonry brick walls in terms of deformation capacity are presented. In particular, attention is paid to the ultimate and the elastic displacement (δ_u and δ_e) obtained from an equivalent bilinearization of the experimental shear - displacement envelopes, and to the resulting ductility ratio μ_u (equal to ratio between ultimate displacement δ_u and elastic displacement δ_e) (Magenes and Morandi, 2008) [50]. Clearly, the results in terms of deformation capacity are influenced by several factors such as the geometry of the specimen, the level of compression and the boundary conditions. Still, it is difficult from the results analyzed herein to find a clear trend regarding the influence of the vertical stress on deformation capacity.

5.6.1.1 Adobe brick walls

In Figure 5.39 and Figure 5.40 the values of the elastic drift (δ_e/h) and the ultimate drift (δ_u/h) of all walls are shown. The elastic drift depends on the strengthening technique. The highest values correspond to the specimens ABW – 2, for which it is equal to 0.78%, and ABW – 5, for which it is equal to 0.65%. The values of ultimate drift are extremely dispersed. The minimum value of ultimate drift is related to the specimen ABW - 1 and it is equal to 0,76%. The mean value of the ultimate drift of all the tests is equal to 1.24%. The values of ultimate ductility of the specimens are very low but quite homogenous and are not extremely dispersed. These walls are characterized by similar mechanical and geometrical properties with respect to the other walls of the same typology. The highest value of the ultimate ductility of all tests corresponds to the specimen ABW – 1, for which it is equal to 2.32, while the minimum value has the specimen ABW – 3, for which it is equal to 1.08, see Figure 5.41.

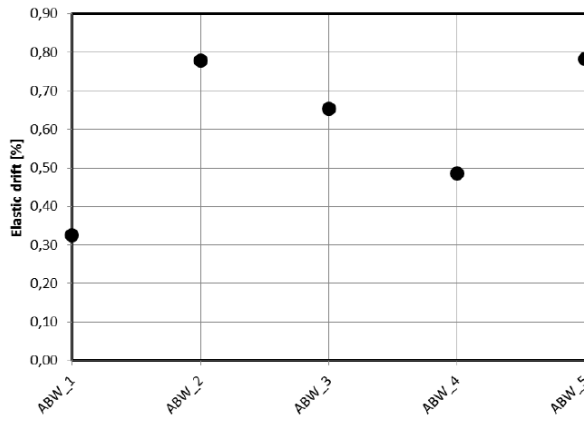


Figure 5.39. Elastic drift of adobe bricks walls.

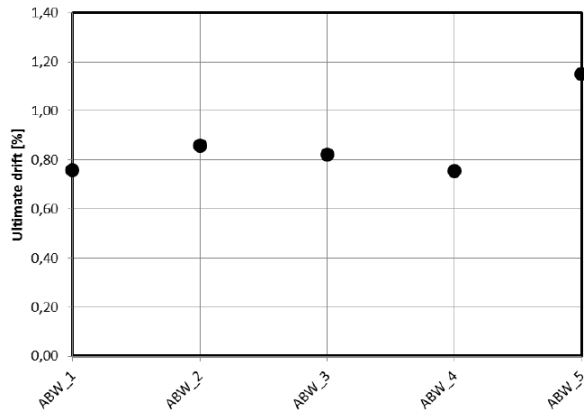


Figure 5.40. Ultimate drift of adobe bricks walls.

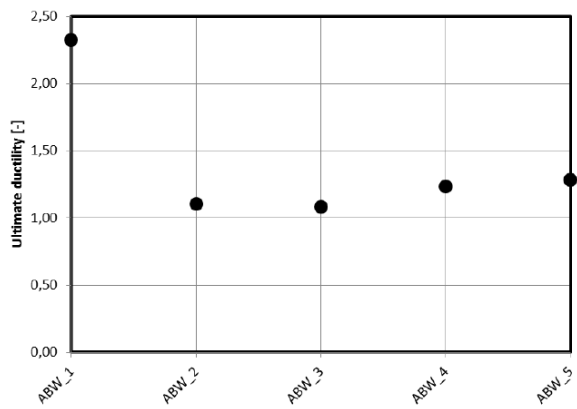


Figure 5.41. Ultimate ductility of adobe bricks walls.

5.6.1.2 Dry clay brick walls

In Figure 5.42 and Figure 5.43, the values of the elastic drift ($\bar{\delta}_e/h$) and the ultimate drift ($\bar{\delta}_u/h$) of all walls obtained from an equivalent bilinearization of the experimental shear – displacement envelopes are shown. In Figure 5.44 the resulting ductility ratio μ_u is shown (Magenes and Morandi, 2008) [50]. The highest value of elastic drift corresponds to the specimens DBW – 1, for which it is equal to 0.53% and DBW – 4, for which it is equal to 0.49%. The minimum value of elastic drift is related to the specimen DBW - 2 and it is equal to 0.36%. The values of ultimate drift are extremely dispersed. The minimum value of ultimate drift is related to the specimen DBW - 2 and it is equal to 0.65%, the maximum value of ultimate drift is related to the specimen DBW – 3, and it is equal 1.03%. The mean value of the ultimate drift of all the tests is equal to 1.0%. The highest value of the ultimate ductility of all tests has the specimen DBW - 3 it is equal to 2.26, while and the minimum value corresponds to the specimen DBW – 2, and it is equal to 1.8.

5.6.1.3 Solid clay brick walls

During the test the detachment of two lowest rows of the bricks and thus a horizontal crack in a bed joint was visible. Due to this phenomenon could not be further addressed the ductile behaviour of wall because it was not reached high plastic deformation.

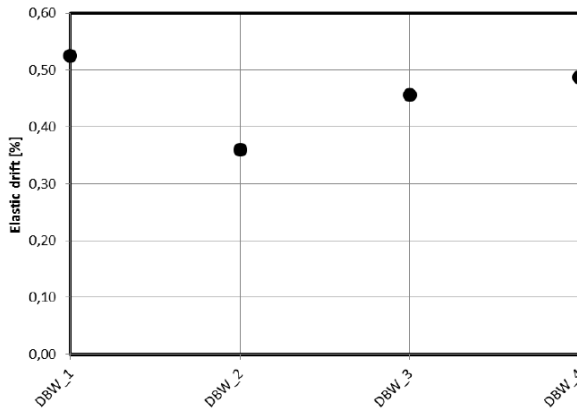


Figure 5.42. Elastic drift of dry clay bricks walls.

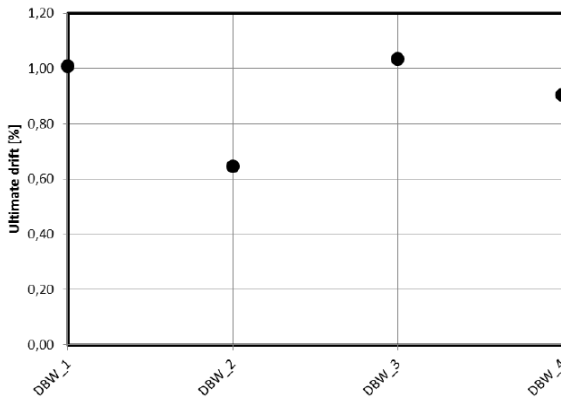


Figure 5.43. Ultimate drift of dry clay bricks walls.

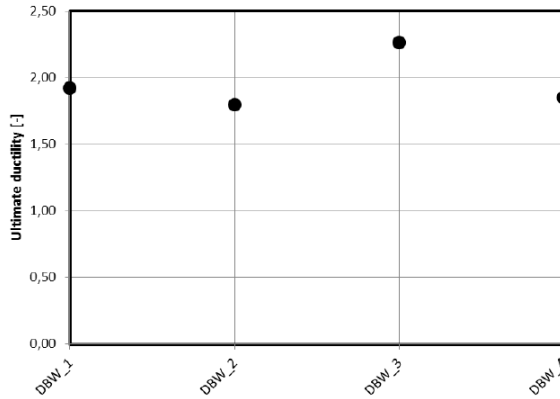


Figure 5.44. Ultimate ductility of dry clay bricks walls.

5.6.2 Energy dissipation

A further comparison is made in terms of energy dissipation. Energy dissipation was calculated from the area of a hysteresis loop. The area was determined from one cycle in a given step.

5.6.2.1 Adobe brick walls

The tests carried out provide several important results concerning adobe brick walls. It has been shown that steel wire ropes on an adobe wall surface increase significantly the energy dissipation of the wall. The effectiveness of the system is evident also in terms of increment of the displacement capacity of the wall. This type of strengthening is very cheap and the most efficient from the point of view of the strengthening among the all used method.

It was observed that the application of the strengthened mortar layers onto the walls surfaces allows the specimen to reach a higher value of energy dissipation. Geo-nets (polyester and polypropylene) have also a better ratio of strength to the strength of brick and, therefore, it is favourable their application. Unlike in the case of steel wire ropes, there is not such a danger of pulling out the strengthening in the out-of-plane. Comparing the energy dissipation of the retrofitted wall by means of geo-nets (polyester) with the unstrengthened adobe brick wall it can be observed that the stiffness of the retrofitted wall is lower than the stiffness of the control wall, even after the intervention.

Comparing the energy dissipation of the retrofitted wall by means of geo-nets (polyester) with the unstrengthened adobe brick wall it can be observed that the stiffness of the retrofitted wall is lower than the stiffness of the control wall, even after the intervention. However, energy dissipation is higher when geo-nets (polypropylene) are used, see Figure 5.45.

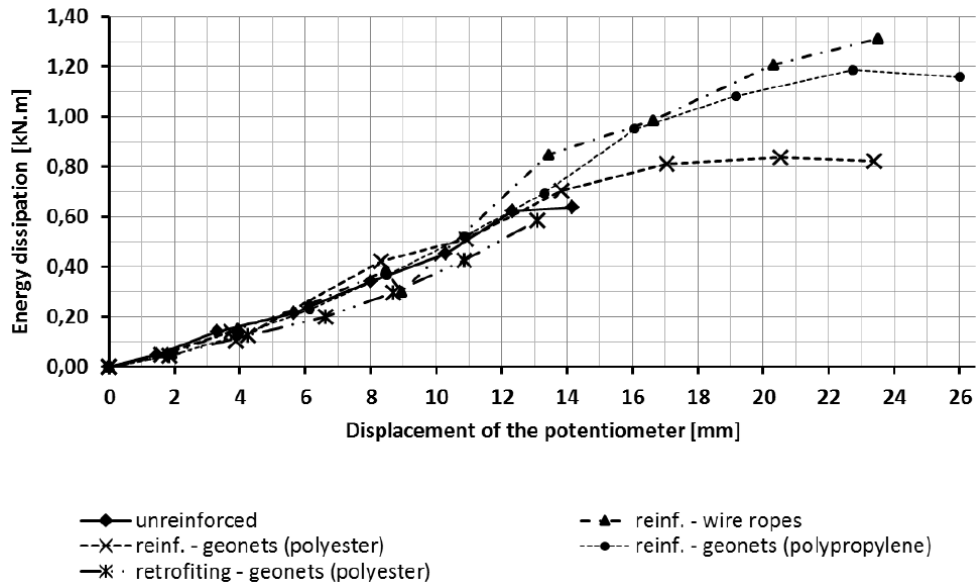


Figure 5.45. Comparison of the energy dissipation between adobe bricks walls.

5.6.2.2 Dry clay brick walls

Tests have shown that the application of the mortar layers strengthened with geo-net (polypropylene) onto the walls surfaces allows the specimen to reach a higher value of energy dissipation. The effectiveness of the strengthening system is evident also in terms of increment of the displacement capacity of the dry brick wall. The wall with strengthening made by polypropylene geo-nets reached the highest value of deformation. The increment was almost double. As mentioned above, this type of strengthening is very cheap and the most efficient from the point of view of the strengthening among all used method.

The unstrengthened specimen achieved a relatively small capacity and deformation. The value was about 7.5 mm. However, the value of energy dissipation in the unstrengthened specimen is higher than the specimens strengthened with steel wire ropes and geo-net (polyester). As mentioned above, geo-nets (polyester and polypropylene) have a better ratio of strength to the strength of brick and, therefore, it

is favourable their application. The highest energy dissipation is registered when geonets (polypropylene) are used, see Figure 5.46.

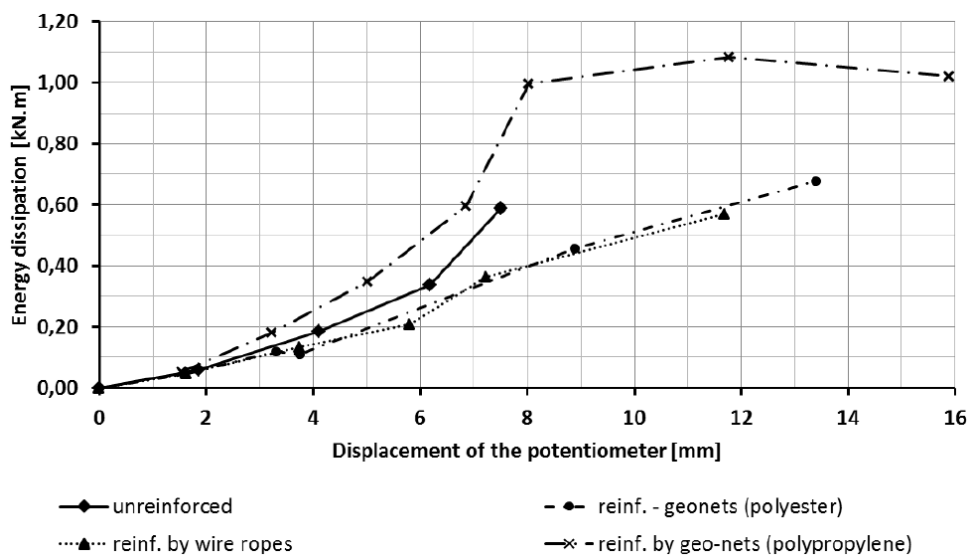


Figure 5.46. Comparison of the energy dissipation between dry clay bricks walls.

5.6.2.3 Solid clay brick walls

During the test was not achieved violation of the strength of the sample due to its large stiffness and also due to the possibility of test equipment. Energy dissipation was also calculated from the area of a hysteresis loop. The area was determined from one cycle in a given step.

This type of wall has very little ductile behaviour. Unstrengthened specimen reached by the violence very small values of displacement. The best result in terms of energy dissipation was again achieved using the strengthening of geo-net (polyester). Detailed development of energy dissipation for the solid brick walls is shown in Figure 5.47.

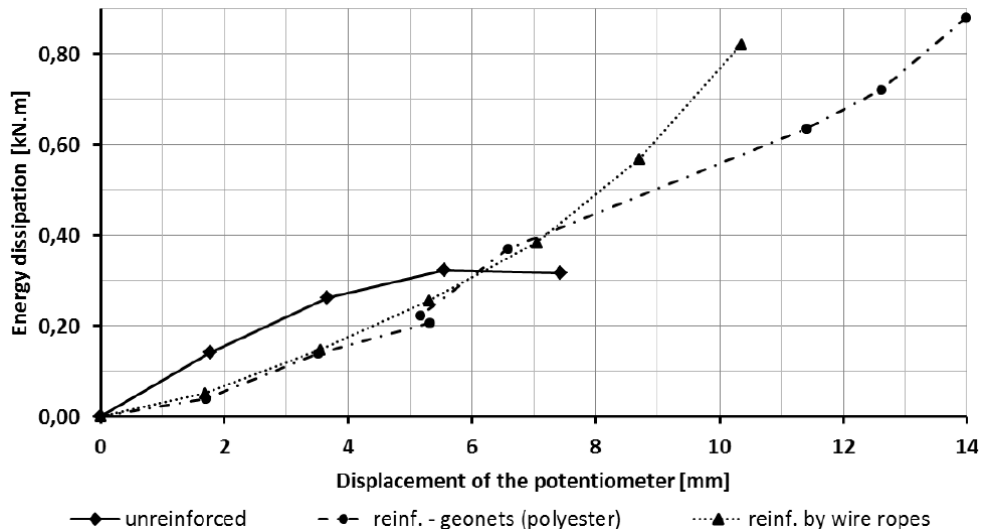


Figure 5.47. Comparison of the energy dissipation between solid clay bricks walls.

5.7 MECHANICAL TESTS ON UNREINFORCED AND REINFORCED MORTAR SPECIMENS

In order to study the mechanical behaviour of the strengthening system employed to reinforce the masonry walls a test campaign on reinforced mortar specimen has been carried out at the ITAM Structural Laboratory. Four series of specimens have been prepared considering two different types of mortar: in particular, the for first group of specimens clay mortar with a low percentage of sand has been employed, while the second group has been realized with lime mortar with addition of Portland cement. For each type of mortar two series of specimens have been casted without net, while other two series of specimens have been prepared enclosing a polyethylene mesh as a reinforcement, also employed in the strengthening of masonry walls. Two identical wooden formworks have been prepared for casting of specimens, whose dimensions and arrangement have been studied in order to allow to obtain elements of different shape to be used for testing under tension, compression and shear forces.

In the present chapter, the details of the specimens preparation, of the type of mechanical tests carried out and the results obtained will be outlined. The tests carried can be used in order to verify the numerical model in order to assess the accuracy of the theoretical approach.

5.7.1 Experimental specimens preparation

The mechanical tests on unreinforced mortar elements and on mortar elements reinforced with the polyester net have been carried out on specimens of different dimensions according to the type of test. In particular, the casting of the different elements has been done employing some wooden frames adequately designed in order to obtain the required specimens. The outline and the indication of dimensions of the frame are reported in Figure 5.48.

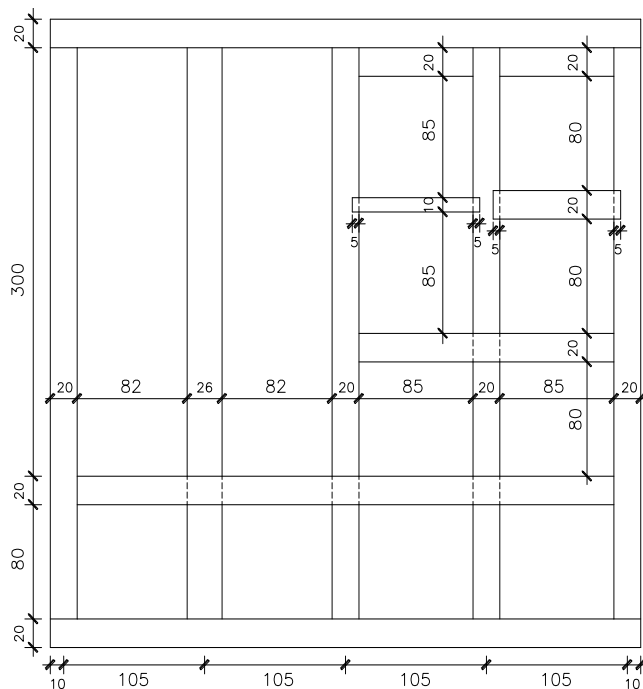


Figure 5.48. Outline of the wooden frame constructed for the casting of reinforced mortar specimens (dimensions in mm).

Two wooden moulds with identical geometry have been prepared, since the experimental campaign includes two identical sets of specimens in terms of dimensions, casted using two different types of mortar. For the first set of specimens the mortar consisted in clay with a low percentage of sand, while for the second set a lime mortar with Portland cement was used. In particular, clay-sand mortar consists of natural clay (5 mm) with mixed-grain sand (0-2 mm), prepared with addition of 25% in volume of water; while lime-Portland cement mortar is composed by grain mixture between 0.0-1.2 mm. The water content is 7.7 litres per 40 kg of material, the bulk density of fresh mortar is 1.7 kg/dm^3 with a time of workability of 3 hours.

For both set the internal reinforcement is represented by a polyester TENCATE geo-net, also employed for the strengthening of masonry walls and showed in Figure 5.49. The same moulds have been also used to cast the unreinforced specimens. The linear temperature expansion coefficient of polyester is about $200 \cdot 10^{-6} \text{ m/mK}$, while for lime mortar and clay mortar is around $8 \cdot 10^{-6} \text{ m/mK}$ and $9 \cdot 10^{-6} \text{ m/mK}$, respectively. For brick masonry this coefficient is about $5.5 \cdot 10^{-6} \text{ m/mK}$.

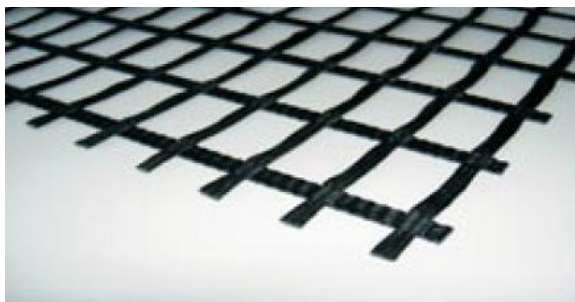


Figure 5.49. Geo-net employed for reinforced mortar specimens.

Each of the wooden frames prepared for the realization of the reinforced mortar samples have been designed in a way to obtain two specimens for tensile tests, which dimensions are $82 \times 300 \times 20 \text{ mm}$, two specimens for shear tests, which dimensions are $85 \times 85 \times 20 \text{ mm}$, and two groups of four elements which dimensions are $85 \times 80 \times 20 \text{ mm}$. These eight elements have been employed in order to construct two specimens in shape of a box to be used for compression tests.

Prior to cast the specimens in the wooden moulds, all the reinforcement elements have been cut according to the dimensions of each elements. In particular, for the elements belonging to the two specimens to be constructed and tested under compression, both orientations of the grid have been considered. The outline of the grid elements and the orientation with which they have been placed in the moulds are illustrated in Figure 5.50.



Figure 5.50. Preparation of the reinforcing mesh and orientation in the mortar specimens.

After the preparation of the net, the two different types of mortar have been prepared and the specimens casted in the wooden moulds, placing the reinforcement in the middle plane of the samples' thickness, as showed in Figure 4.51. The final results for the two sets of specimens is reported in Figure 5.52, for both types of mortar, and with the representation of the position of the mesh on the surface.

After four days of curing the mortar elements have been removed from the moulds and placed in a climate chamber (Figure 5.53(a)) at constant values of temperature and humidity, set at 20°C and 65%, respectively (Figure 5.53(b)). The clay mortar specimens (Figure 5.54(a)) and the lime mortar specimens (Figure 5.54(b)) have been kept in the climate chamber for 28 days prior to be tested. The same procedure has been followed for the unreinforced mortar specimens.



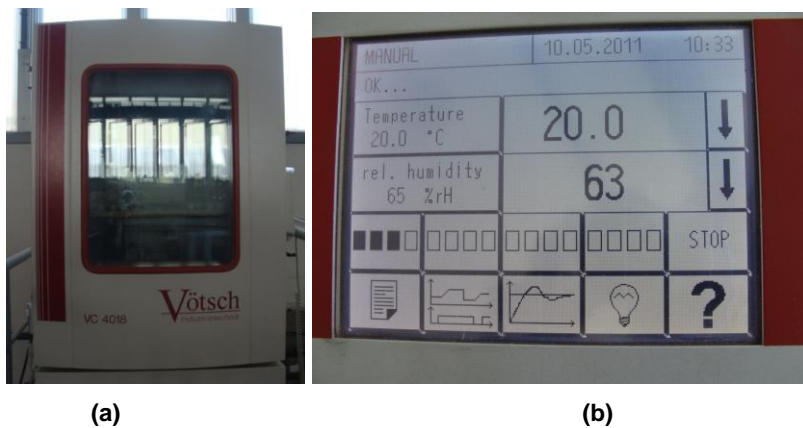
Figure 5.51. Phases of preparation of the mortar samples and positioning of the net.



(a)

(b)

Figure 5.52. Specimens casted in the wooden moulds: clay mortar (a) and lime mortar (b).



(a)

(b)

Figure 5.53. Climate chamber (a) and thermo-hygrometric conditions (b).



Figure 5.54. Reinforced mortar specimens in the climate chamber: clay mortar (a) and lime mortar (b).

After waiting the 28 days for all the sets of mortar elements, the preparation of the specimens for testing has been done; in particular, the pieces for compression specimens, and for shear specimens have been glued in order to obtain the final specimens. In the following pictures, the obtained reinforced mortar specimens are shown: in particular in Figure 5.55 are illustrated the specimens for tensile tests for both clay-sand and lime-Portland cement mortars. It is noticed that, due to an imperfection occurred in the clay-sand mortar, namely a crack in the shorter direction, these two specimens have been cut resulting in a length of 200 mm. In Figure 5.56, the specimens for shear tests have been reported; in particular, two mortar elements have been glued together in order to allow to test the specimen under three points bending test, inducing shear stresses in the two halves of the specimen. Finally, in Figure 5.57 the specimens for compression tests are also shown; four mortar elements have been glued together in order to form a sort of box to be tested under compression. As already said, both orientations of the grid have been considered. The same set of specimens has been realized for the unreinforced elements also, for both type of mortar.

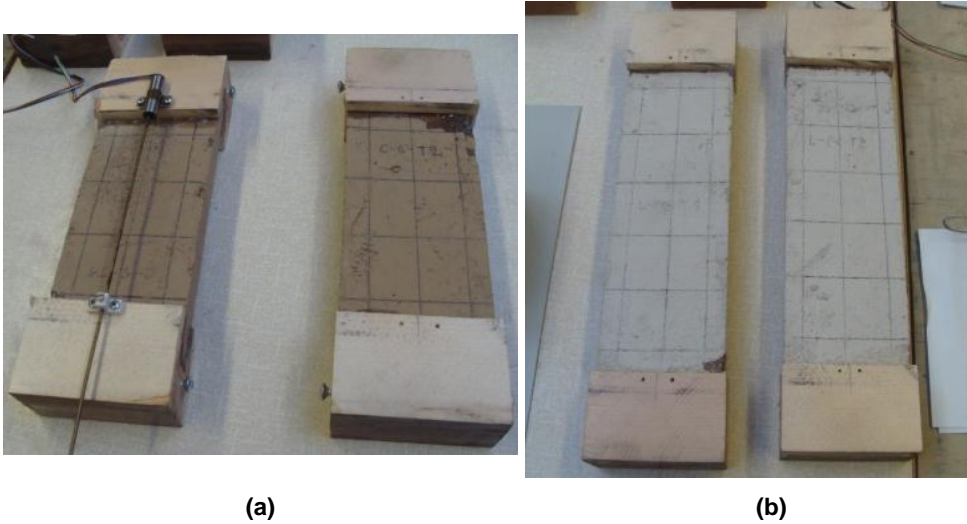


Figure 5.55. Reinforced mortar specimens for tensile tests: clay mortar (a) and lime mortar (b).

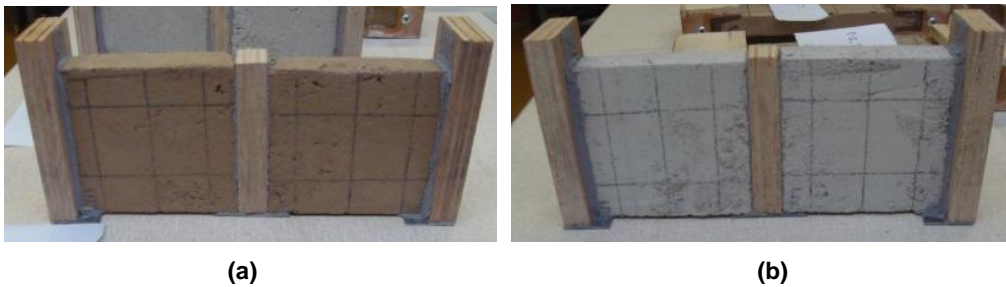


Figure 5.56. Reinforced mortar specimens for three-points bending tests: clay mortar (a) and lime mortar (b).

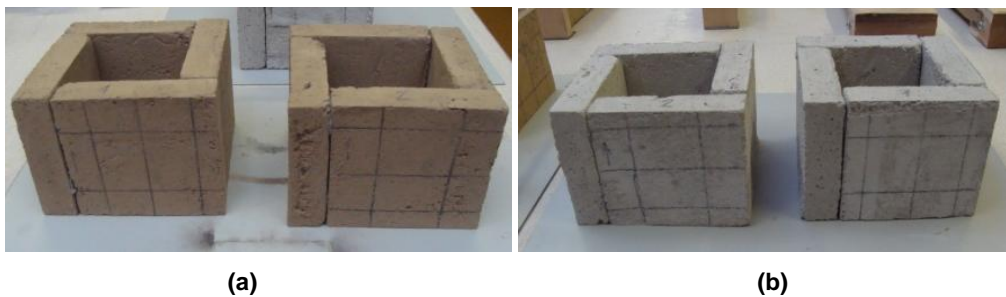


Figure 5.57. Reinforced mortar specimens for compression tests: clay mortar (a) and lime mortar (b).

5.7.2 Tensile tests

In the following section the results obtained from the tensile tests on unreinforced and reinforced mortar specimens are reported.

In the graphs of Figure 5.58 the force – displacement curves for the unreinforced and reinforced mortar specimens have been collected; in particular, Figure 5.58(a) refers to the clay-sand mortar specimens, while Figure 5.58(b) to the lime-Portland cement mortar specimens.

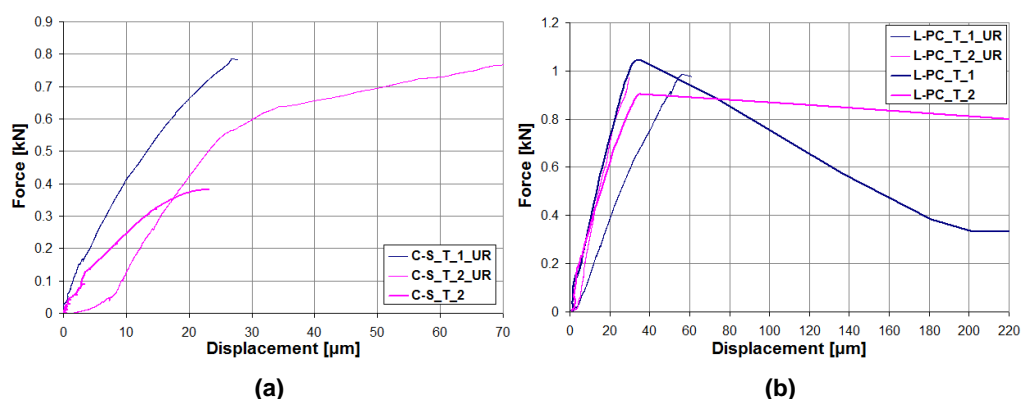


Figure 5.58. Force – displacement curves for unreinforced and reinforced mortar specimens under tensile load: clay mortar (a) and lime mortar (b).

Tensile Tests							
Specimen Name	F _{max} [N]	Width [mm]	Thickness [mm]	Length [mm]	σ_t [MPa]	Mortar Type	Reinforcement
C-S_T_1	–	80.4	19.78	144	–	clay-sand	YES
C-S_T_2	382	81.2	19.94	150	0.24	clay-sand	YES
L-PC_T_1	1045	81.63	20.12	241	0.64	lime-portland	YES
L-PC_T_2	904	81.8	20.68	242	0.53	lime-portland	YES
C-S_T_1_UR	785	81.33	21.57	243	0.45	clay-sand	NO
C-S_T_2_UR	767	83.87	21.79	241	0.42	clay-sand	NO
L-PC_T_1_UR	987	81.3	21.6	244	0.56	lime-portland	NO
L-PC_T_2_UR	972	81.83	21.9	244	0.54	lime-portland	NO

Table 5.8. Results of tensile tests on mortar specimens.

The Table 5.8 summarizes the results from the tensile tests on unreinforced and reinforced specimens. Moreover, in the pictures of Figure 5.59 two of the tested

reinforced mortar specimens for both types of mortar are illustrated. As it can be seen from the pictures, the failure occurred upon the formation of a crack in the direction normal to the tensile load.

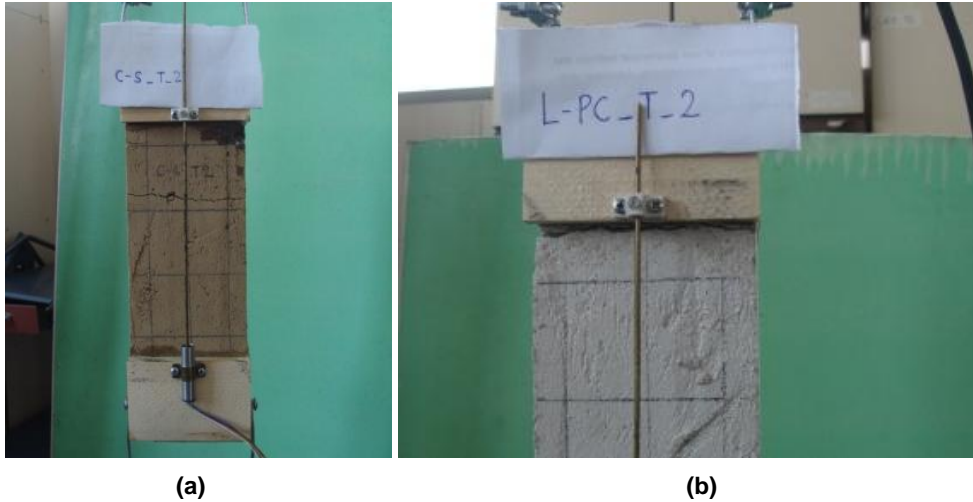


Figure 5.59. Tested reinforced mortar specimens under tensile load: clay mortar specimen (a) and detail of crack in lime mortar specimen (b).

5.7.3 Compressive tests

Compression tests have been also carried out on unreinforced and reinforced specimens, made by two different types of mortar.

In the graphs of Figure 5.60 the force – displacement curves for the unreinforced and reinforced mortar specimens have been collected; in particular, Figure 5.60(a) refers to the clay-sand mortar specimens, while Figure 5.60(b) to the lime-Portland cement mortar specimens. The Table 5.9 summarizes the results from the compression tests on unreinforced and reinforced specimens. Moreover, in the pictures of Figure 5.61 two of the tested reinforced mortar specimens for both types of mortar are illustrated. It is reminded that, for each type of mortar, both orientations of the reinforcing grid have been considered.

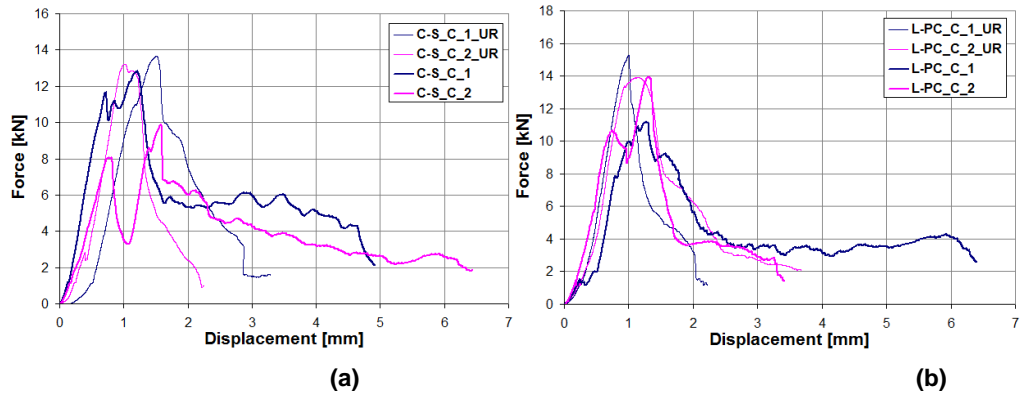
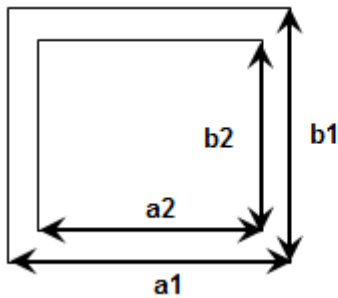


Figure 5.60. Force – displacement curves for unreinforced and reinforced mortar specimens under compression load: clay mortar (a) and lime mortar (b).

Compression Tests											
Specimen Name	Fmax [N]	a1 [mm]	a2 [mm]	t1 [mm]	b1 [mm]	b2 [mm]	t2 [mm]	height [mm]	σ_c [MPa]	Mortar Type	Reinf.
C-S_C_1	12830	104.3	63.06	41.24	104.4	64.7	39.7	79.55	1.88	clay-sand	YES
C-S_C_2	9895	104.2	64.4	39.8	103.8	64.6	39.2	78.6	1.49	clay-sand	YES
L-PC_C_1	11203	105.4	61.75	43.65	105.5	63.65	41.85	80.7	1.56	lime-portland	YES
L-PC_C_2	13950	106.6	64.8	41.8	105.7	64	41.7	79.5	1.96	lime-portland	YES
C-S_C_1_UR	13645	105.8	63.9	41.9	107.3	64.5	42.8	77.65	1.89	clay-sand	NO
C-S_C_2_UR	13213	106.2	64.55	41.65	104.9	61.1	43.8	77.9	1.84	clay-sand	NO
L-PC_C_1_UR	15256	106.8	62.1	44.7	107.8	63.25	44.55	77.2	2.01	lime-portland	NO
L-PC_C_2_UR	13925	106.6	62.5	44.1	106.7	61.25	45.45	77.6	1.85	lime-portland	NO



$thickness1 = a1 - a2$
 $thickness2 = b1 - b2$

Table 5.9. Results of compression tests on mortar specimens.



Figure 5.61. Tested reinforced mortar specimens under compression load: clay mortar (a) and lime mortar (b) specimens.

5.7.4 Shear tests

Shear tests have been also carried out in order to induce shear stresses in specimens. In the following section the results obtained from tests on unreinforced and reinforced mortar specimens are reported. In the graphs of Figure 5.62 the force – deflection curves for the unreinforced and reinforced mortar specimens have been collected; in particular, Figure 5.62(a) refers to the clay-sand mortar specimens, while Figure 5.62(b) to the lime-Portland cement mortar specimens. The Table 5.10 summarizes the results from the tensile tests on unreinforced and reinforced specimens. Moreover, in the pictures of Figure 5.63 two of the tested reinforced mortar specimens for both types of mortar are illustrated. As it can be seen from the pictures, the failure occurred upon the formation of a crack in the direction normal to the tensile load.

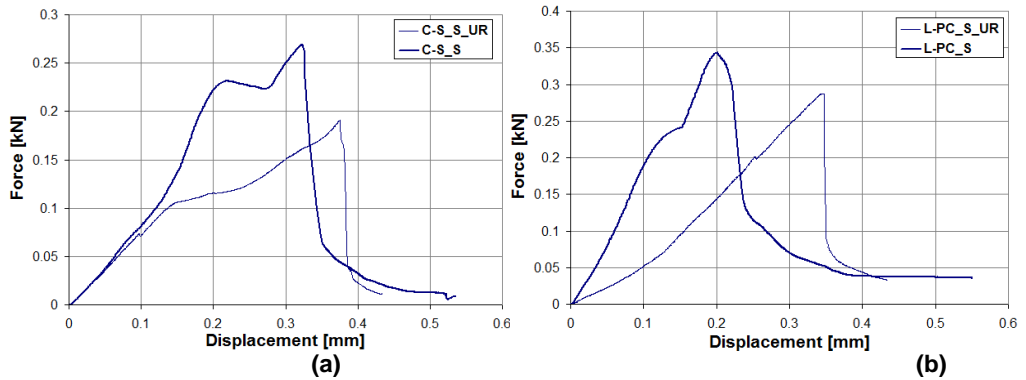


Figure 5.62. Force – deflection curves for unreinforced and reinforced mortar specimens under shear load: clay mortar (a) and lime mortar (b).

Shear Tests								
Specimen Name	Fmax [N]	Width [mm]	Thickness [mm]	Length [mm]	Supports [mm]	τ [MPa]	Mortar Type	Reinforcement
C-S_S	269	82	20.03	185	200	0.082	clay-sand	YES
L-PC_S	344	84.7	19.76	186	200	0.103	lime-portland	YES
C-S_S_UR	190.9	83.5	20.7	184	200	0.055	clay-sand	NO
L-PC_S_UR	287.4	82.8	20.82	187	200	0.083	lime-portland	NO

Table 5.10. Results of shear tests on mortar specimens.

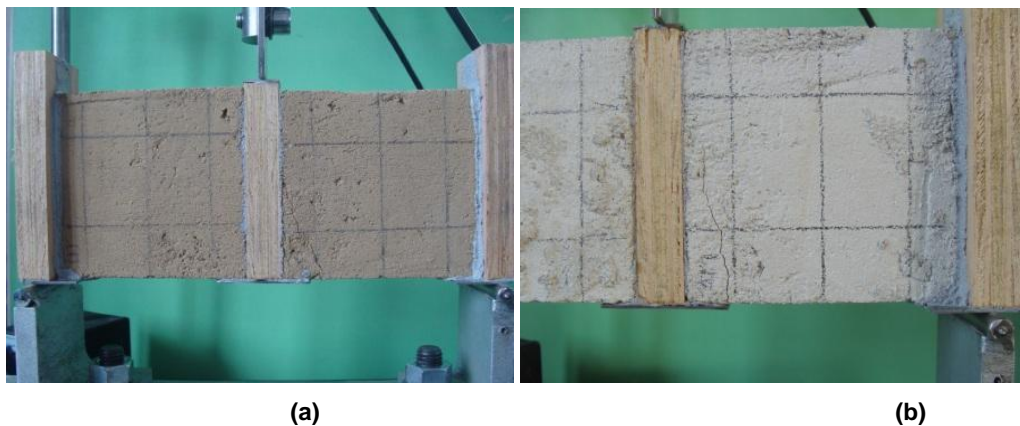


Figure 5.63. Tested reinforced mortar specimens under shear load: clay mortar specimen (a) and detail of crack in lime mortar specimen (b).

5.7.5 Summary of results

In the following table a summary of all the results obtained from the mechanical characterization tests is reported:

Tensile Tests			
Specimen Name	σ_t [MPa]	Mortar Type	Reinforcement
C-S_T_1	-	clay-sand	YES
C-S_T_2	0.24	clay-sand	YES
L-PC_T_1	0.64	lime-portland	YES
L-PC_T_2	0.53	lime-portland	YES
C-S_T_1_UR	0.45	clay-sand	NO
C-S_T_2_UR	0.42	clay-sand	NO
L-PC_T_1_UR	0.56	lime-portland	NO
L-PC_T_2_UR	0.54	lime-portland	NO
Compression Tests			
Specimen Name	σ_c [MPa]	Mortar Type	Reinforcement
C-S_C_1	1.88	clay-sand	YES
C-S_C_2	1.49	clay-sand	YES
L-PC_C_1	1.56	lime-portland	YES
L-PC_C_2	1.96	lime-portland	YES
C-S_C_1_UR	1.89	clay-sand	NO
C-S_C_2_UR	1.84	clay-sand	NO
L-PC_C_1_UR	2.01	lime-portland	NO
L-PC_C_2_UR	1.85	lime-portland	NO
Specimen Name	τ [MPa]	Mortar Type	Reinforcement
C-S_S	0.082	clay-sand	YES
L-PC_S	0.103	lime-portland	YES
C-S_S_UR	0.055	clay-sand	NO
L-PC_S_UR	0.083	lime-portland	NO

Table 5.11. Results of mechanical tests on unreinforced and reinforced mortar specimens.

5.8 CONCLUSIONS

The experimental campaign carried out has dealt with the investigation of the experimental behaviour of brick masonry walls subjected to lateral cyclic tests. The interpretation of the experimental data from the cyclic tests has been carried out in order to evaluate the deformation capacity, energy dissipation, the strength and the elastic stiffness of the walls. The seismic behaviour of the strengthened structural elements was quite good, because although the elements underwent damages, the strengthened system was able to hold the pieces together and collapse was therefore averted.

The following results were obtained through the experimental results. Most effective in terms of strengthening appears to be geo-net (polyester). This method of strengthening does not require complicated the process of preparing against steel wire ropes. It is also cheap in cost. As mentioned above, geo-nets (polyester and polypropylene) have also a better ratio of strength to the strength of brick and, therefore, it is favourable their application.

The wall strengthened by means of technique with steel wire ropes behaves in a quite compact manner since the wire ropes play a very effective role in sewing up the cracks and keeping the masonry blocks together. Some cracks can appear along the mortar joints in the surroundings of the reinforcement and, in general, there is a good redistribution of the stresses and a more widespread crack pattern compared to the unreinforced wall. On the other hand, steel wire ropes also exhibit excellent properties, but in this case it is necessary significant intervention onto the structure than in the previous case.

6 BOND BEHAVIOUR OF FRP REINFORCEMENT ON MASONRY

In the present chapter the experimental results of bond tests on masonry blocks made of yellow tuff and bonded with different types of Fiber Reinforced Plastic (FRP) fabrics carried out at the Laboratory of Materials and Structures of the University of Sannio are presented and analysed. The discussion of results is mainly focused on the assessment of the set-up reliability, the choice of sufficient bonded length for achieving the full bond strength, the evaluation of the effect of a plastering layer and the tuff strength. The results are analysed both in terms of global (failure modes and loads, load-displacement curves) and local behaviour (distribution of axial strains and shear stresses) aimed to evidence the different behaviour of the fibres used (carbon, glass, basalt, linen).

6.1 THE ROLE OF BOND BETWEEN MASONRY AND FRP

The efficiency of external strengthening of masonry elements with Fiber Reinforced Plastic (FRP) materials glued by epoxy adhesive is generally based on the quality of bond developed between the masonry support and the strengthening material; indeed, the failure of the strengthened elements is often caused by the detaching of the FRP reinforcement. This kind of failure, usually indicated as 'debonding' is strictly related to the tensile strength of the masonry stone that is the lowest strength of the coupled materials.

Many experimental studies concerning masonry elements strengthening with FRP materials have already been performed on panels, arches, vaults, laboratory

scaled and real structures (Augenti et al., 2011 [52]; Marcari et al., 2006 [30]; Valluzzi et al., 2002 [22]; Aiello et al., 2009 [53]), but the bond behaviour, which influences the efficiency of each type of strengthening, nowadays is not well established, both on the analytical and experimental point of view. Analogously, design indications for prediction of debonding load in masonry elements (CNR DT 200/R1, 2012) [54] are not diffuse as for concrete elements. The lack of knowledge about this topic is also due to the absence of a standard procedure for performing bond tests and to the large variability of mechanical and physical properties of the masonry support (compressive and tensile strength, Young's modulus, porosity, surface consistency). Furthermore, because masonry elements are an assembling of blocks (natural or artificial) and mortar layers, the latter ones can represent discontinuities along the bonded surface both in terms of strength of the support material and imperfections that, if not well levelled, can be locations for initiating the debonding. It is worth to notice that most of the experimental results available in the technical literature regard bond tests on single masonry blocks, natural (Ceroni and Pecce, 2006 [55]; Aiello and Sciolti, 2008 [56] or artificial (Capozucca, 2010 [57]; Panizza et al., 2008 [58]; Seim and Pfeiffer, 2011 [59]; Mazzotti et al., 2012 [60]), while few tests have been realized on specimens made of more blocks connected by mortar layers (Panizza et al., 2012 [61]; Oliveira et al., 2011 [62]), but without any comparison with the results related to tests on single blocks. Another important topic, which has not been investigated in detail in the experimental tests, is the effect of a plastering layer to consolidate the masonry surface before applying the FRP reinforcement; indeed, all producers generally suggest to use a 'primer' layer made of epoxy resin and then apply the adhesive, while the use of a plastering layer between the primer and the adhesive is not mandatory.

Some efforts have been recently spent into investigate the influence of the set-up (Valuzzi et al., 2012) [63] on the debonding load and for calibrating design provisions with specific coefficients for different masonry supports (new draft of CNR DT200/R1, 2012 [54]; Ceroni et al., 2013 [64]) thanks to the increased amount of experimental data now available in the technical literature. Note that most of the observed phenomena and issues related to bond test procedure (effect of plastering, end anchoring devices, and type of fibres, optimal bonded length, detailing of set-up)

can be considered valid also for masonry supports different from the specific one (tuff) used in the experimental programs herein presented and, more in general, are useful to design retrofitting interventions for the numerous masonry buildings that have to be preserved in Italy.

6.2 EXPERIMENTAL SET-UP FOR BOND TESTS

Several experimental set-ups have been proposed by various researchers for bond tests on concrete elements with FRP laminates or sheets to characterize the bond behaviour and the bond strength, but no standard procedure has been definitely established. Some round robin tests have been recently carried out on both concrete (Guadagnini et al., 2012) [65] and masonry elements (Valluzzi et al., 2012) [63] in order to check the influence of the set-up on the bond strength. The main distinction regards the stress condition that the set-up generates on the support: a) pull-pull scheme where both the reinforcement and the support are loaded in tension or b) pull-push scheme where the support is pushed. In both cases the FRP reinforcement can be applied on two sides (symmetrical scheme) or only one side (asymmetrical scheme).

For masonry elements it is in general difficult to realize a pull-pull bond test; really to realize this scheme, the tensile load can be transferred to the masonry block and FRP reinforcement by means of complex steel frames (Aiello and Sciolti, 2003) [66] or plates (Ceroni and Pecce, 2006) [55].

On the contrary, the pull-push set-up allows overcoming the difficulties of applying tension to the masonry block and, in particular, the asymmetrical scheme can reduce the influence of alignment and positioning problems of the specimens (Mazzotti et al., 2009 [67]; Bilotta et al., 2011 [68]). The pull-push set-up has been frequently realized by inserting the specimen in stiff steel frames and clamping the end of the FRP reinforcement in the grips of universal tensile machines, while the block is compressed by contrasting steel plates (Aiello and Sciolti, 2008 [56]; Valluzzi et al., 2012 [63]), Figure 6.1(a). However, when this configuration is asymmetrical (the FRP reinforcement is glued on one side of the block), the steel frame is stressed by

the additional forces due to the eccentricity of the applied load respect to the block. Thus, to reduce the effect of eccentricity, the asymmetrical push-pull scheme can be better organized in an horizontal set-up (Mazzotti et al., 2009 [67]; Oliveira et al., 2011 [62] where the tensile load is applied to the FRP reinforcement through hydraulic jacks that directly push the lateral faces of the block (Figure 6.1(b)).

Another diffuse set-up is the beam test that was usually adopted for the characterization of the bond law of steel bars in concrete elements; in the case of masonry, two blocks are connected at the bottom by the FRP reinforcement, while at the top by a cylindrical hinge that allows rotation when the vertical load (generally two forces) is applied. For masonry elements, if the ratio length/height of the block is too short, such a set-up can determine a shear failure in the blocks due to the low tensile strength of masonry and without achieving the effective bond strength (Ceroni et al., 2003) [69].

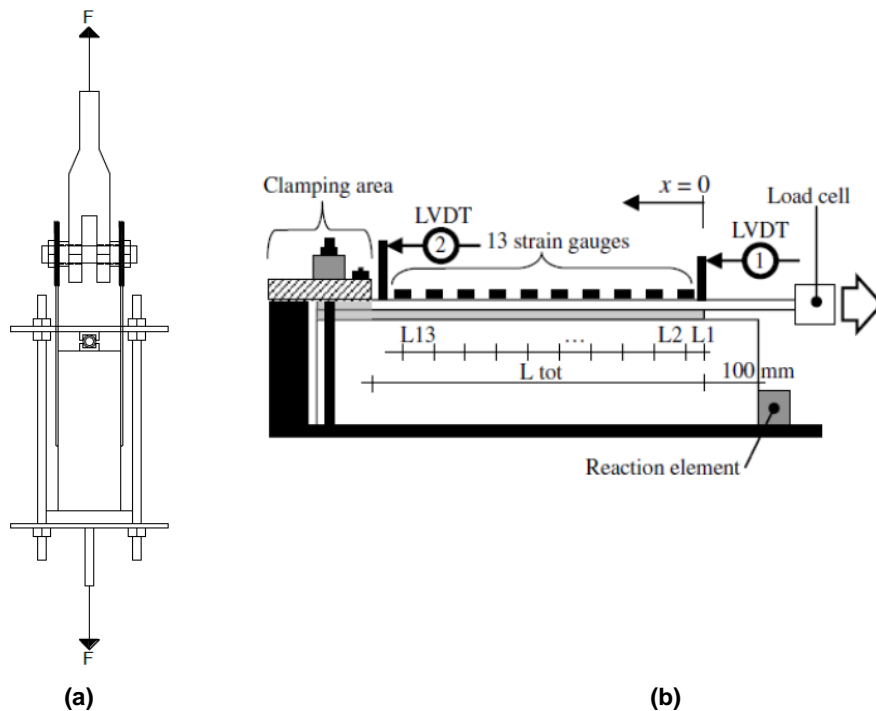


Figure 6.1. Experimental arrangements for pull-push set-up: (a) symmetrical scheme inside a tensile machine (Aiello and Sciolti, 2008) [56]; (b) asymmetrical scheme with a hydraulic jack (Mazzotti et al., 2009) [67].

6.3 EXPERIMENTAL PROGRAMME

6.3.1 Asymmetrical pull-push test set-up and properties of the masonry supports

In the experimental programme, all tests are performed according to an asymmetrical pull-push scheme where the FPR reinforcement is loaded by a mechanical jack. In this scheme the specimen is placed on a horizontal plane in order to minimize imperfections in the alignment; the block is fixed at the unloaded end by means of a steel tie, while a transversal steel prism allows applying compression to the block at the loaded end. In Figure 6.2 the scheme of the test is illustrated. The dimensions of the blocks are $B = 250$ mm, $L = 290$ mm, $H = 110$ mm; the width of the FRP reinforcements is always $b_f = 100$ mm ($b_f/B \sim 0.5 = 0.4$).

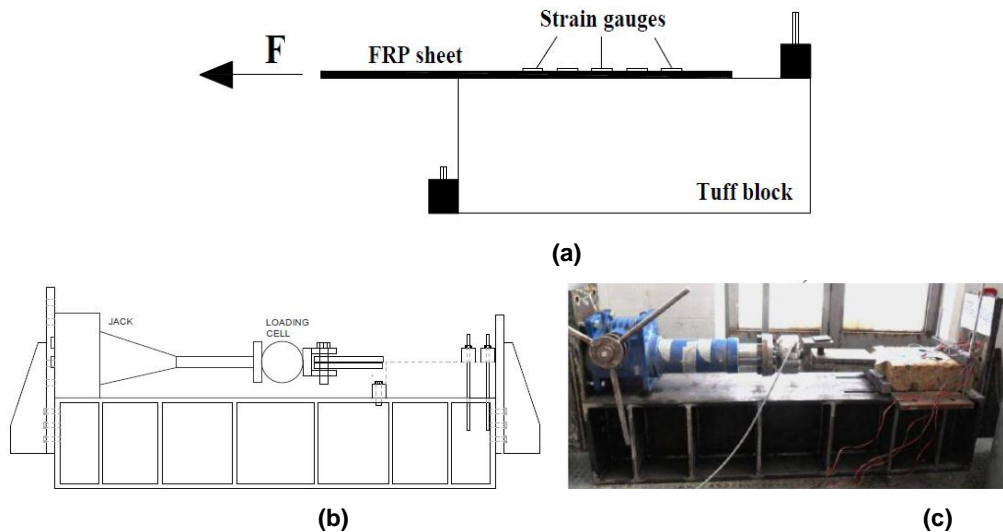


Figure 6.2. Set-up for pull-push bond tests.

Two different qualities of tuff stones (T1 and T2) are used as masonry support. The values of the mean compressive strength of tuff T1 and T2 are 3.8 MPa (CoV = 11%) and 2.1 MPa (CoV = 20%), while the values of the mean tensile

strength are 0.81 MPa (CoV = 13%) and 0.69 MPa (CoV = 20%), evaluated in both cases by means of experimental tests on three specimens.

The FRP system is made of unidirectional sheets made of four types of fibre: carbon, glass, basalt and linen. The nominal values of the Young's modulus and thickness given by manufacturers are: $E_f = 230$ GPa and $t_f = 0.166$ mm for carbon, $E_f = 80.7$ GPa and $t_f = 0.48$ mm for glass, $E_f = 90$ GPa and $t_f = 0.14$ mm for basalt, $E_f = 45$ GPa and $t_f = 0.194$ mm for linen. Note that the axial stiffness of glass and carbon sheets is similar ($E_f \cdot t_f$ is 38410 N/mm for CFRP and 43200 N/mm for GFRP), while is sensibly lower for the basalts and linen fibres (12600 and 8730 N/mm, respectively). The nominal values of the tensile strength given by the manufacturers are: 4830 MPa, 2560 MPa, 1900 MPa, and 710 MPa for carbon, glass, basalt and linen fibres, respectively.

Based on the results of the previous pull-push tests, longer bonded lengths (200 and 300 mm) are used in order to develop the full bond law and achieve the maximum debonding load. Depending on the bonded length, a number of four or five strain gauges are placed along the FRP sheet. The surface of all specimens were brushed before applying the primer. After the primer, the surface was treated or not with an epoxy plaster before the application of the adhesive. No end anchorage systems were used in this experimental program.

6.3.2 Failure modes and loads

In Table 6.1 the following information is reported: bonded length, L_b , type of fibres, type of tuff, presence of a plastering layer. Moreover, in Table 6.1 there are also accounted the failure mode, the maximum tensile load in the FRP reinforcement, F_{max} , and the corresponding stress, σ_{max} , calculated as ratio of F_{max} to the reinforcement transversal area. The ratio σ_{max}/f_u is listed too, in order to check the exploiting of the tensile strength of the fibres.

Finally, for each group of equal specimens, in Table 6.1 the following parameters are listed:

- the average value of the maximum load, $F_{max,av}$;

- the average shear stress, τ_{av} , calculated as $\frac{F_{max,av}}{B_f \cdot L_b}$, i.e. assuming an uniform distribution of shear stresses along the sheet;
- the load variation, F_{max} , that is defined as $\frac{F_{max,av,ref} - F_{max,av}}{F_{max,av,ref}}$, being $F_{max,av,ref}$ the average maximum load of the reference specimens.

Specimen	L_b [mm]	Fibre	Tuff	Plaster	Failure	F_{max} [kN]	$F_{max,av}$ [kN]	$F_{ref,av}$ [kN]	ΔF_{max} [%]	σ_{max} [MPa]	σ_{max}/f_u [-]	τ_{av} [MPa]
TC_200_p_1	200	CFRP	T1	Yes	DC	16.96				1022	0.21	0.85
TC_200_p_2	200	CFRP	T1	Yes	DC	18.56	17.62	21.03	-16	1118	0.23	0.93
TC_200_p_3	200	CFRP	T1	Yes	DC	17.34				1044	0.22	0.87
TC_300_p_1	300	CFRP	T1	Yes	TF	21.14				1274	0.26	0.70
TC_300_p_2	300	CFRP	T1	Yes	DB+ED	22.81	21.03	21.03	-	1374	0.28	0.76
TC_300_p_3	300	CFRP	T1	Yes	SF	19.13				1153	0.24	0.64
TC_300_1	300	CFRP	T1	No	DB	18.11				1091	0.23	0.60
TC_300_2	300	CFRP	T1	No	DB	18.91	18.51	21.03	-12	1139	0.24	0.63
TG_200_p_1	200	GFRP	T1	Yes	DC	14.72				307	0.12	0.74
TG_200_p_2	200	GFRP	T1	Yes	DC	12.52	13.62	19.94	-32	261	0.10	0.63
TG_300_p_1	300	GFRP	T1	Yes	SF	19.29				402	0.16	0.64
TG_300_p_2	300	GFRP	T1	Yes	DB+ED	22.49	19.94	19.94	-	468	0.18	0.75
TG_300_p_3	300	GFRP	T1	Yes	DB	18.04				376	0.15	0.60
TG_300_1	300	GFRP	T1	No	DB	16.42				342	0.13	0.55
TG_300_2	300	GFRP	T1	No	DB	17.23	16.82	19.94	-16	359	0.14	0.57
TL_200_1	200	LFRP	T1	No	TF	8.56				441	0.62	0.43
TL_200_2	200	LFRP	T1	No	TF	8.14	8.35	8.35	-	420	0.59	0.41
TL_300_1	300	LFRP	T1	No	TF	8.13				419	0.59	0.27
TL_300_2	300	LFRP	T1	No	TF	8.29	8.21	8.35	-2	427	0.60	0.28
TC_300_p_b_1	300	CFRP	T2	Yes	DB	16.82				1013	0.21	0.56
TC_300_p_b_2	300	CFRP	T2	Yes	DB+ED	20.10	18.46	18.46	-	419	0.09	0.67
TC_300_b_1	300	CFRP	T2	No	DB+ED	15.03				1073	0.22	0.50
TC_300_b_2	300	CFRP	T2	No	DB	14.54	14.78	18.46	-20	750	0.16	0.48
TG_300_p_b_1	300	GFRP	T2	Yes	DB+ED	20.46				426	0.17	0.68
TG_300_p_b_2	300	GFRP	T2	Yes	DB+ED	17.76	19.11	19.11	-	370	0.14	0.59
TG_300_b_1	300	GFRP	T2	No	DB	13.41				279	0.11	0.45
TG_300_b_2	300	GFRP	T2	No	DB+ED	15.05	14.23	19.11	-26	314	0.12	0.50
TB_300_b_1	300	BFRP	T2	No	DB+ED	11.39				814	0.43	0.38
TB_300_b_2	300	BFRP	T2	No	DB	9.06	10.23	10.23	-	647	0.34	0.30

TF = Tensile fracture of fibre, DB = superficial debonding, DB + ED= debonding with detachment of tuff edge, SF = Sliding of fibre in steel plates; DC = Diagonal cracking in tuff block at the unloaded side

Table 6.1. Geometrical properties of specimens and experimental results.

For specimens made of tuff T1 and bonded with carbon and glass fibres over 200 mm, failure occurs due the formation of a vertical or diagonal crack at the

unloaded end of the reinforcement (Figure 6.3(a)), while for the bond length of 300 mm an effective debonding is attained both for specimens with and without plastering (Figures 6.5(b) and 6.3(c)). Such different failure modes are due to the configuration of the reinforcement with respect to the tuff block that is completely covered when the sheet is 300 mm long and being the end of the sheet coincident with the end of the block. On the contrary, for the bonded length of 200 mm, the specimen has an unreinforced end portion that must withstand the tensile load applied through the reinforcement. This different failure modes lead to attain sensibly lower loads for specimens with $L_b = 200$ mm compared with the case of $L_b = 300$ mm (-16% for carbon and -32% for glass fibres).

Conversely, specimens with carbon and glass fibres bonded over 300 mm and made of tuff T1 reach similar ultimate loads both in the case of plastering or not, i.e. the differences of failure loads are about 5%. This result can be related to the similarity in the axial stiffness of the two reinforcements that, as well known, influences the fracture energy and, thus, the debonding load (CNR DT200/R1, 2012) [54]. By contrast, as previously evidenced, for $L_b = 200$ mm, the specimens with glass fibres attain a failure load about 20% lower than the specimens with carbon fibres.

In the case of the specimens prepared without the plaster and made of tuff T1, a reduction in the debonding load of about 12% for carbon and 16% for glass fibres is observed, showing that the plastering of inhomogeneous surfaces may enhance the effectiveness of the external reinforcement. Moreover, in the case of not plastered surface, the failure occurs with a superficial debonding of the reinforcement involving a very thin layer of tuff (Figure 6.3(b)), while plastering allows to involve a ticker volume of tuff in the debonding phenomenon (Figure 6.3(c)). In most specimens with plastering further edge effects can be observed at the loaded end; in particular, the detachment of a triangular volume of tuff delimited by the steel prism that apply compression to the block occurs (Figure 6.3(d)).

The specimens with carbon and glass fibres bonded on tuff T1, reached a tensile stress at failure in the reinforcement that is a low percentage of the nominal strength, that is about 20-25% and 10-20% for carbon and glass, respectively.

Whereas, for the specimens with linen fibres, the tensile failure of fibres always occur for both values of the bonded length, so that no debonding process is

activated along the interfaces. For these fibres, the tensile stresses at failure result about 60% of the nominal strength.

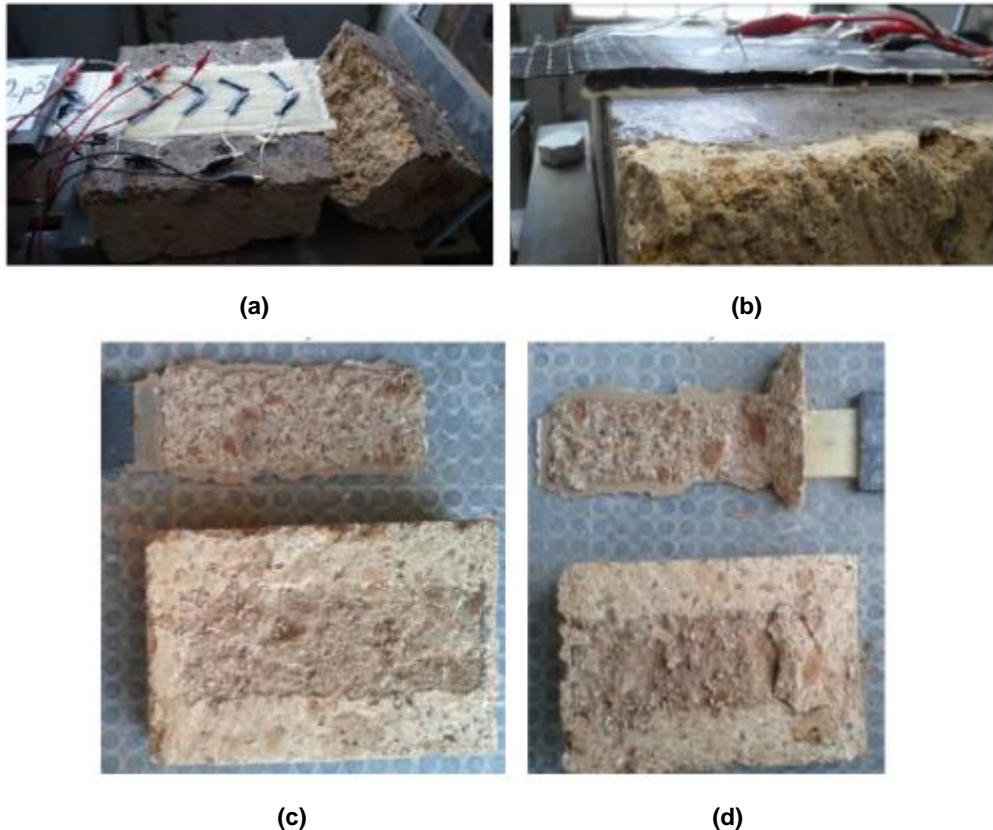


Figure 6.3. Examples of failure modes: (a) Diagonal crack at the free end of the FRP reinforcement; (b) Superficial debonding at the loaded end; (c) Debonding in specimens with plastering; (d) Edge effects in the tuff block at the loaded end.

When a lower strength tuff is used (T2 instead of T1: -45% for the compressive and -15% for the tensile strength, respectively) a reduction of the maximum load is measured in the bond tests. In particular, the reduction is meanly 15% for specimens with carbon fibres both when the plaster is applied or not applied, compared with similar specimens made of tuff T1, while for the glass fibres the reduction is about 15% in case of not plastered specimens and only 5% in the case of plastered ones. Moreover, the specimens made of tuff T2 are more sensibly to the

effect of plastering, since the debonding load decreases of 20-26% when the plaster is not used, while the reduction was variable in the range 12-16% for tuff T1. These results confirm the positive effect of plastering that, probably, allows to reduce the surface inhomogeneity and dampens the influence on the bond strength of the lower strength in the first millimetres of the support involved in the debonding mechanism.

Two specimens made of tuff T2 were bonded with basalt fibres along 300 mm; also for these specimens a debonding failure occurred, but the failure loads result about 50% of the ones observed for the specimens with glass and carbon fibres, which are characterized by a quite triple axial stiffness; the tensile stress in the basalt fibres at failure are equal to about 40% of the nominal strength.

6.3.3 Strain distributions and load-displacement curves

On the basis of strain gauges measurements, the strain variation along the reinforcement can be evaluated at different load levels up to the bond failure. The origin of axis x is always fixed at the loaded end of the reinforcement and the first value of strain is theoretically calculated dividing the applied load by the nominal value of the Young's modulus and by the transversal area of the fibres.

In Figures 6.4(a) and 6.4(b) there are depicted the strain profiles along the sheet registered for two specimens made of tuff T1 and bonded with glass and carbon fibres, respectively, considering the bonded lengths of 200 and 300 mm. The strain profiles show that the effective bond length is not lower than 300 mm. This means that a further increase of the bonded length should not determine relevant increase of the debonding loads.

Moreover, the comparison between strain profiles in specimens with glass and carbon sheets having the same bonded length (300 mm, Figure 6.4(c)) at the same load levels (about 25%, 75% and 90% of F_{max} , being F_{max} comparable for glass and carbon fibres) shows that the distributions are quite similar due to the comparable axial stiffness of the two reinforcements.

In Figure 6.4(d) the strain distributions for two specimens bonded, respectively, with linen and carbon fibres without plaster are compared for $L_b = 300$

mm at two equal load levels. The comparison, clearly, shows a larger deformability of the linen fibres due to their lower axial stiffness; moreover, because the 90% of the failure load of the linen fibres corresponds to only 40% of the failure load of the carbon ones, these ones show a regular trend, while for the linen fibres a local debonding phenomenon is occurring close to the loaded end just before the final tensile failure of the fibres.

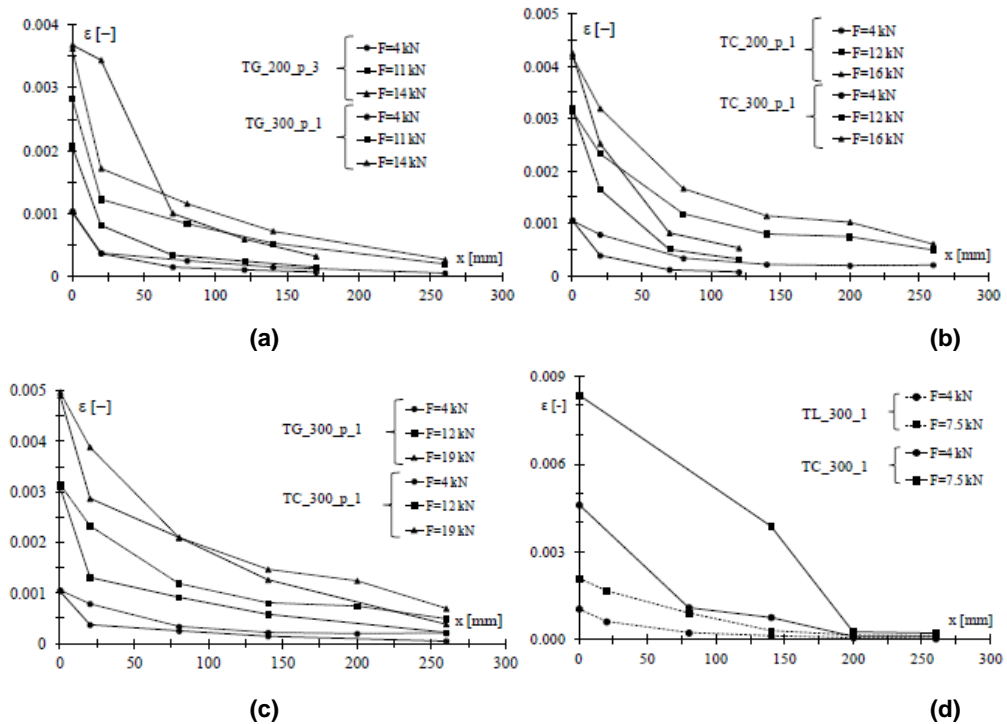
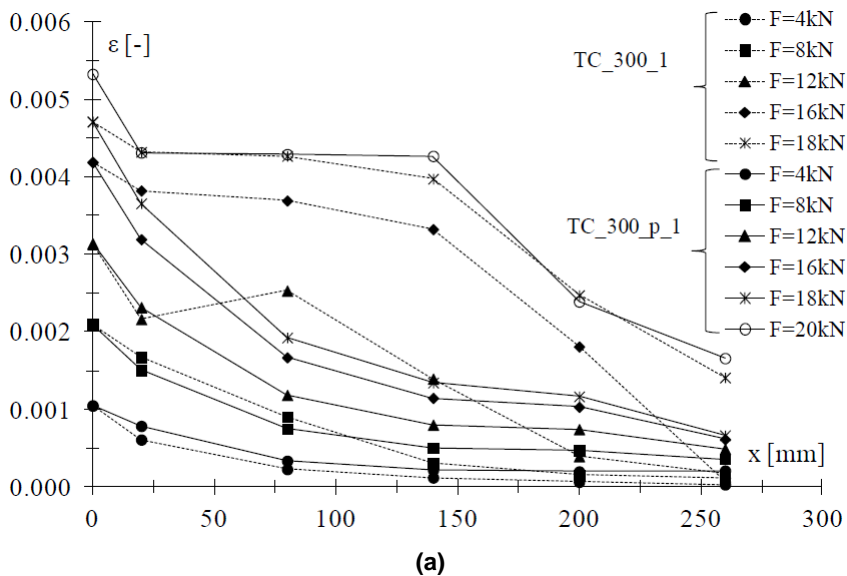


Figure 6.4. Strain profiles in pull-push bond tests in specimens made of tuff T1 with: (a) Glass fibers for $L_b = 200$ mm and $L_b = 300$ mm with plaster; (b) Carbon fibers for $L_b = 200$ mm and $L_b = 300$ mm with plaster; (c) Carbon and glass fibers for $L_b = 300$ mm with plaster; (d) Linen and carbon fibers for $L_b = 300$ mm without plaster.

The effect of plastering on the strain distribution is evidenced in Figures 6.5(a) for two specimens bonded with carbon fibres over 300 mm and made of tuff T1. The same comparison is reported in Figure 6.5(b) for two specimens made of tuff T2. Both graphs show that for specimens without plastering the debonding starts at

lower loads; in particular, for tuff T1 (see Figure 6.5(a)) debonding starts at about 16-18 kN for specimens without plastering instead of about 20 kN, as evidenced by the strain trend that is almost constant in the first 150 mm and with mean values higher than in the case of plastering at the same load levels. These differences are, thus, significant of different interface bond laws with and without the plaster layer: in particular, it can be considered a stiffer bond law in the case of plastering.

The stiffening effect of the plastering is confirmed also by the global experimental load-displacement curves graphed in Figure 6.5(c) for specimens bonded with carbon and glass fibres made of tuff T2. The displacement at the loaded end is calculated by integrating the measured strains along each FRP reinforcement. In Figure 6.5(c) also the global load-displacement curves of two specimens with basalt fibres (without plaster) are graphed. The comparison shows again that the curves of specimens bonded with carbon and glass fibres are comparable both in the case of presence or not of the plastering, while they are sensibly stiffer than the curves of specimens with basalt fibres due to their lower axial stiffness (about 1/3). Moreover, the debonding process in the specimens with basalt fibres seems to be more ductile since larger ultimate displacements are attained. This peculiarity of the basalt fibres was already observed in bond tests on concrete elements externally bonded with different types of Near Surface Mounted bars (Ceroni et al., 2012) [70].



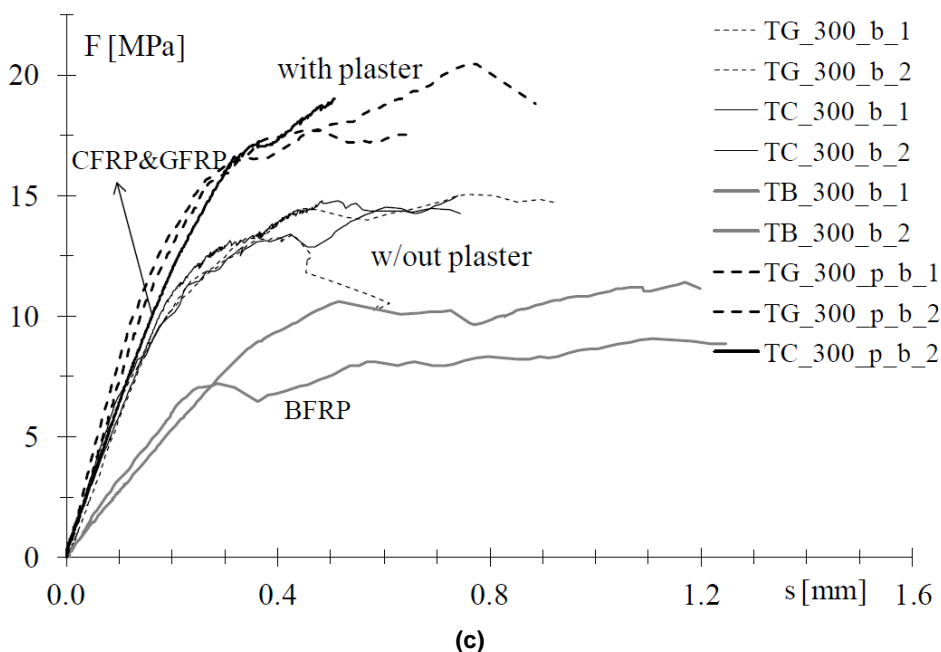
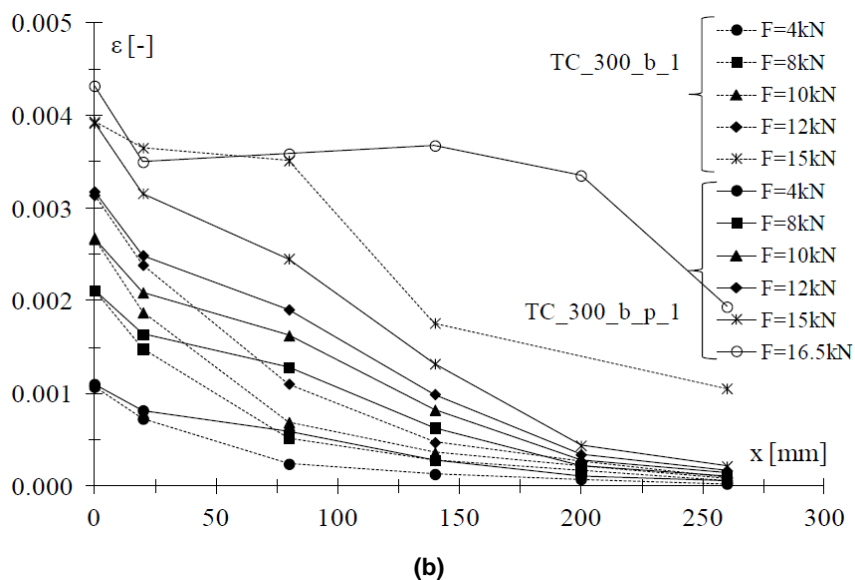


Figure 6.5. Effect of plastering in pull-push bond tests: (a) strain distributions for specimens made of T1 with carbon fibers; (b) strain distributions in specimens made of tuff T2 with carbon fibers; (c) global load-displacement curves for specimens made of T2 with carbon, glass and basalt fibers with and without plaster.

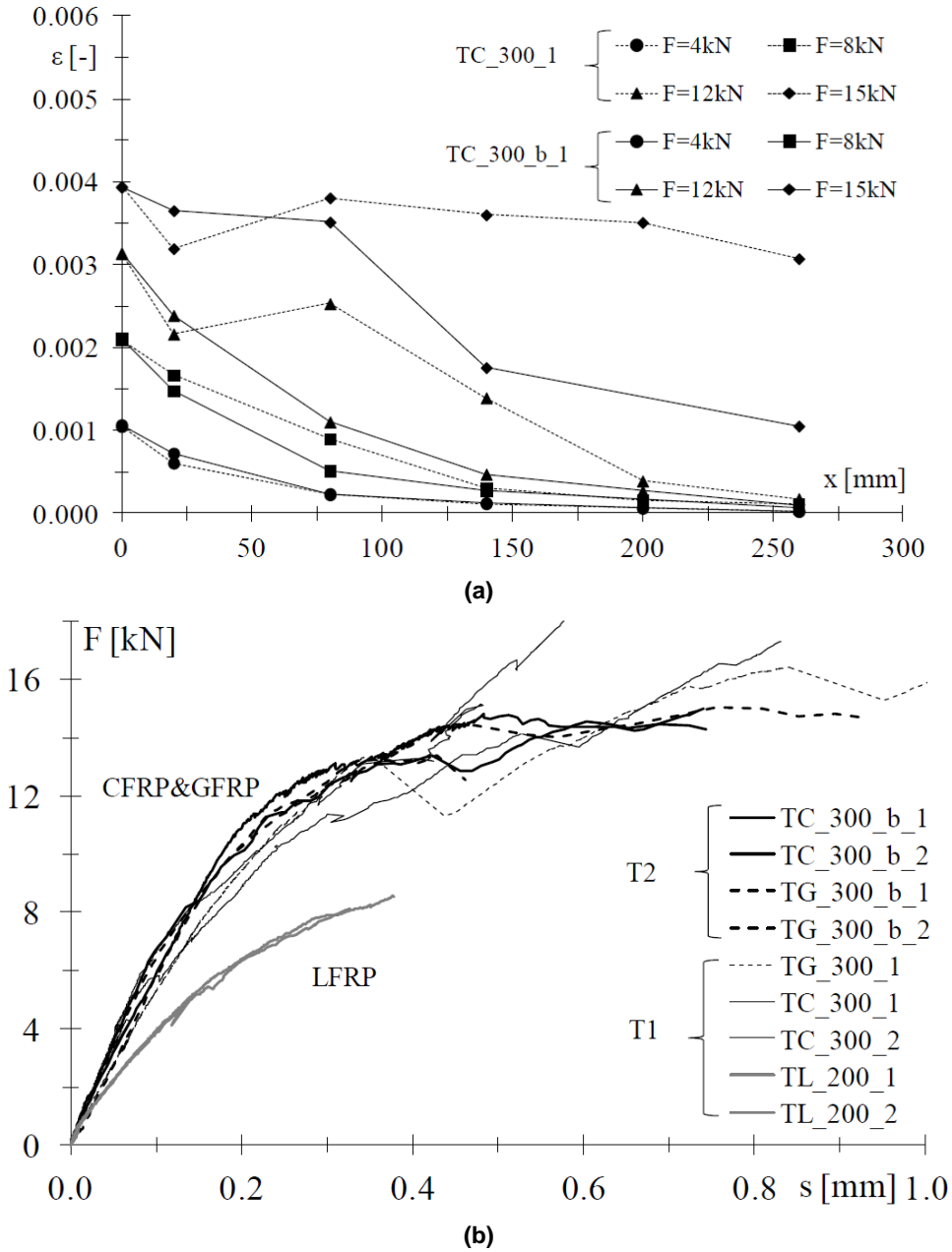


Figure 6.6. Effect of tuff strength (T1 and T2) on the strain distribution in pull-push bond tests with carbon and glass fibers: (a) strain profiles for specimens with carbon fibers; (b) global load-displacement curves for specimens with carbon, glass and linen.

In Figure 6.6(a) the strain profiles for specimens made of tuff T1 and T2 with carbon fibres are reported; the comparison does not evidence significant differences at the same load levels, unless the lower debonding load. This should indicate that the slope of the first branch of the interface bond law could be the same. The global experimental load-displacement curves graphed in Figure 6.6(b) confirm this assumption both for specimens bonded with carbon and glass fibres. In Figure 6.6(b) the global load-displacement curves of two specimens bonded with linen fibres are also graphed; the comparison with the curves of the specimens made of the same tuff T1 and bonded with carbon and glass fibres evidences, as already noted for the basalt fibres, the lower stiffness of the bond law in the case of linen.

6.3.4 Shear stress distributions

In Figure 6.7(a) and b the distribution of shear stresses is graphed for two specimens made of tuff T2: one bonded with carbon (Figure 6.7(a)) and one with basalt fibres (Figure 6.7(b)), both failed for debonding. In both cases it is interesting to notice that approaching the failure load, the shear stress at the loaded end decreases until becomes zero and the peak stress moves towards the undamaged bonded length (Figure 6.7(b)).

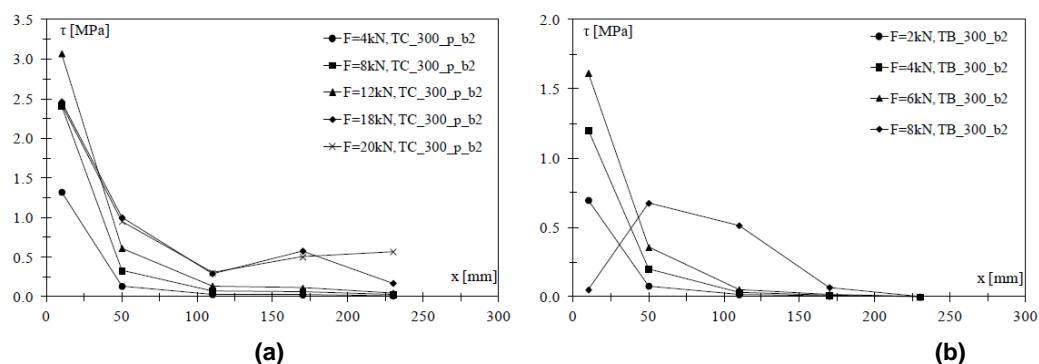


Figure 6.7. Shear stress distributions: (a) specimen made of tuff T2 with CFRP and plaster; (b) specimen made of tuff T2 with BFRP.

In Figure 6.8(a) the shear stress distributions of specimens bonded with glass fibres and made of tuff T2 are graphed with and without the plaster layer; the comparison shows again that the plastering enhances the debonding load. For the specimens without the plaster, the shear stress at the loaded end reduces and becomes zero (i.e. this means the bond law has been completely developed at the loaded end), indeed, at about 12 kN (90% of F_{max}), while for the plastered specimens the same phenomenon occurs at higher loads (about 18 kN, 90% of F_{max}).

Similarly, in Figure 6.8(b) the shear stress distributions are graphed for the specimens with glass fibres without plastering and made of tuff T1 and T2 in order to check the effect of the different strength of the stone; the comparison shows again that for the specimens made of tuff with lower strength (T2) the peak shear stress is achieved at a lower load than the specimens made of higher strength tuff (about 8 kN = 60% F_{max} vs. 12 kN = 70% F_{max}). Moreover, after the shear stress becomes zero at the loaded end, the peak stress moves towards the undamaged bonded length.

These results are significant of bond laws characterized by higher bond strength as the tensile strength of the support increases and when a plaster layer is applied. Moreover, the effects of these two parameters on the shape of the bond law, especially for the softening branch, should be included in the assessment of theoretical bond laws and provisions for the debonding load.

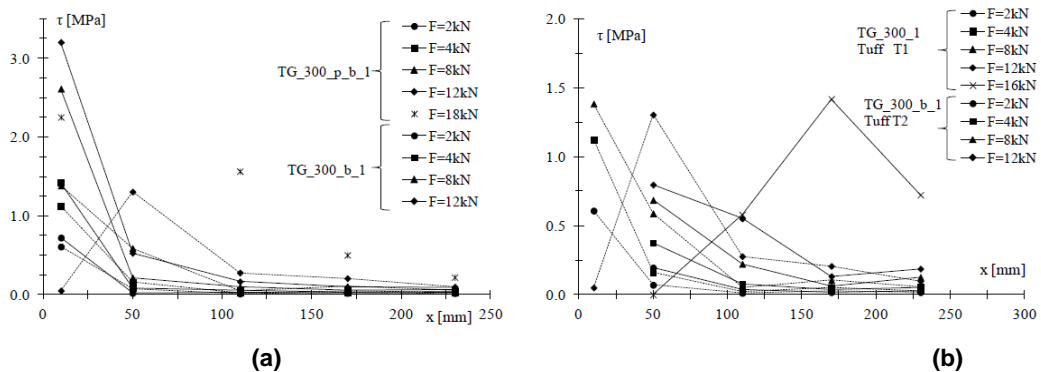


Figure 6.8. Shear stress distributions: (a) Effect of plastering in specimens made of tuff T2 and bonded with glass fibres; (b) Effect of tuff strength (T1 and T2) in specimens bonded with glass fibres and without plastering.

6.4 CONCLUSIVE REMARKS

The results of an experimental programme concerning bond tests on masonry blocks made of a volcanic natural stone named yellow tuff and externally bonded with different FRP fabrics (glass, carbon, linen, and basalt fibres). The features and the phenomena evidenced in the experimental tests and the examination procedure can be considered valid for all types of masonry supports; conversely, the numerical results are clearly specific of the stone considered, but are, however, useful to collect information aimed to design retrofitting interventions for numerous monumental buildings made of such a material in Italy.

The pull-push scheme appeared to be the most suitable set-up for carrying out bond tests on masonry elements and achieve the full bond strength, if an adequate bonded length is assumed (not lower than 250-300 mm). The experimental results obtained in the pull-push set-up programme are discussed in detail in terms of failure mode and loads, focussing the attention on the effect of the bonded length, the plaster layer, the masonry strength, and the axial stiffness of the FRP reinforcement. In particular, the results evidenced that: 1) a bonded length of 300 mm seems to be sufficient to develop the full bond strength for the examined support; 2) when the plaster layer is not applied, the debonding load reduces of about 15% for the more resistant tuff (type T1) and of about 25% in the case of lower compressive strength (type T2, being the strength of T1 about 45% greater than strength of T2); 3) no relevant difference was observed in the results of specimens bonded with carbon and glass fibres having similar axial stiffness; 4) the different axial stiffness of the fibres influences the slope of the load-displacement curves (i.e. basalt and linen compared with glass and carbon fibres); 5) the reduction of the compressive strength of the tuff of about 45% led to a reduction of the debonding load of about 8% and 18% for specimens with and without plastering, respectively.

The local behaviour was examined in terms of distributions of axial strain and shear stress along the external reinforcement, both based on the experimental measures of strains. They confirm the results previously enounced and evidence that, as the debonding process starts, the shear stress at the loaded end reduces

progressively and the peak moves towards the undamaged bonded length. Detailed numerical analyses need to assess the local behaviour in terms of interface bond law.

Finally, it can be concluded that the interface bond law, τ - s , and the debonding load, if suitable set-ups and bonded lengths are adopted for achieve the full bond strength, depend on the masonry strength, including also the effect of a plastering, the mechanical properties of the FRP reinforcement, i.e. the axial stiffness, and the presence of end anchoring devices, which, clearly, are as more effective as the bonded length are lower.

7 BEHAVIOUR AND MODELLING OF MASONRY

It is known that masonry is a material whose behaviour differs depending on the considered direction, due to the fact that the mortar joints surrounding masonry units, acting as planes of weakness, modify the mechanical properties and introduce a level of anisotropy. The characteristics of masonry should be reflected in the modelling technique adopted to study a particular mechanical aspect of such material, which also determines the level of accuracy of the model. This aspect clarifies that all modelling strategies are useful for understanding of masonry structures behaviour with different scale of observation.

Figure 7.1 illustrates two different techniques for material description each of which has his own characteristics and field of application; in particular one can refer either to a micro-modelling or to a macro-modelling strategy (Lourenço, 2004) [71]. Micro-modelling is generally applied to small elements or portion of structures which require a more detailed representation, allowing the investigation of localized phenomena, while macro-modelling is employed for global modelling of entire structures in which the dimensions of the elements are large enough to neglect any unevenness in the stress distribution along the element. The characteristics of the macro-models and the small computational effort involved allow using them in cases that require fast analysis with a not very high level of detail.

Possible levels of details in masonry modelling are referred to as:

- Detailed micro-modelling: blocks and mortar joints are described as continuous elements, while the unit/mortar interface is described through discontinuous elements.
- Simplified micro-modelling: blocks are described as continuous elements, while the mortar joints and the unit/mortar interface behaviour is concentrated

in discontinuous elements.

- Macro-modelling: blocks, mortar joints and unit/mortar interface are smeared in a continuous element and material.

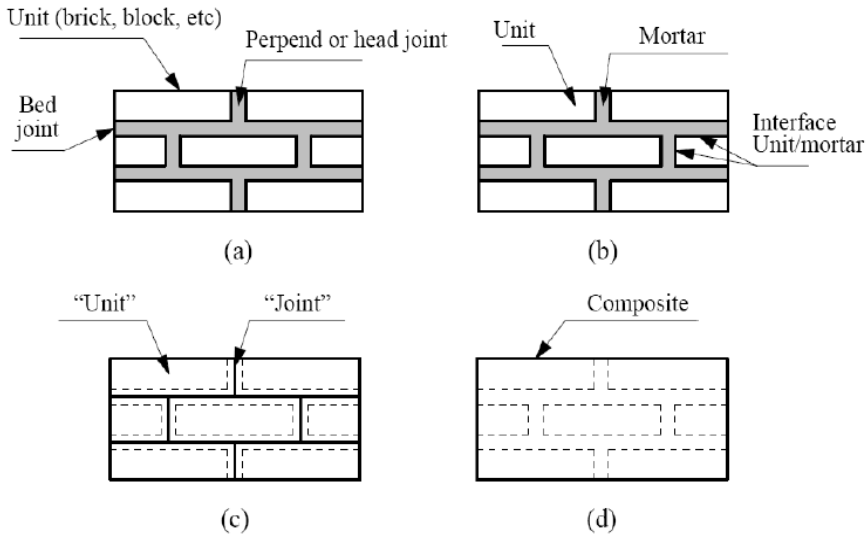


Figure 7.1. Modelling techniques for masonry: masonry element (a); detailed micro-modelling (b); simplified micro modelling (c); macro-modelling (d) [71].

In the first type of approach, the Young modulus, the Poisson's coefficient and, optionally, the inelastic properties of units and mortar are taken into account. The interface between units and mortar joints represents a potential surface of cracking or sliding, with an reduced initial stiffness in order to avoid the interpenetration of continuous material. This allow the combined action between units, mortar and interface to be studied, at a very detailed level, as it was under the effect of a magnifying glass. In the second approach, each joint, composed by mortar and two unit/mortar interfaces, is concentrated in an 'average' interface, while the blocks are extended in order to keep unchanged the geometry. Masonry is, in this case, considered as a set of elastic blocks, connected between potential cracking/sliding surfaces along the joints. However, such modelling strategy implies the losing of accuracy since the Poisson's effect of mortar is not accounted for in the model. Finally, the third approach makes no distinction between different blocks and mortar

joints, but considers the masonry as a anisotropic continuous and homogeneous material. Clearly, macro-modelling is mainly oriented to practical applications thank to the restrained calculation time and an easier mesh definition. Such type of modelling should be considered when a compromise between accuracy and efficiency is necessary. A detailed modelling of masonry structures asks for a comprehensive definition of the materials. Anyway, masonry properties are influenced by a huge number of factors, such as the blocks and mortar characteristics, the width and configuration of mortar joints, the dimensions and anisotropy of blocks, the quality of workmanship, the environmental exposition conditions.

Due to such diversity and variability, the research in the field of masonry started to address its field of investigation towards complex numerical models only recently, in contrast to traditional design rules based on experience. Moreover, the production of experimental data, necessary for the calibration of numerical models, met some difficulties due to the wide variety of materials and possible test configurations. Also, only the values of strength are commonly considered, without any regard for deformation parameters; in fact, the literature there is a lack in terms of information about the post-peak softening behaviour of the material.

In literature works it is possible to find analyses carried out on structural masonry models implemented with different levels of accuracy and precision. In the following, the mechanical characteristics of masonry are examined and a review of such models is made with particular concern to a micro-modelling approach, when discontinuous structural models are employed, and a macro-modelling approach, when finite element continuous structural models are used.

7.1 MECHANICAL CHARACTERIZATION OF MASONRY AND ITS CONSTITUTIVE MATERIALS

Properties and behaviour of a masonry element strongly depends on the properties of it constitutive materials. In order to determine these parameters, a number of tests can be performed in order to obtain values such as the compressive, tensile and shear strength of both blocks and mortar. Compressive tests are easy to

perform and give a good estimation of the global quality of employed materials, while tests for the analysis of the uniaxial post-peak behaviour, and of the bi-axial behaviour of the blocks are less diffuse in the literature, as it is also for tests under cyclic loads. For this reason, it is difficult to correlate the tensile strength of blocks to their compressive strength, since different types of material, different production systems and different methods for production of holes are available.

Moreover, not so many tests on biaxial behaviour of blocks are reported in the literature. For what concerns the mortar, the tensile strength is generally obtained from three-points bending tests, while the compressive strength is obtained from tests performed on the half specimens resulting from bending tests. Another important aspect of quasi-brittle materials, such as the clay, rocks, mortar, concrete is their softening behaviour. It consists of the gradual loss of mechanical resistance after the strength of the material has been reached, while the deformation imposed to the specimen increases. Such a behaviour is due to progressive internal cracking of elements, caused by the heterogeneity of material, the presence of voids and defects, the different phases in the building process. In fact, since before the application of loads, there is the presence of micro-cracks both in the blocks and in the mortar, also due to the shrinkage effect during the curing of materials.

Once the peak load is reached, an acceleration in the formation of cracks and the opening of macro-cracks is registered. In a deformation controlled tests, the formation of macro-cracks leads to the softening behaviour and to the localization of cracks in a small area, while the remaining part of the specimen unloads. During a compressive tests there is a significant dependence of the constitutive behaviour on the constrain conditions and dimensions of specimens. In the tensile test, the softening behaviour was well identified by the model by (Hordijk, 1991) [72], while the shear crisis is described by the friction model by Coulomb. The inelastic behaviour of the material can be defined by means of the tensile and compressive fracture energy G_f and G_c , respectively calculated as the integral of $\sigma - \epsilon$ diagrams. The second mode fracture energy G_f^{II} is calculated as the integral of the $\tau - \delta$ diagram, obtained from a shear tests on a masonry specimen, as the II mode represents the failure mechanism typical of panels subjected to shear loading, in which a sliding at the interface

between the horizontal mortar joint, in which a micro-crack generates, and the block element.

7.1.1 Uniaxial compressive behaviour

In order to obtain a good estimation of the actual compressive strength of a masonry prism, a test according to RILEM, Figure 7.2(a), can be performed, even though such test configuration is not so diffuse because it is not so cheap if compared to the classical compressive tests on cylindrical or cubic specimens employed in case of characterization of concrete.

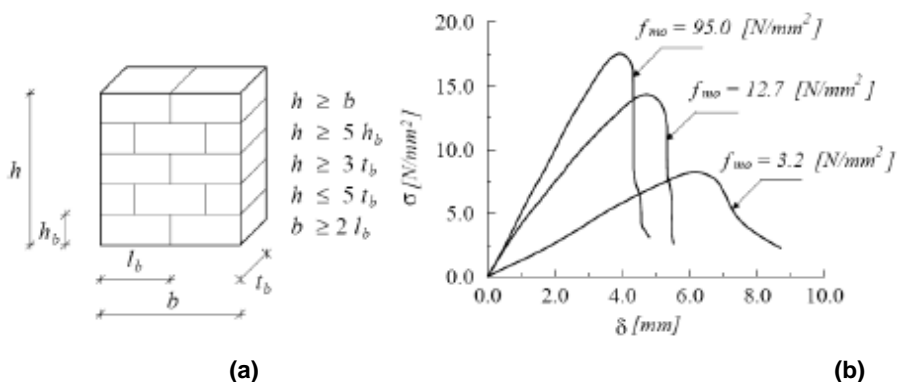


Figure 7.2. Specimen for RILEM test and compressive constitutive diagram.

In Figure 7.2(b), some examples of load-displacement diagram obtained on prismatic specimens with dimensions of 500 x 250 x 600 mm³ are illustrated. The value of fracture energy G_c resulting from the tests is quite high since the specimen is quite big. The compressive behaviour of masonry in the direction parallel to horizontal joints is less investigated. Such an anisotropic behaviour with respect to the compressive strength can be taken into account using a ratio between strengths, normal and parallel to horizontal joints, varying between 0.2 and 0.8 (Hoffman and Shubert, 1994) [73].

7.1.2 Uniaxial tensile behaviour

The low tensile strength of masonry is due to the low value of bond between mortar bed joints and masonry blocks. In masonry made with blocks with low value of tensile strength and high value of bond strength, the collapse can occur when the tensile strength of the blocks is reached and, as a first approximation, the strength of masonry can be assumed equal to the strength of the block. This is evident from the study carried out by (Bakes, 1985) [74], where a specimen made by four layers of blocks is tested under tensile load, as illustrated in Figure 7.3.

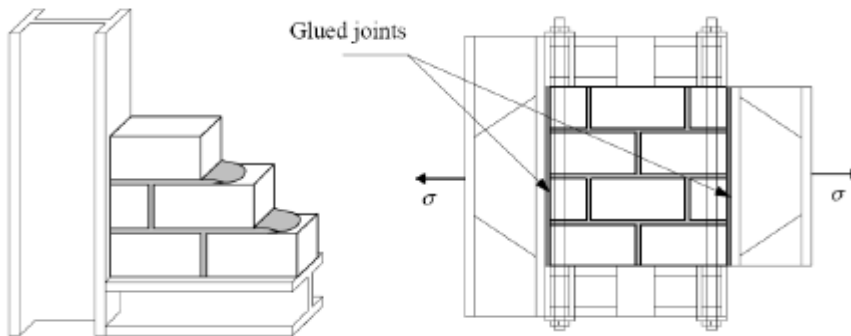


Figure 7.3. Set-up for tensile test on masonry.

The load is applied by means of steel plates connected at the two ends of the specimen by means of a special glue. The whole load-displacement curve is obtained under displacement control. Two different types of collapse are possible, depending on the relative strength between mortar joints and blocks, as depicted in Figure 7.4.

In the first type of crisis, cracks follow horizontal and vertical mortar joints. A typical stress-displacement diagram shows a residual plateau when the strain increases. The post-peak response of the specimen is governed by the I mode fracture energy of head joints and by the II mode fracture energy of bed joints. In the second type of crisis, cracks are almost vertical through the blocks and head joints. A typical stress-displacement diagram shows a progressive softening of stress. The post-peak response is, in this case, governed by the I mode fracture energy of blocks and head joints.

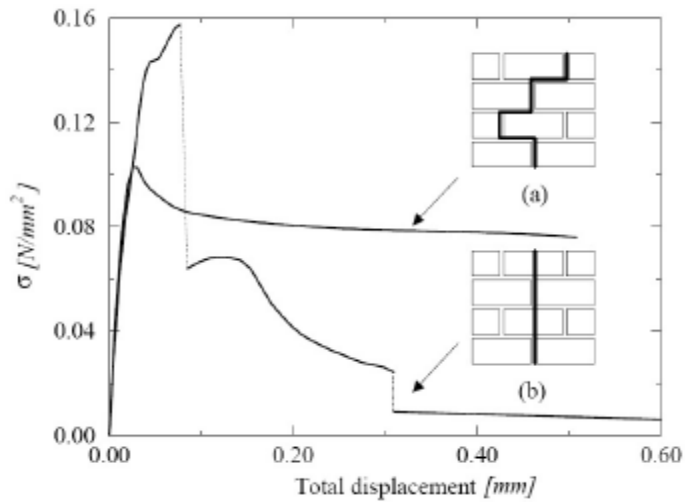


Figure 7.4. Load-displacement curve from tensile test on masonry.

7.1.3 Biaxial behaviour

Behaviour of masonry under biaxial stress states cannot be comprehensively described by means of a biaxial constitutive law. The influence of a biaxial stress state was investigated till the peak of stress in order to obtain an envelope curve of the biaxial law, which cannot be described in terms of principal stresses only, because of the anisotropy of the material. Therefore, the biaxial behaviour should be described by means of the whole stress vector with respect to a reference system of the material. In Figure 7.5, the experimental results of an experimental campaign carried out on masonry elements subjected to biaxial load varying the rotation angle is reported by (Page, 1981) [75] and (Page, 1983) [76].

In general, if the uniaxial tensile loading condition is considered, the crisis is attained through cracking and sliding along mortar joints. The influence of a lateral tensile load is not well known, because of the lack of experimental data. The presence of a lateral compressive load, reduces the tensile strength because induces a damage in the composite material, a sliding in the joints and micro-cracking in the blocks. In the cases of tensile/compressive loads, the crisis is due to cracking, sliding

of joints, or a combination of both mechanisms. Similar types of crisis are in the case of uniaxial compression. In case of uniaxial compression, the crisis is typically associated to the splitting of the central portion of the specimen, in a plane parallel to its free surface, depending on the orientation of principal stresses. For stress ratios much lower or much higher than one, the rotation angle plays a fundamental role and the crisis is due to a combined mechanism, involving both the crisis of mortar joints and the lateral splitting. The increment in terms of compressive strength under compressive biaxial loads can be explained by the friction at the interfaces between mortar and blocks. It is also noticed, however, that diagrams such as the ones reported in Figure 7.5 cannot be valid for any type of masonry, since if the characteristics of materials, blocks and mortar, and the assembly of the composite material are changed, different behaviours and collapse modality will be obtained.

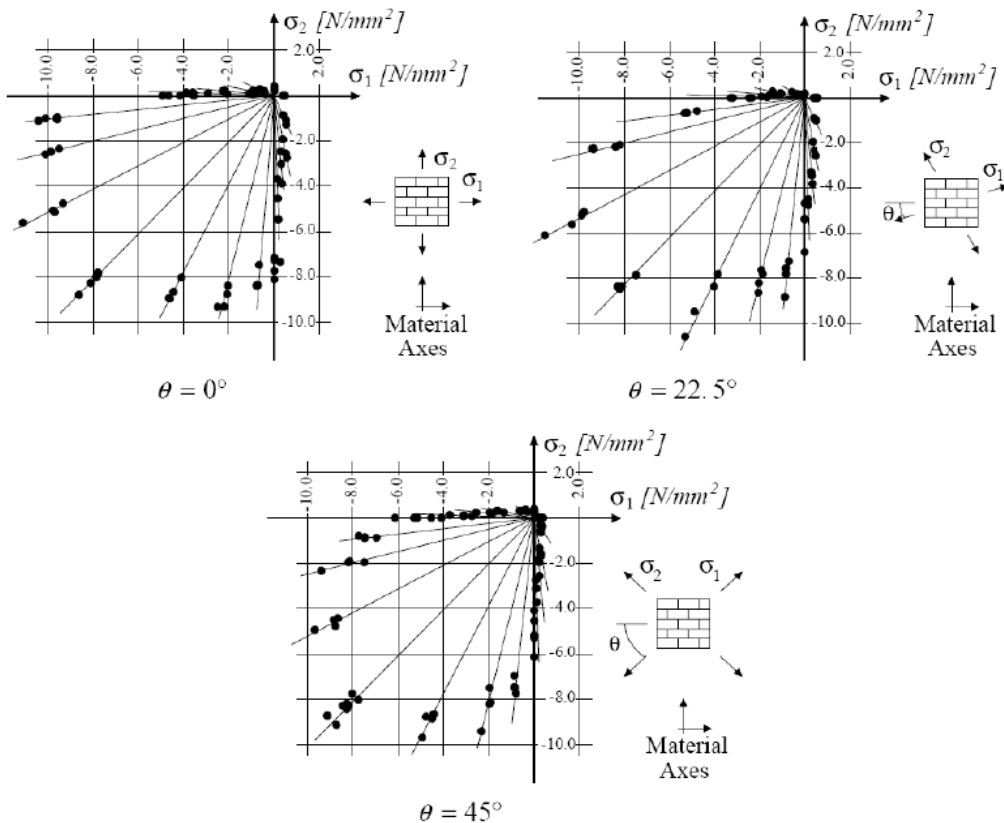


Figure 7.5. Biaxial strength of clay brick masonry.

7.2 MICRO-MODELLING

Discontinuous modelling produces micro-models which can be used to study the behaviour of masonry at a more detailed level and useful to calibrate some physical or mechanical material parameters. The weakness introduced by the presence of the horizontal and vertical mortar joints plays an important role in the anisotropic behaviour of the masonry element, making necessary a more detailed material description which can be able to directly take into account the presence of units, joints and interface behaviour.

The main advantage in the employment of micro-models consists in the possibility to describe the behaviour of the element considering all the different collapse mechanisms. In a simplified micro-modelling approach it is possible to employ interface elements in order to individuate and describe cracking, crushing and sliding planes. This is possible through the use of composite interface models, which are able to include a tensile *cut-off* for the I mode failure, a *friction model* according to Coulomb for the II mode failure, and a *cap mode* for the compressive failure, as described in Figure 7.6.

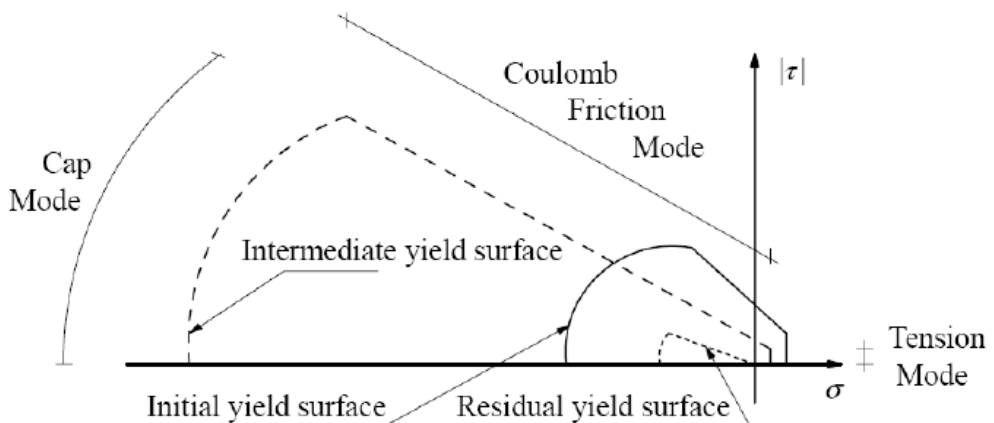


Figure 7.6. Composite interface model.

However, considering such surfaces as the only possible planes where all the plasticity phenomena are concentrated lead to a quite rigid modelling, which is anyway rather strong and stable from the numerical point of view, and which is able to follow the loading behaviour of a structure completely, till the total decay of stiffness. The limited relevance given to the numerical modelling of masonry is also confirmed by the scarcity of such type of models, even though in the last decades some attempts in the employment of interface elements was done. Nevertheless, not all the possible softening phenomena occurring after cracking and all the possible failure mechanisms are considered by such type of simplified modelling. In fact, an accurate micro-modelling strategy must include all the main failure mechanisms involved in masonry behaviour (Figure 7.7), taking into account cracking of joints (a), sliding of blocks over head/bed joints, due to low normal compressive stress (b), direct tensile cracking of blocks (c), vertical or diagonal cracking of units, when the level of normal stress does not activate friction phenomena (d), crushing of masonry (e), (Lourenço and Rots, 1997) [77].

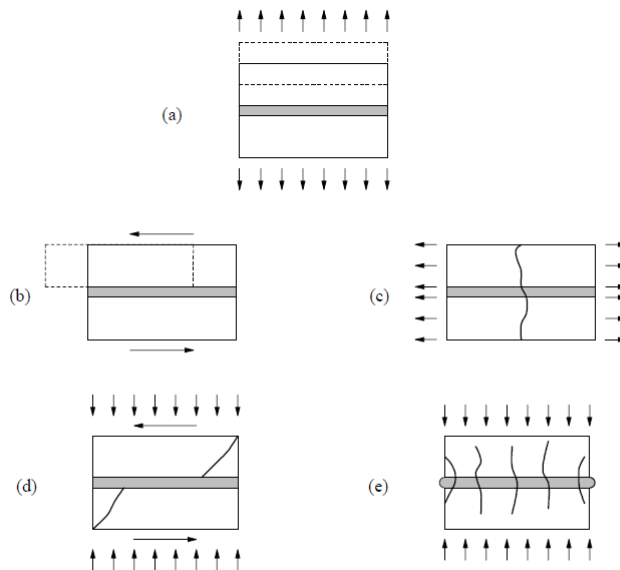


Figure 7.7. Masonry failure mechanism: joint cracking (a); joint sliding (b); unit vertical cracking (c); unit diagonal cracking (d); masonry crushing (e).

Analyses based on a discontinuous model of masonry are indicated for small elements or portions of structures, because of the high number of material parameters to be known, with particular focus on the non-linear properties of the unit-joint interface. Attempts over the years to model masonry non-linearity via interface elements are very few and neither all failure mechanisms nor the softening behaviour after cracking are comprehensively taken into account, limiting the applicability of such model to the pre-peak field.

Different modelling strategies can be pursued taking into account a different level of detail and ways to represent the non-linear behaviour, which can be concentrated in the mortar joints and in potential vertical cracks in the centre of the block. It is clear that failure mechanisms (a) and (b) involve the joints, (c) is a mechanism involving the units, (d) and (e) are combined mechanisms involving both units and joints. In an interface model, the damage is lumped in relatively weak joints and, if necessary, in potential tensional cracks in the blocks located in the vertical mid plane of every unit, as described by Figure 7.8.

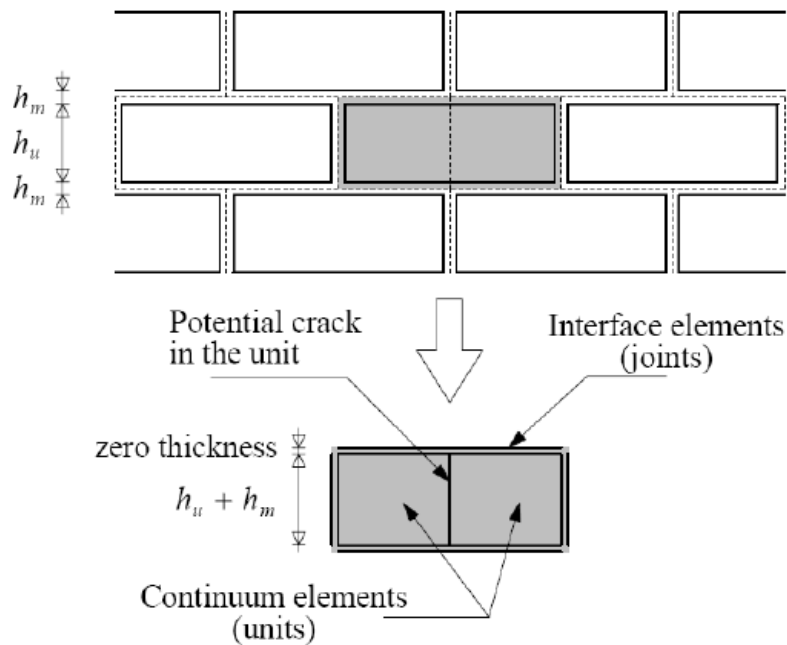


Figure 7.8. Interface model and position of interfaces.

Such potential cracks allow the reproduction of a 'jump' from a head joint to another one, which is a typical behaviour of masonry; consequently, the yield criterion of the interface must include all previously described mechanisms, apart from the uniaxial tensile cracking of the block. The interface elements allow to introduce some discontinuities in the displacement field and their behaviour is described through a law between the tensile stress and the relative displacement at the interface. The linear elastic law between can be expressed by means of the classical relation:

$$\sigma = D \cdot \varepsilon$$

where, for a bidimensional configuration:

$$\sigma = \{\sigma, \tau\}^T$$

$$D = \text{diag}\{k_n, k_s\}$$

$$\varepsilon = \{\Delta u_n, \Delta u_s\}^T$$

where n and s are, respectively, the normal and tangential component of the stress. The elastic stiffness matrix D can be obtained from the properties of two components of masonry (blocks and mortar) and from the thickness of joints.

The Figure 7.8 illustrates that, since the interface elements have zero thickness, it is necessary that the dimensions of blocks are extended in order to incorporate the joints thickness h_m in both directions. As a result, the elastic properties of the extended blocks and the interface joints must be adequately corrected in order to get correct results. A possible method is based on the reduction of the block stiffness and the use of interface elements with a very low stiffness, in order to avoid interpenetration of continuous elements. Considering the relative dimensions of masonry constituents, an alternative is the assumption that the elastic properties of the blocks are kept unchanged and to consider as components of the stiffness matrix D the following values:

$$k_n = \frac{E_u E_m}{h_m(E_u - E_m)}; k_s = \frac{G_u G_m}{h_m(G_u - G_m)};$$

where E_u and E_m are the Young moduli and G_u and G_m are the shear stiffness moduli for blocks and mortar, respectively; h_m is the actual joint thickness.

The values of stiffness obtained from previous formulations do not lead to a penalizing approach, implying that the overlapping effect of consecutive blocks under compressive loads is appreciable. However, this is an intrinsic aspect of the formulation of interface elements and it is independent from the value of normal stiffness, even though it is clear that the lower the stiffness is, the higher is the overlapping effect. The interface model include a *cap mode* for compression, in which the inelastic compressive behaviour of masonry is concentrated. This is a phenomenologic representation of the masonry crushing, since actually the process of compression failure is related to the characteristics of the microstructure of blocks and mortar, and of their interaction; in the model the failure mechanism is represented in a way that the constitutive stress-strain behaviour can be reproduced.

Discontinuous modelling analysis can be carried out using finite elements (Lofti and Shing, 1994) [78], (Lourenço and Rots, 1997) [77], discrete elements (Lemos, 1998) [79] or limit analysis (Baggio and Trovalusci, 1998) [80], (Orduña, 2003) [81].

A finite element-based modelling technique allow to describe potential unit cracks, mortar joint cracks, slip and crushing surfaces through interface elements, able to represent the material non-linearity. In particular, a numerical implementation of this simplified modelling strategy is presented in (Lourenço, 1994) [82], which has been assumed that all the inelastic phenomena occur in the interface elements; also, such type of models are able to follow the entire load path of a structure until total degradation of stiffness. This is a case of a composite interface model defined by a tension cut-off failure, a Coulomb friction envelope for shear failure and a cap mode for compressive failure, described on the basis of the modern plasticity concepts and, unlike from previous cases, taking into account the softening behaviour after crack slip.

While referring to discrete elements, they can be rigid or deformable elements connected between their vertexes, sides or faces and allow considering potential interpenetration and a real or adjusted damping coefficient. The contacts between elements are not fixed and during the deformation process there can be the formation of new points of connection. Discrete elements permit to grasp the behaviour of large displacement systems and each block has the advantage to be mesh independent, but a correct modelling of the structure require a high number of contact points at the interfaces.

7.3 MACRO-MODELLING AND HOMOGENIZATION TECHNIQUES

The use of macro-models in the analysis of masonry structures, made by a high number of blocks and joints, is based on the definition of a law between average stresses and strains. The presence of more than one constituent element in a material can be solved by means of the hypothesis of homogeneity only if the discontinuity, or the presence of a phase with respect to the other one, is negligible according to the assumed level of detail. Another condition that is necessary to be verified in order to apply this approach is that the ratio between the stiffness of different constituents is close to the unity. However, it is clear that it is not always simple or possible to estimate such stiffness ratio, as it is the case of materials characterized by the presence of a stiff phase and a cracked phase. The consideration at the base of this approach is, in any case, important since it makes clear that, from the practical standpoint, it can be convenient to look at a certain material as a homogeneous material, provided that the structural dimensions are bigger enough compared to the type of inhomogeneity.

Masonry is a composite material made by blocks and mortar, usually arranged in a periodic way. The knowledge of the actual values of mechanical properties and of the actual geometry of both units and mortar joints allow the mechanical behaviour of the structure to be numerically reproduced. Nevertheless, a basic limitation in this operation is that even a simplified micro-modelling is unfeasible in the case of a real masonry construction, that is composed by a large number of

blocks. An alternative is thus represented by the possibility to describe the behaviour of the material in terms of average stresses and average strains, assuming the masonry as a homogeneous material.

Continuous modelling is a feasible approach to evaluate the behaviour of complete masonry structures, in which the approximation to consider a homogeneous material, described through a relation between average values of stresses and strains, is reasonable. The study of masonry structures through continuous numerical models is complex mainly because the available experimental data are often lacking and it is not always possible to describe comprehensively the mechanical behaviour of the material. Furthermore, in non-linear analysis the knowledge of the post-peak phase of material plays a fundamental role in the reliability of the analysis results. These difficulties are further stressed by the complex anisotropic behaviour of masonry. For a proper description of anisotropic quasi-brittle materials behaviour different criteria for tension and compression should be formulated, with the implementation of plasticity concepts including different hardening and softening laws along each material axis.

Many theoretical anisotropic plasticity models are available (Hill, 1948) [83], (Hoffman, 1967) [84], (Tsai and Wu, 1971) [85], some of which successively have been numerically implemented in the works of (De Borst and Feenstra, 1990) [86], (Shellekens and De Borst, 1990) [87], considering an elastic-perfectly-plastic Hill yield criterion and an elastic-perfectly-plastic Hoffman yield criterion, respectively. Recently, attempts are given to simulate the hardening behaviour, but there are very poor numerical implementation and numerical testing data.

A step forward in the formulation of anisotropic models was done by establishing a composite yield criterion to describe anisotropic materials subjected to plane stress (Lourenço, 2000) [88]. In particular, tension and compression were treated as two independent yield criteria, with reference to different mechanisms of crisis. In particular, traditional formulations for isotropic quasi-brittle materials have been considered and extended to describe the orthotropic behaviour. The formulations of isotropic quasi-brittle materials generally consider different inelastic criteria for tension and compression, namely the Drucker-Prager and Rankine criteria, also used for concrete. To model the behaviour of orthotropic materials as masonry, a

Hill type yield criterion for compression and a Rankine type yield criterion for tension can be considered.

Other simplified modelling techniques (Sacco, 2009) [89], (Avossa et al., 2009) [90] are based on the description of the plastic and cracked material behaviour using a Drucker-Prager plasticity model, which is able to simulate the typical friction behaviour of masonry, or a concrete-type model. In the concrete-type model the elastic behaviour of material can be bounded by a surface, as that proposed by William and Warnke for ceramic materials, associated to a smeared cracking model for tension behaviour and a crushing behaviour for compression. A softening law and a tension cut-off for tensile behaviour are also defined.

A certain importance in the modelling of anisotropic and non-homogeneous materials is played by the homogenization techniques (Anthoine, 1997) [91], (Lourenço et al., 2006) [92]. In (Lourenço et al., 2006) [92] a review of different homogenization techniques of masonry components is presented. In particular, in the case of masonry brick walls modelling, such methodology can help to describe the material with a medium-high level of accuracy, keeping a certain degree of simplicity in the characteristics of the finite element model. The regularity of the assemblage and the recurring of a basic cell are the basic requirements the masonry element should have for the application of a homogenization procedure. Through this techniques it is possible to obtain an anisotropic constitutive law starting from constitutive law and geometry of the materials composing the masonry, without necessarily knowing its global characteristics. These techniques lead to the definition of a quite accurate macro-model starting from the micro-model of masonry, even if the global characteristics are not completely known.

7.3.1 Elasto-plastic homogenization of layered materials

The homogenization techniques are becoming more and more diffuse among the scientific community as a method of investigation and analysis of masonry structures. In fact, a method which can give the possibility to set global constitutive laws in terms of average stress and strains starting from constitutive behaviour of

single components represents an important step forward in the modelling of masonry. It follows that a modification of the geometry of components, if required, does not need the employment of a different mechanical model, or the need for costly experimental tests. This is a very relevant aspect if the fact that masonry can be built considering a very wide variety of arrangements of blocks and mortar. On the other hand, the knowledge of constitutive materials and their mechanical properties represents an important issue, considering the intrinsic difficulties in their direct evaluation, often requiring the use of indirect methodologies. In general, the homogenization theory of media with periodical geometric arrangement and periodical distribution of mechanical parameters is applied with reference to an elementary cell.

The rigorous application of this theory to the analysis of non-linear behaviour of a complex elementary masonry cell implies the solution of the problem for all the possible macroscopic loading conditions, since it is not possible to apply the principle of superposition of effects. Thus, the comprehensive definition of constitutive laws of the homogenized material require a very high number of calculations. Consequently, since the aim of the analysis is mainly the study of large structural systems, these techniques have been employed with some approximations. Generally, the homogenization is carried out in two steps, with the introduction of mortar joints. In this case, masonry can be seen as a layered material, as depicted in Figure 7.9, in a way to significantly simplify the problem.

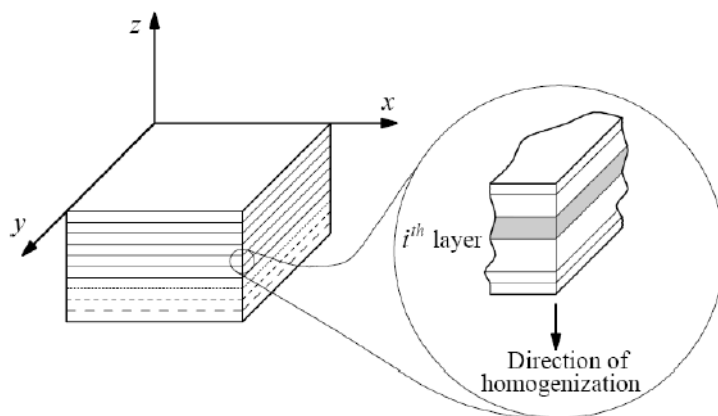


Figure 7.9. Layered composite material with periodical characteristics.

Clearly, the elementary masonry cell cannot have a layered structure, but several authors proposed an approximated approach based on two homogenization steps under the hypothesis of layered material, as illustrated in Figure 7.10.

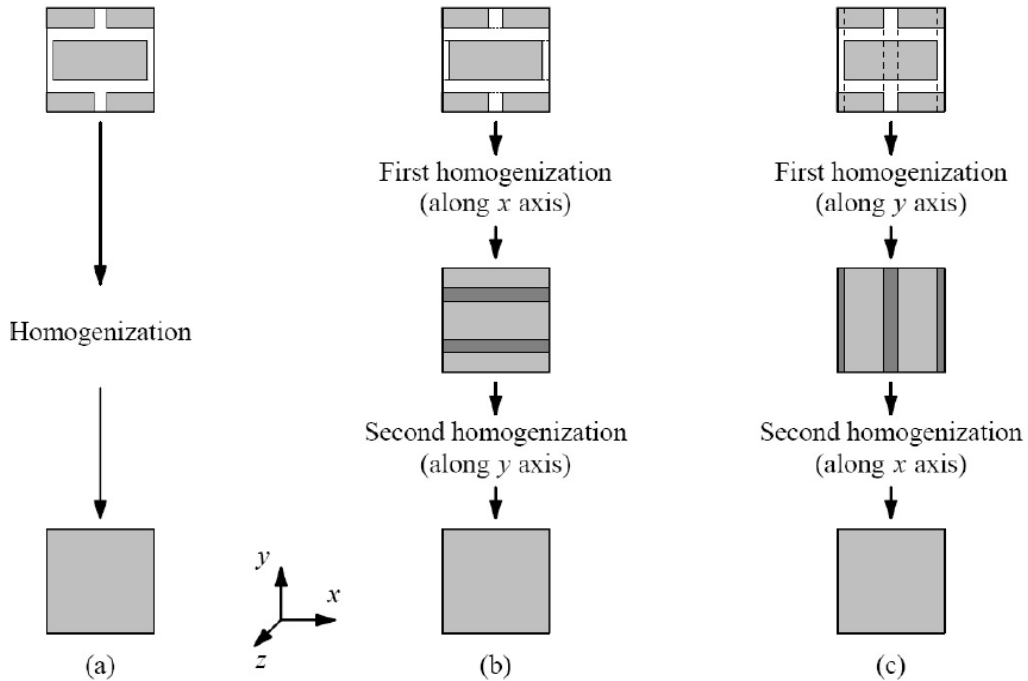


Figure 7.10. Two-steps homogenization procedure usually adopted for masonry structures.

This methodology consists of a first step, in which the horizontal homogenization is performed, involving blocks and vertical joints; and a second step the vertical homogenization is made, involving the material homogenized in the first step and the horizontal joints, Figure 7.10(b). The opposite methodology, instead, performs in the first step the vertical homogenization, involving blocks and vertical joints and horizontal joints, while in the second step performs a horizontal homogenization, with the material homogenized in the first step, Figure 7.10(c). In general, the first presented approach is referred to as *homogenization x-y*, while the second approach is referred to as *homogenization y-x*. It is worth to notice that final results can be different, with respect to the employed approach, highlighting that this does not result in an objective procedure, even in the case of linear elastic analysis.

In presence of non-linearity this behaviour is emphasized. In the last case some attention should be placed, if the non-linear behaviour is included in the model, mainly regarding the softening behaviour where some mistakes can be encountered, due to the non-layered structure of masonry and to the high difference in the stiffness of blocks and mortar. In the softening behaviour should be also included the dilatancy effect, because if it is absent unrealistic solutions are sometimes found.

The main advantage in the use of homogenization techniques concerns the reproducibility of the model. Once the properties of constitutive materials have been defined, the behaviour of the composite material can be obtained without the need for a high quantity of experimental data. Consequently, the change in the geometry, such as for example the dimensions of blocks or the thickness of joints, or their configuration, can be handle just in a numerical way. Anyway, at the present state of knowledge, it is necessary to keep on carrying out the experimental research with the aim of confirm the numerical results. The base for a correct application of the homogenization methodologies is represented by the existence and availability of results from tests carried out under displacement control and with different level of detail. Only through the comparison between numerical results and experimental evidences it is possible to reach the appropriate level of confidence compared to the real behaviour of masonry structures.

7.3.2 Anisotropic continuous models

The actual constitutive model of masonry is characterized by a certain level of anisotropy, due to the geometrical arrangement of blocks and mortar joints, even if the properties of the latter are generally isotropic. In order to model the masonry as a composite material it is necessary to implement numerical models to describe the anisotropic plasticity, which are a generalization of isotropic models. It is well known that most of the building materials is characterized by a certain degree of anisotropy. Materials like as wood are naturally anisotropic and metallic laminates feature better mechanical properties in a predominant direction, enhanced when plastic deformations are higher. Other materials are anisotropic as a result of the production

or construction process, such as for example the reinforced concrete, masonry and fiber-reinforced composite materials. It is noticed that, while different anisotropic plasticity models were proposed from a pure theoretical and experimental point of view, only a small quantity of calculations and numerical implementations have been actually made. The difficulties in the accurate modelling of anisotropic modelling are not only due to the fact that the experimental results, also relative to the post-peak behaviour, are lacking, but also to the intrinsic difficulties in such a model.

In order to model the mechanical behaviour of anisotropic composite materials it is necessary to have criteria able to describe the complex phenomena governing the failure. Some examples include those work where an elastic – perfectly plastic yielding criterion according to Hill or according to Hoffmann have been implemented. Initially, the hardening behaviour could be simulated by means of a fracture model according to Besseling, but not so many efforts have been made in this direction. More recent studies have tried to include a hardening behaviour in the Hill yielding criterion or a linear hardening in a modified Von Mises yielding criterion (dependent on the normal stress) with the scope to reproduce the uniaxial tensile or compressive behaviour, but not both of them. The fact that only few anisotropic models have been successfully implemented and tested is not strange, if the difficulties associated to isotropic plasticity models for non-linear analysis are considered.

A step forward in the formulation of anisotropic models was done through the definition of a composite yielding criterion for the modelling of anisotropic materials under plane stress states. In particular, for tension and compression, two independent yielding criteria were considered, with respect to different failure mechanisms. The first one is associated to a more localized fracture process, referred to as cracking, while the second one is associated to a more distributed fracture process, referred to as crushing of material. An accurate analysis of masonry structures on the basis of a macro-model (or composite model) needs the description of the material for every stress state. Nevertheless, some difficulties arise since there are no comprehensive experimental data concerning the constitutive behaviour of the material, but also due to the difficult combination of an anisotropic elastic model and an anisotropic inelastic model. The yielding surface developed in the continuous anisotropic material model

combined the advantages of modern plasticity concepts with an effective description of the anisotropic behaviour of the material, which includes different branches of hardening/softening along every material direction. It is also noticed that a orthotropic description of the yielding surface is not possible only in terms of principal stresses. For plane stress states it is necessary a graphic representation in terms of stress vector $(\sigma_x, \sigma_y, \tau_{xy})$. It is assumed that the material axes are defined by the direction of mortar bed joints (x direction) and the direction of mortar head joints (y direction). Another possible description cab be made by means of principal stresses and an angle θ , which represents the angle of rotation between the principal axes and material axes. Clearly, different principal stress diagram will be obtained, when varying the angle θ .

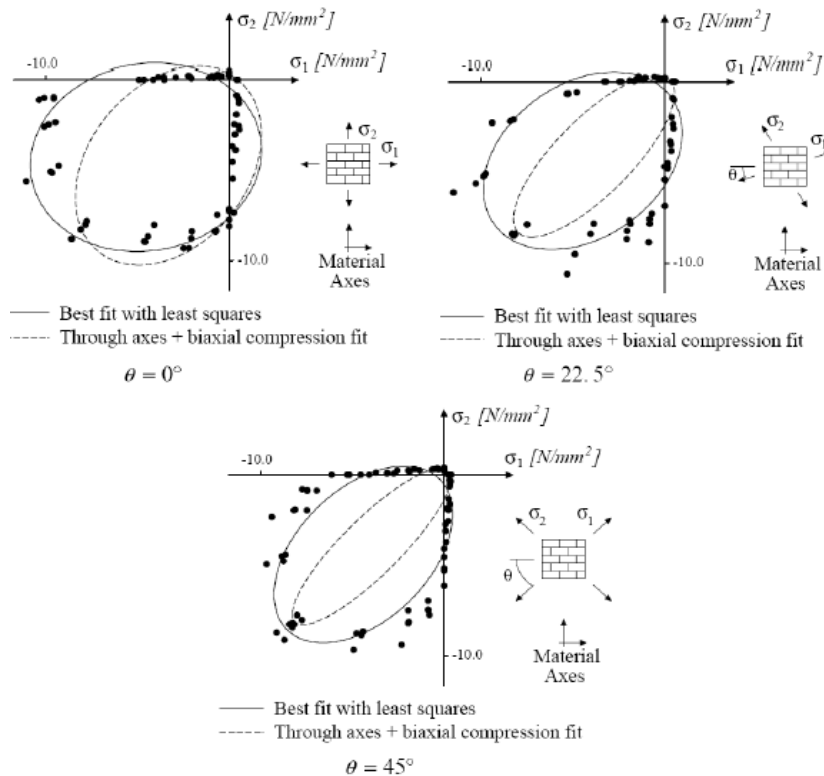


Figure 7.11. Comparison between the yielding domain according to Hoffman and the experimental data.

For the macro-modelling of masonry, basically it is possible to refer to two different approaches. The first approach consists in the description of material through a yielding criterion. The Hoffman yielding criterion is quite flexible and easy to use, even though may lead to results not always in accordance with the experimental ones and shows zero tensile strength, as it is shown in Figure 7.11.

The comparison of experimental data with the curves for different values of uniaxial strength and compressive failure with $\sigma_x = \sigma_y$ e $\theta = 0^\circ$ evidences a poor agreement of diagrams for high values of the angle and an overestimation of the strength in the case of tension-compression. A single surface which can be in good agreement with the experimental data would be extremely complex for the description of the non-linear behaviour, making this approach not feasible. It is preferable to adopt a second approach consisting in the extension of traditional formulations for isotropic quasi-brittle materials for the description of orthotropic behaviour. Generally, the formulation of quasi-brittle isotropic material consider different inelastic criteria for tension and compression; in particular, it can be possible to refer to the Rankine and Drucker-Prager criteria, also employed for concrete. In order to model the orthotropic behaviour of the material, the Hill yield criterion can be used for compression and a Rankine yield criterion can be used for tension, as illustrated in Figure 7.12.

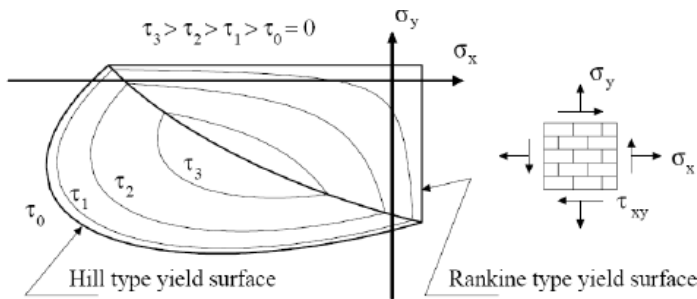


Figure 7.12. Continuous yielding criterion for different level of tangential stress.

7.4 CRACKING MODELS

In order to model the cracks formation in a material, the discrete crack concept is the most refined approach to model the crack formation in a material being based on modelling an interface element between two solid elements and capable to introduce a geometrical displacement discontinuity, but unfortunately this approach is not very computationally suitable to be applied in finite element method. From the point of view of numerical and computational implementation the smeared crack concept is certainly more viable, considering the cracked solid as a continuum and describing its behaviour in terms of stress-strain relation. Obviously, in the latter case it is evident that material is continuum by assumption only, being discontinuous the nature of phenomenon. Effort must be done to calibrate smeared crack model in order to average the real cracking process and to let it be able to reproduce all possible involved mechanisms.

A review of numerical models capable to reproduce cracking in quasi-brittle materials based on different cracking concepts is presented (Rots and Blaauwendraad, 1989) [93]; a distinction is made in:

- discrete cracking concept, associated to the notion of a discontinuum,
- smeared cracking concept, associated to the notion of a continuum, based on (in function of the orientation of the smeared crack):
 - fixed single crack approach, if the orientation of the crack is kept constant;
 - fixed multi-directional crack approach, if the orientation of the crack is updated stepwise;
 - rotating crack approach, if the orientation of the crack is updated continuously.

Regarding the approach to the element deformation, plasticity models are characterized by reversible and irreversible deformation, called elastic and plastic strains, respectively. Irreversible, or permanent, deformations can be seen during the unloading process. The basic assumption in the elasto-plastic model is that the total increment of deformation is the sum of an elastic part ϵ^e and a plastic part ϵ^p according to the following relation:

$$\varepsilon = \varepsilon^e + \varepsilon^p.$$

The stress and deformation history of the material is generally taken into account through the introduction of an internal parameter k , governed by a specific evolutive law. The elasto-plastic behaviour can be described on the basis of the following elements:

- The relationship between stress and strain in the elastic field, defined on the basis of total quantities:

$$\sigma = D \cdot \varepsilon^e$$

where D is the stiffness matrix.

- The yielding criterion, which specify the stress condition when the plastic field starts. This condition can be written as a function of the stress vector and the internal parameter k :

$$f(\sigma, k) = 0$$

If the value of the yielding function is lower than zero, the stress state can be assumed to be elastic, and no plastic strains are registered.

- The flow rule, relating the increment of inelastic deformation to the stress state.
- The hardening function, which specify the evolution of the internal hardening parameter k . In general, this evolution is given as a function of the stress vector and the plastic strain rate vector:

$$\dot{k} = h(\sigma, \dot{\varepsilon}^p).$$

In general, with the yielding criterion the existence of the increment of plastic deformation is defined, with the flow rule the direction is set, and with the hardening function the yielding condition is modified when the plastic strain increases.

According to the Figure 7.13, the yielding criterion according to Tresca represents a condition of maximum shear stress, which can be expressed in terms of principal stresses ($\sigma_1 \geq \sigma_2 \geq \sigma_3$):

$$f(\sigma, k) = |\sigma_1 - \sigma_3| - \bar{\sigma}(k),$$

where $\bar{\sigma}(k)$ represents the relationship between the uniaxial yielding stress and the hardening parameter k .

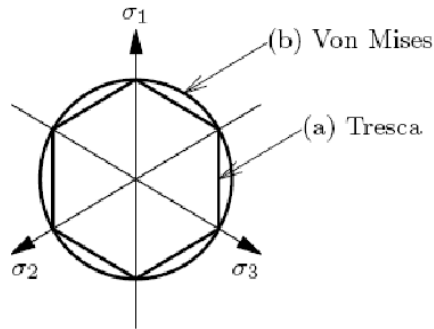


Figure 7.13. Yielding criteria according to Tresca and Von Mises.

Always considering the Figure 7.13, the yielding criterion according to Von Mises represents an approximation of the Tresca's criterion. The formulation of the criterion is as follows:

$$f(\sigma, k) = \sqrt{3}J_2 - \bar{\sigma}(k) = \sqrt{\frac{1}{2}\sigma^T P \sigma} - \bar{\sigma}(k),$$

where P is the projection matrix.

The function of the internal hardening parameter k , when the plastic strain increases, is given by the hardening hypothesis . In the case of strain hardening, the criterion is given by the following relation:

$$\dot{k} = \sqrt{\frac{2}{3}(\dot{\epsilon}_1^p \dot{\epsilon}_1^p + \dot{\epsilon}_2^p \dot{\epsilon}_2^p + \dot{\epsilon}_3^p \dot{\epsilon}_3^p)};$$

while in the case of work hardening, the criterion is given by the following assumption:

$$\dot{W}^P = \sigma^T \cdot \dot{\epsilon}^P \equiv \bar{\sigma}(k)\dot{k}.$$

7.4.1 Discrete cracking models

The firstly introduced, and most realistic, approach developed in order to model cracking of materials is the discrete crack concept, in which a given crack, or system of cracks, is reproduced by the possibility to generate a separation between elements of a finite element modelled body. Nevertheless, as already pointed out, this kind of approach is not simply implementable and easily manageable in finite element method, due to the existence of intrinsic limitations and complexities that can restrict its use.

In fact, a problematical aspect of discrete crack modelling is the necessity to allow the model not having fixed nodal connections, that may change during the loading process and update according to the evolution of cracking. The second fundamental drawback of the concept relies on the necessity to identify and preventively set down the possible crack path, since it is generally constrained to follow the element edges, although some attempts to define a few techniques in order to introduce the possibility for a crack to further develop through a finite element (Blaauwendraad, 1985) [94].

However, if the failure mechanism of a system can be recognized a-priori, the associated crack path can be identified and the orientation of potential cracks be set in the model. Fundamental issue for the correct application of such modelling approach is the appropriate selection of the interface element simulating the geometry discontinuity, and its dummy stiffness. The dummy value of the initial stiffness is employed to simulate the uncracked state, rigidly connecting facing element nodes. Once a given condition is reached, such as maximum stress, the crack initiates and the element stiffness is changed. The crack tension stresses are generally described via a constitutive model, through which they are linked to the relative displacement across the crack by a factor representing phenomena like tension-softening and aggregate interlocking.

7.4.2 Smearred cracking models

The other possible approach that may be followed in the cracking behaviour description of brittle materials is based on the assumption for the medium to be continuous in spite the character of cracking phenomenon is not. The idea is to smear cracks that may initiate and propagate upon loading, their effect in the modification of geometrical and mechanical characteristics of element, in a continuum, in order to describe its behaviour in terms of stress-strain relations only, in the form firstly introduced by Rashid in 1968, (Rashid, 1968) [95].

Based on this approach, the application of smeared crack concept features passing from an initial isotropic behaviour to an orthotropic one upon cracking, without introduce modification in the finite element model mesh, or imposing limitations on the orientation of crack planes, as well as the material axes of orthotropy.

Due to the outlined aspects, and also considering the computational process, smeared crack concept seems to be a more easily viable path for description of crack formation in materials. Furthermore, such a concept may be much more powerful and more faithful to reality if applied in cases of distributed cracks and if the spacing between each crack is rather small compared to the representative dimensions of continuum.

Different approach can be followed in the framework of the application of smeared crack concept, but the main distinction can be made is between fixed and rotating crack, based on the assumption about the orientation of crack. The former approach is characterized by the assumption of fixed orientation for crack during the whole computational phase, while in the latter the orientation of crack is allowed to rotate according to principal strain axes rotation. In between the two previously described approach, the fixed multi-directional approach can also be introduced.

Smearred cracking models are based on the decomposition of total strain ε , in an elastic strain ε^e and a cracking strain ε^{cr} :

$$\varepsilon = \varepsilon^e + \varepsilon^{cr}.$$

Such decomposition of strain allows to combine the cracking model with a plasticity model for the material. The decomposition gives the possibility to model a given number of cracks, which can contemporarily open in the element. The fundamental feature of the multi-directional cracking model is the possibility to refer the stress s_i and the deformation e^{cr}_i to the system defined by the n-t coordinates, relative to the crack i, as illustrate in Figure 7.14.

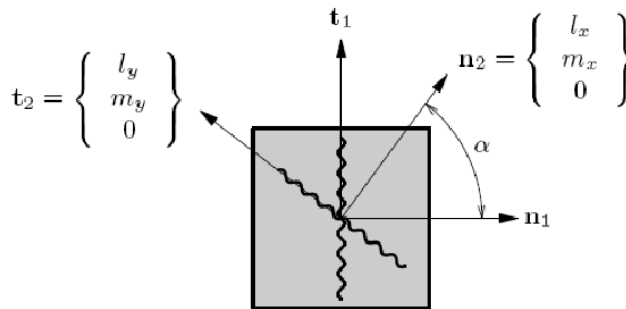


Figure 7.14. Multi-directional cracking model.

The relationship between ε^{cr} the deformation and the vector e^{cr} is given by:

$$\varepsilon^{cr} = Ne^{cr},$$

while the relationship between the stress σ and the vector s_{cr} is given by:

$$s^{cr} = N^T \sigma,$$

where N is the transformation matrix. An basic hypothesis is that cracking stress are given as a function of cracking strains:

$$s^{cr} = f(e^{cr}).$$

It is possible to model the combined effect between different cracks by means of a general formulation, but taking into account this aspect may lead to a level of

detail too high and not always essential. For this reason, the cracking stress are considered in function of the corresponding cracking strain only:

$$\begin{cases} s_1^{cr} = f(e_1^{cr}) \\ s_2^{cr} = f(e_2^{cr}) \\ \dots \\ s_i^{cr} = f(e_i^{cr}) \\ \dots \\ s_n^{cr} = f(e_n^{cr}) \end{cases}$$

Thus, the model is based on a criterion for the crack formation and on a relationship between cracking stresses and strains. The formation of cracks is governed by a criterion for tensile cut-off and by the definition of a threshold angle between two consecutive cracks. For the initiation of further cracks codes, such as DIANA TNO, apply the following two criteria, which must be simultaneously fulfilled:

- the principal stress exceeds the maximum stress;
- the threshold angle between an existing crack and the principal stress direction exceeds a threshold value.

7.4.2.1 Fixed single crack approach

The fixed crack concept assumes the local crack axes to remain unaltered upon loading. The stress-strain law adopted in fixed smeared cracking is defined regarding to a system of fixed principal axes of orthotropy, according to the direction normal to the crack (related to mode I) and two orthogonal direction tangential to the crack (related to mode II and mode III). The original formulation by (Rashid, 1968) [95] and some others developments in the early years, provided null normal and shear stresses along the crack, once it has formed. After, the initial isotropic stiffness moduli have been reintroduced taking into account some reduction, in order to do not definitively disregard the even slight capability of the material to transmit tension stresses normally and tangentially to the crack, and taking into account the higher numerical problems related to the sudden discontinuity which creates when switching

from the initial isotropic linearly-elastic behaviour to an orthotropic behaviour with zero stiffness moduli. Such reduction factors are the so called ‘shear stiffness reduction’ or ‘shear retention factor’ β , when applied to the initial shear modulus G , and ‘normal stiffness reduction factor’ μ , when applied to the initial Young’s modulus E .

Another important advance in the formulation of smeared crack model is achieved when the concept of strain-decomposition is introduced, taking into advantage the possibility to distinguish between the strain due to cracking and the strain of the solid part of material between cracks. The strain-decomposition is in a certain way closer to the discrete crack concept, in which an interface finite element is used to model the separation of the solid material.

The model based on the total deformation was developed on the basis of the theory originally proposed by Vecchio & Collins; the extension to the three-dimensional field of this theory was proposed by Selby & Vecchio and represents the theoretical description of the model also implemented in numerical code, such as DIANA TNO. A constitutive model based on the total strain directly describes the stress as a function of the strain. In a ‘fixed crack model’ the relationship between stress and strain is evaluated in a fixed coordinate system, meaning that the cracking directions n and t are fixed. The basic concept of the ‘total strain crack model’ is that the stress is evaluated in along the axis defined by the cracking direction. The strain vector ε_{xyz} in the system $x y z$ of the element is updated by means of the strain increment $\Delta\varepsilon_{xyz}$ according to the following relation:

$$\varepsilon_{xyz}^{t+\Delta t, i+1} = \varepsilon_{xyz}^t + \Delta\varepsilon_{xyz}^{t+\Delta t, i+1}$$

and it is transformed in the strain vector in the cracking direction by means of the matrix T ,

$$\varepsilon_{nst}^{t+\Delta t, i+1} = T \varepsilon_{xyz}^{t+\Delta t, i+1}$$

For the ‘fixed crack model’ the transformation matrix is fixed at the moment of cracking and the compressive behaviour is evaluated in the reference system defined

compression and tension, in order to model the stiffness deterioration in compression and tension separately.

For tension, the unloading parameters are given by:

$$r_k = \begin{cases} 0 & \text{se } \varepsilon_{i+1}^{t+\Delta t} > \alpha_k \\ 1 & \text{se } \varepsilon_{i+1}^{t+\Delta t} \leq \alpha_k \end{cases} \text{ con } k = 1, \dots, n_{str}$$

while in compression are given by:

$$r_k = \begin{cases} 0 & \text{se } \varepsilon_{i+1}^{t+\Delta t} > \alpha_k \\ 1 & \text{se } \varepsilon_{i+1}^{t+\Delta t} \leq \alpha_k \end{cases} \text{ con } k = n_{str} + 1, \dots, 2 \cdot n_{str}$$

Thus, the internal variables are:

$$\alpha_{xyz}^{t+\Delta t} = \alpha \cdot W \Delta \varepsilon$$

where W is a matrix defined as:

$$W = \begin{cases} W_{k,k} = 1 - r_k & \text{con } k = 1, \dots, n_{str} \\ W_{k+n_{str},k} = 1 - r_k & \text{con } k = n_{str} + 1, \dots, 2 \cdot n_{str} \end{cases}$$

The stress in the j direction is given by:

$$\sigma_j = f_j(\alpha, \varepsilon_{nst}) \cdot g_j(\alpha, \varepsilon_{nst}).$$

The uniaxial relationship between stress and strain f_i is usually not only a function of the internal variable α_j , but also of the internal variables and strains in the other directions $f_i(\alpha, \varepsilon)$. The loading-unloading function indicated with $g(0 \leq g \leq 1)$ is given by:

$$g_j = \begin{cases} 1 - \frac{\alpha_j - \varepsilon_j}{\alpha_j} & \text{se } \varepsilon_j > 0 \\ 1 - \frac{\alpha_{j+nstr} - \varepsilon_j}{\alpha_{j+nstr}} & \text{se } \varepsilon_j < 0 \end{cases}$$

The uniaxial relationship between stress and strain is connected to the material's strength in the cracking directions f , multiplied by the loading-unloading function g .

7.4.2.2 Fixed multi-directional crack approach

The concept of strain decomposition originally introduced in fixed smeared crack model, has been considered again in order to further decompose crack strain and uncracked material strain. In particular, when referring to the crack strain the sub-decomposition allow to independently take into account the different contributions of a set of cracks simultaneously occurring at a given point. The state of cracking originating at a given point in the solid material is, thus, exemplified by multi-directional cracks, namely a set of fixed cracks each of them described by a local strain vector, a traction vector, and a transformation matrix.

The field of application of multi-directional crack approach includes axis-symmetric and plane-strain analysis, in the cases of biaxial or triaxial tension, where the separate behaviour of two or three expected orthogonal crack can be usefully modelled. Moreover, the utility of the use of multi-directional cracking can also be seen in tension-shear conditions, cases in which a crack generates in tension and then proceeds in tension-shear, producing a rotation of the principal stress axes with respect to the fixed crack axes.

In order to overcome the problem of difference between the system of principal axes and crack axes two possibility may be considered. The first one is an internal alternative within the multi-directional fixed crack approach, and allows the formation of a new crack when the angle of inclination between the existing crack and the current direction of principal stress exceeds a given threshold value. The other possibility is given by the application of the rotating crack approach.

7.4.2.3 Rotating crack approach

As previously stated, within the fixed crack approach a discrepancy between the principal stress directions and the crack axes. In the rotating crack approach, the axes of orthotropy, defined upon cracking, are allowed to co-rotate with the principal strain directions. This kind of approach needs the non-linear stress-strain relation to be specified for the principal directions only.

An important difference between multi-directional crack and rotating crack approaches is given by the fact that while the former controls the formation of subsequent cracks via the threshold angle, the rotating concept assumes the crack orientation to change continuously.

In the 'rotating crack model' the transformation matrix T , previously introduced for the case of smeared cracking, directly depends on the strain vector:

$$T = T(\overset{t+\Delta t}{i+1}\varepsilon_{xyz})$$

An advantage of rotating crack approach is that it can be based on the strain decomposition concept for both crack and uncracked material. The strain decomposition is also necessary when the model is to be combined with plasticity, creep or thermal loading.

The rotating crack approach does not preserve permanent memory of the damage orientation, while the fixed crack approach does. Due to this difference, the rotating crack concept does not allow to re-activate the defects during a subsequent loading process. Furthermore, the modality to take into account the shear effect is different between fixed and rotating cracking. Within the fixed crack approach the shear effect is taken into account using of a crack shear relation, making complicate the analysis because the axes of principal stress do not coincide with the axes of principal strain anymore. In rotating crack approach, instead, a unique shear term is defined, that is responsible for the coaxiality between principal stresses and strains, also if the possibility of incorporate different shear models is lost, and the crack always occur in a principal direction.

8 ANALYSIS AND ASSESSMENT METHODS FOR MASONRY STRUCTURES

In the following sections the main aspects related to the analysis methods for masonry structures are illustrated. Masonry buildings represent one of the most vulnerable classes of structures and in the last decades have been widely studied, in order to address some of the most important issues related to their structural behaviour, particularly under seismic actions. However, there are still many aspects remaining open, mainly regarding assessment methods, strengthening strategies and techniques, availability of adequate design-assessment strengthening standards and codes of practice.

8.1 ANALYSIS AND ASSESSMENT METHODS

The seismic analysis and assessment of masonry buildings started to represent a relevant matter of investigation in the last decades and after the seismic events occurred in Italy and worldwide. The need of assessment procedures based on static non-linear analyses has been clear since the first approach to the problem, meaning that the classical methods based on elastic analysis have been soon considered inadequate to describe the seismic response of masonry structures.

The development of non-linear analysis methods for masonry allows to perform the seismic analysis of buildings in order to assess their global response, principally dependent on the in-plane strength of the walls, at a limited computational cost. Such methods are based on the description of the masonry building through the

use of *macro-elements*, with dimensions depending on openings or inter-storey height, and adequately designed to simplify the structure.

The applicability and validity of macro-elements models has been substantially demonstrated for sufficiently regular geometrical configurations, but the discussion regarding their validity in application to building described by complex configurations, often found in historic centres, is still open. An extensive comparison between different approaches for the nonlinear modelling of masonry walls subjected to in-plane forces was carried out within the “Catania Project” financed in the late 1990s by GNDT. It was observed that the results of nonlinear analyses are sensitive to the modelling assumptions on the response of masonry spandrels. Also, the necessity to better develop the experimental information on the seismic response of unreinforced masonry spandrels, to be used to validate analytical models based on macro-elements or more refined approaches, is evidenced.

Due to the peculiarity of the behaviour of masonry constructions, the evaluation of their response against seismic actions cannot be properly described through linear elastic analysis. Such method of analysis, in fact, is not able to take into account all the aspects by which the behaviour of these class of structures is influenced, and mainly due to the characteristics of material and structural resisting system.

An important aspect is related to the distribution of internal forces at ultimate limit state in a masonry building, which is not governed by the elastic stiffness of elements, but by equilibrium and compatibility relationships between forces and the strength criteria. This last observation also leads towards the employment of static non-linear analysis methods, instead of modal elastic response spectrum analysis, which provide non-equilibrated results; thus a correct definition of the modalities and limits of use of linear analyses on masonry is needed.

8.2 NON-LINEAR RESPONSE OF URM WALLS

Non-linear behaviour of masonry walls is highly complicated. Non-linearity is mainly dependent on cracking and crushing of masonry which is heterogeneous and

anisotropic by nature. Depending on the mechanical properties, boundary conditions, axial load level and aspect ratio of the wall, different failure mechanisms are observed. Each failure mechanism possesses its own strength and displacement characteristics. Thus, in order to define the non-linear behaviour of a masonry wall, its failure mode needs to be determined first.

To illustrate the effect of failure mechanism on response, hysteretic behaviour of two masonry walls under cyclic load reversals are illustrated in Figure 8.1 (Magenes and Calvi, 1997) [96].

In case of flexural response such as rocking of a pier, response is roughly non-linear elastic with low hysteretic energy dissipation, considerable displacement capacity and limited strength degradation (see Figure 8.1(a)). On the other hand, in case of shear dominated response such as diagonal tension failure, non-linear response is characterized by higher hysteretic energy dissipation, limited displacement capacity, sudden strength and stiffness degradation (see Figure 8.1(b)).

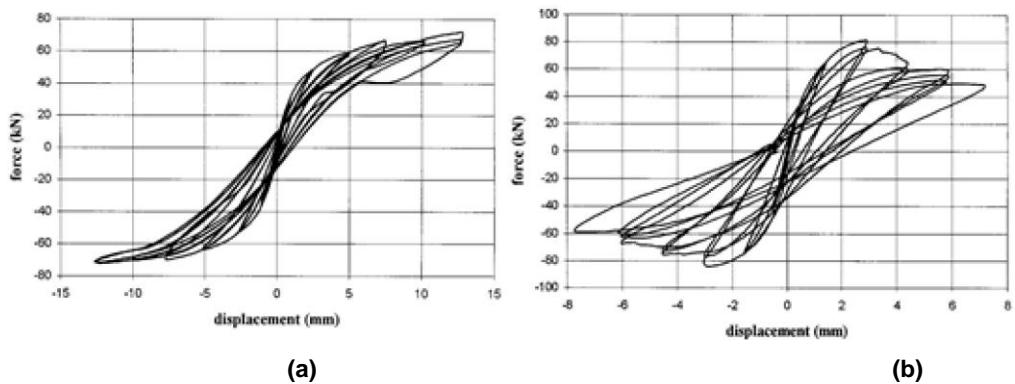


Figure 8.1. Hysteretic response of masonry walls: a) flexure dominated response, b) shear dominated response (Magenes and Calvi, 1997) [96].

8.2.1 Failure modes of URM walls

Depending on the difficulty in analytical modelling, the knowledge about non-linear behaviour of masonry is mostly extracted from experimental studies. Four

primary in-plane failure modes of URM walls such as rocking, bed joint sliding, diagonal tension failure along masonry units or along head and bed joints in a stair stepped fashion and toe crushing (see Figure 8.2) are identified in these experimental works.

However, even four primary discrete failure mechanisms are not sufficient to define inelastic behaviour of a masonry wall. Initiation of a failure mechanism might originate another failure mechanism (Tian Yi et al., 2006) [97] or overturning moment due to lateral loads might increase or decrease axial load on the walls of a URM building, turning flexural failure to shear dominated failure (Magenes et al., 1995) [98].

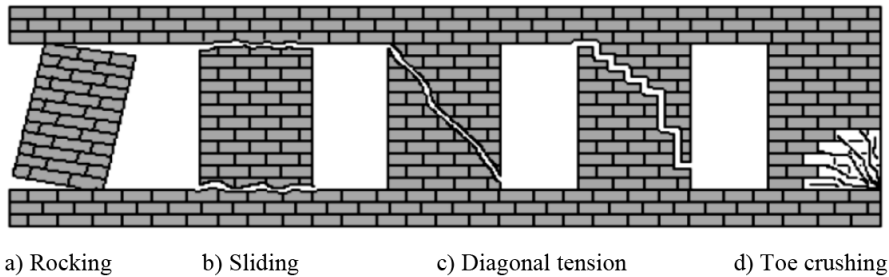


Figure 8.2. Failure Modes of In-plane Masonry Walls (Tian Yi et al., 2006) [97].

As a result, ultimate failure of a pier might be idealized as a combination of four primary modes. The summarized experimental results suggest that aspect ratio and vertical stress are the most important factors in determination of the failure mechanisms of URM walls. Rocking and sliding governs the response under low levels of axial force and high aspect ratio. These failure modes are capable of exhibiting large ultimate drifts. At higher levels of axial force and low aspect ratios, toe-crushing and diagonal tension failures are more common. Although these failure modes are typically assumed to be brittle, if diagonal crack is formed in a stair stepped manner, large displacement capacities have been observed due to the resulting sliding deformations (Moon, 2004) [99].

Definitions and related nonlinear response characteristics of four primary failure modes of URM walls are illustrated below.

8.2.2 Softening behaviour of URM walls

Lateral stiffness of URM walls degrade with the increase in lateral displacement. Softening of the lateral resistance in URM takes place due to progressive internal crack growth reducing effective area of the wall which resists lateral load. This phenomenon is observed in several experimental studies. While some authors tried to relate post-elastic stiffness degradation to lateral drift, others assume that post-elastic stiffness might be taken as zero for practical purposes.

According to (Gürel et al., 2005) [100] elastic lateral stiffness values of the unreinforced masonry columns decrease dramatically with the increase in lateral displacements caused by cracking and second-order effects. P- Δ effects for masonry piers might be ignored since limit states for the ultimate drift of piers are low. However cracking results in significant stiffness drop especially for shear dominant mechanisms.

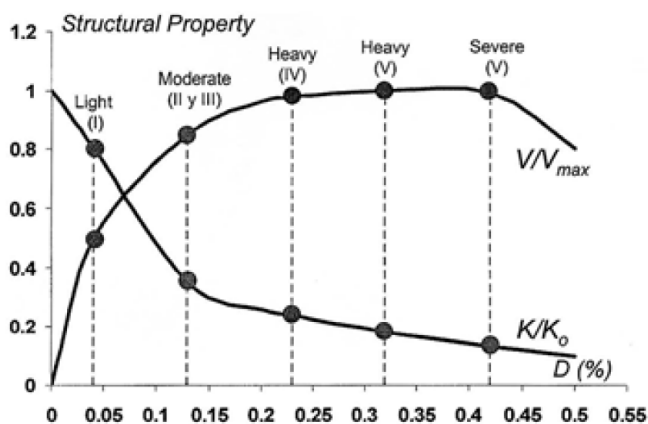


Figure 8.3. Evolution of damage and structural degradation in confined masonry walls failing under diagonal tension (Ruiz-García and Alcocer, 1998) [101].

Based on an experimental study on in-plane loaded full scale masonry walls and half scale confined masonry buildings through shaking table tests, (Ruiz-García and Alcocer, 1998) [101] established a relationship between damage, lateral drift, crack pattern, degradation of lateral strength and stiffness of confined masonry walls (see Figure 8.3). In structural level, they observed that stiffness decays at low drift

ratios, even before inclined cracking takes place. They explained this fact by flexural cracking, micro-cracking not visible by naked eye, local loss of mortar bond and adjustment of brick position. They also stated that after first inclined cracking, stiffness decay increased with drift until maximum strength is reached. At larger drift ratios stiffness remained nearly constant (Alcocer et al., 2004) [102].

In Figure 8.3, lateral stiffness (K) corresponding to a particular level of inter-story drift (D) is normalized by initial stiffness (K_0). Similarly, shear force (V) corresponding to a particular level of inter-story drift is normalized by maximum shear strength of masonry wall (V_{max}). Decrease in lateral stiffness starts in the very first stages of loading, just after the formation of first hairline cracks. After the formation of first diagonal cracking due to diagonal tension, lateral stiffness decreases to 35% of its initial value. Decrease in lateral stiffness and increase in shear force is parabolic until the walls are heavily damaged. Afterwards both shear force and lateral displacement tend to be constant till masonry walls fail at a ultimate drift level of 0.5%.

According to experimental studies made by (Tomazevic et al., 1996) [103] it is observed that independent of vertical load and loading history, shape of the stiffness degradation function is constant. The change in stiffness of a pier might be related with lateral displacement using the following equation. Utilizing stiffness degradation parameters proposed by Tomazevic, stiffness degradation functions are drawn for different levels of vertical force on piers (see Figure 8.4).

$$\frac{K}{K_e} = \alpha \left(\frac{d}{d_{Hmax}} \right)^\beta$$

where K is the lateral stiffness, K_e is the secant stiffness evaluated at the occurrence of the first significant cracks, d is the lateral displacement, d_{Hmax} is the lateral displacement evaluated at maximum resistance and α , β are parameters of stiffness degradation.

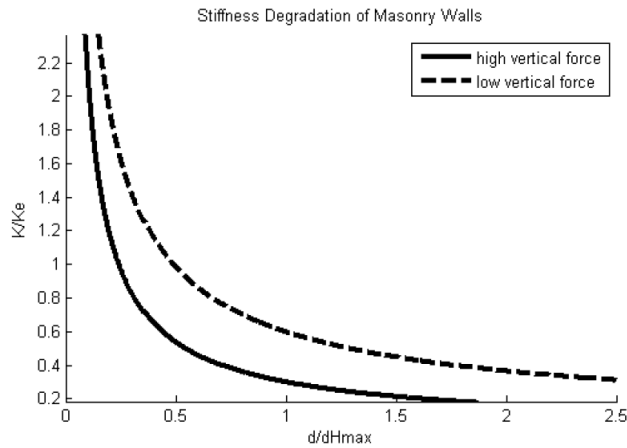


Figure 8.4. Stiffness degradation function for different levels of vertical load, proposed by (Tomazevic et al., 1996) [103].

(Bosiljkov et al., 2005) [104] investigated the effect of precompression on the stiffness degradation of URM walls. According to an experimental study result, shape of the stiffness degradation curve for cantilever elements depend on the level of precompression (see Figure 8.5). Figure 8.5 also verifies the previous equation in the way that although stiffness degradation function depends on level of precompression, its shape remains unchanged.

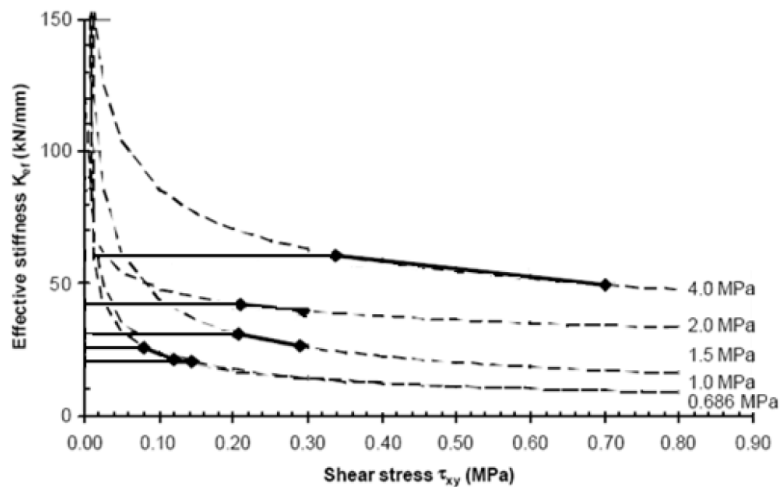


Figure 8.5. Stiffness degradation vs. shear stresses for different levels of precompression (Bosiljkov et al., 2005) [104].

Similar observations were also made by (Tian Yi et al., 2006) [97]. According to the experimental research on a full-scale two-story URM frame which is tested in a quasi-static fashion, it is observed that effective elastic modulus of the masonry decreased rapidly from the initial value of 7 GPa to about 0.9 GPa at a roof displacement of 6.4 mm which corresponds to an inter-story drift of about 0.14% for the first story and about 0.05% for the second story. At this stage only 13% of initial stiffness could be preserved.

The reason why large elastic stiffness of squat masonry walls decreases rapidly, with a small increase in lateral drift, is explained by (Anderson and Brzev, 2009) [105]. They state that the response is initially elastic until cracking takes place. Then there is a large drop in stiffness. This is particularly pronounced after the development of diagonal shear cracks. After a few major cracks develop, the load resistance is taken over by the diagonal strut mechanism. However, the stiffness drops significantly shortly after the strut mechanism is formed, and can be considered to be zero for most practical purposes.

8.3 NON-LINEAR MODELLING OF MASONRY BUILDINGS

8.3.1 Macro-elements modelling technique

When a simple model of a masonry structure is needed one can refer to a modelling approach based on the use of structural elements as components of the entire structure. This kind of approach is the simplest method to describe the whole structure and its overall behaviour; it is based on the use of different mono- and bi-dimensional elements, such as beams, plates or shells, to model piers, walls, slabs, constituting the building. In particular, the use of structural components through which define an equivalent analytical model of a masonry walls structure gives different modelling options (Figure 8.6) such as a lumped mass model, a beam model, a macro-panel model (Seible and Kingsley, 1991) [106].

The simplest analytical model of a masonry structure is based on the use of lumped masses and structural parameters at each floor level (Figure 8.6(b)); this type

of modelling permits to study the global behaviour of the structure taking into account the dynamic features and the material non-linearity with a reasonable approximation. Due to the simplicity of this model, it is not serviceable to predict global failure mechanism or local damage of masonry elements.

To describe the actual geometry of the structural components in a more accurate manner one can be used beam elements connected through joints (Figure 8.6(c)). Using an equivalent frame it is possible to obtain more static and dynamical information on the behaviour of the structure, namely the pattern of local failure mechanisms development and the global collapse type, and also tri-dimensional analyses can be carried out.

The higher level of detail that a macro-elements modelling approach permits to achieve is represented by the approximation of the structure by panel components (Figure 8.6(d)). Examples are (Brencich et al., 1998) [107], (Cattari et al., 2005) [108]. The wall-system building is approximated by bi-dimensional elements, which can be either rigid or deformable, principally subjected to in-plane actions. Also, such bi-dimensional elements can be employed to study the evolution of damage phenomena while subjected to increasing loads or for kinematic limit analysis.

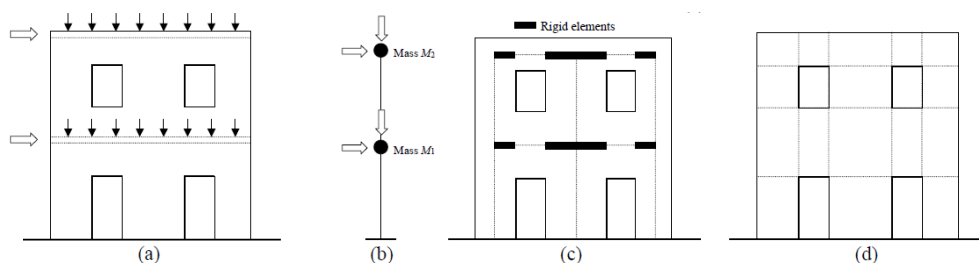


Figure 8.6. Structural components modelling techniques for masonry wall system (a): lumped masses (b); equivalent frame (c); panel system (d) [71].

8.3.2 Equivalent Frame Modelling

Equivalent frame method is a simple way to conduct nonlinear analyses on Unreinforced Masonry (URM) structures. Reduced amount of data is required to

describe material property among other modelling strategies since homogenous, isotropic material idealization is made. Local nonlinear behaviour of each wall is described with nonlinear hinges whose force displacement properties are usually defined from experimental test results. Being both simple and effective, a wide range of studies to improve the reliability of the Equivalent Frame Modelling is found in the literature. Attempts to simulate nonlinear behaviour of URM with equivalent frame models are summarized below:

(Gilmore et al., 2009) [109] proposed an equivalent frame model to perform pushover analysis of confined masonry buildings. Structural degradation of confined masonry walls is associated with shear behaviour and a rotational shear spring to idealize nonlinear response of masonry walls is proposed. Rotational spring is used to relate shear force on the wall with inter-story drift due to shear deformation. For this purpose hinge is located at the bottom of the wall (see Figure 8.7).

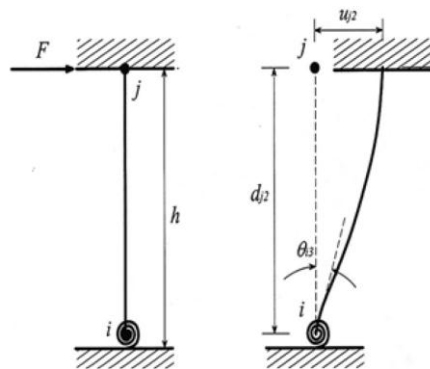


Figure 8.7. Modified wide column model for push-over analysis (Gilmore at al., 2009) [109].

The proposed force-deformation relationship of the springs is independent of aspect ratio and axial load level (see Figure 8.8). It is determined from idealized backbone curve for confined walls which are build using confined handmade clay brick used in Mexico.

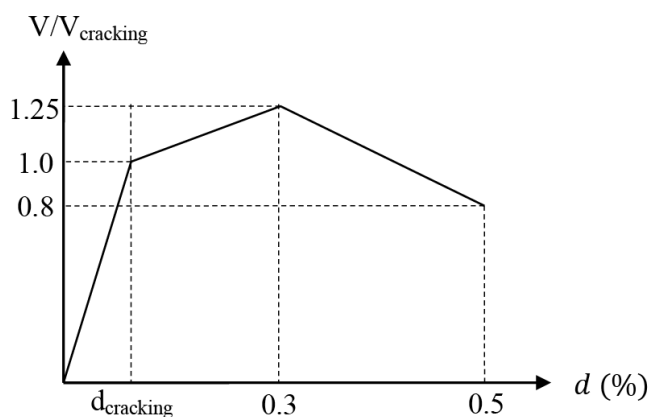


Figure 8.8. Idealized backbone curve for confined masonry walls (Gilmore et al., 2009) [109].

Finally a lateral load distribution proportional to modal shape of fundamental mode is used for pushover analysis of a typical confined masonry building in Mexico whose experimental results are satisfactory captured with the proposed computer model.

(Kappos et al., 2002) [110] conducted elastic and plastic comparative analyses on two and three dimensional masonry structures aiming to evaluate accuracy of equivalent frame modelling technique. In elastic analyses of a two dimensional perforated wall, equivalent frame and finite element models are formed. Extend of rigid offsets to be employed in equivalent frame model (i.e. full horizontal rigid offsets, full horizontal and vertical rigid offsets and full horizontal and half vertical rigid offsets) and diaphragm constraint are determined as parameters under evaluation. According to analysis results, equivalent frame model with full horizontal and vertical rigid offset yields results closest to finite element model. Also effect of diaphragm constrain is found to be negligible for planar structures whereas crucial for three dimensional structures. For nonlinear analyses finite element model is generated using ANSYS and equivalent frame model is generated using SAP2000. After proposed model is validated against test data conducted in University of Pavia and Ismes laboratory, Equivalent Frame Modelling is found to be effective and reasonably accurate for nonlinear analysis of masonry buildings.

(Salonikios et al., 2003) [111] conducted comparative inelastic analyses on nonlinear equivalent frames and finite element models of 2D masonry frames. Influence of different lateral force distributions on pushover analysis of masonry frames is investigated due to the fact that important fraction of the total mass is distributed along the wall height in masonry buildings which makes it harder to determine load distribution during pushover analyses.

In equivalent frame modelling of masonry elements, flexural and shear hinges are employed together. It is claimed that when an URM building is subjected to earthquake both bending and shear mechanisms are activated and failure will first appear at the location with the smallest strength. Thus, moment-rotation hinges are located at both ends and shear-displacement hinge is located at the mid-span of the element (see Figure 8.9). The constitutive laws of the plastic hinges are defined according to FEMA 273 [112].

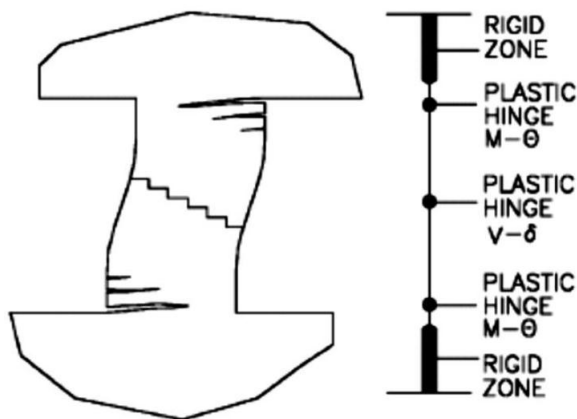


Figure 8.9. Modelling Details for Piers in the Computer Program (Salonikios et al., 2003) [111].

Lateral load distributions imposed on the structure are uniform distribution, inverse triangular distribution and first mode shape distribution. According to analysis results, lateral load distribution does not have an effect on base shear capacity of the structure since ultimate condition is reached by shear failure of all piers in the first storey. Comparing initial stiffnesses under different lateral distribution of lateral loads, higher stiffness under uniform distribution is observed. Although same shear is

applied to base story piers for different load distributions, shear force at the upper story piers are higher for inverse rectangular and modal distribution than uniform distribution. Thus a lower roof displacement is observed for uniform distribution of lateral forces.

(Pasticier et al., 2007) [113] aimed to utilize SAP2000 for seismic analyses of masonry buildings using Equivalent Frame Modelling. In nonlinear modelling of masonry piers, two rocking hinges at the end of the rigid offsets and one shear hinge at the middle of the pier is used. On the other hand, only one shear hinge was introduced for nonlinear modelling of spandrels. Lateral loads are applied by assuming the inverted triangular distribution. Since SAP2000 does not allow for automatic update of shear strengths due to change in axial load level caused by overturning effect, two different axial load distribution on piers are tested. In the first distribution, axial load on piers are calculated under dead loads only whereas in the second distribution hinge properties are determined under axial load levels calculated by applying dead loads and increasing the lateral loads up to the attainment of the elastic limit of the frame.

According to analysis results, ultimate strength and top displacement are not affected due to different methods to determine axial load distribution on piers. It is stated that main drawback of the SAP2000 which is the impossibility to update the strengths of the piers based on the variation of axial force seem not to be so crucial in pushover analyses on equivalent frames.

Two different distributions of lateral loads (i.e. uniform distribution, inverted triangular distribution) are utilized for pushover analyses. In inverted triangular distribution the collapse is due to storey mechanism at the second story, while with the uniform distribution mechanism occurred at the base story.

(Belmouden and Lestuzzi, 2007) [114] come up with an equivalent frame model for seismic analysis of masonry buildings. Unlike other proposed models up to the present, analytical model is based on smeared crack and distributed plasticity approach. Moreover interaction between both axial force-bending moment and axial force-shear force are considered. Inelastic flexural as well as inelastic shear deformations are allowed for piers and spandrels. Translational shear springs are added at the middle of the span and flexural hinges are added at the ends of the

span. However since piers and spandrels are discretized into series of slices, nonlinearity is distributed along the length of the spans (see Figure 8.10).

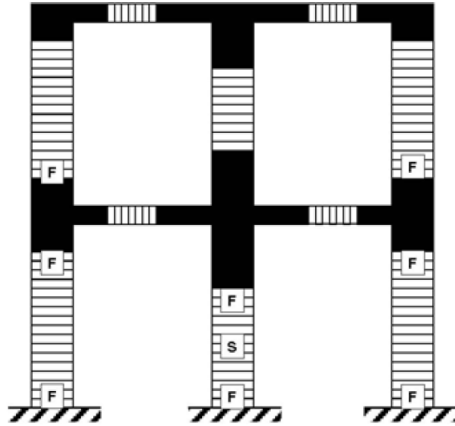


Figure 8.10. Spread Nonlinearity Approach in EFM (Belmouden and Lestuzzi, 2007) [114].

Spandrels which provide coupling to piers are modelled as elastic and the length of the spandrels are taken equal to zero moment length which is updated at each step of the pushover analysis depending on the end moments of the spandrels. Reliability of the model is sustained by comparing model results with experimental results conducted in University of Pavia.

(Roca et al., 2005) [115] studied 2D wall panels as equivalent systems of one-dimensional members, namely equivalent frames. Force deformation characteristic of masonry in compression is modelled with Kent and Park model. Axial force-shear force interaction is considered through use of Mohr-Coulomb criterion as biaxial stress envelope. After comparing numerical model with experimental results conducted by D'Asdia in 1972, it is concluded that Equivalent Frame Modelling is capable of predicting failure mechanism and ultimate loading capacity of load-bearing wall masonry systems.

(Penelis, 2006) [116] developed a method for pushover analysis of URM buildings using Equivalent Frame Modelling. Rotational hinges using lumped plasticity approach are utilized at the ends of structural elements for nonlinear action. Constitutive law of the nonlinear springs is defined by moment rotation curve of each

element under constant axial load where rotation is taken as sum of rotation due to flexure and rotation due to shear. Since axial force-bending moment interaction is ignored in material model, axial load level on piers at which hinge properties defined are determined by a linear analysis where in addition to gravity loads and an estimate of lateral load corresponding to base shear capacity is taken into account. Use of vertical rigid offsets is avoided claiming that vertical rigid offsets restrain the extent of cracking unrealistically. Finally model proposed by Penelis is verified with experimental results conducted at the University of Pavia and Ismes laboratory at Bergamo.

(Magenes and Fontana, 1998) [117] proposed a method named as SAM (Simplified Analysis of Masonry Buildings) for simplified non-linear seismic analysis of masonry buildings through equivalent frame idealization of URM walls subjected to in-plane loadings. Constitutive relation of structural members is idealized as elastic-perfectly plastic where shear strength of members are calculated from simple strength equations in literature. A limit to total chord rotation (i.e. flexural rotation plus shear rotation) is assigned as 0.5% for shear failures and 1% for flexural failures. An effective height is used for structural elements in terms of rigid end offsets proposed by (Dolce, 1989) [118] for the definition of the stiffness matrix in the elastic range. After generation of computer model, parametric analyses are made to determine rigid offset length. Due to analysis results, full rigid offsets in piers and spandrels prevailed full rigid offset in spandrels only and no rigid offsets at all.

8.3.3 Limit analysis

Limit analysis is an analysis method especially used to estimate the maximum load that a structure can sustain prior to failure. It is based on the application of the limit theorems of plasticity over possible ultimate mechanisms. In order to consider various possible ultimate mechanisms an iterative solution is required (Roca et al., 2005) [115]. It might be regarded as a practical computational tool for failure pattern and ultimate load calculation of URM structures since it only requires a reduced number of material parameters (Oliveira, 2003) [119].

(Orduña, 2003) [120] applied limit analysis method to URM structures which are modeled as assemblages of rigid blocks connected through joints (see Figure 8.11). Proposed model composed of rigid-perfectly plastic blocks possessing yield surfaces. For critical stress levels on the yield surface, the material becomes plastic and flows normal to the direction of yield surface. In order to apply limit analysis to URM structures some assumptions are made:

- masonry has no tensile strength;
- masonry has an infinite compressive strength;
- sliding failure cannot occur;
- failure occur under small displacements.

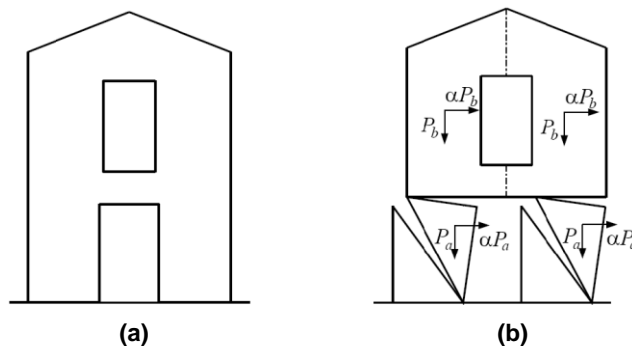


Figure 8.11. Limit analysis model for perforated URM wall; a) wall, b) failure mechanism (Orduña, 2003) [120].

9 NUMERICAL MODELLING OF MASONRY UNDER COMPRESSIVE LOADING

The present chapter describes the finite elements modelling of masonry panels tested against compressive loading under displacement control, with the aim to investigate their non-linear behaviour. The FE modelling has been carried out by means of the code DIANA 9.4.4 [121], based on the displacement method and developed by TNO Institute starting from 1972. In the present research the code has been employed in order to model, through three-dimensional finite elements, the non-linear behaviour of the masonry panel, using a micro-modelling technique able to take into account different characteristics for mortar joints and units. Afterwards, a bi-dimensional macro-modelling approach has been followed in order to calibrate a homogenized equivalent material. Specifically, two models have been constructed, three-dimensional and bi-dimensional, with the intent to reproduce as best as possible the specimen's behaviour and to highlight the differences between two approaches. The homogeneous macro-model shows the same behaviour of the complex model, but has a different computational cost, useful for future analytical applications. For an accurate calibration and experimental comparison of the results given by the numerical models, the tests carried out by (Augenti and Parisi, 2010) [122] on tuff masonry panels have been considered.

9.1 EXPERIMENTAL DATA

The aim of the research carried out by (Augenti and Parisi, 2010) [122] is to define a mathematical model able to describe the non linear behaviour of masonry

panels made by Neapolitan yellow tuff subject to uniaxial compression. The specimens were tested under compression both in the orthogonal and parallel direction to the mortar bed joints. The dimensions of tuff blocks employed in the construction of the specimens are $300 \times 150 \times 100 \text{ mm}^3$, with a unit weight of 12.50 kN/m^3 . A hydraulic mortar with a content of pozzolana with average to low mechanical properties was used. Preliminary tests on both material composing the masonry specimens were carried out, in order to evaluate their mechanical properties. The mean compressive strength of tuff blocks, f_{bm} , is 4.13 MPa , while the Young's modulus and shear modulus are, respectively, $E_b = 1540 \text{ MPa}$ and $G_b = 440 \text{ MPa}$. The mean compressive strength of mortar is $f_{mm} = 2.5 \text{ MPa}$. Masonry panels were built with dimensions of $610 \times 650 \times 150 \text{ mm}^3$.



Figure 9.1. Specimen under uniaxial compressive load along the direction orthogonal to bed joints.

Eight monotonic compressive tests were performed along the direction orthogonal to mortar bed joints, while seven monotonic compressive tests were performed in the direction parallel to mortar bed joints. The considered test set-up,

according to the ASTM C1314-03b and ASTM E11-04, can be employed to carry out tests both under load control and displacement control. In order to read the deformations during the tests, two LVDT (linear variable differential transformers) transducers were employed on both sides of the specimens; the first one orthogonal and the second one parallel to the loading direction. The test set-up is illustrated in Figure 9.1.

In order to elaborate the experimental results, the compressive stress was evaluated as the ratio between the compressive force applied on top of the wall and the area of the horizontal cross-section of the panel, while the axial deformation was calculated as the average displacement given by the transducers and their length. These parameters allowed to obtain the experimental σ - ϵ diagram, reported in Figure 9.2.

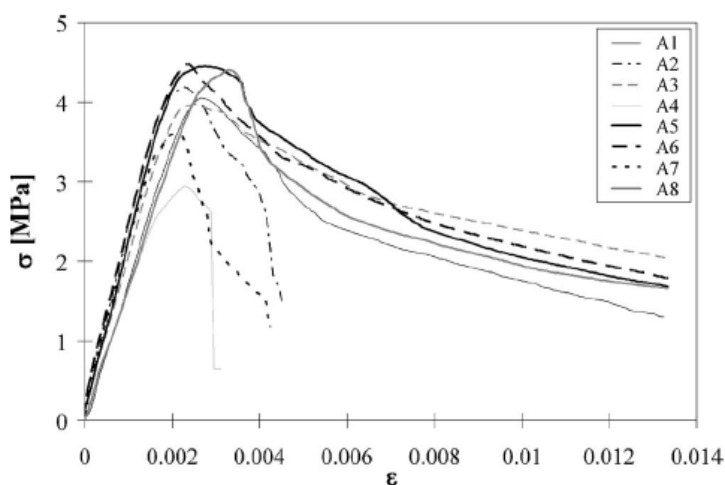


Figure 9.2. Results of the compressive tests along the direction orthogonal to bed joints.

The comparison with the experimental tests shows that the elastic part of the curve is quite well defined and characterized by a low dispersion of data. A higher dispersion of experimental values is found regarding the peak stress. The post-elastic behaviour is much more dispersed, due to the causalities related to the fracture process of the material. As a result, there are higher uncertainties concerning the value of fracture energy. However, the amplitude of the interval of confidence

constructed on the mean curve does not increase, for higher values of strain, as it is shown in Figure 9.3.

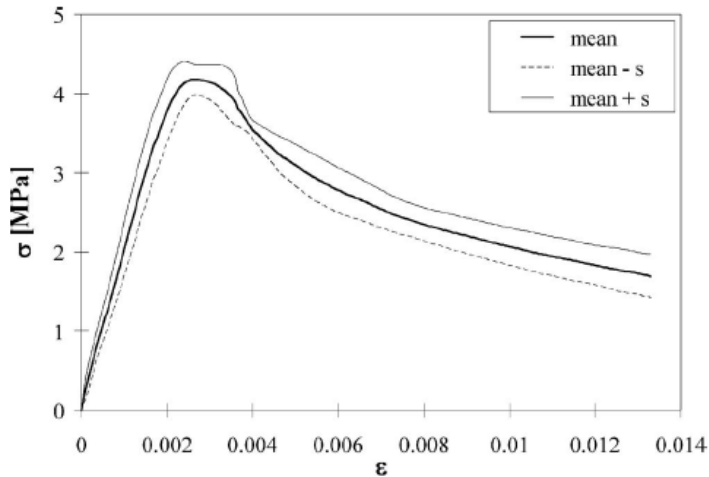


Figure 9.3. Interval of confidence of the mean curve.

Mean values, \bar{x} , standard deviation, s , and the coefficient of variation, CoV , were evaluated with respect to the following values:

σ_p : compressive strength;

σ_r : residual stress;

ϵ_p : strain corresponding to the compressive strength;

ϵ_u : ultimate strain;

$\mu_\epsilon = \epsilon_u / \epsilon_p$: ductility;

$E_{1/3}$: secant modulus corresponding to 1/3 of the compressive strength;

$E_{1/2}$: secant modulus corresponding to 1/2 of the compressive strength;

$\nu_{1/3}$: Poisson's coefficient corresponding to 1/3 of the compressive strength;

$\nu_{1/2}$: Poisson's coefficient corresponding to 1/2 of the compressive strength;

$G_{1/3}$: shear modulus corresponding to 1/3 of the compressive strength;

$G_{1/2}$: shear modulus corresponding to 1/2 of the compressive strength.

The values of such parameters are summarized in Table 9.1.

	σ_p (MPa)	σ_r (MPa)	σ_r/σ_p (%)	ε_p (%)	ε_u (%)	μ_ε
\bar{x}	3.96	1.45	36.4	0.244	1.67	6.57
s	0.50	0.34	5.90	0.022	1.22	4.60
CoV (%)	12.5	23.4	16.2	9.06	73.1	70.0
	$E_{1/3}$ (MPa)	$E_{1/2}$ (MPa)	$\nu_{1/3}$	$\nu_{1/2}$	$G_{1/3}$ (MPa)	$G_{1/2}$ (MPa)
\bar{x}	2,222	2,159	0.22	0.27	917	854
s	372	335	0.06	0.07	162	137
CoV (%)	16.7	15.5	26.8	27.2	17.7	16.1

Table 9.1. Results from compressive tests along the direction orthogonal to bed joints.

According to the same procedure, seven masonry panels with same dimensions were tested under compression along the direction parallel to bed joints, which results are shown in terms of σ - ε behaviour and mechanical parameters are reported in Figure 9.4 and Table 9.2.

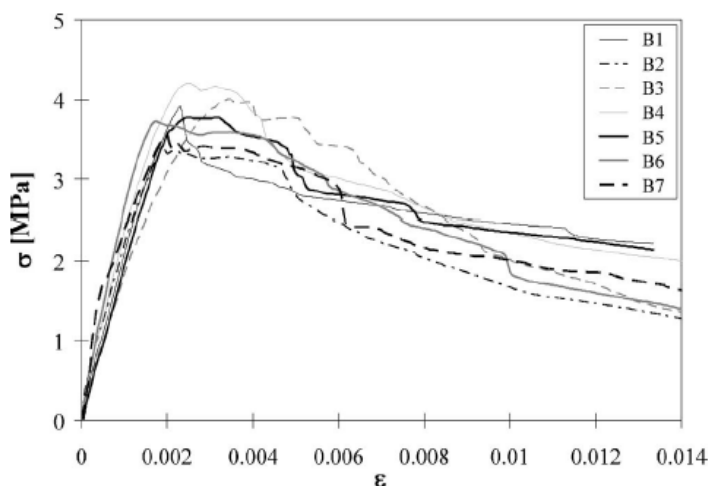


Figure 9.4. Results of the compressive tests along the direction parallel to bed joints.

	σ_p (MPa)	σ_r (MPa)	σ_r/σ_p (%)	ε_p (%)	ε_u (%)	μ_ε
\bar{x}	3.85	1.69	44.0	0.240	2.49	10.6
s	0.21	0.41	10.5	0.055	1.10	4.33
CoV (%)	5.56	24.0	23.8	22.7	44.2	40.7
	$E_{1/3}$ (MPa)	$E_{1/2}$ (MPa)	$\nu_{1/3}$	$\nu_{1/2}$	$G_{1/3}$ (MPa)	$G_{1/2}$ (MPa)
\bar{x}	2,074	2,016	0.24	0.35	857	777
s	258	261	0.20	0.27	186	217
CoV (%)	12.5	12.9	81.9	76.0	21.7	28.0

Table 9.2. Results from compressive tests along the direction parallel to bed joints.

On the basis of the elaboration of experimental values obtained from compressive tests, different curves have been constructed following different analytical procedures: (1) mean and characteristic σ - ε constitutive laws, (2) maximum likelihood σ - ε constitutive law. The former method gives curves obtained by the evaluation of the values of stresses having non exceeding probabilities of 50% and 5%. The latter method gives curves with stresses having the maximum probability of occurrence at each axial strain. Moreover, the non-linear regression curve was derived, with reference to the data set having normal stresses and axial strains normalized to their peak values, for both compression in the direction orthogonal to bed joints and in the direction parallel to bed joints. Such curves were elaborated in order to be used as constitutive laws for macro-modelling of masonry panels by means of finite element methods.

Because of the strong nonlinearity of curves, the writers decided to define constitutive equations by sectioning the data set over two different strain ranges and by applying the least-squares method of estimation. In the following the polynomials defining the compressive constitutive law in the direction orthogonal to bed joints are reported:

$$\bar{\sigma} = -0.7144 \cdot \bar{\varepsilon}^3 + 0.4549 \cdot \bar{\varepsilon}^2 + 1.2595 \cdot \bar{\varepsilon} \quad \text{for } 0 \leq \bar{\varepsilon} \leq 1.12$$

$$\bar{\sigma} = -0.0107 \cdot \bar{\varepsilon}^3 + 0.1388 \cdot \bar{\varepsilon}^2 - 0.6487 \cdot \bar{\varepsilon} + 1.545 \quad \text{for } 1.12 \leq \bar{\varepsilon} \leq 5$$

where:

$$\bar{\sigma} = \frac{\sigma}{\sigma_p}$$

$$\bar{\varepsilon} = \frac{\varepsilon}{\varepsilon_p}$$

These formulations were obtained through an iterative procedure, in such a way to comply with the continuity of the first derivative in the counterflexure point at $\bar{\varepsilon} = 1.12$.

The same procedure was pursued in the case of compression in the direction parallel to bed joints, yielding the following relations:

$$\bar{\sigma} = -0.3593 \cdot \bar{\varepsilon}^3 - 0.2814 \cdot \bar{\varepsilon}^2 + 1.6407 \cdot \bar{\varepsilon} \quad \text{for } 0 \leq \bar{\varepsilon} \leq 1$$

$$\bar{\sigma} = 0.0008 \cdot \bar{\varepsilon}^5 - 0.0168 \cdot \bar{\varepsilon}^4 + 0.1351 \cdot \bar{\varepsilon}^3 - 0.4970 \cdot \bar{\varepsilon}^2 + 0.6739 \cdot \bar{\varepsilon} + 0.702$$

for $1 \leq \bar{\varepsilon} \leq 6$

In the following figures, the theoretical constitutive laws assessed in the described work are compared with the mean curves obtained from the experiments, for the case of compression in the direction orthogonal to bed joints (Figure 9.5(a)) and in the direction parallel to bed joints (Figure 9.5(b)).

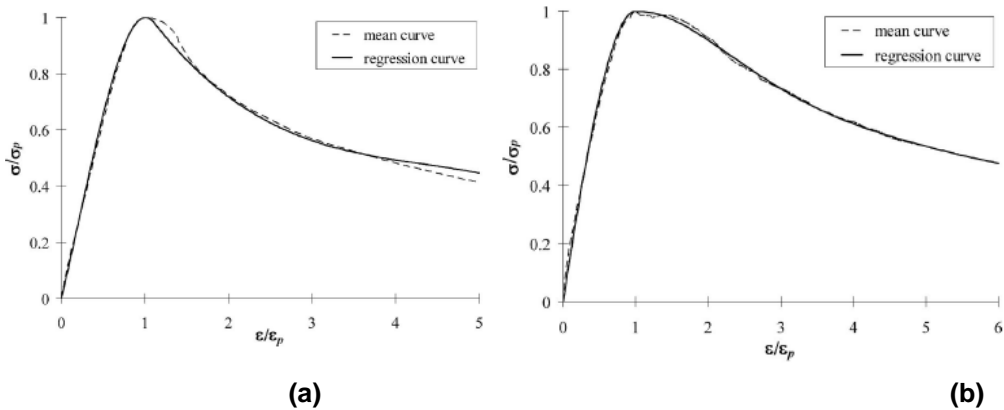


Figure 9.5. Comparison between mean curves from experiments and analytical constitutive model for compressive lading orthogonal (a) and parallel (b) to bed joints.

9.2 THREE-DIMENSIONAL FINITE ELEMENT MICRO-MODELLING OF MASONRY PANELS

The aim to model through finite element methods the masonry panels described in the previous section necessarily implies an analysis and a verification of different modelling approaches given by the code DIANA 9.4.4. In the present work a three-dimensional model has been developed in order to be used in following macro-modelling approaches, unlike other previous cases in which bi-dimensional models and elements have been employed.

The three-dimensional model of the masonry panel subjected to compressive loading in the direction orthogonal to bed joints has been built through a micro-modelling. Mortar joints and units have been described through different sets of non-linear mechanical properties.

Possible approaches for modelling and numerical simulation of non-linear behaviour of fragile or quasi-fragile materials through smeared cracking approaches are basically the following two: a total strain based approach, fixed crack concept or rotating crack concept, and a multi-directional crack approach based on strain decomposition.

9.2.1 Adopted finite elements

The three-dimensional model of the masonry panel subjected to compressive loading has been built using 3-D solid “brick” elements. In this case, both the masonry blocks and the mortar joints composing the structure of the wall are modelled with 20-noded elements. The element used for this purpose is illustrated in Figure 9.6 and is defined by the coordinates of 20 nodes. The employed element is an isoparametric element characterized by a quadratic interpolation of geometry and displacements and Gauss integration. The polynomials for the translations u_{xyz} can be expressed as

$$\begin{aligned}
 u_i(\xi, \eta, \zeta) = & a_0 + a_1\xi + a_2\eta + a_3\zeta + a_4\xi\eta + a_5\eta\zeta \\
 & + a_6\xi\zeta + a_7\xi^2 + a_8\eta^2 + a_9\zeta^2 + a_{10}\xi\eta\zeta + a_{11}\xi^2\eta \\
 & + a_{12}\xi^2\zeta + a_{13}\xi\eta^2 + a_{14}\xi\zeta^2 + a_{15}\eta^2\zeta + a_{16}\eta\zeta^2 \\
 & + a_{17}\xi^2\eta\zeta + a_{18}\xi\eta^2\zeta + a_{19}\xi\eta\zeta^2.
 \end{aligned}$$

Typically, a rectangular brick element approximates the following strain and stress distribution over the element volume. The strain ϵ_{xx} and stress σ_{xx} vary linearly in x direction and quadratically in y and z direction. The strain ϵ_{yy} and stress σ_{yy} vary linearly in y direction and quadratically in x and z direction. The strain ϵ_{zz} and stress σ_{zz} vary linearly in z direction and quadratically in x and y direction. By default DIANA applies a 3x3x3 integration scheme. A suitable option in a patch of more than one element is 2x2x2 which yields optimal stress points. Schemes lower than 2x2x2 or higher than 3x3x3 are unsuitable.

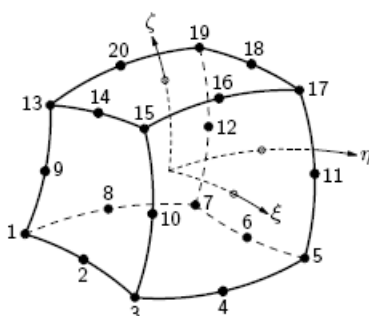


Figure 9.6. Finite Element (CHX60) used for 3-D model of masonry panels.

9.2.2 Adopted non-linear material model

The non-linear model adopted for description of both materials of the masonry panels is a multi-directional fixed crack model. In such model, cracking phenomena occurring in quasi-brittle materials during loading are smeared into continuum and are described through a combination of tension cut-off, tension softening and shear retention.

In particular, the criterion showed in Figure 9.7 has been employed for the modelling of the material behaviour of both joints and units.

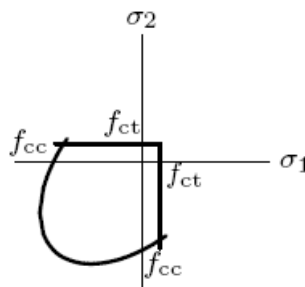


Figure 9.7. Material model adopted for mortar and bricks.

For the tension side, a cut-off based on constant value of strength has been considered, as illustrated in Figure 9.8. Moreover, a linear tension softening has been employed (Figure 9.9), resulting in a crack stress equal to zero at ultimate crack strain.

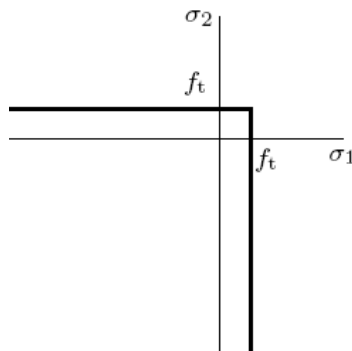


Figure 9.8. Tensile cut-off criterion.

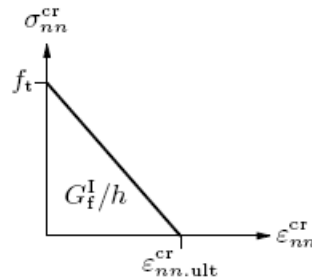


Figure 9.9. Linear tension softening.

In case of linear tension softening the relation of the crack stress is given by:

$$\frac{\sigma_{nn}^{cr}(\varepsilon_{nn}^{cr})}{f_t} = \begin{cases} 1 - \frac{\varepsilon_{nn}^{cr}}{\varepsilon_{nn}^{cr}.ult} & \text{if } 0 < \varepsilon_{nn}^{cr} < \varepsilon_{nn}^{cr}.ult \\ 0 & \text{if } \varepsilon_{nn}^{cr}.ult < \varepsilon_{nn}^{cr} < \infty \end{cases}$$

with a ultimate crack strain equal to:

$$\varepsilon_{nn}^{cr}.ult = 2 \frac{G_f^I}{h f_t}$$

Regarding the shear behaviour, due to the cracking of the material the shear stiffness is usually reduced. This reduction is generally known as shear retention. In case of full shear retention the elastic shear modulus G is not reduced. In case of a reduced shear stiffness, the shear retention factor β is less or equal to one, but greater than zero. In this case a constant shear retention has been adopted, according to Figure 9.10.

For compression a Von Mises criterion has been chosen, which represents a yield condition in terms of a smooth approximation of the Tresca yield condition: a circular cylinder in the principal stress space, as is illustrated in Figure 9.11.

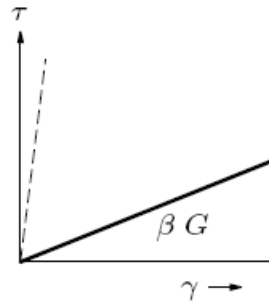


Figure 9.10. Constant shear retention.

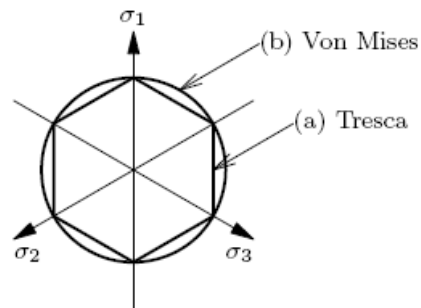


Figure 9.11. Tresca and Von Mises yield conditions.

The yield function of Von Mises is given by the square root formulation:

$$f(\boldsymbol{\sigma}, \kappa) = \sqrt{3J_2} - \bar{\sigma}(\kappa) = \sqrt{\frac{1}{2}\boldsymbol{\sigma}^T \mathbf{P} \boldsymbol{\sigma}} - \bar{\sigma}(\kappa)$$

where $\bar{\sigma}(\kappa)$ is the uniaxial yield strength as a function of the internal state variable κ . The projection matrix \mathbf{P} is given by:

$$\mathbf{P} = \begin{bmatrix} 2 & -1 & -1 & 0 & 0 & 0 \\ -1 & 2 & -1 & 0 & 0 & 0 \\ -1 & -1 & 2 & 0 & 0 & 0 \\ 0 & 0 & 0 & 6 & 0 & 0 \\ 0 & 0 & 0 & 0 & 6 & 0 \\ 0 & 0 & 0 & 0 & 0 & 6 \end{bmatrix}$$

The flow rule is generally given by the associated flow rule $g \equiv f$, which results for the plastic strain rate vector in

$$\dot{\epsilon}^p = \dot{\lambda} \frac{\mathbf{P}\sigma}{2\bar{\sigma}}$$

The non-linear behaviour of materials in compression is described by a parabolic function (Figure 9.12) defined by three characteristic values. The strain $\alpha_c/3$, at which one-third of the maximum compressive strength f_c is reached, is:

$$\alpha_{c/3} = -\frac{1}{3} \frac{f_c}{E}$$

The strain α_c , at which the maximum compressive strength is reached, is

$$\alpha_c = -\frac{5}{3} \frac{f_c}{E} = 5\alpha_{c/3}$$

Finally, the ultimate strain α_u , at which the material is completely softened in compression, is

$$\alpha_u = \alpha_c - \frac{3}{2} \frac{G_c}{h f_c}$$

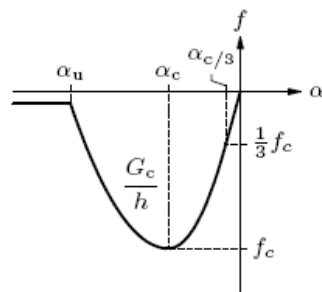


Figure 9.12. Parabolic compressive behaviour.

The parabolic compression curve is finally described by the following formulation:

$$f = \begin{cases} -f_c \frac{1}{3} \frac{\alpha_j}{\alpha_{c/s}} & \text{if } \alpha_{c/s} < \alpha_j \leq 0 \\ -f_c \frac{1}{3} \left(1 + 4 \left(\frac{\alpha_j - \alpha_{c/s}}{\alpha_c - \alpha_{c/s}} \right) - 2 \left(\frac{\alpha_j - \alpha_{c/s}}{\alpha_c - \alpha_{c/s}} \right)^2 \right) & \text{if } \alpha_c < \alpha_j \leq \alpha_{c/s} \\ -f_c \left(1 - \left(\frac{\alpha_j - \alpha_c}{\alpha_u - \alpha_c} \right)^2 \right) & \text{if } \alpha_u < \alpha_j \leq \alpha_c \\ 0 & \text{if } \alpha_j \leq \alpha_u \end{cases}$$

9.2.3 Geometry definition and meshing

Being the masonry wall described via a three-dimensional model, the dimensions of the elements derive directly on the geometric characteristics and the adopted mesh. In particular, the dimensions of the tested walls are 610 x 650 x 150 mm and depends directly on the dimensions of the solid finite elements. The geometry is illustrated in Figure 9.13 and has been constructed with respect to the actual position of masonry units, bed joints and head joints.

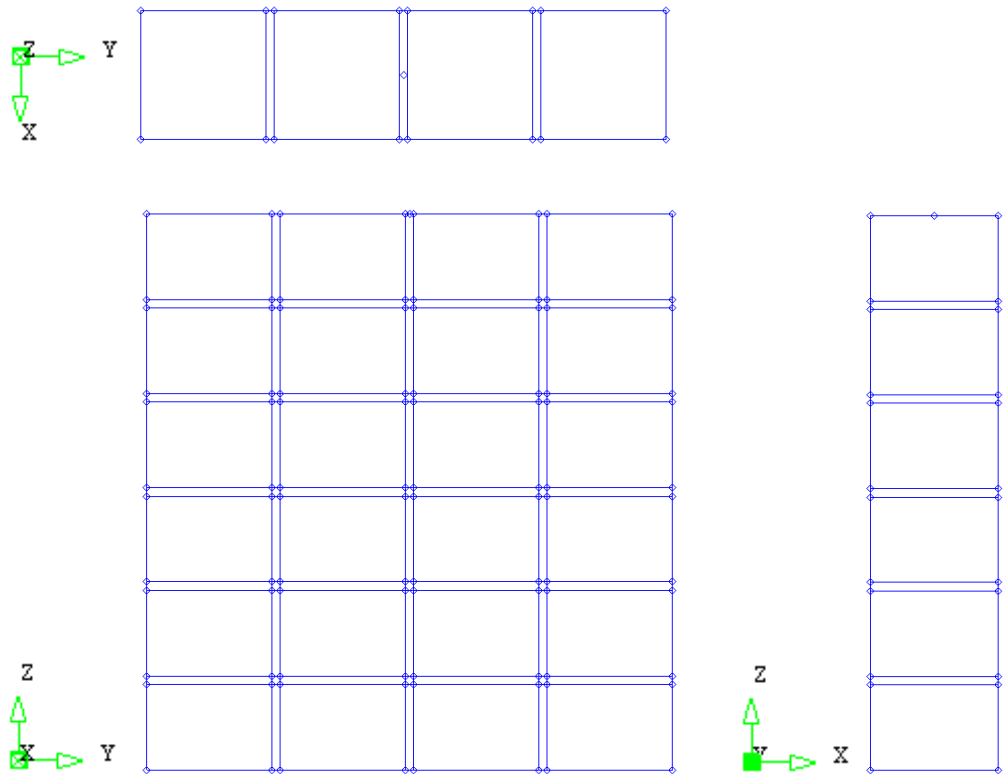


Figure 9.13. Three-dimensional geometry definition for the masonry panel.

The geometry of the panel was then discretized through a three-dimensional mesh of solid elements described in the previous section. In particular, the mesh is composed by 1748 elements, with a total of 8900 nodes, as it can be seen from Figure 9.14. Regarding the dimensions of the finite elements, the meshing division resulted in a size (X, Y, Z) of $33.33 \times 36.25 \times 37.5 \text{ mm}^3$ for the biggest unit element and $33.33 \times 36.25 \times 10 \text{ mm}^3$ for the biggest joint element.

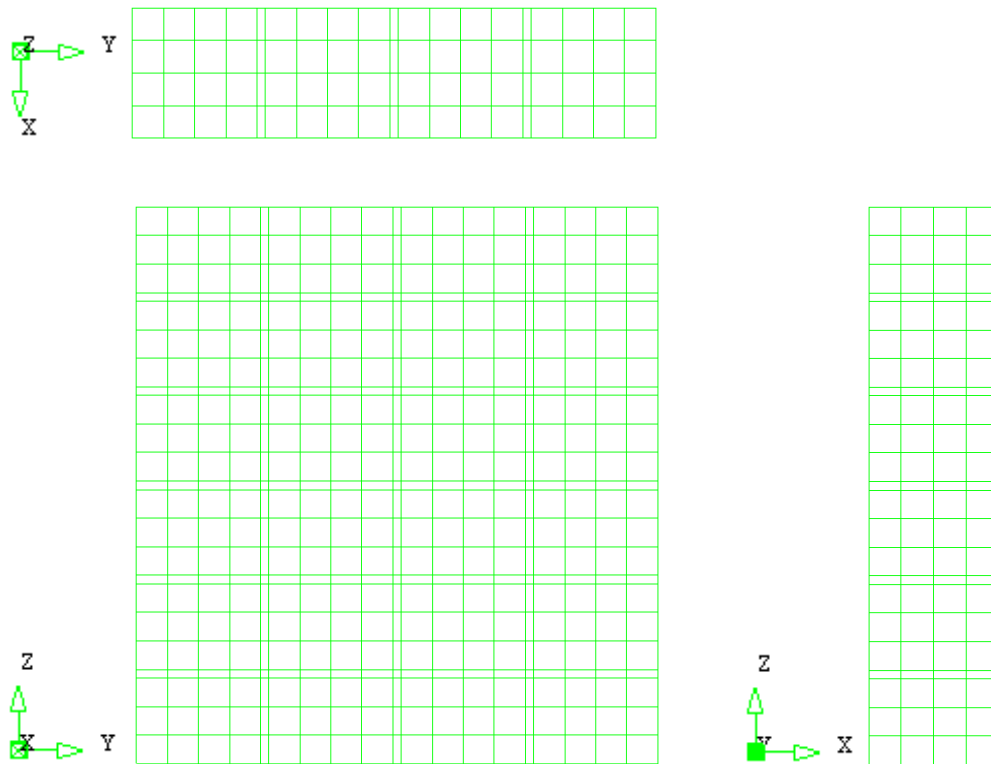


Figure 9.14. Three-dimensional mesh division for the masonry panel.

In order to reproduce the actual constraint conditions during the experimental test of the panels, high attention has been paid to the modelling of constraints imposed onto the model. The base of the panel has been considered fixed, in order to reproduce the impossibility of the element to translate upon the application of compressive loading. For all the nodes belonging to the top face of the wall, a rigid constraint in the same direction of the applied vertical load has been defined, in order to assure a uniform vertical displacement to the top of the wall during the analysis, as imposed by the presence of the top rigid beam. Since the top rigid beam is a C steel profile, the displacements of the nodes on the top surface of the wall have been constrained in X direction, while it has been chosen to leave free the possible displacements in the Y direction. Since the analysis carried out is a non-linear

analysis, due to the high non-linearity of the material, it has been chosen to apply a load in terms of control of displacement on top surface of the panel.

As previously outlined, the modelling of the panels has been carried out taking into account the presence of masonry blocks and mortar joints, allowing the assignment of different material properties for both elements. In Figure 9.15 the model, with the assignment of different materials for blocks and joints is illustrated. A three-dimensional view of the model in terms of geometry, mesh and materials assignment is reported in Figure 9.16.

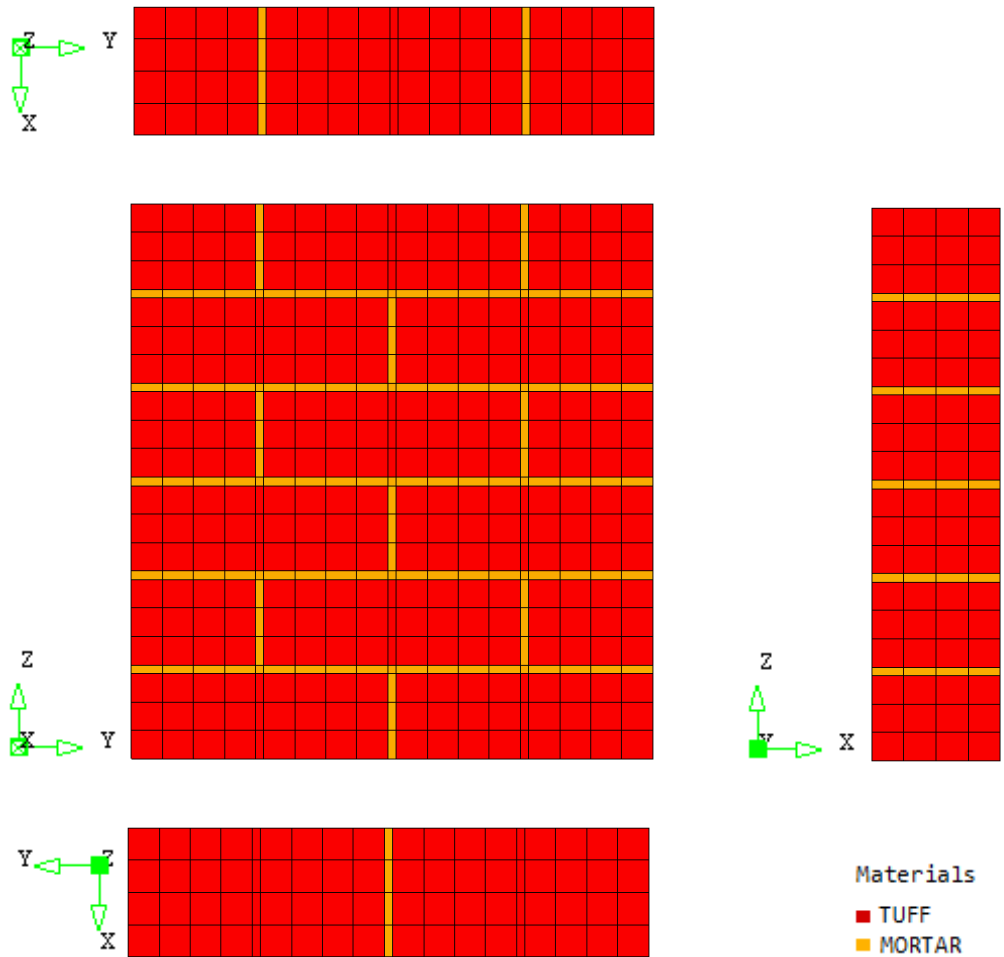


Figure 9.15. Material assignment for the masonry panel.

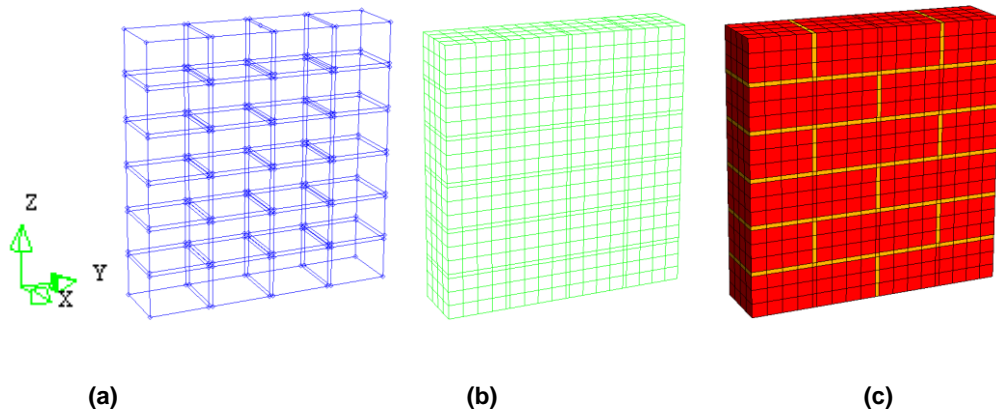


Figure 9.16. Three-dimensional modelling of the masonry panel: geometry definition (a), meshing (b) and material assignment (c).

9.3 RESULTS AND COMPARISONS WITH EXPERIMENTAL CURVES

From experimental tests for mechanical characterization of materials employed to build the masonry panels described in the work by (Augenti and Parisi, 2010) [122] the following values have been obtained: the masonry blocks made by Neapolitan yellow tuff have a unit weight $\rho = 12.50 \text{ kN/m}^3$, the mean compressive strength of tuff stone is $f_{bm} = 4.13 \text{ MPa}$, the Young's modulus of tuff stone is $E_b = 1540 \text{ MPa}$, while the shear modulus is $G_b = 444 \text{ MPa}$. The mean compressive strength of pozzolana-based mortar is $f_{mm} = 2.5 \text{ MPa}$. The mechanical properties have been summarized in Table 9.3, together with other mechanical parameters adopted in the numerical modelling. Such parameters have been found in the literature (Parisi et al., 2012) [123] and regarding the same materials employed in the present model. Regarding the Modulus of elasticity of the materials, as it is reported in the table, a value of 2200 MPa has been assumed for both materials, since using the values given in the table the results from the numerical models in terms of non-linear $\sigma - \varepsilon$ curves are less stiff than the experimental ones. The value of 2200 MPa represents the value of the secant modulus of elasticity of between 1/3 and 1/2 of the compressive strength obtained from the tests on the masonry panels tested by (Augenti and Parisi, 2010) [122] in the direction orthogonal to bed joints.

Material	Tensile strength	Compressive strength	Young's modulus	Shear modulus
	f_t [MPa]	f_c [MPa]	E [GPa]	G [GPa]
Tuff	0.23	4.13	1.54	0.44
Mortar	1.43	2.50	1.52	0.66

Table 9.3. Mechanical properties for tuff units and mortar joints (Parisi et al., 2012) [123].

In the following some results in terms of $\sigma - \varepsilon$ curves are reported. The curves have been obtained by means of a non-linear analysis on the masonry panel modelled with the characteristics described in the previous section. The analysis have been conducted in control of displacement. The vertical displacement was divided by the panels' height, while the axial reaction was divided by the horizontal cross-section of the wall.

All the cases reported in the following plots have been obtained considering the following parameters for the model, which were kept constant (Table 9.4). As it can be noticed, the only parameters left undetermined are the compressive fracture energies of both elements composing the masonry wall. Such parameters have been calibrated in order to get a proper fitting of the numerical non-linear curve with the experimental ones.

Element	Young's modulus	Poisson's coefficient	Shear retention factor	Tensile strength	Tensile fracture energy	Ultimate tensile strain	Compressive strength
	E [MPa]	ν [-]	β [-]	f_t [MPa]	G_{ft} [N/mm]	$\varepsilon_{t,ult}$ [-]	f_c [MPa]
Joint	2200	0.15	0.20	0.23	0.0103	1.28E-03	2.50
Unit	2200	0.15	0.20	1.43	0.00257	7.31E-04	4.13

Table 9.4. Mechanical properties for tuff units and mortar joints assumed in the model.

In Figure 9.17 the results of three cases are reported. In particular, the compressive fracture energy $G_{fc,b}$ of tuff blocks was set to a value of 6.0 N/mm, while three different values for the compressive fracture energy $G_{fc,j}$ of mortar joints have been considered, as it is reported in Table 9.5. It can be noticed that the stiffness of

the stress-strain curve given by the model is in good agreement with the average stiffness of the experimental curves. Also in terms of strength the model gives a good result, being the peak value of the numerical curve very similar to the value of the regression curve and to the strength measured from the experiments. The effect of the relative values of compressive fracture energies of mortar joints and tuff blocks can be seen in the post-peak behaviour of the models. If the compressive fracture energy of the blocks is kept constant, the influence of the compressive fracture energy of the mortar joints can be seen.

Case	Element	
	Joint	Unit
	$G_{fc,j}$ [N/mm]	$G_{fc,b}$ [N/mm]
1	0.8	6.0
2	1.0	6.0
3	1.5	6.0

Table 9.5. Compressive fracture energy for tuff units and mortar joints assumed in the model.

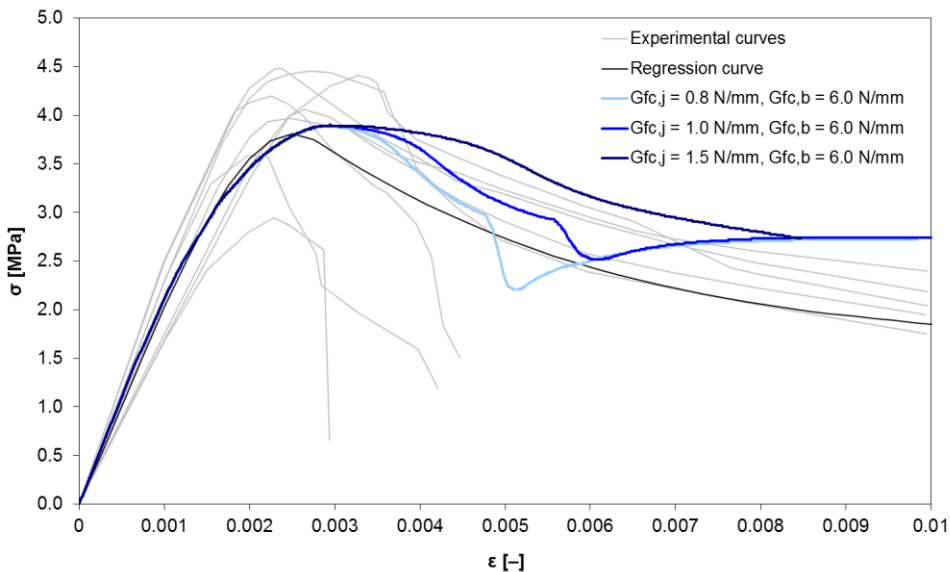


Figure 9.17. Comparison between the numerical curves obtained for $G_{fc,b} = 6.0$ N/mm and the experimental results.

In Figure 9.18 the results of two more cases are illustrated. For these cases, the compressive fracture energy $G_{fc,b}$ of tuff blocks was set to a value of 3.2 N/mm, lower than the previous cases, while two different three values for the compressive fracture energy $G_{fc,j}$ of mortar joints have been considered, as it is reported in Table 9.6. With respect to the curves obtained in the previous analyses, in this case it is noticed that, for a value of compressive fracture energy of the joints of 0.8 N/mm, the effect of the compressive fracture energy of the blocks is negligible. Instead, for a higher value of compressive fracture energy of the joints, it is noticed that a higher value of compressive fracture energy of the blocks allow the non-linear curve to keep a higher resistance when the deformation increases in the post-peak branch.

Case	Element	
	Joint	Unit
	$G_{fc,j}$ [N/mm]	$G_{fc,b}$ [N/mm]
4	0.8	3.2
5	1.0	3.2

Table 9.6. Compressive fracture energy for tuff units and mortar joints assumed in the model.

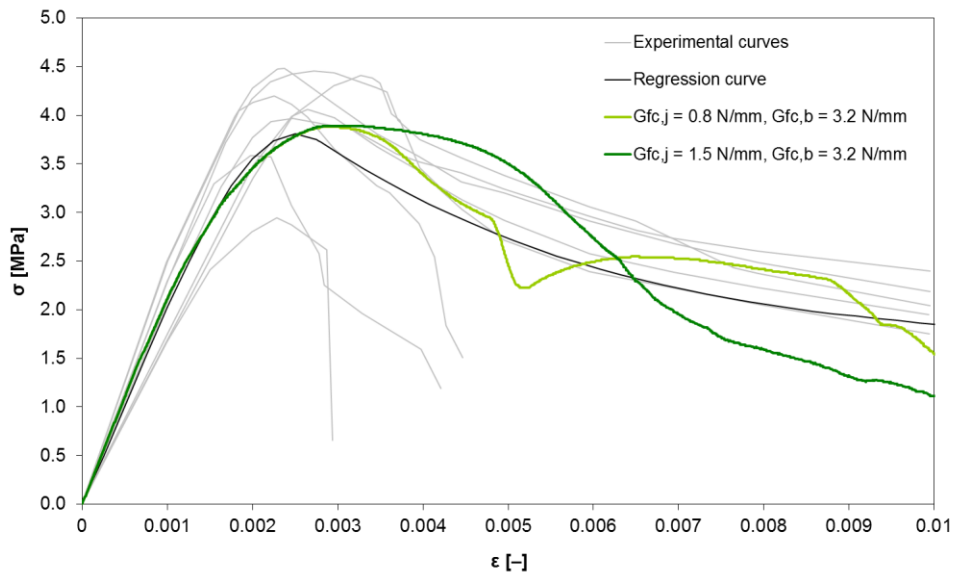


Figure 9.18. Comparison between the numerical curves obtained for $G_{fc,b} = 3.2$ N/mm and the experimental results.

In Figure 9.19 a final case is reported, obtained considering a compressive fracture energy $G_{fc,b}$ of tuff blocks of 4.5 N/mm and a compressive fracture energy $G_{fc,j}$ of mortar joints of 1.5 N/mm, as reported in Table 9.7. The curve obtained from this analysis fits quite well the experimental curves in terms of stiffness, compressive strength and softening behaviour.

Case	Element	
	Joint	Unit
	$G_{fc,j}$ [N/mm]	$G_{fc,b}$ [N/mm]
6	1.5	4.5

Table 9.7. Compressive fracture energy for tuff units and mortar joints assumed in the model.

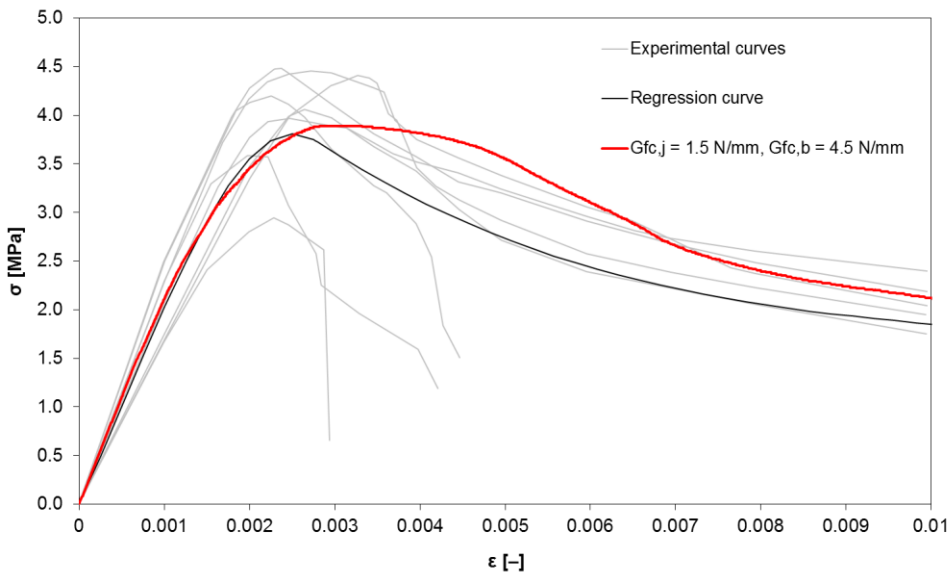


Figure 9.19. Comparison between the numerical curve obtained for $G_{fc,j} = 1.5$ N/mm and $G_{fc,b} = 4.5$ N/mm and the experimental results.

9.4 EQUIVALENT BIDIMENSIONAL FINITE ELEMENTS MACRO-MODELLING OF MASONRY PANELS

A bi-dimensional macro-model of the tested panels has been constructed and a homogenized equivalent material has been calibrated starting from the results obtained from the analyses on the three-dimensional detailed model. The reduced computational cost of the simplified model is useful for future analytical applications.

The bi-dimensional model of the masonry panel has been built using 2-D flat plane stress elements (membrane elements). With reference to Figure 9.20, these elements must be plane (the coordinates of the element nodes must be in one flat plane, the xy plane of the element). They must be thin (the thickness t must be small in relation to the dimensions b in the plane of the element). Loading F must act in the plane of the element. Plane stress elements are characterized by the fact that the stress components perpendicular to the face are zero: $\sigma_{zz} = 0$. These elements may only be applied if there is no bending outside the plane of the structure.

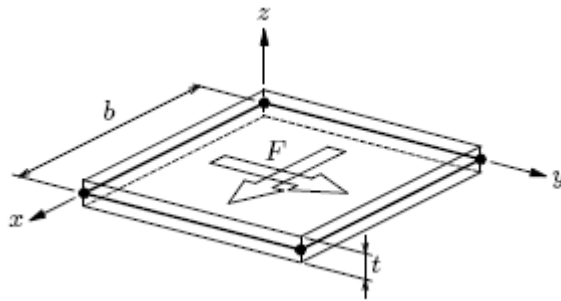


Figure 9.20. Flat plane stress element.

The element used in the bi-dimensional model is illustrated in Figure 9.21 and is an eight-node quadrilateral isoparametric plane stress element. It is based on quadratic interpolation and Gauss integration. The polynomial for the displacements u_x and u_y can be expressed as:

$$u_i(\xi, \eta) = a_0 + a_1\xi + a_2\eta + a_3\xi\eta + a_4\xi^2 + a_5\eta^2 + a_6\xi^2\eta + a_7\xi\eta^2$$

Typically, this polynomial yields a strain ϵ_{xx} which varies linearly in x direction and quadratically in y direction. The strain ϵ_{yy} varies linearly in y direction and quadratically in x direction. The shear strain γ_{xy} varies quadratically in both directions. By default Diana applies 2x2 integration which yields optimal stress points, 3 x 3 is a suitable option. Schemes higher than 3 x 3 are unsuitable.

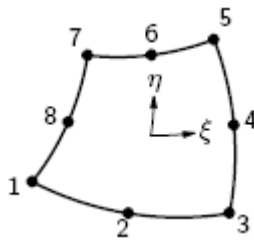


Figure 9.21. Finite Element (CQ16M) used for 2-D model of masonry panels.

The geometry of the panels is illustrated in Figure 9.22(a), and is made by surfaces having overall dimension of 610 x 650 mm. The thickness of the wall is equal to 150 mm and is given as an attached property to the shell elements. As illustrated in Figure 9.22(b), the mesh of the panel is composed by 440 elements, with a total of 1405 nodes. The dimensions (X, Y) of the elements is 30.50 x 29.55 mm².

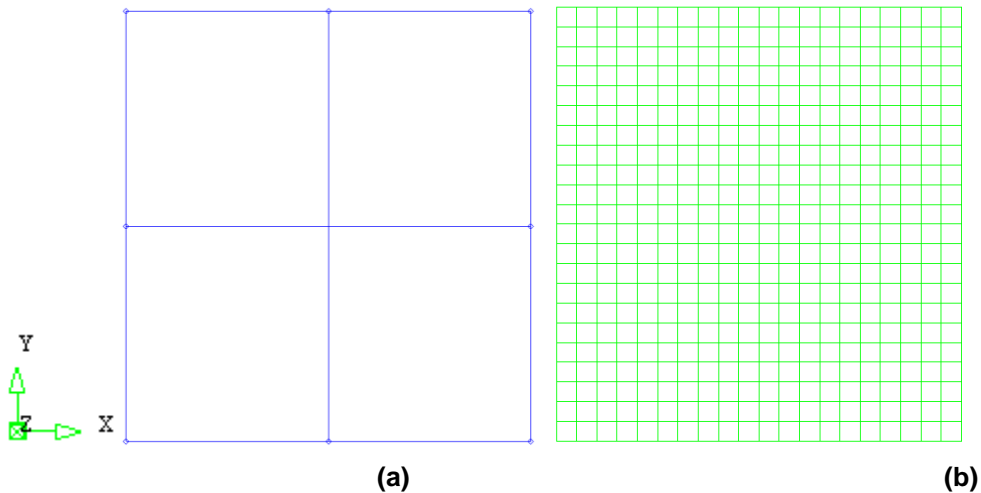


Figure 9.22. Two-dimensional geometry definition (a) and meshing (b) for the masonry panel.

The actual constraint conditions of the panel during the experiments have been assigned to the model: the base of the panel has been considered fixed, since element cannot translate during application of compressive loading, while all the nodes belonging to the top line of the model have been constrained by means of a rigid beam in the direction of the applied vertical load. The possible displacements in the X direction have been left free.

Regarding the material used in the bi-dimensional modelling of the panels, the same non-linear model used in the detailed three-dimensional model has been adopted. The cracking model is again a multi-directional fixed crack model, defined by a tension cut-off according to Rankine, a constant shear retention, and a Von Mises criterion for compression. Also in this case the tension softening law is linear up to the ultimate tensile strain, while for non-linear compression behaviour the $\sigma - \epsilon$ curve obtained from the analysis on the three-dimensional model reported in Figure 9.19 is assumed for a comparison.

The homogeneous material employed in the analysis has a Young's modulus $E = 2200$ MPa and a Poisson's coefficient $\nu = 0.15$. The tensile strength assumed for the homogeneous material is the lowest value of tensile strength between two materials constituting the masonry wall, mortar and tuff, and it is equal to $f_t = 0.23$ MPa, corresponding to tuff units. For the ultimate tensile strain it has been considered the value corresponding to the mortar, which is the lowest value between the two components the masonry. This assumption resulted in a tensile fracture energy $G_{ft} = 2.146 \cdot 10^{-3}$ N/mm for the homogeneous material. The mechanical properties employed for the definition of the homogenous material are summarized in Table 9.8.

Young's modulus	Poisson's coefficient	Shear retention factor	Tensile strength	Tensile fracture energy	Ultimate tensile strain
E [MPa]	ν [-]	β [-]	f_t [MPa]	G_{ft} [N/mm]	$\epsilon_{t,ult}$ [-]
2200	0.15	0.20	0.23	$2.146 \cdot 10^{-3}$	7.31E-04

Table 9.8. Mechanical properties for the homogeneous material assumed in the model.

In Figure 9.23 the result in terms of $\sigma - \epsilon$ curve obtained from the analysis on the bi-dimensional model. The constitutive curve is compared with the $\sigma - \epsilon$ curve

obtained from the detailed three-dimensional model, showing good agreement. The choice of mechanical parameter previously discussed evidences the negligible effect of the tensile properties and the important role of the compressive behaviour in the constitutive curve of the wall.

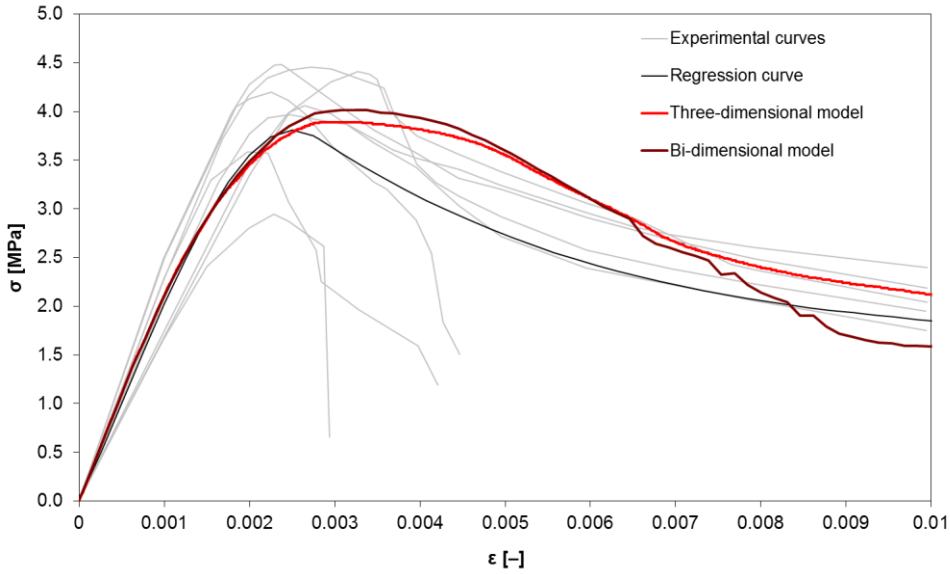


Figure 9.23. Comparison between bi-dimensional homogeneous model and detailed three-dimensional model.

10 NUMERICAL MODELLING OF MASONRY PANELS TESTED AT THE ITAM AND EFFECT OF THE FRP REINFORCED MORTAR LAYER

The present chapter deals with the numerical modelling via finite element method of masonry panels subjected to cyclic in-plane loading tested at the Institute of Theoretical and Applied Mechanics (ITAM) of Prague (Czech Republic). The details of the experimental campaign on masonry walls, the geometrical and mechanical characteristics of the panels and the results obtained from the tests have been described in Chapter 5 of the present work.

The unreinforced masonry panel made by adobe bricks has been modelled first and the non-linear mechanical parameters of the material have been calibrated by comparison with the global force – displacement curve obtained from the experiments, as well as with the cracking and damage pattern experienced by the wall. A macro-modelling technique has been considered and a homogeneous material has been calibrated in which the effect of the characteristics of mortar joints and masonry units are smeared. For this purpose, the non-linear finite element code DIANA 9.4.4 [121] has been employed.

Afterwards, the panels strengthened by means of mortar layers reinforced with composite grids applied on both surfaces have been modelled. The reinforcement has been modelled by means of an equivalent grid embedded in a surface representing the layer of mortar applied to the wall's faces.

The effect of the reinforcement on the strength and displacement capacity of the wall is evidenced through the analysis of the reinforced wall disregarding the presence of the mortar and taking into account the mortar layers only. Also, the case of strengthening made by means of a glass FRP grid is investigated evidencing the

potential effect of a different amount of reinforcement in the overall capacity of the wall. Thus, a parametric analysis has been carried out considering two types of masonry materials characterized by different values of strength, namely adobe brick masonry and tuff block masonry, and three values of shape factor for the wall, namely 1.0, 1.3 and 2.0, in order to investigate the effect of the reinforcement on elements which may have failure modes dominated by shear or flexure.

10.1 MODELLING OF THE UNREINFORCED MASONRY PANEL

For modelling of unreinforced masonry panels a simplified bidimensional model has been constructed. The unreinforced adobe brick masonry panel first has been modelled by means of a macro-modelling technique. The mechanical characteristics of mortar joints and masonry units are smeared into a continuous equivalent material. The non-linear characteristics of the equivalent material have been calibrated through the comparison with the results from the experimental tests.

As previously described, the masonry walls have been tested under the application of a vertical prestressing load and afterwards a cyclic in-plane horizontal load was added. In order to keep the model as simple as possible, it has been subjected to the vertical load, as in the experiments, while the horizontal load has been monotonically increased.

The results from the modelling of the unreinforced panel, will then considered for the modelling of the walls reinforced by means of polymeric grids embedded in a layer of mortar.

10.1.1 Adopted finite elements

The finite elements employed in the modelling of the walls are bi-dimensional flat plane stress elements (membrane elements), which are thin elements (the thickness is small compared to the dimensions in the plane), the loading lays in the plane of the element and the stress components perpendicular to the face are zero.

In particular, an eight-node quadrilateral isoparametric plane stress element (Figure 10.1) has been considered, based on quadratic interpolation and Gauss integration. The polynomial for the displacements u_x and u_y can be expressed as:

$$u_i(\xi, \eta) = a_0 + a_1\xi + a_2\eta + a_3\xi\eta + a_4\xi^2 + a_5\eta^2 + a_6\xi^2\eta + a_7\xi\eta^2$$

Typically, this polynomial yields a strain ϵ_{xx} which varies linearly in x direction and quadratically in y direction. The strain ϵ_{yy} varies linearly in y direction and quadratically in x direction. The shear strain γ_{xy} varies quadratically in both directions.

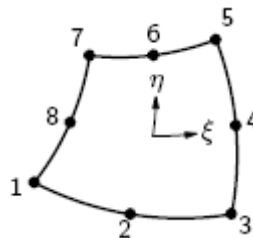


Figure 10.1. Finite Element (CQ16M) used for 2-D model of masonry panels.

10.1.2 Adopted non-linear material model

A common modelling strategy employed for description of the behaviour of fragile and quasi-fragile materials is based on the combination of a smeared cracking model for the tensile behaviour with a plasticity model for compressive behaviour. However, it was noticed that when an element is subjected to simultaneous tensile and compressive stress states, such kind of modelling may be affected by numerical convergence problems.

In order to describe the behaviour of quasi-fragile materials, such as masonry, it is possible to consider the Rankine Principal Stress model, which is able to handle combined tension and compression. The behaviour of elements subjected to a bi-axial stress state, in which tension and compression along two principal directions arise simultaneously in one stress point, can be modelled through the

yielding criterion according to Rankine coupled with a yielding criterion for compression according to Von Mises or Drucker-Prager, for example.

With reference to the bidimensional model of the masonry panels, the material description was made on the basis of a Rankine/Von Mises criterion, as illustrated in Figure 10.2, considering an exponential softening law for tension, see Figure 10.3(a), and a parabolic softening law for compression, see Figure 10.3(b), based on fracture energy.

The combination of yield conditions of Rankine and Von Mises, for description of tensile and compressive regime, respectively, is suitable to describe biaxial stress states and is especially applicable to plane stress states. The combined yield surface is given by:

$$f_1(\sigma, \kappa_1) = \sqrt{\frac{1}{2}\sigma^T P_{ra} \sigma} + \frac{1}{2}\pi_1^T \sigma - \bar{\sigma}_1(\kappa_1)$$

$$f_2(\sigma, \kappa_2) = \sqrt{\frac{1}{2}\sigma^T P_{vm} \sigma} - \bar{\sigma}_2(\kappa_2)$$

$$f_3(\sigma, \kappa_3) = \pi_3^T \sigma - \bar{\sigma}_3(\kappa_3)$$

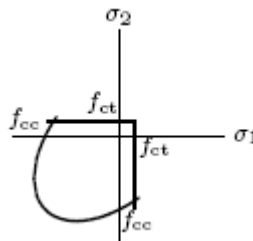


Figure 10.2. Rankine/Von Mises plasticity model used for brick masonry panels.

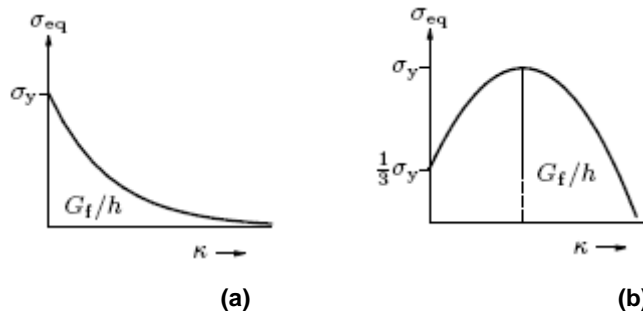


Figure 10.3. Adopted non-linear laws: exponential tensile softening (a) and parabolic compressive law (b).

10.1.3 Geometry definition and meshing

The unreinforced brick masonry panels has been described though a bidimensional model. The geometry is illustrated in Figure 10.4(a), and is made by a surface having dimensions of 1050 x 1367 mm. The thickness of the wall is equal to 240 mm and is given as an attached property to the shell elements. As can be seen from Figure 10.4(b), the mesh of the panel is composed by 2401 elements, with a total of 7400 nodes. The dimensions (X, Y) of the elements is 21.49 x 27.90 mm².

The actual constraint conditions of the panel during the experiments have been assigned to the model: the base of the panel has been considered fixed, since element cannot translate during application of compressive loading, while to all the nodes belonging to the top line of the model has been applied a rigid beam constraint in the direction of the applied horizontal load.

The model has been loaded through the application of the dead weight, depending of the unit weight of the materials used for mortar and bricks, a vertical prestressing load on top equal to 80 kN, which was kept constant during the application of the horizontal load. Such load was applied in terms of displacement and was monotonically increased during the non-linear analysis, which was carried out under displacement control. The application of constraints and loads, respectively, is illustrated in Figure 10.4(b) and Figure 10.4(c).

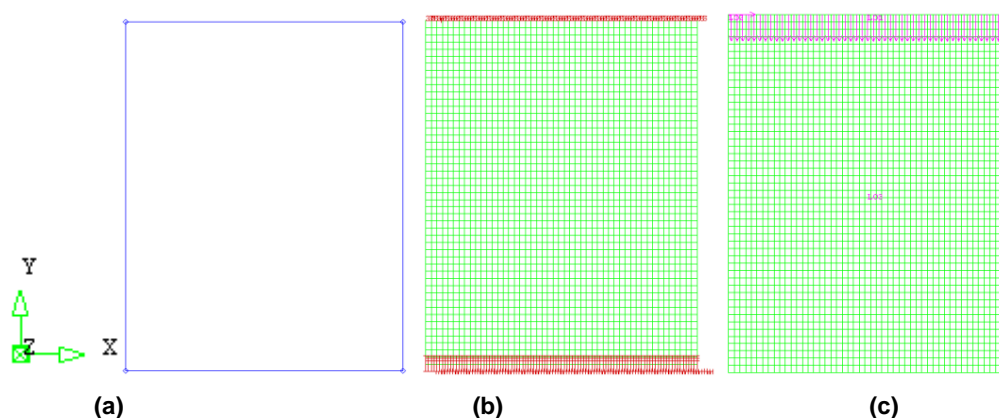


Figure 10.4. FE model of adobe masonry panel: geometry definition (a), mesh and constraints assignment (b) and loading conditions (c).

10.2 RESULTS AND COMPARISONS WITH EXPERIMENTAL TESTS

The characterization tests provided information about mechanical parameters of materials employed to build the masonry panels tested under in-plane cyclic loading.

In the following, the mechanical properties assumed in the model of the unreinforced masonry panels made by adobe bricks are reported. The unit weight assumed for the equivalent homogeneous material is $\rho = 22.0 \text{ kN/m}^3$. The strengths of the homogeneous material have been assumed on the basis of the results of the numerical modelling of the masonry panels tested under compressive loading, described in Chapter 9, for which a ratio of about 90% between the compressive strength of the composite material (blocks + joints) and the compressive strength of the blocks was found. The tensile strength of the mortar joints was found not to influence the numerical results. Therefore, the tensile strength assumed for the homogeneous material of the adobe panels, is the value of tensile strength corresponding to adobe bricks, which is equal to $f_t = 1.66 \text{ MPa}$, while for the compressive strength a reduced value of 90% of the compressive strength of adobe bricks, equal to $f_c = 2.67 \text{ MPa}$, has been assumed.

As previously described, before the application of the horizontal load, a vertical prestressing load of 80 kN evenly distributed on top of the wall was applied. In this phase, the deformation characteristics of the masonry wall were obtained by means of the data recorded by four LVDT transducers placed on the panel's surface. The modulus of elasticity of the adobe brick masonry wall in the direction orthogonal to bed joints was ranging from a value of 1000 MPa to 1500 MPa. An average value $E = 1300 \text{ MPa}$ was assumed for the equivalent homogenous material employed in the model.

The described mechanical parameters are summarized in Table 10.1, and have been kept constant during the analyses for calibration of both tensile and compressive fracture energies of the equivalent material. These parameters have been evaluated in order to get a satisfactory approximation of the experimental force – displacement curve. Different cases of non-linear analysis have been run in order to investigate the effect of such parameters. In particular, the effect of the compressive

fracture energy on the non-linear behaviour of the panel has been examined, and some cases of analysis are reported in Table 10.2.

A value of 0.01 N/mm has been assumed for the fracture energy in tension, following the values proposed by (Lourenço, 1996) [9] for types of masonry with similar value of strength, and being close to the value of fracture energy adopted for mortar joints in the model of masonry panels subjected to compression, studied in Chapter 9. The assumed value of tensile fracture energy has been kept constant, while different values have been considered for the compressive fracture energy, adopted according to the recommendations given by (Lourenço, 2009) [124] in the case of material with compressive strength values below 12 MPa. In this case, the ductility index d_u , measured as the ratio between the fracture energy and the strength (in tension or compression), is equal to 1.6 mm, yielding to a value of compressive fracture energy of about 4 N/mm. The value recommended by Lourenço has been assumed to be a upper bound for the assumed interval of values for the compressive fracture energies, ranging from 2.0 N/mm to 4.0 N/mm, and also similar to the compressive fracture energy of the tuff calibrated in the previous Chapter.

Unit weight	Young's modulus	Poisson's coefficient	Tensile strength	Compressive Strength
ρ [kN/m ³]	E [MPa]	ν [-]	f_t [MPa]	f_c [MPa]
22.0	1300	0.15	1.66	2.67

Table 10.1. Mechanical properties for the equivalent material assumed in the model of unreinforced masonry wall.

Case	Tensile fracture energy	Compressive fracture energy
	G_{ft} [N/mm]	G_{fc} [N/mm]
1	0.01	2.0
2	0.01	3.0
3	0.01	4.0

Table 10.2. Cases of fracture energies for $G_{ft} = 0.01$.

The non-linear curves obtained from the analyses are plotted in Figure 10.5. In the figures the couple of values of tensile and compressive fracture energies (G_{ft} , G_{fc}) are directly reported. From the plot it is noticed that the effect of the compressive fracture energy is negligible. However, the trend is an increase of shear strength and a less sharp softening branch as the fracture energy increases.

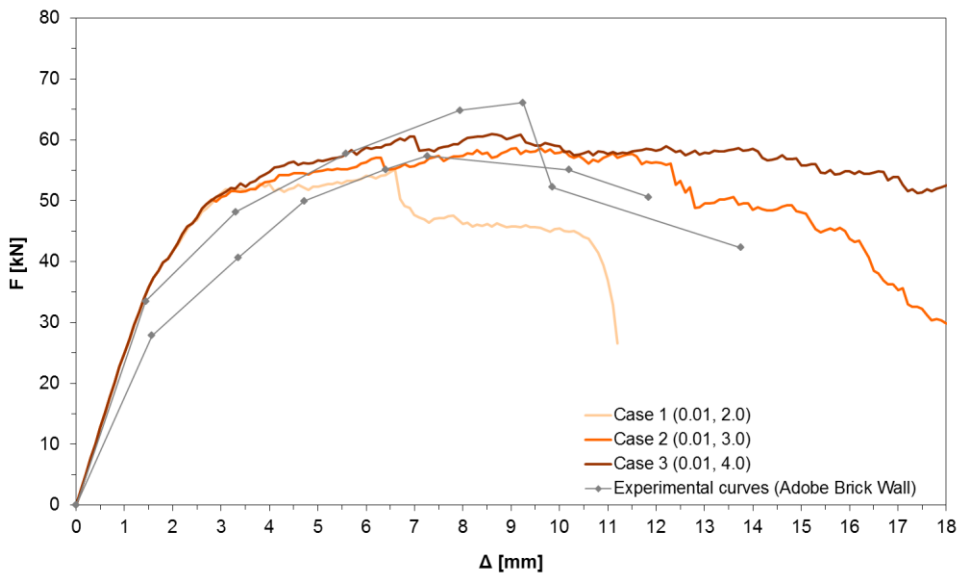


Figure 10.5. Comparison between numerical curves obtained for different values of compressive fracture energy ($G_{ft} = 0.01$ N/mm).

The effect of the tensile fracture energy has been studied as well. In this case, further non-linear analyses have been run for a level of compressive fracture energy of 3.0 N/mm. As summarized in Table 10.3, the compressive fracture energy is kept constant, while different values of tensile fracture energy have been assumed. With respect to the case of $G_{ft} = 0.01$ N/mm, three more values have been considered for the tensile fracture energy, considering variations of -10% (0.009 N/mm), +10% (0.011 N/mm) and +20% (0.012 N/mm). The results of the analysis are illustrate in Figure 10.6, evidencing that there is a relevant effect of the tensile fracture energy on the shear strength of the masonry panels, much higher than in the case of variation of

the compressive fracture energy. In particular, the shear strength increases as the fracture energy in tension increases.

Case	Tensile fracture energy	Compressive fracture energy
	G_{ft} [N/mm]	G_{fc} [N/mm]
4	0.009	3.0
2	0.010	3.0
5	0.011	3.0
6	0.012	3.0

Table 10.3. Cases of fracture energies for $G_{fc} = 3.0$ N/mm.

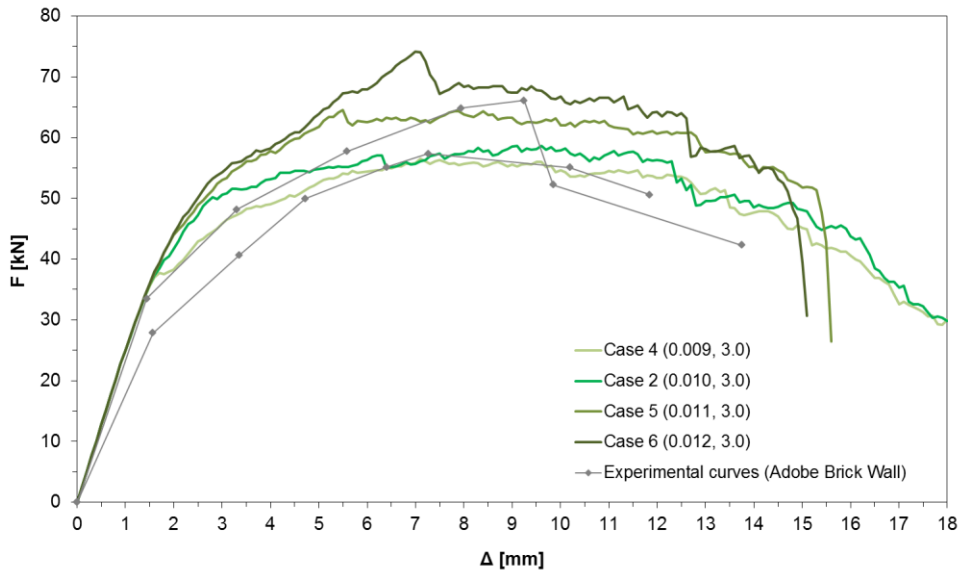


Figure 10.6. Comparison between numerical curves obtained for different values of tensile fracture energy ($G_{fc} = 3.0$ N/mm).

On the basis of the behaviour of the non-linear curves when varying the values of tensile and compressive fracture energies, three further cases of analysis have been finally considered, in order to calibrate the fracture energies for a best fitting with the experimental force – displacement curves. In Figure 10.7 the results of these three cases are reported. In particular, three sets of tensile fracture energy G_{ft}

and compressive fracture energy G_{fc} have been considered, as reported in Table 10.4, which allow to get numerical curves very close to the experimental ones. Finally, in Figure 10.8, the curve corresponding to $G_{ft} = 0.011$ N/mm and $G_{fc} = 2.8$ N/mm (Case 8) has been chosen as the best fitting one. For the same case, the constitutive diagram describing the isotropic stress – strain behaviour of the homogenized material are reported for tension (Figure 10.9(a)) and compression (Figure 10.9(b)).

Case	Tensile fracture energy	Compressive fracture energy
	G_{ft} [N/mm]	G_{fc} [N/mm]
7	0.012	2.9
8	0.011	2.9
9	0.011	2.8

Table 10.4. Combination of tensile and compressive fracture energies assumed in the model.

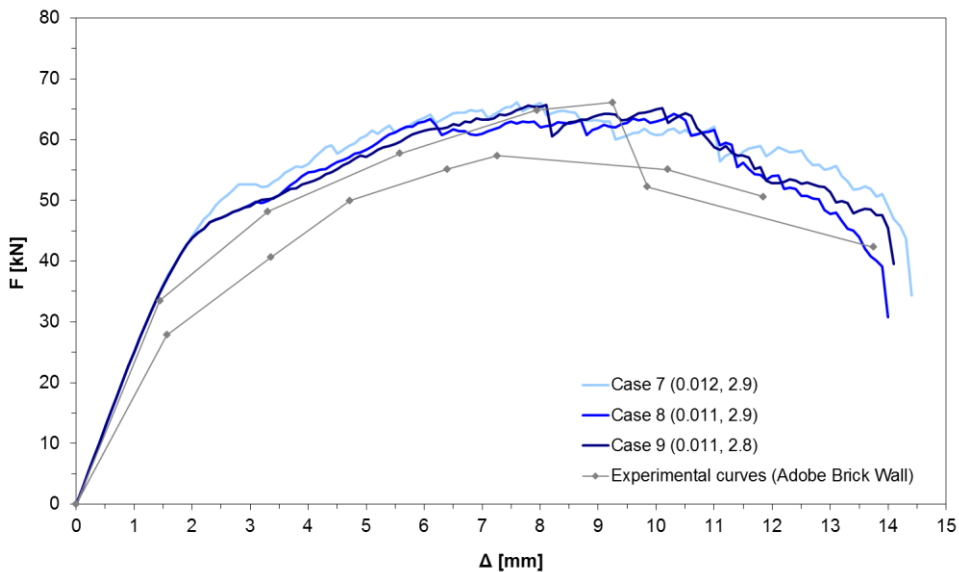


Figure 10.7. Comparison between numerical curves obtained for three sets of fracture energy (G_{ft} , G_{fc}) values.

All the curves present a stiffness slightly higher than the experimental one, but it should be taken into account that the wall was tested against cyclic loads, while the numerical analysis has been carried out considering a monotonic load. The curve illustrated in the final plot reaches the same maximum load of the tested wall and has similar behaviour.

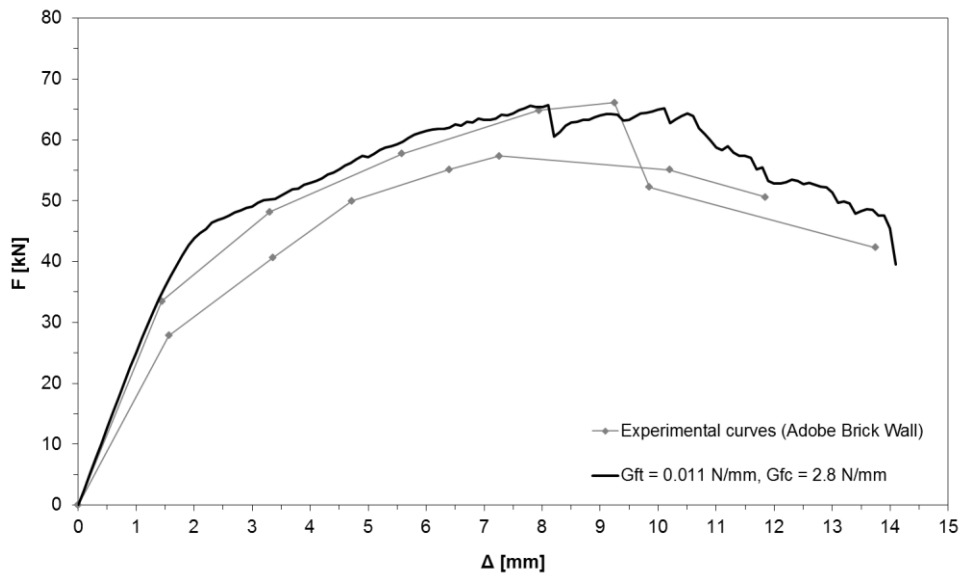


Figure 10.8. Comparison between the numerical curve obtained for $G_{ft} = 0.011$ N/mm, $G_{fc} = 2.8$ N/mm and the experimental envelope curves for the unreinforced adobe brick wall.

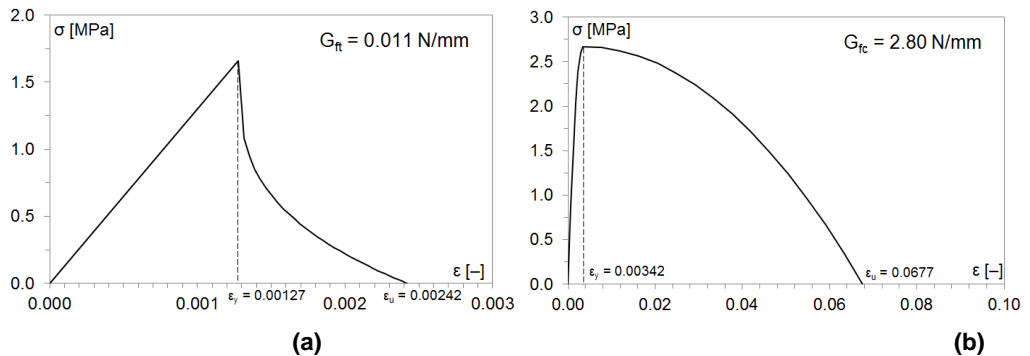


Figure 10.9. Constitutive laws for the homogeneous adobe masonry material: tension (a) and compression (b).

With reference to the numerical curve presented in Figure 10.8, obtained for values of fracture energies G_{ft} and G_{fc} equal to 0.011 N/mm and 2.8 N/mm, respectively, the stress state is then analysed. In the pictures of Figure 10.10, the principal stresses (maximum and minimum) have been shown for different levels of the horizontal displacement of top of the wall. The maximum value of displacement considered is 14 mm, corresponding to a horizontal force reduction of 30% compared to the peak value. The displacement considered are 3 mm, 6 mm and 10 mm, corresponding to about 20%, 45% and 70% of the maximum displacement. It can be noticed that, even for low values of the horizontal displacement, principal tensile stresses are very high in the tensile area of the wall's base, compared to other parts of the panel. As the horizontal displacement increases, principal tensile stresses progress towards the middle of the wall. They also give an indication of the area interested by tensile cracks. The area interested by high principal compressive stresses at the base of the wall is wider for higher values of horizontal displacements and, when the compressive strength is reached, it moves towards the mid point of the wall's base. In the centre of the wall, tensile and compressive stresses are inclined of an angle close to 45°.

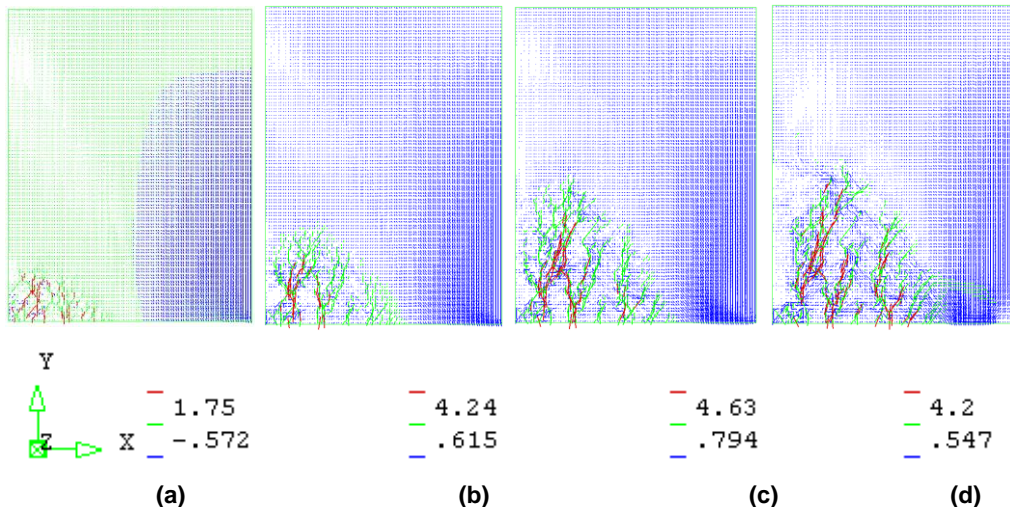


Figure 10.10. Vectors for principal stresses at different load level: horizontal displacement of 3 mm (a), 6 mm (b), 10 mm and (c) and 14 mm (d).

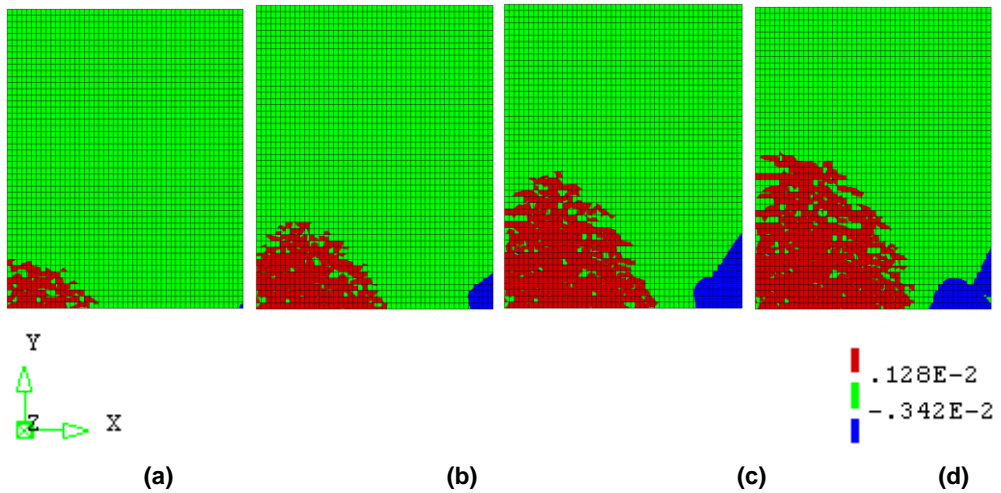


Figure 10.11. Vertical strain ϵ_{yy} different load level: horizontal displacement of 3 mm (a), 6 mm (b), 10 mm and (c) and 14 mm (d).

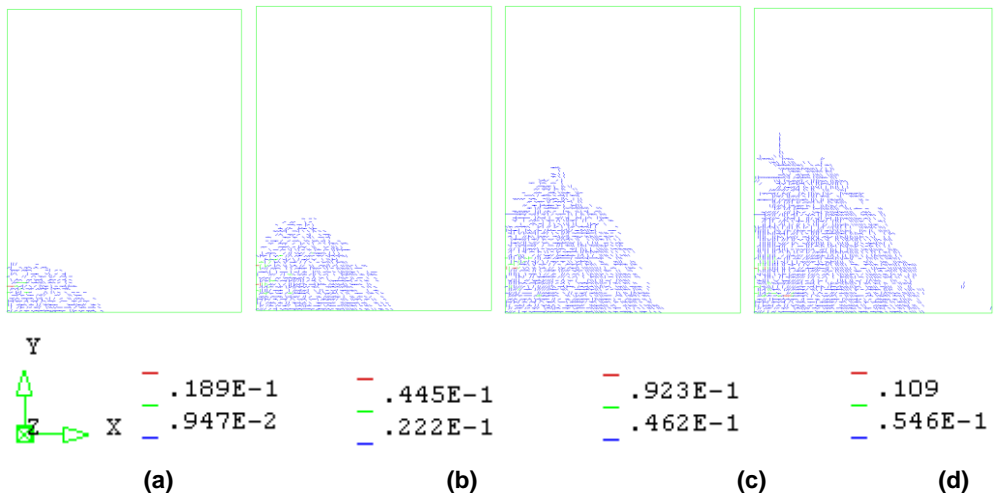


Figure 10.12. Crack pattern at different load level: horizontal displacement of 3 mm (a), 6 mm (b), 10 mm and (c) and 14 mm (d).

For the same steps of analysis considered in the case of the principal stresses, the behaviour of vertical strains ϵ_{yy} is represented in the pictures collected in Figure 10.11. For a better understanding, with red colour have been indicated the elements of the walls in which the strain corresponding to the tensile strength is

exceeded, while with blue colour have been indicated the elements of the walls in which the strain corresponding to the compressive strength is exceeded. The elements indicated with green colour have a strain between these two values. Starting from low load levels, the tensile damage in the direction orthogonal to bed joints is progressing in the area interested by a tensile regime, going from the base of the wall towards the limit of the compressed strut, which is becoming narrower as the load increases. For higher values of the horizontal displacement, compressive damage also appears, due to crashing of elements at the opposite side of the wall's base. In these areas, the compressive strength of the material is reached and the vertical compressive strain is equal or higher than the strain corresponding to the maximum stress. For comparison purposes, in Figure 10.12 is reported the tensile cracking pattern, when the horizontal displacement increases. The steps of analysis considered are the same then the ones considered for previous pictures. Horizontal cracks appear for low levels of the horizontal load at the wall's foot. This is in agreement with the experimental evidence, since the wall suffered high damage at the base due to joint opening starting from low load levels. For higher level of the horizontal load, a wider area is interested by tensile cracks.

10.3 MODELLING OF THE REINFORCED MASONRY PANEL

The calibration of parameters adopted in the finite element model of the unreinforced adobe brick wall presented in the previous sections has been used for modelling of the reinforced masonry walls.

The material behaviour is described through the same model than in the case of the unreinforced masonry wall. The Rankine Principal Stress model has been used, combining the yield conditions of Rankine and Von Mises for tensile and compressive regime, respectively. An exponential softening law was assumed for tension, while a parabolic behaviour was assumed for compression.

The homogeneous material has equivalent mechanical properties calibrated by comparison with the experimental non-linear curves (Figure 10.8). The mechanical

properties of the adobe brick masonry are summarized in Table 10.5, and have been also employed in the model of the reinforced panel.

Unit weight	Young's modulus	Poisson's coefficient	Tensile strength	Tensile fracture energy	Ultimate tensile strain	Compressive strength	Compressive fracture energy	Ultimate compressive strain
ρ [kN/m ³]	E [MPa]	ν [-]	f_t [MPa]	G_{ft} [N/mm]	$\epsilon_{t,ult}$ [-]	f_c [MPa]	G_{fc} [N/mm]	$\epsilon_{c,ult}$ [-]
22.0	1300	0.15	1.66	0.011	2.42E-03	2.67	2.8	6.77E-02

Table 10.5. Mechanical properties for the equivalent material adopted for adobe brick masonry.

Also in this case a simplified bidimensional model has been constructed using quadrilateral eight-node flat plane stress elements, already described in the case of the unreinforced masonry wall model. The constraint conditions are the same of the unreinforced masonry panel model, namely the base of the panel has been considered fixed, and to all the nodes on top line of the wall has been applied a rigid beam constraint in the direction of application of the horizontal load. The reinforcement has been modelled by means of an equivalent grid embedded in a surface representing the layer of mortar applied to the wall's face (Figure 10.13).

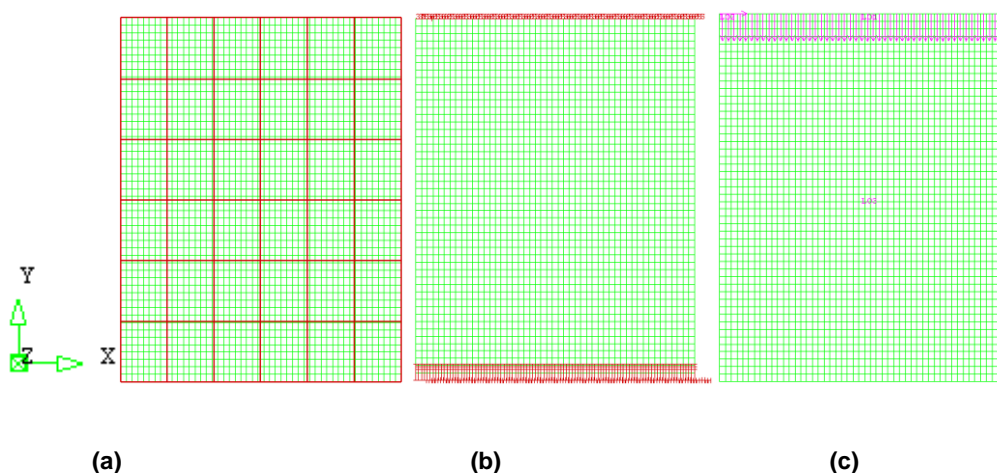


Figure 10.13. FE model of reinforced adobe masonry panel: reinforcement layer (a), mesh and constraints assignment (b) and loading conditions (c).

The mesh of the panel is composed by 4802 elements, with a total of 14408 nodes. Considering the embedded layer of reinforcement, the model has 7203 elements with 21808 nodes.

10.3.1 Modelling of the reinforcement system

The strengthening system of the panels is represented by mortar layers reinforced with composite grids applied on both surfaces of the panel. Such reinforcing element has been modelled by means of a surface, having the characteristics of the mortar layers, to which the reinforcement in form of an equivalent grid is embedded. The surface representing the mortar layers has been considered perfectly bonded to the wall.

In DIANA a reinforced structure can be modelled by plain elements and steel-reinforcement bars. In the present case, the composite grid reinforcement is composed of a series of bars which are located at a fixed intermediate distance from each other, so this has been modelled as a reinforcement grid. Bars in the grid are oriented in two orthogonal directions.

To the plain elements different nonlinear material properties will be assigned than to the reinforcements, in order to account for cracking failure under tensile stresses and crushing failure at compressive and shear stresses, for the former, and for elastic or elasto-plastic behaviour for the latter.

For the modelling of the strengthening system, the reinforcement elements have been considered fully embedded in the concrete elements and displacements and strains of reinforcements and elements are fully coupled.

Embedded reinforcements add stiffness to the finite element model. The contribution of the reinforcement stiffness to the stiffness of the respective mother element is automatically calculated. The main characteristics of these elements are:

- Reinforcements are embedded in structural elements, the so-called mother elements.
- Reinforcements do not have degrees of freedom of their own.

- By default, reinforcement strains are computed from the displacement field of the mother elements, implying perfect bond between the reinforcement and the surrounding material.

The technique of embedding allows the geometries of the reinforcement to be different from the geometries of the mesh. This permits to generate the finite element mesh without having to anticipate on the location of reinforcements.

In the present case, plane shaped reinforcement grids have been used, which may be embedded in various families of elements: plane stress, curved shell and solid (Figure 10.14). Depending on the element family and the specified location points, the plane of the grid may be curved or flat. Grids may also be embedded in plane strain or axisymmetric elements where they have the shape of a line. The total area of the grid is considered to be divided in several particles. Each particle contributes to the stiffness of the element that embeds it. The definition of a particle depends on the dimensionality of the embedding structural element.

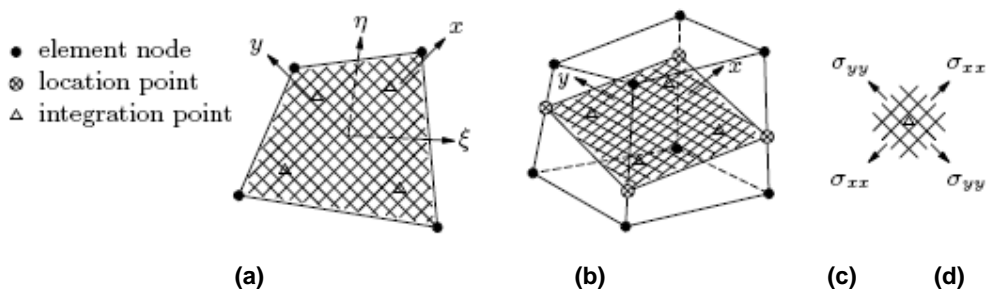


Figure 10.14. Grid reinforcement: particle in 2-D (a); particle in solid (b); stresses (c).

Two-dimensional elements may be fully or partly covered by one or more particles of grid reinforcement. Solid elements embed a particle of grid reinforcement completely. The so-called location points define the position of the particles in the finite element model.

Usually, the embedding elements (and for solids the location points) are determined automatically by DIANA from input of larger sections; this process is called pre-processing of reinforcement location.

In the model of the reinforced wall, grid reinforcement have been embedded in a mesh plane stress elements (Figure 10.15). A particle of a grid reinforcement may cover the complete area of the embedding plane stress element or only part of the area of the element. This example specifies a grid reinforcement with one section. The nodes of the section are input with node numbers. DIANA automatically determines which elements are fully or partly covered by the grid (the ones marked in gray).

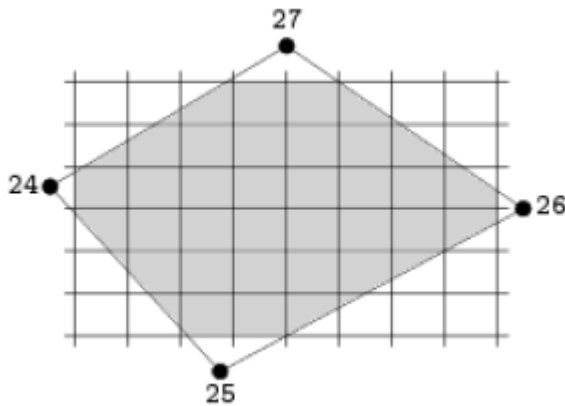


Figure 10.15. Grid reinforcement in plane stress element.

The mechanical behaviour of the equivalent reinforcement layer has been defined with Young's modulus in the linear range up to failure in tension, while the mortar layer is defined by a Rankine Principal Stress model as in the case of the adobe brick masonry.

The mechanical properties of the polymeric grid, provided by the manufacturer, and of the mortar layer assumed in model are summarized in Table 10.6 and 10.7, respectively. The tensile and compressive strength of the mortar used for the reinforcement layers have been assumed as the average values provided by the characterization tests on the clay/sand mortar specimens described in Chapter 5. For the compressive fracture energy of the mortar layers the value, previously calibrated for the adobe masonry, for the case of the unreinforced panel (2.8 N/mm) was considered and scaled by a factor calculated as the ratio between the

compressive strengths of the mortar layer and the adobe masonry, which is about 70%. This was possible since the mortar has the same composition of the bricks. On the contrary, the tensile fracture energy of the mortar has been determined by calibrating the FE model as described in the following section.

Equivalent thickness X	Equivalent thickness Y	Young's modulus	Poisson's coefficient	Tensile strength
$t_{eq,X}$ [mm]	$t_{eq,Y}$ [mm]	E [MPa]	ν [-]	f_t [MPa]
0.247	0.283	2650	0.3	270

Table 10.6. Mechanical properties for the polymeric grid adopted in the model.

Layers thickness	Unit Weight	Young's modulus	Poisson's coefficient	Tensile strength	Tensile fracture energy	Compressive Strength	Compressive fracture energy	Ultimate compressive strain
t [mm]	ρ [kN/m ³]	E [MPa]	ν [-]	f_t [MPa]	G_{ft} [N/mm]	f_c [MPa]	G_{fc} [N/mm]	$\epsilon_{c,ult}$ [-]
40	19.0	1300	0.15	0.44	0.12	1.87	2.05	6.97E-02

Table 10.7. Mechanical properties for the mortar layers adopted in the model.

The equivalent thickness t_{eq} of the reinforcement represents the area of the cross-section per unit length of the grid, as from the Figure 10.16. In the case of the modelled panel, such value is equal to 0.247 mm and 0.283 mm, respectively for X and Y directions, considering two layers of reinforcement.

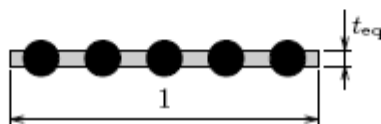


Figure 10.16. Equivalent thickness of the reinforcement grid.

10.4 EFFECT OF THE COMPOSITE GRID

The non-linear analysis on the model of the reinforced masonry panel, presented in the previous section and considering the mechanical characteristics of the reinforced mortar layer previously described, yield to the result illustrated in the Figure 10.17, together with some other cases, considered in order to calibrate the value of the tensile fracture energy associate to the best fitting curve, as summarized in Table 10.8.

The numerical curves show a negligible effect of the tensile fracture energy on the strength when it is higher than 0.06 N/mm, while some influence can be observed on the softening branch. Thus, the comparison show that the curve corresponding to $G_{ft} = 0.12$ N/mm and $G_{fc} = 2.05$ N/mm is the best fitting of the experimental one. It is worth to notice that, however, all the numerical curves presents a degradation of stiffness in the loading branch lower than the experimental curve. Nevertheless, it is reminded that the experimental curve represents the envelope of the non-linear cycles of the laboratory test. The numerical curve approximates well the strength and the displacement capacity of the experimental case.

In Figure 10.18, both unreinforced and reinforced curves have been reported in order to highlight the effect of the reinforced mortar layer on the capacity of the masonry wall.

Case	Tensile fracture energy	Compressive fracture energy
	G_{ft} [N/mm]	G_{fc} [N/mm]
1	0.04	2.05
2	0.06	2.05
3	0.12	2.05
4	0.50	2.05

Table 10.8. Cases of fracture energies for the mortar layers.

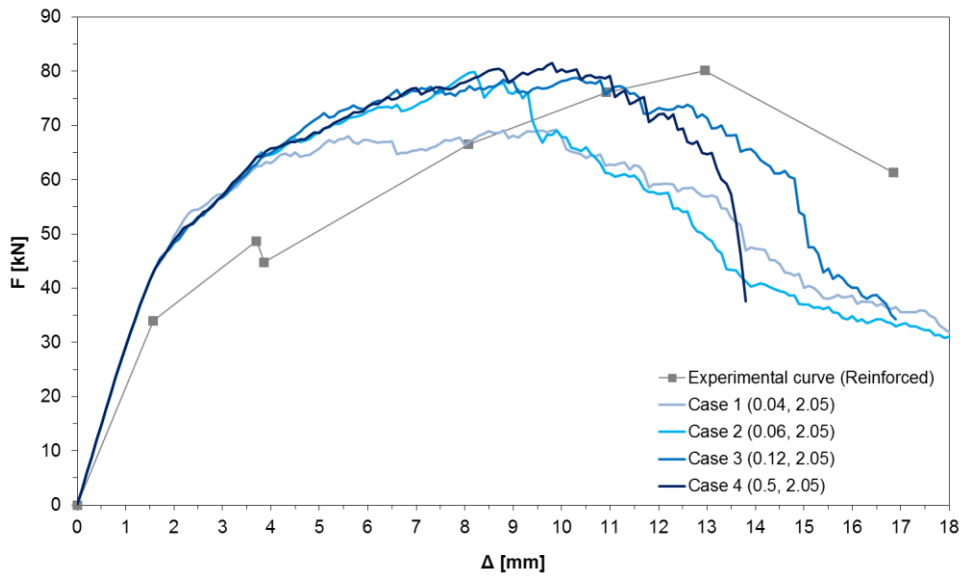


Figure 10.17. Comparison between the numerical curve and the experimental envelope curve for the reinforced adobe brick wall.

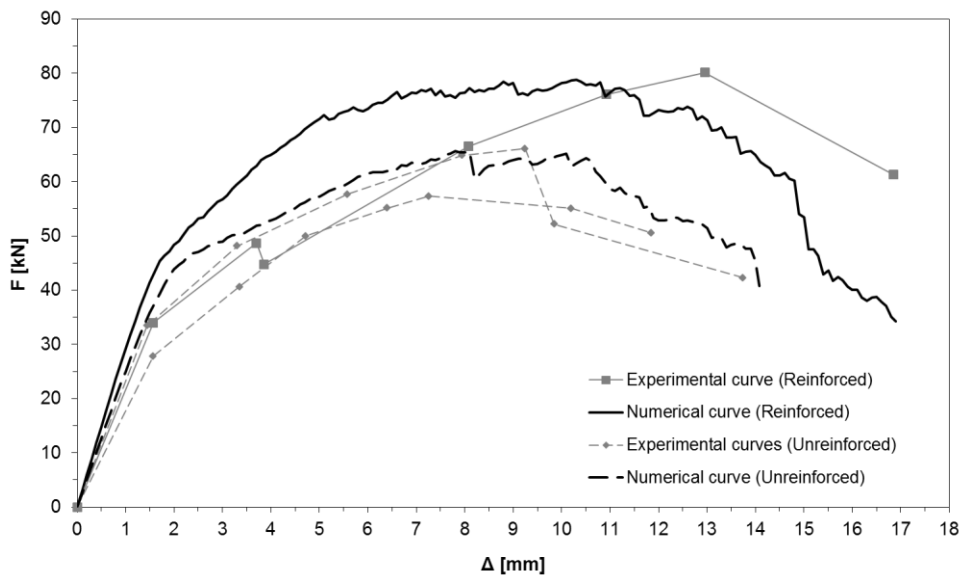


Figure 10.18. Comparison between the numerical curve and the experimental envelope curves for the unreinforced and reinforced adobe brick wall.

A further analysis has been run considering a masonry wall reinforced by means of the only mortar layer applied onto its surfaces. In this case the grid was not considered in the model in order to see its contribution to the wall's capacity. Figure 10.19 shows the comparison between the case in presence of the grid, already reported in Figure 10.18, and the case without the grid, together with the curve of the unreinforced panel. The panel reinforced with mortar layers and frp grid reaches a strength increment of 20%, while in the case of reinforcement with mortar without frp grid the panel reaches a strength increment of 16%. It can be noticed that there is a minimum effect on the strength increment due to the presence of the polyester grid and that the main contribution to the strength increment is due to the mortar layers.

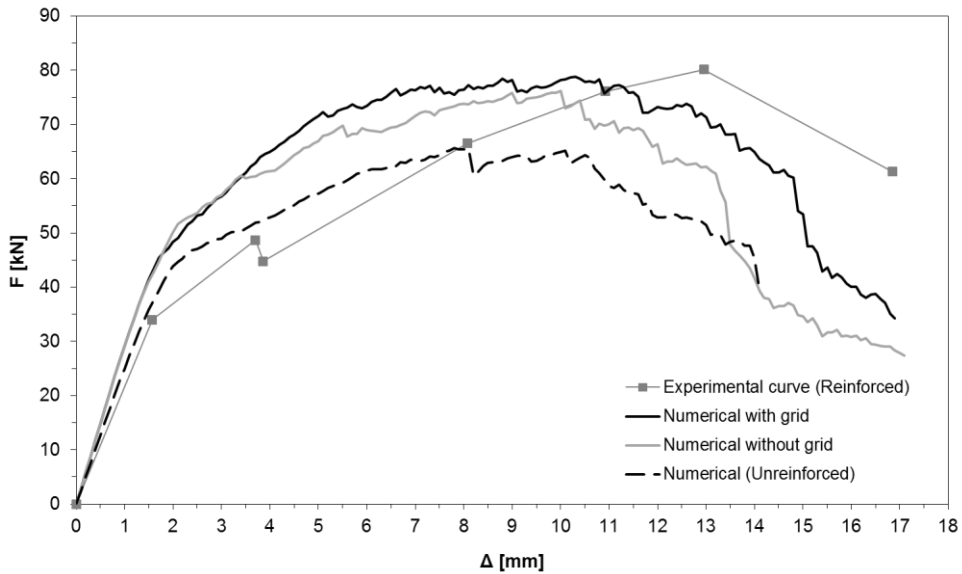


Figure 10.19. Comparison between the numerical curve for the case with and without polymeric grid.

In order to check the effect of the grid, the behaviour of the tested masonry panels has been studied also considering different types of materials. In particular, the non-linear curve obtained from the model strengthened by means of layers of mortar embedding a polyester grid, that is the one used in the experimental tests, has been compared with the non-linear curve in case a glass fiber reinforced polymer

grid. The GFRP grid has a Young's modulus of 80700 MPa and a tensile strength of 45 kN/m. The results of the analysis is reported in Figure 10.20. In case the glass fiber reinforcement grid is used, the numerical model gives an increment in terms of strength of about 50% with respect to the unreinforced panel, compared to the increment of only 20% attained in the case of reinforcement made of the polyester grid.

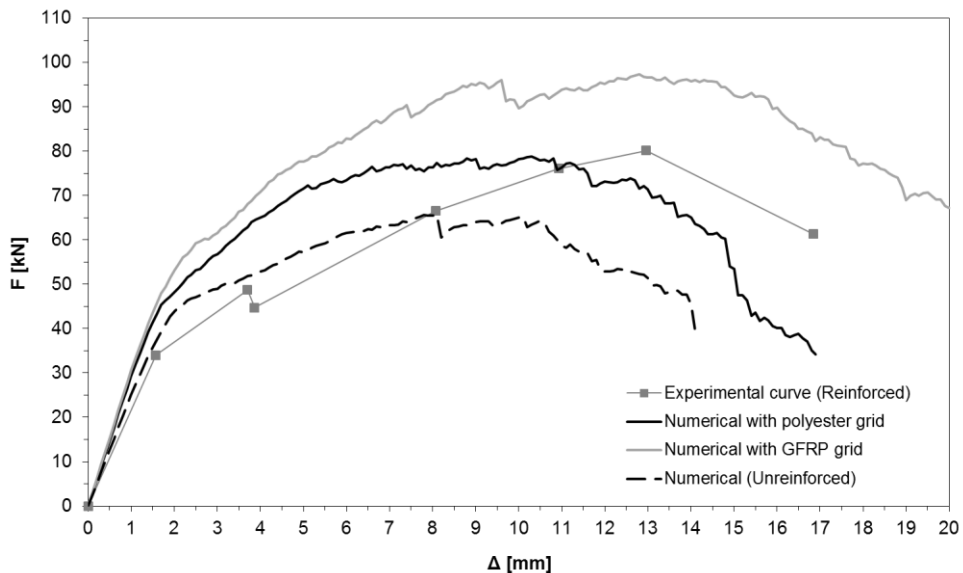


Figure 10.20. Comparison between the numerical curve for the wall reinforced with polyester grid and GFRP grid.

10.5 PARAMETRIC ANALYSIS ON THE FRP EFFECT ON SHEAR MASONRY WALLS

In the following the results of a parametric non-linear analysis on masonry walls reinforced by means of mortar layers embedding a composite grid are reported. Several analysis have been performed on the reinforced bidimensional macro-model described in the previous sections and calibrated against the results obtained from the experimental tests.

The influence of different parameters, which characterize the mechanical properties of the strengthening system, on the non-linear behaviour of the reinforced masonry wall has been investigated. In particular, parameters related to the compressive strength of the mortar layers and the axial stiffness of the composite grid have been taken into account, in terms of variation with respect to the plane masonry wall.

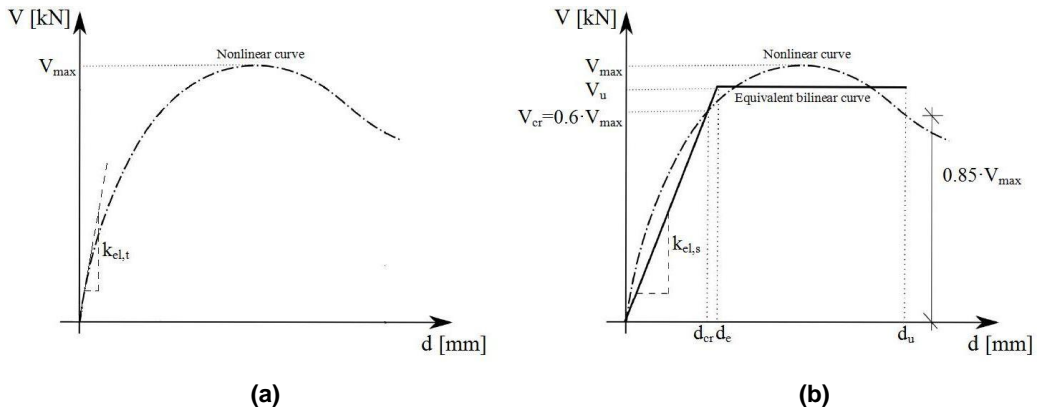


Figure 10.21. Definition of mechanical parameters from the nonlinear shear – displacement curve (a) and construction of the equivalent bilinear curve (b).

Different mechanical parameters, defining the non-linear behaviour of the reinforced masonry walls, have been evaluated. The results of the analysis have been expressed in terms of non-linear shear force versus horizontal displacement of top of the wall, as illustrated in Figure 10.21(a). The elastic tangential stiffness $k_{el,t}$ and the peak horizontal force V_{max} are results considered in the analysis. With reference to the plot reported in Figure 10.21(b), the definition of an equivalent bilinear curve has been performed starting from the shear – displacement curve resulting from the analysis. The equivalent bilinear curve is defined by an elastic secant stiffness $k_{el,s}$, defined by considering the secant to the non-linear curve at V_{cr} , equal to $0.6 \cdot V_{max}$, and by a ultimate displacement d_u , corresponding to strength degradation of 15%. The yielding value defining the strength of the equivalent bilinear curve V_u has been then calculated matching the area under the non-linear curve and the area under the equivalent bilinear curve. The ductility of the reinforced wall has

been finally evaluated by relating the ultimate horizontal displacement d_u to the elastic horizontal displacement d_e . The variation of such parameters is assumed to be an indication of the influence of the mechanical characteristics of the strengthening system onto the global capacity of a wall reinforced by means of the application of mortar layers containing a composite grid.

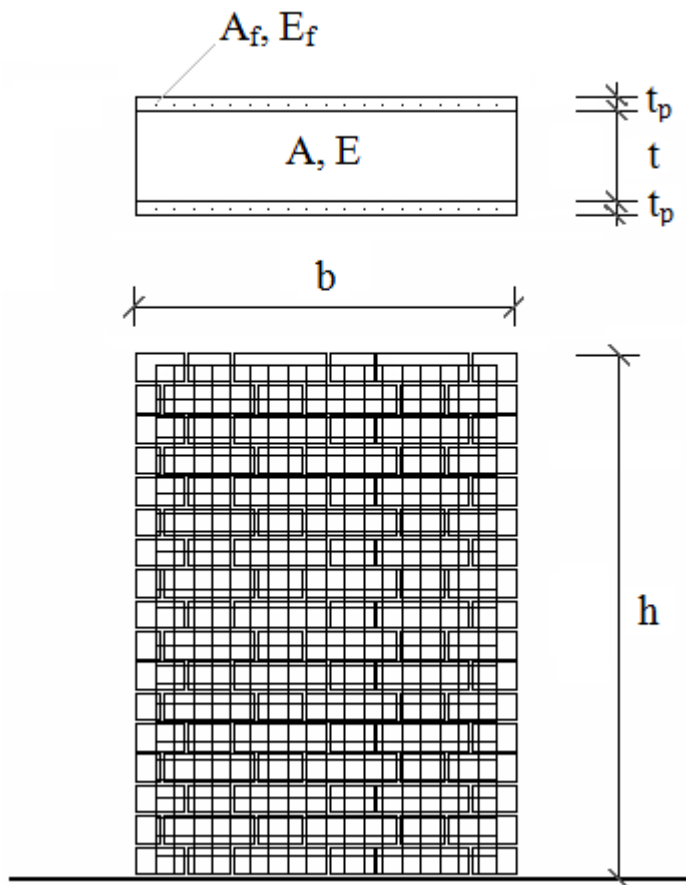


Figure 10.22. Outline of the reinforced masonry wall.

With respect to the symbols indicated in the Figure 10.22, outlining the reinforced masonry panel and illustrating the horizontal cross-section of the specimen, the parametric analyses have been intended to be carried out considering the variation of the mechanical properties of the composite reinforcement. In

particular, the axial stiffness of the composite grid $E_f A_f$, has been varied with respect to the axial stiffness of the plane masonry wall EA . Also, the influence of the compressive strength of the external mortar layers $2t_p f_{cp}$ has been considered and varied with reference to the compressive strength of the wall's masonry f_c , and it is controlled by the parameter $r = 2t_p f_{cp} / f_c$.

Two types of masonry have been considered: an adobe brick masonry, already described in previous sections, and a tuff masonry, characterized by a compressive strength of 1.0 MPa and a Young's modulus of 800 MPa. The values of mechanical parameters of the reinforced panels and the ranges of variation are specified in Table 10.9 and 10.10.

Material	E [MPa]	f_c [MPa]	f_t [MPa]	G_{fc} [N/mm]	G_{ft} [N/mm]
Adobe masonry	1300	2.67	1.66	2.8	0.011
Tuff masonry	800	1.0	0.05	0.9	0.0012
Reinforcement mortar	1300	1.87	0.44	2.05	0.12

Table 10.9. Values for the mechanical parameters for adobe and tuff reinforced masonry walls assumed in the parametric analysis.

Masonry unit	Masonry			Reinforcement mortar			FRP grid	
	t [mm]	f_c [MPa]	E [MPa]	t_p [mm]	f_{cp} [MPa]	E_p [MPa]	$t_{f,eq,Y}$ [mm]	E_f [MPa]
Adobe	240	2.67	1300	20	1.87	1300	0.283	2650
				30			(The axial stiffness $E_f A_f$ is varied up to 40 times the reference value)	
				40				
Tuff	240	1.00	800	20	1.87	1300	0.283	2650
				30			(The axial stiffness $E_f A_f$ is varied up to 30 times the reference value)	
				40				

Table 10.10. Values for the geometrical and mechanical parameters assumed in the parametric analysis.

The parametric cases of analysis are summarized in the Table 10.11 and 10.12 for adobe and tuff masonry respectively, with reference to different values aspect ratio h/b considered for the masonry panel, namely 1.0, 1.3 (corresponding to the tested panels) and 2.0.

Some examples of the horizontal force – displacement curves obtained from the parametric analysis are illustrated in the plots of Figure 10.23, in the case of mortar layers' thickness of 30 mm and shape factor $h/b = 1.0$, and in the plots of Figure 10.24, in the case of mortar layers' thickness of 30 mm and shape factor $h/b = 1.0$, comparing the case of adobe and tuff masonry walls. For a complete report of all the plots of the behaviour of the various mechanical parameters previously introduced one can refer to the Appendix of the present work.

It is finally noticed that the analysis have been conducted under some hypotheses. For example the model is bidimensional, so that the effect connected to the third dimension are neglected, a homogeneous and isotropic material has been considered for the masonry, and the assumption of perfect bond was made for the interface between the reinforced mortar layer and the wall's surface. In particular, the consistency of the latter hypothesis should be adequately checked and further studies on bond between such type of reinforcement system on a masonry substrate are needed, since the resistance and the overall capacity of the wall might be affected and reduced due to debonding phenomena.

Shape factor			Reinforcement mortar thickness	Reinforcement mortar strength				Reinforcement grid stiffness			
h [mm]	b [mm]	h/b [-]	t_p [mm]	$t \cdot f_c$ [N/mm]	$2t_p \cdot f_{pc}$ [N/mm]	$r = 2t_p \cdot f_{pc} / t \cdot f_c$ [-]	Variation [-]	EA [N/mm]	$E_t A_{t,y}$ [N/mm]	$E_t A_{t,y} / EA$ [-]	Variation [-]
1000	1000	1.0	-	641	-	-	-	312000	-	-	-
1000	1000	1.0	20	641	75	0.12	-	312000	750	0.0024	-
									7500	0.0240	10
									14999	0.0481	20
									18749	0.0601	25
									22499	0.0721	30
									26248	0.0841	35
			29998	0.0961	40						
			30	641	112	0.17	1.50	312000	750	0.0024	-
									7500	0.0240	10
									14999	0.0481	20
									18749	0.0601	25
									22499	0.0721	30
									26248	0.0841	35
			29998	0.0961	40						
			40	641	149	0.23	2.00	312000	750	0.0024	-
									7500	0.0240	10
									14999	0.0481	20
									18749	0.0601	25
22499	0.0721	30									
26248	0.0841	35									
29998	0.0961	40									
1367	1050	1.3	-	641	-	-	-	312000	-	-	-
1367	1050	1.3	20	641	75	0.12	-	312000	750	0.0024	-
									7500	0.0240	10
									14999	0.0481	20
									22499	0.0721	30
									29998	0.0961	40
									750	0.0024	-
			7500	0.0240	10						
			14999	0.0481	20						
			22499	0.0721	30						
			29998	0.0961	40						
			30	641	112	0.17	1.50	312000	750	0.0024	-
									7500	0.0240	10
									14999	0.0481	20
									22499	0.0721	30
									29998	0.0961	40
									750	0.0024	-
			7500	0.0240	10						
			14999	0.0481	20						
22499	0.0721	30									
29998	0.0961	40									
40	641	149	0.23	2.00	312000	750	0.0024	-			
						7500	0.0240	10			
						14999	0.0481	20			
						22499	0.0721	30			
						29998	0.0961	40			
						750	0.0024	-			
7500	0.0240	10									
14999	0.0481	20									
22499	0.0721	30									
29998	0.0961	40									

continues...

Shape factor			Reinforcement mortar thickness	Reinforcement mortar strength				Reinforcement grid stiffness			
h [mm]	b [mm]	h/b [-]	t_p [mm]	$t \cdot f_c$ [N/mm]	$2t_p \cdot f_{pc}$ [N/mm]	$r = 2t_p \cdot f_{pc} / t \cdot f_c$ [-]	Variation [-]	EA [N/mm]	$E_t A_{t,y}$ [N/mm]	$E_t A_{t,y} / EA$ [-]	Variation [-]
2100	1050	2.0	–	641	–	–	–	312000	–	–	–
2100	1050	2.0	20	641	75	0.12	–	312000	750	0.0024	–
									2475	0.0079	3.3
									4950	0.0159	6.6
									7500	0.0240	10
									14999	0.0481	20
									22499	0.0721	30
			29998	0.0961	40						
			30	641	112	0.17	1.50	312000	750	0.0024	–
									2475	0.0079	3.3
									4950	0.0159	6.6
									7500	0.0240	10
									14999	0.0481	20
									22499	0.0721	30
			29998	0.0961	40						
			40	641	149	0.23	2.00	312000	750	0.0024	–
									2475	0.0079	3.3
									4950	0.0159	6.6
									7500	0.0240	10
14999	0.0481	20									
22499	0.0721	30									
29998	0.0961	40									

Table 10.11. Cases of analysis for the adobe brick masonry wall.

Shape factor			Reinforcement mortar thickness	Reinforcement mortar strength				Reinforcement grid stiffness			
h [mm]	b [mm]	h/b [-]	t_p [mm]	$t \cdot f_c$ [N/mm]	$2t_p \cdot f_{pc}$ [N/mm]	$r = 2t_p \cdot f_{pc} / t \cdot f_c$ [-]	Variation [-]	EA [N/mm]	$E_t A_{t,Y}$ [N/mm]	$E_t A_{t,Y} / EA$ [-]	Variation [-]
1000	1000	1.0	–	240	–	–	–	192000	–	–	–
1000	1000	1.0	20	240	75	0.31	–	192000	750	0.0039	–
									7500	0.0391	10
									14999	0.0781	20
									22499	0.1172	30
			30	240	112	0.47	1.50	192000	750	0.0039	–
									7500	0.0391	10
									14999	0.0781	20
									22499	0.1172	30
			40	240	149	0.62	2.00	192000	750	0.0039	–
									7500	0.0391	10
									14999	0.0781	20
									22499	0.1172	30
1367	1050	1.3	–	240	–	–	–	192000	–	–	–
1367	1050	1.3	20	240	75	0.31	–	192000	750	0.0039	–
									7500	0.0391	10
									14999	0.0781	20
									22499	0.1172	30
			30	240	112	0.47	1.50	192000	750	0.0039	–
									7500	0.0391	10
									14999	0.0781	20
									22499	0.1172	30
			40	240	149	0.62	2.00	192000	750	0.0039	–
									7500	0.0391	10
									14999	0.0781	20
									22499	0.1172	30
2100	1050	2.0	–	240	–	–	–	192000	–	–	–
2100	1050	2.0	20	240	75	0.31	–	192000	750	0.0039	–
									7500	0.0391	10
									14999	0.0781	20
									22499	0.1172	30
			30	240	112	0.47	1.50	192000	750	0.0039	–
									7500	0.0391	10
									14999	0.0781	20
									22499	0.1172	30
			40	240	149	0.62	2.00	192000	750	0.0039	–
									7500	0.0391	10
									14999	0.0781	20
									22499	0.1172	30

Table 10.12. Cases of analysis for the tuff block masonry wall.

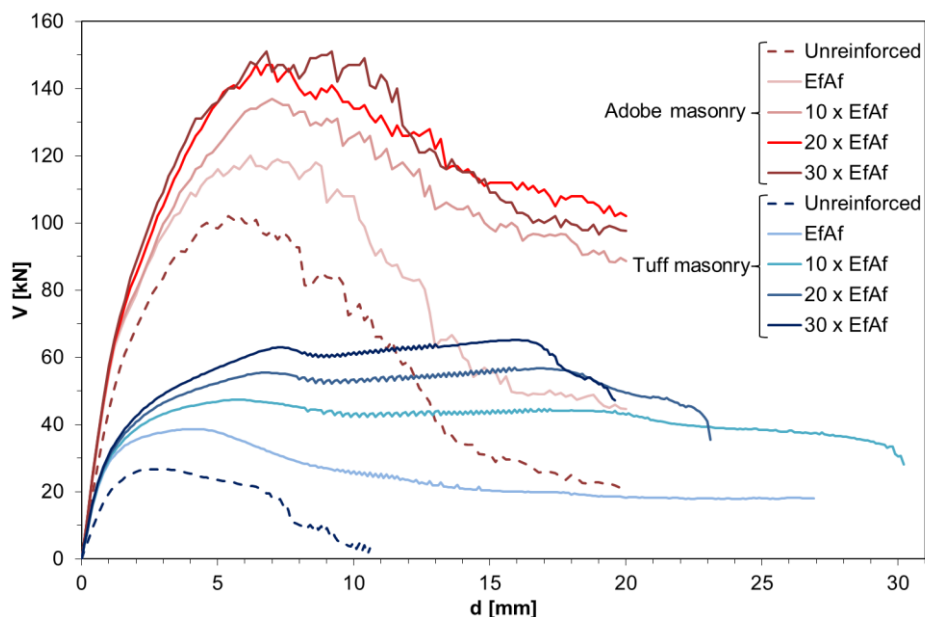


Figure 10.23. Effect of FRP grid axial stiffness: numerical curves for adobe and tuff masonry for mortar layer thickness $t_p = 30$ mm and shape factor $h/d = 1.0$.

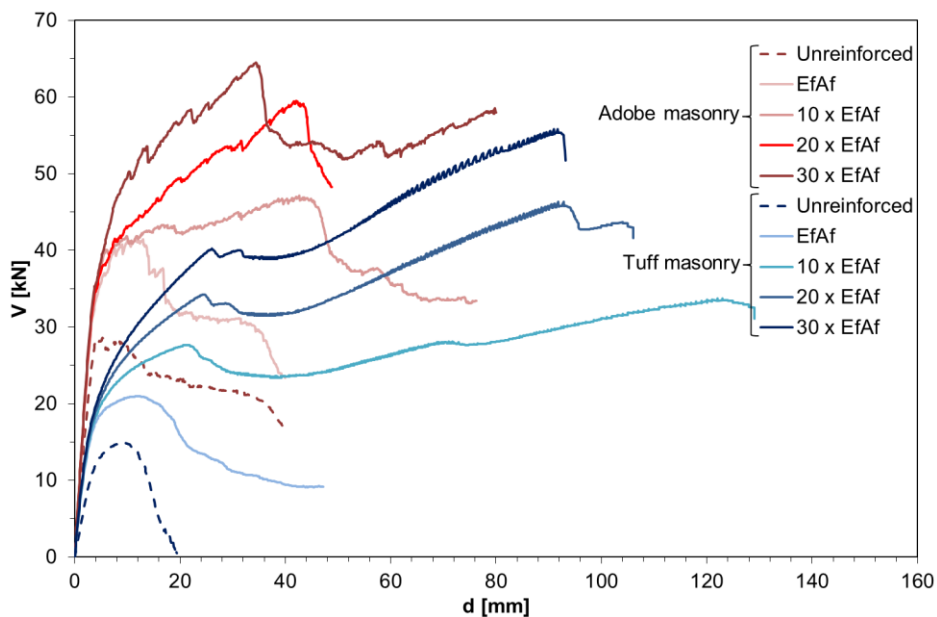


Figure 10.24. Effect of FRP grid axial stiffness: numerical curves for adobe and tuff masonry for mortar layer thickness $t_p = 30$ mm and shape factor $h/d = 2.0$.

Figure 10.23 and 10.24 show that the non-linear curves associated to tuff panels are characterized by a higher ductility compared with the curves associated to adobe masonry, which have a softening branch with higher slope.

The results from the parametric analysis evidence how the elastic stiffness of the reinforced element varies when increasing the amount of reinforcement and/or its axial stiffness. The effect is the same for both type of masonry and for all the shape factors considered. The increment of the axial stiffness of the reinforcement produces an increment of the elastic stiffness of the masonry walls, as it can be seen from the plots in Figure 10.25, reporting, as an example, the case of adobe masonry (Figure 10.25(a)), and tuff masonry (Figure 10.25(b)) walls having a shape factor $h/b = 1.0$. The results show that the effect of the reinforcement on the elastic stiffness is quite linear about 30 to 60% higher (depending on the aspect ratio of the wall) in the case of tuff masonry, which is characterized by a lower Young modulus (about 40%), compared to the case of adobe masonry.

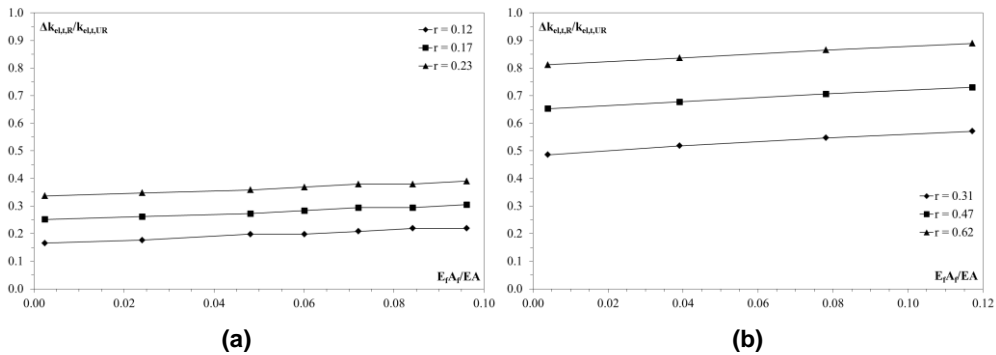


Figure 10.25. Tangent elastic stiffness increment due to reinforcement for adobe (a) and tuff (b) masonry walls with shape factor $h/b = 1.0$.

The effect of the reinforcement on the wall's strength has been also evidenced by means of the parametrical analysis. In Figures 10.26, 10.27 and 10.28 the strength increment $\Delta V_{\max,R}/V_{\max,UR}$ is plotted versus the axial stiffness of the reinforcement normalized to the axial stiffness of the masonry panel for $h/b = 1.0, 1.3$ and 2.0 . The graphs show a quite linear trend, nevertheless some discontinuities due to numerical convergence problems are present. With respect to the unreinforced

masonry panel, the strength of the walls with shape factor $h/b = 1.0$ increases between 18% and 83% for adobe masonry (see Figure 10.26(a)), and between 33% and 193% for tuff masonry (see Figure 10.26(b)). On the walls having shape factor $h/b = 1.3$ it has been obtained an increment of strength between 6% and 96% for adobe masonry (see Figure 10.27(a)), and between 29% and 238% for tuff masonry (see Figure 10.27(b)). Considering the walls with shape factor $h/b = 2.0$, in the reinforced case the strength increases between 18% and 170% for adobe masonry (see Figure 10.28(a)), and between 29% and 335% for tuff masonry (see Figure 10.28(b)). It is reminded that the ratio between the compressive strength of adobe masonry and tuff masonry is 2.67.

Furthermore, the results showed that the effect of the axial stiffness of the composite grid is higher for walls having shape factor $h/b = 2.0$ (see Figure 10.28), characterized by a flexural behaviour, compared to the walls having shape factor $h/b = 1.0$ (see Figure 10.26), characterized by a shear behaviour. The walls with shape factor $h/b = 1.3$ have an intermediate mechanical behaviour (see Figure 10.27)) and the parametric analysis provided values of increment of the horizontal shear force closer to the values obtained for the walls with shape factor $h/b = 1.0$. In particular, for the case of adobe masonry (see Figures 10.26(a), 10.27(a) and 10.28(a)) the increment of strength for panels with $h/b = 2.0$ due to the axial stiffness of the reinforcement is from 31 to 54% higher than in the case of panels with $h/b = 1.0$, depending on the mortar layer's thickness, while it is from 47 to 53% for the case of tuff masonry (see Figures 10.26(b), 10.27(b) and 10.28(b)).

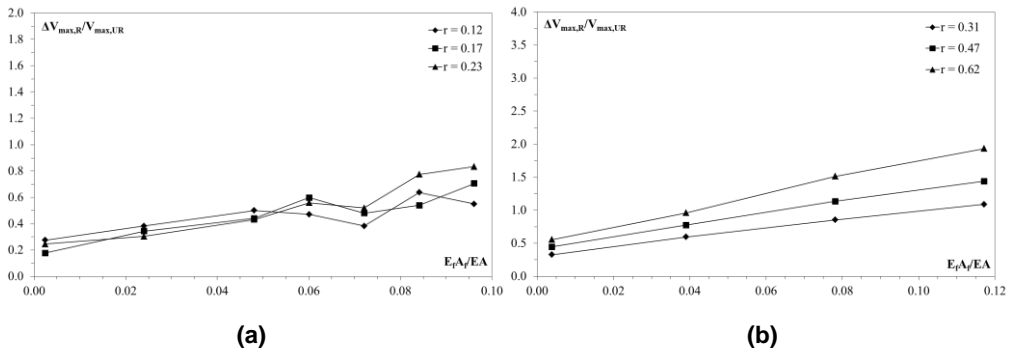


Figure 10.26. Maximum horizontal force increment due to reinforcement for adobe (a) and tuff (b) masonry walls with shape factor $h/b = 1.0$.

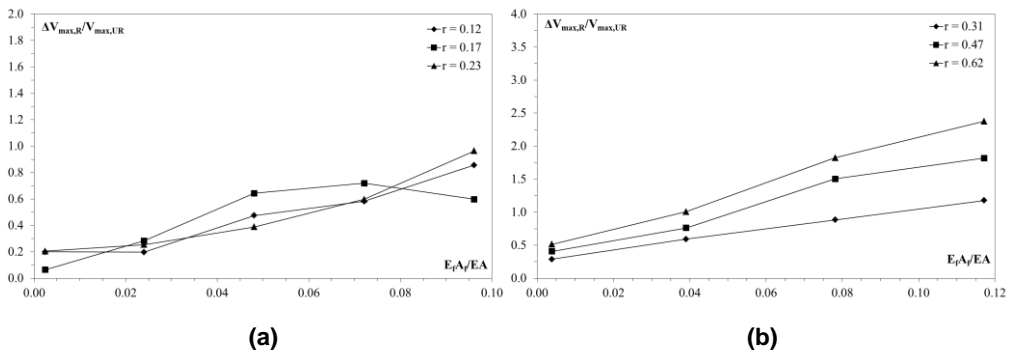


Figure 10.27. Maximum horizontal force increment due to reinforcement for adobe (a) and tuff (b) masonry walls with shape factor $h/b = 1.3$.

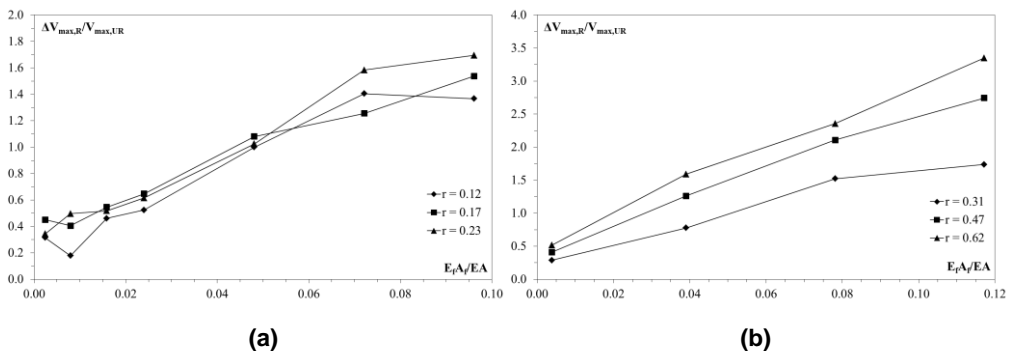


Figure 10.28. Maximum horizontal force increment due to reinforcement for adobe (a) and tuff (b) masonry walls with shape factor $h/b = 2.0$.

The analysis of results obtained from the parametric analysis evidences also that the effectiveness of the reinforcement stiffness on the displacement capacity, controlled through the drift d_r , is higher in the case of the considered tuff masonry, which has a lower compressive strength compared to adobe masonry. For low values of aspect ratio ($h/b = 1.0$) of the wall, the drift increases with the axial stiffness of the reinforcement, while for high values of the aspect ratio ($h/b = 2.0$), the maximum possible value of the drift is reached for low values of axial stiffness of the reinforcement. After the maximum value of drift is reached it is almost constant for the case of adobe, while it reduces as the stiffness increases for the case of tuff. Considering the adobe masonry panels (see Figures 10.29(a), 10.30(a) and 10.31(a)), for an aspect ratio $h/b = 1.0$, the value of drift ranges from 0.88% to 1.44%. Adobe walls with aspect ratio $h/b = 1.3$ have similar behaviour the walls with aspect ratio $h/b = 1.0$, having values of drift ranging from 0.97% to 1.38%, while for adobe walls with aspect ratio $h/b = 2.0$ the drift ranges from 0.81% to 2.71%. For the tuff masonry panels (see Figures 10.29(b), 10.30(b) and 10.31(b)), the drift ranges from 0.68% and 1.96%, for $h/b = 1.0$, and from 0.73% and 2.80%, for $h/b = 1.3$. For $h/b = 2.0$ the drift of tuff masonry panels ranges from 0.85% and 4.67%.

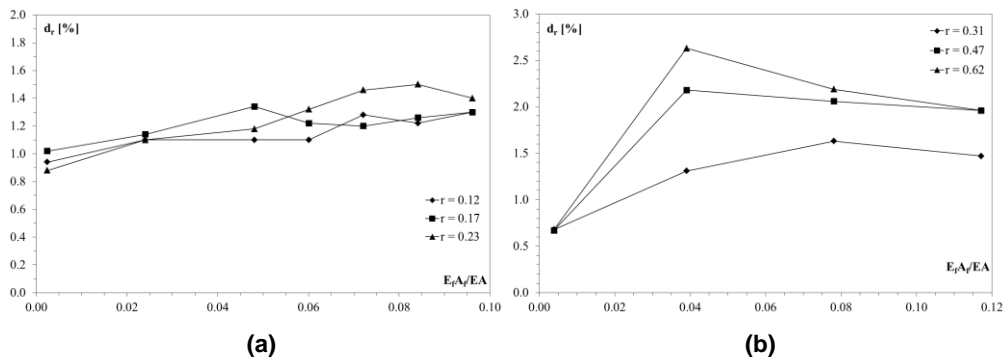


Figure 10.29. Drift increment due to reinforcement for adobe (a) and tuff (b) masonry walls with shape factor $h/b = 1.0$.

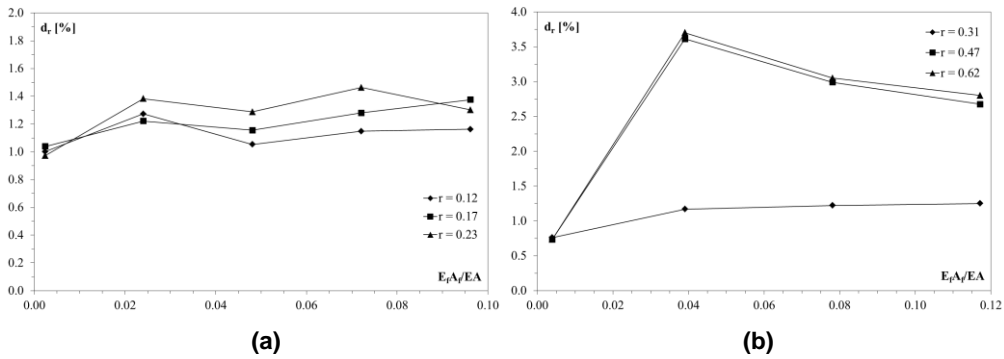


Figure 10.30. Drift increment due to reinforcement for adobe (a) and tuff (b) masonry walls with shape factor $h/b = 1.3$.

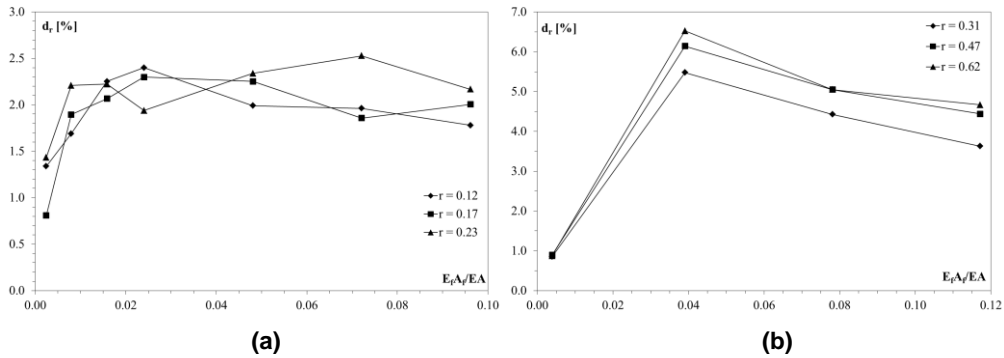


Figure 10.31. Drift increment due to reinforcement for adobe (a) and tuff (b) masonry walls with shape factor $h/b = 2.0$.

Considering the effect of the mortar layers reinforced with the composite grid on the strength of masonry panels, the values provided by the model presented in Figures 10.26, 10.27 and 10.28 are collected in the plots of Figure 10.32 and 10.33, for adobe bricks and tuff block masonry, respectively. In the graphs, all the values (1.0, 1.3 and 2.0) for the factor h/b are considered, in order to evidence the effect of the reinforcement on walls with a different shape and, consequently, a different failure mechanism. In Figures 10.32 and 10.33 the linear regression lines referred to three values of h/b (1.0, 1.3 and 2.0) are reported, nevertheless the effect of the mortar layer for a fixed value of $E_f A_f$ is relevant. In particular, this effect increases for higher values of $E_f A_f$ and it is greater for $h/b = 2.0$.

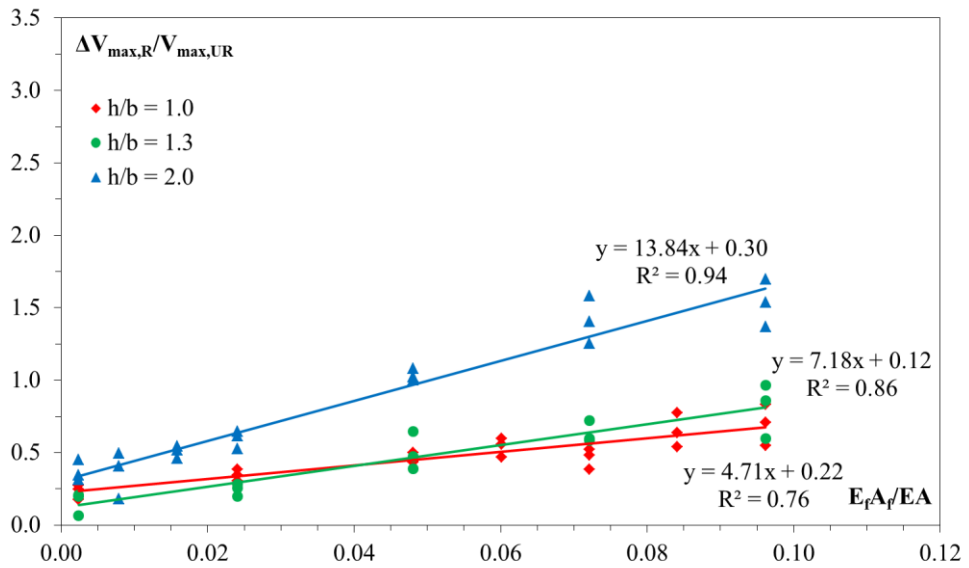


Figure 10.32. Strength increments and regression for adobe masonry walls for $h/b = 1.0, 1.3$ and 2.0 .

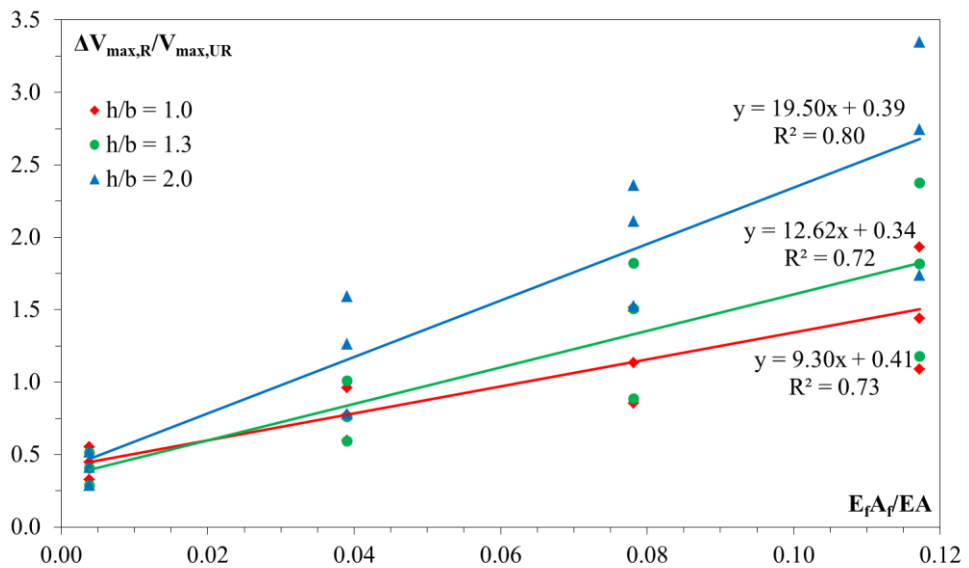


Figure 10.33. Strength increments and regression for tuff masonry walls for $h/b = 1.0, 1.3$ and 2.0 .

In general, the shear strength increase is more relevant for tuff that has lower mechanical properties. Moreover, the graphs show that the same shear strength increase can be achieved with different combination of reinforcement percentage and mortar layer thickness. As example in Figure 10.34 the cases of different reinforcement configurations providing similar increment of strength compared to the unreinforced wall are reported for adobe and tuff panels, respectively.

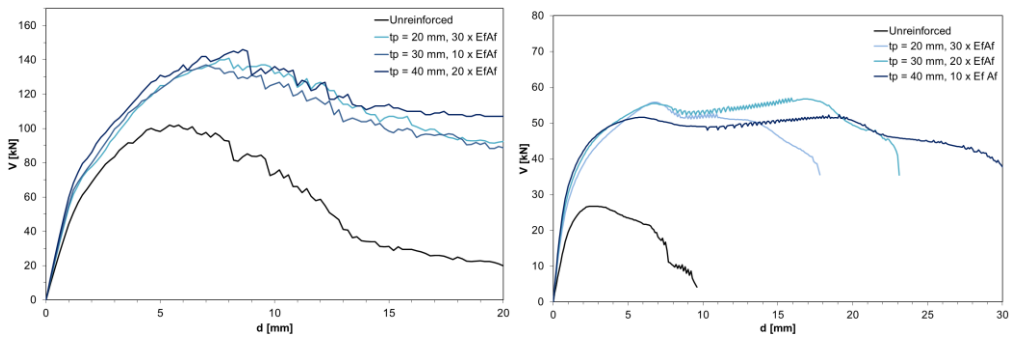


Figure 10.34. Non-linear curves of adobe (a) and tuff (b) panels with $h/b = 1.0$ for different reinforcement configurations providing similar strength increment.

The variation of the parameters considered in the parametric analysis has been also plotted with respect to the parameter $f_{pc}A_i / f_cA$, where A_i is the equivalent area of reinforcement calculated as $A_p + n_f A_f$, considering the homogenization factor $n_f = E_f / E_p$. In Figures 10.35, 10.36, 10.37, the strength increment $\Delta V_{max,R} / V_{max,UR}$ is plotted versus the axial stiffness of the reinforcement normalized to the axial stiffness of the masonry panel for $h/b = 1.0, 1.3$ and 2.0 . From the figures it can be seen that similar increments of strength can be obtained by means of different strengthening configurations, with respect to the thickness of the reinforcement mortar and amount of frp reinforcement. Furthermore, the graphs show that the same value of the parameter $f_{pc}A_i / f_cA$ can lead to have different results in terms of strength, stiffness and displacement increase, depending on the amount of external reinforcement and mortar. The report of all the plots of the behaviour of the various mechanical parameters obtained from the parametric analysis can be found in the Appendix of the present work.

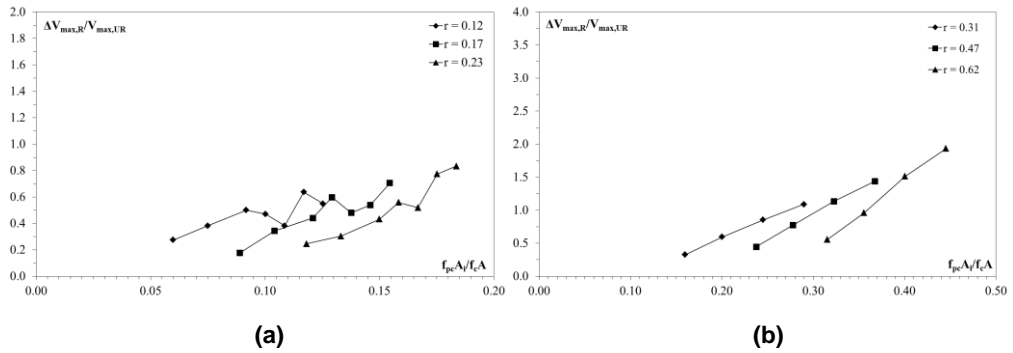


Figure 10.35. Maximum horizontal force increment due to reinforcement for adobe (a) and tuff (b) masonry walls with shape factor $h/b = 1.0$ versus $f_{pc}A_i / f_cA$.

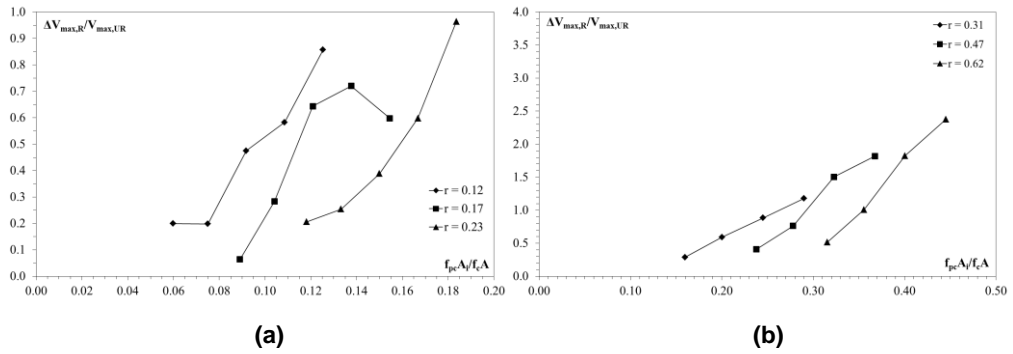


Figure 10.36. Maximum horizontal force increment due to reinforcement for adobe (a) and tuff (b) masonry walls with shape factor $h/b = 1.3$ versus $f_{pc}A_i / f_cA$.

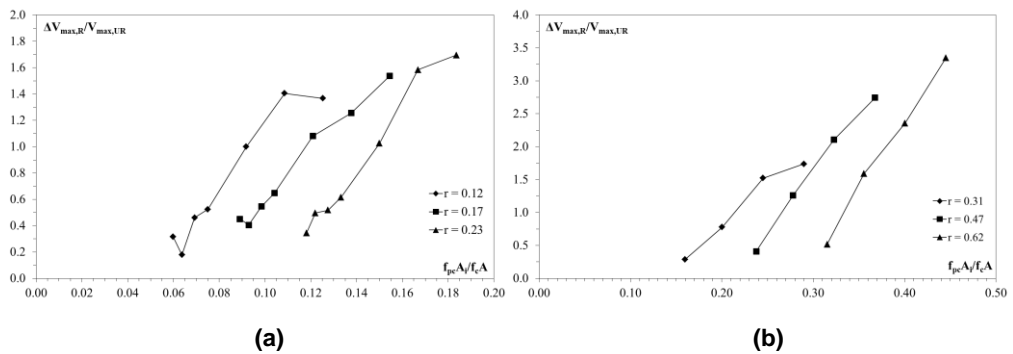


Figure 10.37. Maximum horizontal force increment due to reinforcement for adobe (a) and tuff (b) masonry walls with shape factor $h/b = 2.0$ versus $f_{pc}A_i / f_cA$.

11 MODELLING OF A REINFORCED MASONRY BUILDING

In the present chapter a case study of an existing masonry building strengthened by FRP is presented. The building considered is represented by a historical palace sited in the city of Ariano Irpino, Italy. The description of the building morphology and the characteristics of the structural elements is carried out. The geometric and mechanical survey of the structure and the results of non-destructive and destructive investigations are presented. The considered masonry building has been then modelled through a simplified method, defining an equivalent three-dimensional frame. Finally, the results of several pushover analyses for the unstrengthened structure and the structure strengthened are presented. The cases of strength increment only and strength and ductility increments are considered.

11.1 DESCRIPTION OF THE BUILDING

The building known as ‘Palazzo Bevere-Gambacorta’ is placed in the historic centre of the city of Ariano Irpino, Italy, between two small squares: Bevere and San Francesco Squares. Such a position gives particular value to the building, despite of several transformations and modifications experienced by the urban surroundings. The building has a favourable exposition since its main front looks to South, while two smaller sides look to East and West, as it is shown in Figure 11.1.

The construction of the building started in the XVIII century in between two adjacent streets, Via Bevere and Vicolo Mancini, and was completed during several phases along the time. The first historical information regarding the building date back

to the beginning of the XIX century. In Figure 11.2 it is reported a historical photo of the building showing its southern façade.



Figure 11.1. Palazzo Bevere-Gambacorta in the historic centre of the city of Ariano Irpino.



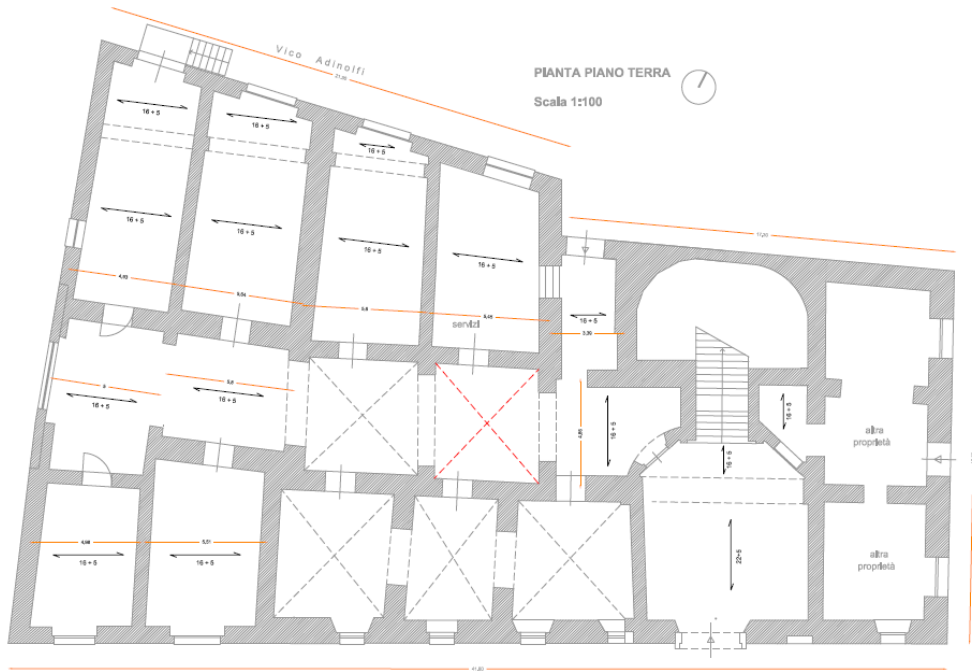
Figure 11.2. Historical photo of Palazzo Bevere-Gambacorta.

11.2 GEOMETRY AND STRUCTURAL ARRANGEMENT

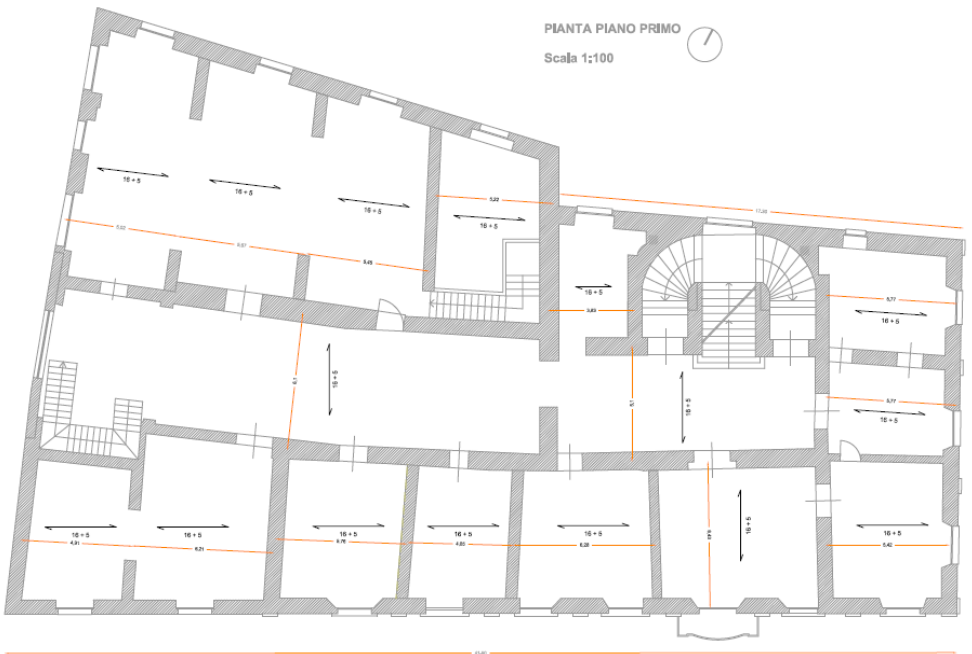
The building is structured over three levels: the ground floor, a first floor and an attic which allows to reach the terrace roof. In Figure 11.3(a) and 11.3(b) the floor plan of the ground level and first level, respectively, are reported. The first floor is connected with the ground floor through staircase, as it can be seen from the cross section along the short side and along the long side, reported in Figures 11.4(a) and 11.4(b), respectively.

The structure has a quite regular shape having overall dimensions of 42 x 27 m, with the northern side slightly larger. Also, on the western side, along Via Mancini, the building has an appendix of about 10 x 8 meters, nowadays used for dwellings.

The external masonry walls belonging to the southern and eastern façades are made with a regular texture and horizontal clay bricks courses, mainly at the ground floor. The entrance of the building is placed in the southern façades, which is characterized by a portal dating back to XVIII century, made by local limestone blocks and with its jambs slightly opened inwards. Another characteristic aspect of the main façade is represented by the ground floor's windows, having clay bricks jambs and lintels with high keystone. At the first floor the façades are made by rectangular openings, seven on the southern side and three on the eastern side, with pilaster in between over which is placed a capital and a masonry lintel.



(a)



(b)

Figure 11.3. Floor plans of Palazzo Bevere-Gambacorta: ground floor (a) and first floor (b).

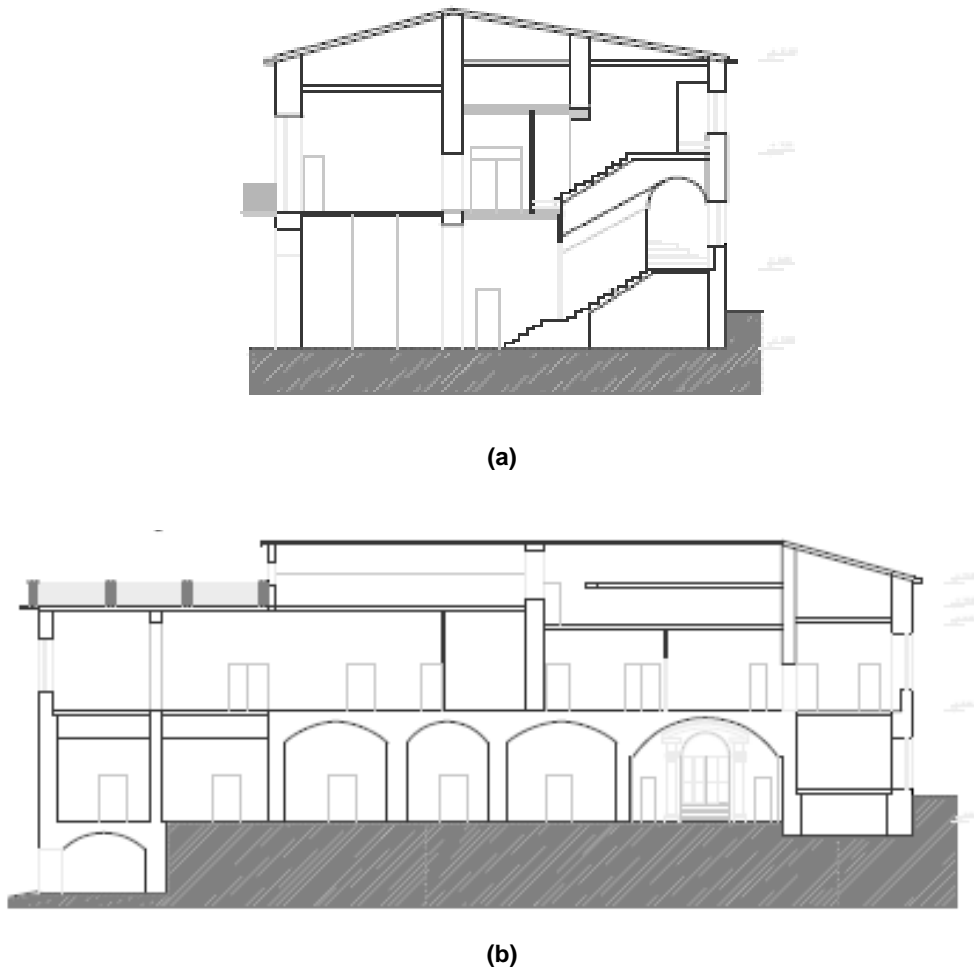


Figure 11.4. Cross-sections of Palazzo Bevere-Gambacorta along the short (a) and long side (b).

The inner space of the structure is defined by the presence and repetition of cellular units with square or rectangular shape, representing a suitable arrangement for a bear walls masonry building. In fact, the floor plans of the first two floors can be superimposable and with corresponding structural elements. The internal height of the floors, measured in different rooms, ranges within 4.10 and 4.80 meters and no openings for the elevator are present in the slabs.



Figure 11.5. Example of slab with steel profiles.



Figure 11.6. Example of original wooden slab.

Different types of slabs can be found in the structure. Most of them are made by double standard 'T' shaped steel profiles and hollow clay elements (see Figure 11.5). Some rooms are covered by means of original masonry cross-vaults, while the most ancient slabs are made by wooden beams supported by the perimeter walls, covered by a wood planking (see Figure 11.6).

The floor slabs have signs of decay and damage and show problems in the fulfil their structural function of bearing vertical loads and redistribution of horizontal loads. Therefore, in the analysis new floors rigid in the plane are considered.

11.3 INSPECTION AND MATERIAL CHARACTERIZATION

The inspection of the building is necessary in order to get enough information in the process of evaluation of the safety of an existing structure and in the identification of the optimal design solution for the intervention of static reinforcement. The important role of diagnosis and inspection phases is reflected in the knowledge level of the structure as defined by the Italian building code 'Norme Tecniche per le Costruzioni 2008' [125] and the connected 'Circolare 617/2009' [126]. On the basis of the knowledge level, in fact, it can be determined the confidence factor FC, which defines the reducing coefficients to be applied to the material's strength and the type of analysis to be carried out.

For existing masonry structures, one can refer to the section C8A.1A of the Circolare n. 617 where the data necessary for the identification of the knowledge level are specified. According to the document, the knowledge level LC2 can be reached when the geometrical survey is carried out, extensive in-situ investigations have been performed on constructive details and on material properties. The corresponding confidence factor is $FC = 1.2$.

The knowledge of the existing building can be reached through the historical research concerning the age and phases of construction, the geometrical and morphological survey, the decay and damage survey, with the identification of the cracking patterns and deformation evidences, the identification of the employed constructive techniques and the mechanical characterization of materials. The

comprehensiveness of the information obtained determines the knowledge level for the design.

The geometry of the building was obtained from pre-existing surveys, including detailed values for walls thickness, dimension and position of openings, presence of horizontal slabs and vaults, foundation structures. Therefore, the geometry knowledge of the building is detailed. Regarding the constructive details, the following aspect have been inspected:

- (a) Quality of the connection between vertical walls, which proved to be very poor or absent;
- (b) Quality of the connection between horizontal elements and walls (which is however irrelevant since the slabs will be replaced);
- (c) Typology of masonry and its constructive characteristics.

The analysis of the constructive detail of the building can be assumed to be widespread.

11.3.1 Analytical materials survey

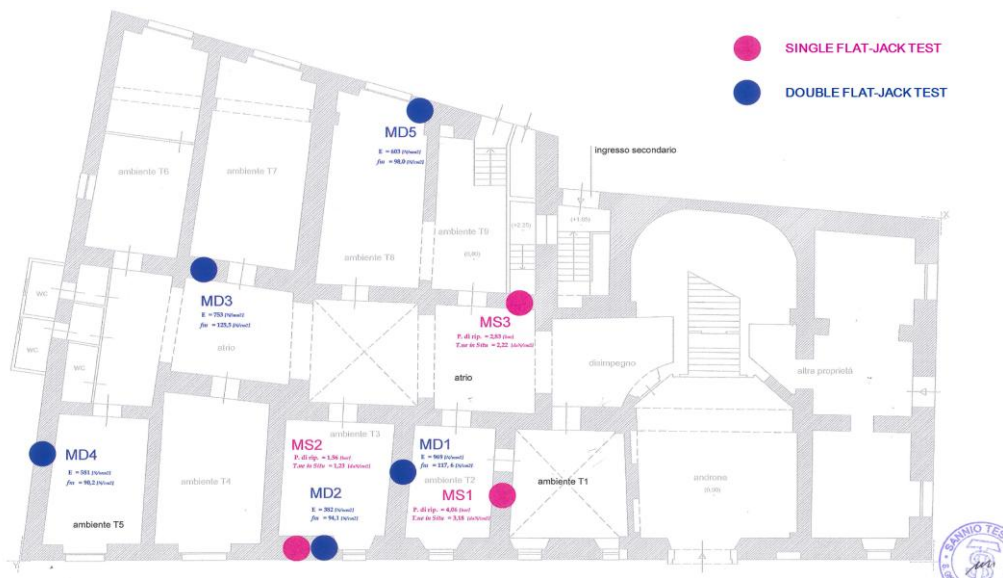
The material survey of the building has been carried out with respect to every portion of wall, with the identification of the constructive typology and materials arrangement of masonry. In the building various types of masonry are present. However, for the scope of this analysis, only the worst type of masonry was considered for the whole building, that is a mixed stone masonry named PI in the following (see Figure 11.7).



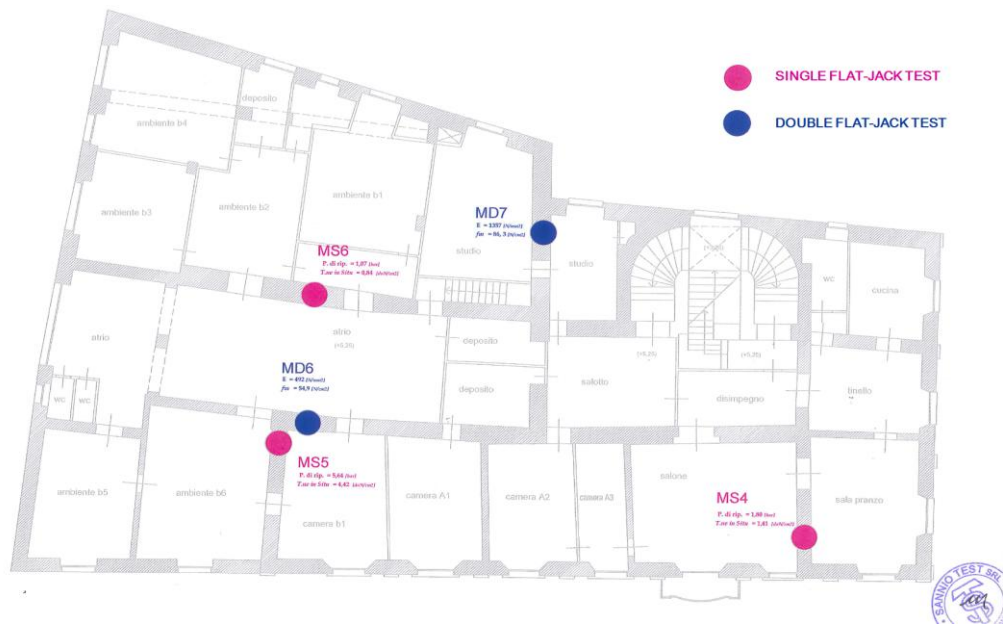
Figure 11.7. Pictures of the considered type of masonry (PI).

11.3.2 In-situ tests

In-situ tests have been carried out, in particular double flat-jack tests. The aim of the double flat-jack test is the evaluation of the strength and the modulus of elasticity of the material. Some single flat-jack tests have been also carried out in order to evaluate the current stress state of the masonry, but the results are not significant since the project of the intervention considers the demolition and reconstruction of all the slabs with a change of the loads. A total of 7 double flat-jack tests (5 at the ground floor and 2 at the first floor) and 6 single flat-jack tests (3 at the ground floor and 2 at the first floor) has been carried out (see Figure 11.8). All the tests with flat jacks have been performed on the masonry type PI, made by mixed limestone blocks and mortar, since it is the most inhomogeneous type and appeared to be in the worst conditions from the visual inspection. If the extreme values provided by the double flat-jack tests have been disregarded, a mean compressive strength of 0.97 MPa and a mean elasticity modulus of 778 MPa have been found for the irregular limestone masonry.



(a)



(b)

Figure 11.8. Position of the single and double flat-jack tests execution: ground floor (a) and first floor (b).

On the basis of the prescriptions given by the Circolare 617/2009, when a knowledge level 2 is reached, the values to be used for the strength of materials can be taken from the Table C8.A.2.1 considering the average values of the given interval, if they are lower than those obtained from the tests.

11.3.3 Foundation excavations

In order to inspect the typology of foundations, some excavations have been performed. The position of the excavations is reported in Figure 11.9. The observed depth of the foundation walls is about 1.50 meters. In some zones of the structure a depth of 2.0 meters has been also measured. Some pictures of the foundation excavations are reported in Figure 11.10.

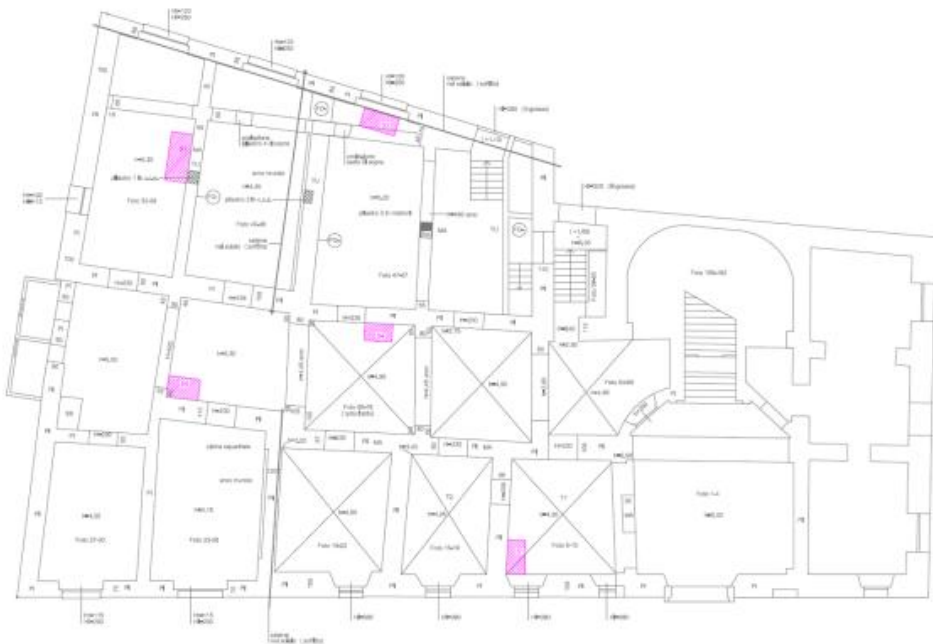


Figure 11.9. Position of the foundation excavations.



Figure 11.10. Particular of the foundation structures.

11.4 MODELLING OF THE BUILDING IN THE SOFTWARE TREMURI

The numerical modelling of the masonry building has been carried out using the TREMURI software package (Galasco et al., 2002) [127]. The hypothesis at the base of the three-dimensional modelling is that the load bearing structure of the masonry building with respect to gravity and horizontal seismic loads is defined by the vertical and horizontal elements of the structure. In particular the masonry walls represent the bearing elements, while the floors distribute the loads to the vertical walls and are considered as plane stiff elements. The local flexural behaviour of the floors and the wall out-of-plane response are not take into account since they are considered negligible with respect to the global building response, which is governed by their in-plane behaviour. It is noted that a global seismic response is possible only if the connection between vertical and horizontal elements is adequate. Non-linear frame elements are used in order to model the masonry walls, defined through a constitutive relationship to approximate the actual damage of the panel.

The in-plane behaviour of the structure depends on the characteristics of an equivalent frame (see Figure 11.11(a)), where each wall of the is subdivided into piers and lintels (modelled by non-linear beams) connected by rigid areas (nodes). The deformation of the nodes have been considered to be negligible since the observation

of damages induced on masonry buildings by the earthquakes showed that these areas are not affected by high cracking. Furthermore, the model can include the presence of stringcourses, tie rods, previous damage states, heterogeneous masonry areas, gabs and irregularities (Galasco et al., 2006) [128]. The non-linear macro-element model, representative of a whole masonry panel, is adopted for the 2-nodes elements representing piers and lintels, while rigid end offsets are used to transfer static and kinematic variables between element ends and nodes.

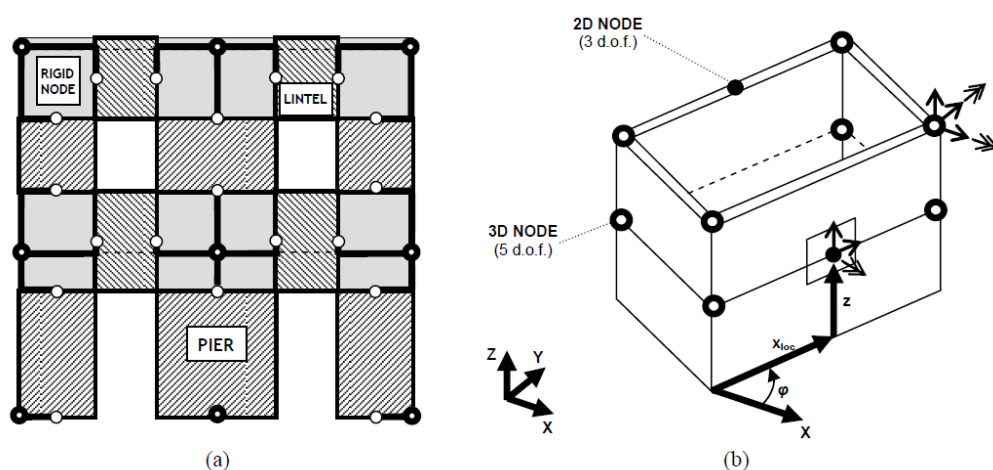


Figure 11.11. Macro-element modelling of a masonry wall (a); 3-D building model assembling (b) [128].

In order to model the three-dimensional frame representing the whole masonry building, a global Cartesian coordinate system (X, Y, Z) is defined for spatial identification of the vertical planes of the walls. For each wall, these planes are defined by the coordinates of one point and the angle formed with X axis. This allows the walls to be modelled as planar frames in the local coordinate system and internal nodes can still be 2-dimensional nodes with 3 d.o.f.. The 3D nodes connecting different walls in corners and intersections need to have 5 d.o.f. in the global coordinate system $(u_x, u_y, u_z, r_x, r_y)$: the rotational degree of freedom around vertical Z axis can be neglected because of the membrane behaviour adopted for walls and floors. These nodes can be obtained assembling 2D rigid nodes acting in each wall plane (Figure 11.11(b)) and projecting the local degrees of freedom along global

axes. Floor elements, modelled as orthotropic membrane finite elements, with 3 or 4 nodes, are identified by a principal direction. Since the 2D nodes do not have degrees of freedom along the direction orthogonal to the wall plane, in the calculation, the nodal mass component related to out-of-plane degrees of freedom is shared to the corresponding dofs of the nearest 3D nodes of the same wall and floor. This solution then allows to carry out static and dynamic analyses with components of the seismic acceleration applied along any direction.

A non-linear beam element model (Figure 11.12) has been implemented in the TREMURI (Galasco et al., 2002) [127] in together with the macro-element with additional degrees of freedom, described by:

- Initial stiffness given by elastic (cracked) properties;
- bilinear behaviour with maximum values of shear and bending moment as calculated in ultimate limit states;
- redistribution of the internal forces according to the element equilibrium;
- detection of damage limit states considering global and local damage parameters;
- stiffness degradation in plastic range;
- secant stiffness unloading;
- ductility control by definition of maximum drift (Δ_u) based on the failure mechanism, according to the Italian building code: $\Delta_u = (\bar{\delta}_s - \bar{\delta}_i) / h$, being $\bar{\delta}_s$ and $\bar{\delta}_i$) the displacements at the top and at the base of the element, respectively, and h its height.
- element expiration at ultimate drift without interruption of global analysis.

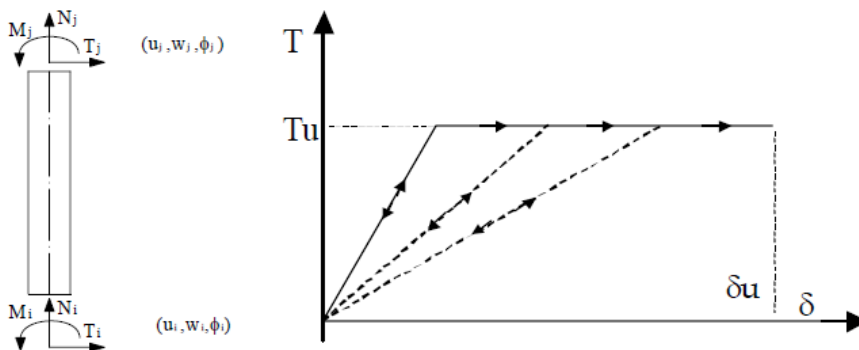


Figure 11.12. Non-linear beam degrading behaviour [128].

The position of the vertical and horizontal elements in the model can be seen from Figure 11.13 for the ground floor and the first floor of the building. In the figure the presence of slabs and vaults is indicated with different colours. In the floor plans illustrated in Figure 11.14, the orientation of the slabs is reported with respect to each level. Finally, in Figure 11.15 two three-dimensional view of the model are illustrated.

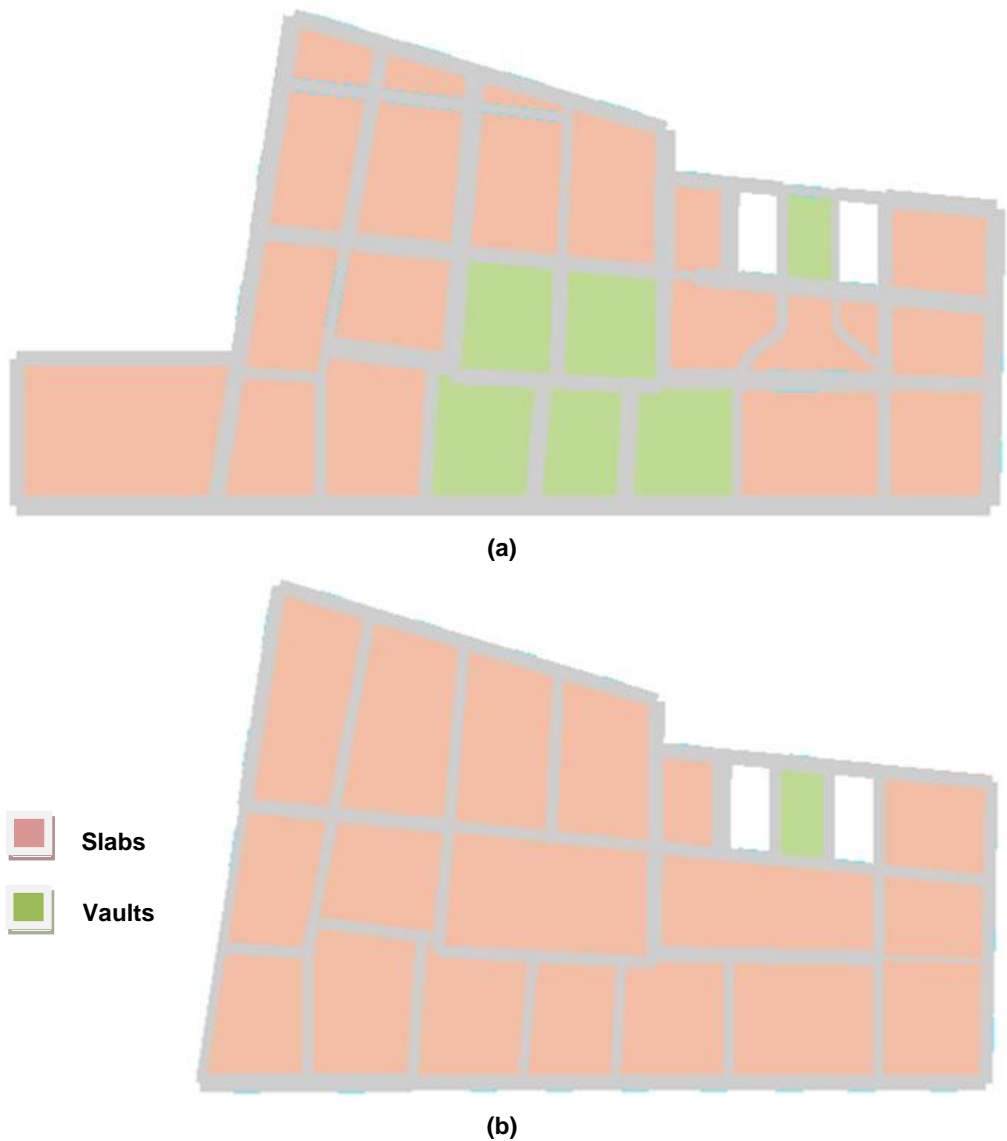
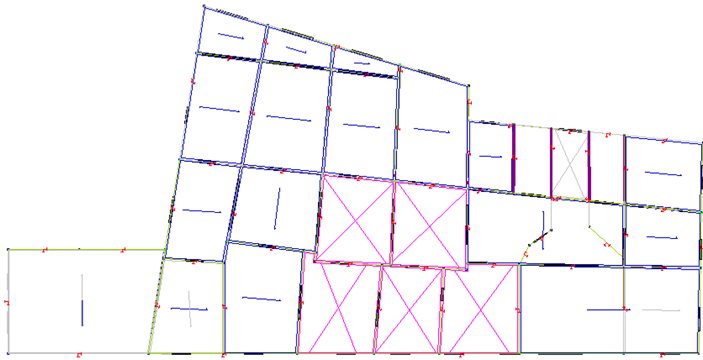


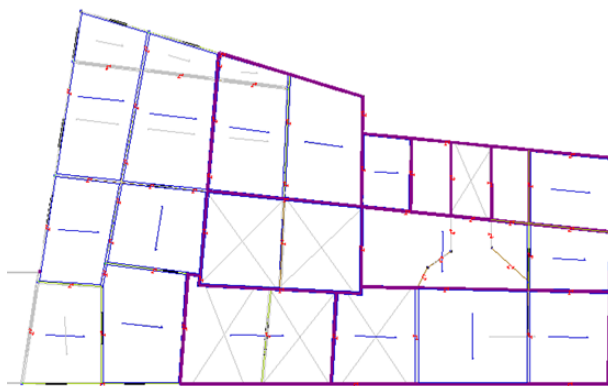
Figure 11.13. Position of walls, slabs and vaults in the model of the building: ground floor (a) and first floor (b).



(a)



(b)



(c)

Figure 11.14. Orientation of slabs in the model of the building: basement level (a), ground floor (b) and first floor (c).

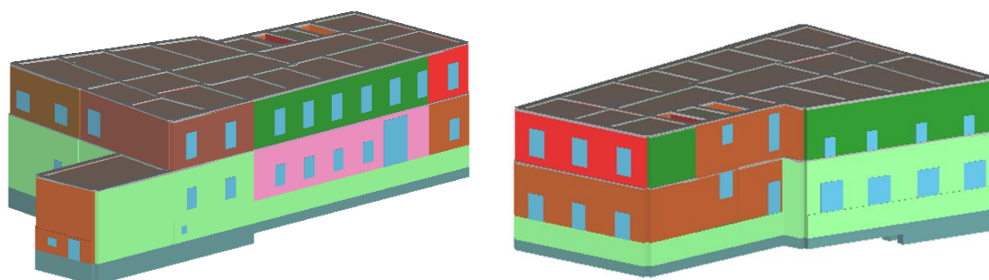


Figure 11.15. Three-dimensional views of the model of the building.

11.5 SEISMIC HAZARD ASSESSMENT

The Italian building code ‘Norme Tecniche per le Costruzioni 2008’ [125] defines the seismic hazard for a given site on the basis of a seismic source zone model ZS9 developed by (Meletti and Montaldo, 2007) [129] and on the parameters estimated by the Italian National Institute of Geophysics and Volcanology (INGV), with respect to a regular grid having 5 km spacing and covering the whole Italian territory with 10751 nodes. Probabilistic seismic hazard analysis (PSHA) by INGV allowed to estimate seismic hazard at each site of the reference grid.

The seismic hazard parameters provided by Italian building code are the reference peak horizontal acceleration on soil type A (namely, the bedrock for any other soil type), a_g ; the maximum amplification factor of the horizontal acceleration response spectrum, F_0 ; and upper limit of the period of the constant spectral acceleration branch on soil type A, T_C^* . Such parameters are defined to a given return period T_R , depending on the reference period V_R and the probability of exceeding the a_g value in V_R , denoted as R_{VP} .

For the building considered in this study a building class II have been assumed, corresponding to an importance coefficient $C_U = 1.0$. The seismic hazard parameters for the considered case are summarized in Table 11.1 for the different limit states.

Limit state	T_R [years]	a_g [g]	F_o [-]	T_C^* [s]
Operational (SLO)	30	0.059	2.379	0.285
Limited damage (SLD)	50	0.078	2.343	0.317
Life safety (SLV)	475	0.249	2.378	0.372
Near collapse (SLC)	975	0.349	2.320	0.423

Table 11.1. Seismic hazard parameters for Ariano Irpino, Italy.

A soil type B (corresponding to a shear velocity $V_{s,30}$ between 360 m/s and 800 m/s within a 30 m-deep soil deposit) and a topographic class T1 (i.e., a ground surface with average slope between 0 and 15°) are assumed. The Italian code provides soil factor S as the product of a stratigraphic amplification factor S_s by a topographic amplification factor S_T . The upper limit of the period of the constant spectral acceleration branch, T_C is evaluated as a factor related to soil type, C_C times the period T_C^* . The lower limit of the period of the constant spectral acceleration branch is then defined as $T_B = T_C/3$, while the lower limit of the period of the constant spectral displacement branch is defined as $T_D = 4a_g/g + 1.6$, being g the acceleration of gravity. The obtained parameters are summarized in Table 11.2.

Limit state	S_s [-]	C_C [g]	S_T [-]	S [-]	T_B [s]	T_C [s]	T_D [s]	PGA_{dem} [g]
Operational (SLO)	1.200	1.414	1.0	1.200	0.134	0.403	1.836	0.071
Limited damage (SLD)	1.200	1.384	1.0	1.200	0.146	0.439	1.913	0.094
Life safety (SLV)	1.163	1.341	1.0	1.163	0.166	0.498	2.595	0.289
Near collapse (SLC)	1.076	1.306	1.0	1.076	0.184	0.553	2.995	0.375

Table 11.2. Parameters of the elastic spectra for every limit state.

11.6 PUSH-OVER ANALYSIS

11.6.1 Unreinforced building

The seismic codes, such as the Eurocode 8 [130] and the Italian Norme Tecniche per le Costruzioni D.M. 2008, give the possibility to apply a non-linear static

(pushover) analysis for the assessment of existing buildings. This procedure is characterized by several matters of discussion particularly if the application to masonry building is considered. For example, a three-dimensional pushover analysis requires the definition of a predefined pattern for horizontal forces induced by the earthquake, which is not easy to define if the non-linear degradation of the material of the structure is considered. Adaptive pushover analysis of masonry buildings should be taken into consideration, where the load pattern is directly derived by a step-by-step, depending on the actual deformed shape evaluated during the analysis. The non-linear static analysis procedure adopted in the Eurocode 8 and in the Italian seismic code, both for design and assessment, is based on a maximum displacement prediction, which depends on the definition of an equivalent elastic perfectly plastic s.d.o.f. structure, derived from a capacity curve obtained by a pushover analysis. This kind of analysis requires a predefined pattern of horizontal forces to be applied to the structure and, keeping constant the relative force ratios, the horizontal displacement of a control node is incremented. However the choice of control node and force distribution is not univocal and results may depend on it.

For the case study the pushover analyses have been carried out with respect to the principal directions of the building, taking into account the two main orientations of the seismic resistant elements, represented by the walls placed along the earthquake direction. Regarding the masonry typology, it was previously said that the building is characterized by a very wide distribution of materials and block-mortar joint arrangements.

E [MPa]	f_c [MPa]	τ [MPa]	G [MPa]
800	1.0	0.0292	180

Table 11.3. Mechanical properties of the considered material.

For the sake of simplicity, the following analyses were carried out considering an homogeneous distribution of material, with reference to a masonry with the following mechanical properties (Table 11.3). It is the case of a tuff masonry with

compressive strength of 1.0 MPa and Young's modulus of 800 MPa. The other parameters were obtained from the range of values suggested in the section C8A.1A of the Circolare n. 617, considering a knowledge level LC2.

The results of the pushover analysis are summarized in Table 11.4 in terms of comparison between displacement capacity (d_u) and demand (d_{max}) imposed by the seismic action for both SLU and SLD. Four cases of analysis were considered according to the directions +/-X and +/-Y. Two types of horizontal forces distributions were considered, proportional to the building's masses distribution over height and proportional to the 1st vibration mode. It is noted that the SLU displacement capacity of the unreinforced structure is highly insufficient if compared to the displacement demand imposed by the earthquake. For the SLU, the minimum safety factor is about 0.4, while the SLD is always satisfied. In the table α_e is the multiplier of the horizontal forces to which the structure is subjected if considered perfectly elastic and it is defined considering that the horizontal top displacement corresponding to the collapse of the inelastic system and the corresponding elastic system are equal; while α_u is the multiplier of the horizontal forces corresponding to the collapse condition at the ultimate limit state.

Earthquake direction	Force distribution	d_{max} SLU [mm]	d_u SLU [mm]	q^* SLU [-]	d_{max} SLD [mm]	d_d SLD [mm]	α_u [-]	α_e [-]
+X	proportional to masses	32.9	13.3	3.523	6.3	9.0	0.500	1.212
+X	proportional to 1 st mode	37.3	15.7	3.798	8.0	11.4	0.499	1.246
-X	proportional to masses	33.0	13.3	3.419	6.2	12.6	0.500	1.505
-X	proportional to 1 st mode	37.0	15.0	3.688	7.8	13.1	0.490	1.388
+Y	proportional to masses	32.8	17.3	3.284	5.9	10.2	0.608	1.334
+Y	proportional to 1 st mode	36.4	19.0	3.377	7.2	14.4	0.597	1.526
-Y	proportional to masses	32.9	17.8	3.353	6.1	9.9	0.617	1.306
-Y	proportional to 1 st mode	36.5	20.0	3.475	7.3	14.3	0.616	1.503

Table 11.4. Results of the pushover analysis for the unreinforced building.

11.6.2 Reinforced building

For the reinforced building, an intervention corresponding to a shear strength increment of masonry panels of 100% was then considered, with reference to the results of the parametric analysis on tuff walls 240 mm thick. The reinforcement configuration which gives such an increment corresponds to the application of frp grid reinforced mortar layers 20 mm thick on the surfaces of the masonry wall. In the case of the building the presence of the reinforcement with frp grid and mortar layers is not directly modelled as in the case of the detailed finite element modelling described in the previous chapter. Thus, the effect of the reinforcement is taken into account assuming increments in the strength of materials and in the maximum displacement of the panels. The compressive strength of the material considered in the model was increased considering an equivalent cross-section constituted by the masonry wall and two external layers of mortar. For 20 mm thick mortar layers, the obtained equivalent compressive strength is equal to 1.12 MPa, with an increment of 12% compared to the unreinforced case. The same consideration has been made for the evaluation of the equivalent modulus of elasticity of the reinforced material, equal to 871 with an increment of 8.9% with respect to the modulus of elasticity of the unreinforced masonry (800 MPa). Regarding the shear strength of the reinforced panel, the mean value given by the section C8A.1A of the Circolare n. 617 divided by the factor FC has been assumed and multiplied by a factor equal to 2, since an intervention corresponding to a shear strength increment of 100% was considered.

As summarized in Table 11.5, in the first case the analysis was carried out considering the increment of strength only, while in the second case also the increment of the available horizontal drift was considered. The considered reinforcement solution could allow to reach a drift about 2.6 times higher than the corresponding unreinforced case. This resulted in a value of drift higher than the maximum value of drift which was possible to be considered in the software. For this reason the maximum value of drift was considered, equal to 1.0%. The results of the first strengthened case are reported in Table 11.6.

Material	E [MPa]	Var.	f _c [MPa]	Var.	τ [MPa]	Var.	G [MPa]	Var.	Shear drift [%]	Var.
Plane masonry	800	-	1.0	-	0.0292	-	180	-	0.4	-
Increment of strength (1 st Intervention)	871	8.9%	1.12	12%	0.0584	100%	196	8.9%	0.4	0%
Increment of strength and ductility (2 nd Intervention)	871	8.9%	1.12	12%	0.0584	100%	196	8.9%	1.0	150%

Table 11.5. Mechanical parameters considered for the different cases of analysis.

Earthquake Direction	Force distribution	d _{max} SLU [mm]	d _u SLU [mm]	q* SLU [-]	d _{max} SLD [mm]	d _d SLD [mm]	α _u [-]	α _e [-]
+X	proportional to masses	29.6	15.7	2.688	5.1	13.6	0.631	1.796
+X	proportional to 1 st mode	33.9	19.8	3.019	6.1	16.6	0.657	1.809
-X	proportional to masses	29.1	14.2	2.476	5.1	13.5	0.609	1.834
-X	proportional to 1 st mode	32.8	25.4	2.686	6.0	13.0	0.819	1.614
+Y	proportional to masses	28.0	17.2	2.169	5.2	11.9	0.717	1.798
+Y	proportional to 1 st mode	31.7	23.3	2.274	6.1	18.4	0.798	2.120
-Y	proportional to masses	28.5	19.0	2.298	5.2	11.4	0.751	1.715
-Y	proportional to 1 st mode	32.3	24.4	2.441	6.1	17.6	0.808	2.013

Table 11.6. Results of the pushover analysis for the reinforced building (Increment of strength).

It is noted that even in case of an increment of 100% in terms of shear strength of the masonry panels the displacement demand is higher than the capacity of the structure (the minimum safety factor is about 0.5, that is about the same of the unstrengthened condition) and further increases of shear strength do not allow the structure to be checked. Increasing also the ductility (of about 150% for shear deformability and 67% for flexural deformability) through the available horizontal drift, the pushover analysis provided the results summarized in Table 11.7. In this case it

was obtained that the displacement required (the minimum safety factor is about 1). capacity of the building is higher than the displacement imposed by the earthquake for every considered direction. In conclusion the increment of the strength has a negligible effect respect to the effect of the ductility increment.

Earthquake direction	Force distribution	d_{\max} SLU [mm]	d_u SLU [mm]	q^* SLU [-]	d_{\max} SLD [mm]	d_d SLD [mm]	α_u [-]	α_e [-]
+X	proportional to masses	29.4	31.4	2.592	5.1	12.6	1.052	1.736
+X	proportional to 1 st mode	33.6	41.0	2.860	6.1	17.4	1.049	1.899
-X	proportional to masses	28.9	30.1	2.419	5.1	14.1	1.032	1.926
-X	proportional to 1 st mode	32.8	40.9	2.581	6.0	18.0	1.162	2.004
+Y	proportional to masses	28.0	42.0	2.168	5.2	13.1	1.268	1.904
+Y	proportional to 1 st mode	31.7	46.1	2.271	6.1	16.0	1.321	1.937
-Y	proportional to masses	28.3	41.8	2.254	5.2	13.2	1.331	1.878
-Y	proportional to 1 st mode	32.3	48.8	2.426	6.1	17.1	1.236	2.027

Table 11.7. Results of the pushover analysis for the reinforced building (Increment of strength and ductility).

As an example, the pushover curves for the direction +X and +Y of the building are respectively reported in Figure 11.16 and 11.17, for the case of distribution of forces proportional to masses.

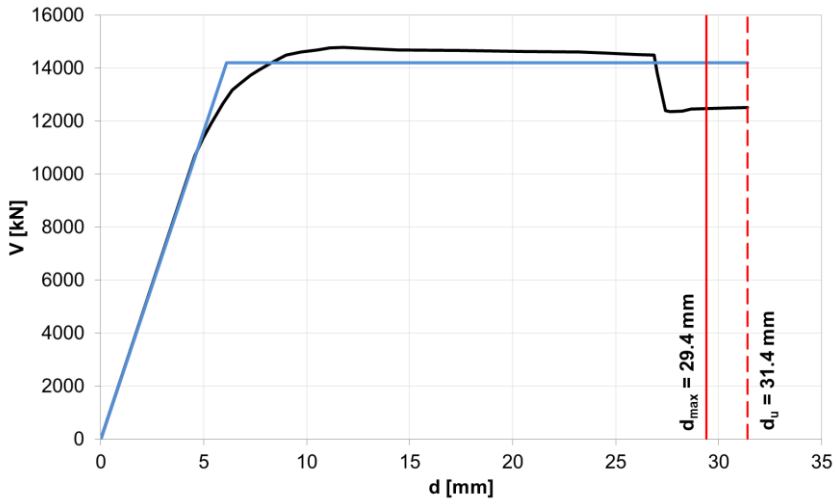


Figure 11.16. Pushover curve for +X direction for force distribution proportional to masses.

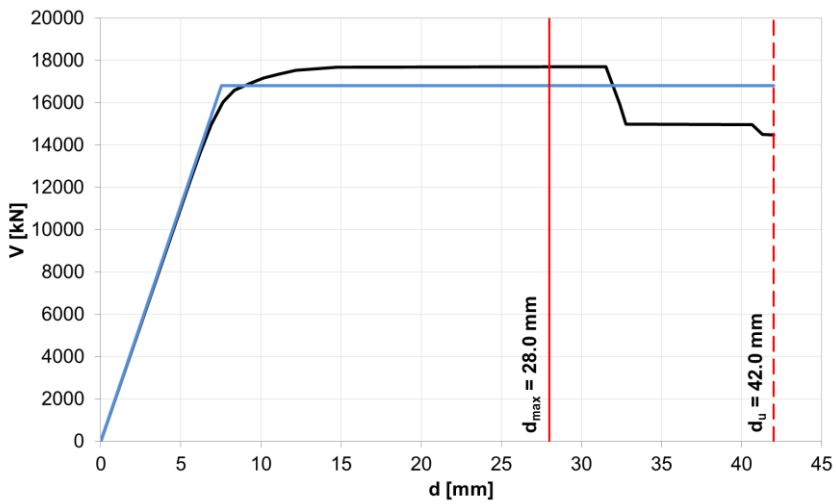


Figure 11.17. Pushover curve for +Y direction for force distribution proportional to masses.

12 CONCLUSIONS AND FUTURE DEVELOPMENTS

The main issues investigated in the present work are related to the study of the structural behaviour and the definition of simplified strategies for global modelling of masonry buildings subjected to seismic actions. The effect of strengthening of masonry walls by means of FRP grid reinforced mortar layers is studied. In particular, the strengthening technique taken into account in the research is represented by externally applied mortar panels embedding a FRP reinforcement in form of bi-directional grid. The mortar encloses the reinforcement passing through the grid's openings allowing an effective mechanical interlocking that assures a composite behaviour of the system. In addition, the use of lime- or cement-based mortar allows the development of a better bonding between the strengthening system and the surface of the masonry panel. The effectiveness of the collaboration between reinforcement and substrate has been also investigated in the course of the research program.

The described FRP reinforced mortar panels are applied on the surfaces of the unreinforced masonry wall (URM) in a symmetric configuration, and can be also connected to the substrate by means of an adequate anchoring system. The research was aimed to assess the effectiveness in the upgrading of the overall behaviour of the strengthened URM walls. The retrofitting of masonry elements through FRP grid reinforced mortar layer allows to increase the in-plane shear resistance, provide the system an enhanced ductility, assure a higher integrity and reduce the damage of the panels in order to contain serviceability problems. Thus, the performances of the URM walls strengthened by means of this reinforcing system have been investigated.

An experimental program on prototypes as well as the FEM modelling of the system was carried out in order to replicate the structural behaviour of the assemblage.

First of all, the main issues concerning the reinforcement and strengthening of masonry walls, especially with regards to horizontal actions induced by earthquake, have been analysed and some of the more common traditional techniques have been reviewed, particularly highlighting some of the disadvantages or drawback of each of them. Furthermore, a detailed bibliographic research has been carried out on the more recent strengthening techniques for masonry walls which make use of innovative materials, such as Fiber Reinforced Polymers. In particular, the literature review has been focused on the reinforcement of masonry walls by means of mortar layers reinforced with grids in FRP, considering the main developments in terms of both experimental and theoretical fields.

The considered strengthening technique is characterized by a number of advantages if compared to other possible FRP-based strengthening methods; particularly, a greater resistance to fire action has to be remarked, a good compatibility and bond with the substrate material, particularly in the case of masonry, vapour permeability. The main interest in the study of this strengthening technique is related to the promising possibility it offers in the upgrading in-plane shear behaviour of the system to which it is applied and one of the important issue to address is also the assessment of the effectiveness of the considered strengthening system in the improvement of the overall ductility of the reinforced elements. Moreover, the choice of a cementitious material for the reinforcement layers is due to some advantages, mainly related to its highly compatibility in terms of physical and mechanical properties with the tuff substrate. In addition, for strengthening of walls exposed to high temperature or environmental effects, the application of a sufficiently thick layer of cementitious mortar substantially ensures a protection for the reinforcing grid and improves the long-term behaviour of the strengthening system.

The study has been firstly focused on the characterization of the mechanical behaviour of the masonry in compression by means of finite element modelling. For this purpose, the influence of the presence of mortar joints, as well as the influence of different non-linear parameters on the post-peak behaviour of the material has been

investigated. Afterwards, an experimental campaign on masonry panels reinforced by means of mortar layers has been carried out. The layers of mortar contained an embedded polymeric grid and were applied in a symmetric fashion onto the external surfaces of the panels. The experimental tests have been carried out on adobe masonry walls, being adobe a material used to produce bricks with mechanical properties similar to Italian clay bricks. The effectiveness of the reinforcement technique with mortar layers and fibers has been studied through cyclic tests on panels horizontally loaded in their plane.

The reinforcement of such elements by means of polymeric grids has the purpose to give ductility resources to the system, to provide better integrity to the wall and to reduce the damage of panels in service conditions. The results obtained can be used for the design of retrofitting interventions of masonry in seismic areas.

The experimental tests allowed to observe that compared to the typical crack pattern usually found in plane masonry walls, with the formation of classical X-shaped main cracks, when the wall is strengthened with reinforced mortar layer it presents a more widespread and diffused crack pattern. The mortar layer reinforced with a polymeric grid has also the effect of redistributing the stresses originated upon loading and, thus, to spread the crack pattern over a wider area of the wall surface. The experimental tests evidenced also the necessity to study the interface behaviour between the external reinforcement and the masonry substrate to which it is applied represented by the wall in the evaluation of the effectiveness of this kind of reinforcement. Since the reinforced mortar layer applied on the wall surfaces is slightly thin and due to the different stiffness compared to the substrate, it can be subjected to out-of-plane forces that may cause its detachment. This effect has been registered in the portion of the strengthening layer localized in the central area of the specimen. Comparing the behaviour of the reinforced wall with the unreinforced control specimen, it has been observed that the application of the reinforced mortar layers onto the wall's surfaces allows the specimen to reach a higher value of strength, with an increment of about 20%, and produces an enhancement in terms of ductility. Considering the retrofitted wall the strengthening with reinforced plaster allow the specimen to reach a strength of about 70% of the original situation.

Furthermore, the FRP reinforcement was designed to provide tensile strength to a masonry wall, so that the strength and ductility of the masonry wall are increased, which both improves the behaviour of the wall during an extreme loading event as the earthquake is. Common FRP composites are completely elastic until failure, even though some attempts have been made recently to introduce some ductility into the composite material by using a combination of different modulus fibres. The main disadvantage with using FRP materials for reinforcement is that they have brittle failure modes. FRP materials may fail by rupturing or, if no mechanical anchorage is provided, by debonding from the substrate material. Tensile force in the FRP is transferred through the adhesive to the masonry via shear stresses. When the shear strength of the adhesive or the superficial layer of brick is exceeded, debonding occurs. Debonding may also occur along the interface between the brick and adhesive or the interface between the adhesive and FRP. Both rupture and debonding failure modes are brittle in nature, potentially leading to non-ductile behaviour and catastrophic collapse.

Moreover, when inorganic matrixes are used, in place of common polymeric adhesives, the debonding surface is no longer localized in the superficial layer of the support material, but rather inside the matrix, which represents the weaker element. Therefore, one of the limitation in the application of reinforcement in inorganic matrixes is related to the actual debonding strength, that represents one of the fundamental collapse mechanisms of the strengthening system.

In order to go deep into the debonding phenomenon of composite materials employed to strengthen masonry elements, an experimental campaign regarding bond tests on yellow tuff blocks has been carried out, using different types of fibers (glass, carbon, basalt and linen). Tests have been conducted by means of a testing device designed for the purpose and in order to assess the influence of several mechanical parameters (type of fiber, bonded length, type of treatment of the substrate material's surface, tuff strength).

In particular, the experimental results evidenced that: 1) debonding was the most frequently observed failure mode and did not allow use the full tensile strength of the fibers; 2) a bonded length of 300 mm seems to be sufficient to develop the full bond strength for the examined support; 3) when the plaster layer is not applied, the

debonding load reduces of about 15% for the more resistant tuff and of about 25% in the case of lower compressive strength; 4) no relevant difference was observed in specimens with carbon and glass fibers having similar axial stiffness; 5) the different axial stiffness of the fibers (i.e. linen and basalt compared with glass and carbon fibers) influences the slope of the load-displacement curves; 6) the reduction of compressive strength of the support of about 45% led to have a reduction of the debonding load of about 15%.

The last part of the research regards the numerical modelling of the masonry walls unreinforced and reinforced by the mortar layers with the composite grids. For this purpose, the main issues investigated concern the study of possible approaches for modelling of masonry panels, the numerical study of masonry panels subjected to compressive loading by means of micro- and macro-modelling and the numerical modelling of masonry walls reinforced by means of polymeric grids embedded in mortar layers subjected to in-plane loading. The aim was to define the effectiveness of the strengthening technique in the upgrading and retrofitting of the overall behaviour of masonry walls with respect to the in-plane shear resistance and overall ductility.

The finite elements modelling of masonry panels tested by other researchers against compressive loading was first carried out, with the aim to investigate their non-linear behaviour. Masonry panels have been modelled through finite elements method, by using the non-linear code DIANA 9.4.4. For the tuff masonry panels subjected to compressive loading a micro-modelling as well as an equivalent homogeneous macro-modelling was performed, in order to study the non-linear behaviour and calibrate a homogenized equivalent material. The differences between the two approaches have been evidenced. The homogeneous macro-model shows the same behaviour of the complex model, but has a different computational cost, useful for future analytical applications to entire buildings.

The numerical modelling via finite elements methods of masonry panels subjected to cyclic in-plane loading tested at the Institute of Theoretical and Applied Mechanics (ITAM) of Prague (Czech Republic) was also carried out. The unreinforced masonry panel made by adobe bricks has been modelled first and the non-linear mechanical parameters of the material have been calibrated by comparison with the

global force – displacement curve obtained from the experiments, as well as with the cracking and damage pattern experienced by the wall. A macro-modelling technique has been considered and a homogeneous material has been calibrated in which the effect of the characteristics of mortar joints and masonry units are smeared. For this purpose, the non-linear finite element code DIANA 9.4.4 has been employed. The values of compressive and tensile fracture energy of materials have been calibrated in order to obtain numerical curves comparable with the experimental ones, even though they were obtained from cyclic tests.

Afterwards, the panels strengthened by means of mortar layers reinforced with composite grids applied on both surfaces have been modelled. The effect of the reinforcement on the strength and displacement capacity of the wall is evidenced. The reinforcement has been modelled by means of an equivalent grid embedded in a surface representing the layer of mortar applied to the wall's faces.

Through the numerical model a wide parametric analysis has been conducted to evaluate the effect of the amount and type of FRP on the stiffness, strength and ductility of the masonry wall. The results show that the most important parameter of the FRP material used for the strengthening is the axial stiffness (EA), while for the mortar the two parameters are the thickness and the strength in compression. Two types of masonry materials have been considered, characterized by different values of compressive strength. The analysis showed that the reinforcement plays a more effective role on the lower quality masonry. Moreover, it has been noticed that similar increments of strength can be obtained by means of different strengthening configurations, with respect to the thickness of the reinforcement mortar and amount of frp reinforcement.

On the basis of the results obtained from the experimental and the numerical analysis, the model of a masonry building by means of equivalent frame elements has been implemented by the software Tremuri in order to assess the influence of the reinforcement in the overall seismic capacity of the structure. The software uses the approach of the equivalent frames and executes a non-linear analysis of the building.

The analyses carried out show that the increment of ductility obtained with the application of the FRP with the mortar layer is more effective than the increment of strength.

The results provided by the described research activity represent a basis for developments of future work and investigations. The experimental results and data provided by the laboratory tests showed the behaviour of masonry elements made by different types of bricks and can be used in further studies in order to investigate the behaviour of masonry elements made by other types of masonry, in terms of arrangement of units and mortar joints, mechanical characteristics of the employed materials, age of the construction.

The bond between the system made by a mortar layer embedding a composite grid can be studied more in detailed both from the experimental and numerical point of view since it represents a key point in the effectiveness of the intervention.

Also, further analysis can be carried out regarding the evaluation of the effectiveness in terms of increase of strength and ductility when different materials and techniques are used for the intervention on vulnerable masonry building. Further numerical analysis can be carried out considering different modelling strategies for the description of the seismic behaviour of masonry building, in order to compare them and provide indications for design purposes.

REFERENCES

- [1] Tomažević, M. (1999). *Earthquake-resistant design of masonry buildings*. Imperial College Press, London, England.
- [2] Meyer, P., Ochsendorf, J., Germaine, J., and Kausel, E. (2007). *The impact of high-frequency/low-energy seismic waves on unreinforced masonry*. *Earthquake Spectra*, Vol. 23, No. 1, pp. 77–94.
- [3] ElGawady, M.A., Lestuzzi, P., and Badoux, M. (2007). *Static cyclic response of masonry walls retrofitted with fiber-reinforced polymers*. *Journal of Composites for Construction*, Vol. 11, No. 1, February 1, 2007, ASCE pp. 50–61.
- [4] Prota, A., Marcari, G., Fabbrocino, G., Manfredi, G., and Aldea, C. (2006). *Experimental in-plane behavior of tuff masonry strengthened with cementitious matrix–grid composites*. *Journal of Composites for Construction* Vol. 10, No. 3, June 1, 2006, ASCE pp.223–233.
- [5] Lignola, G.P., Prota, A., and Manfredi, G. (2009). *Nonlinear analyses of tuff masonry walls strengthened with cementitious matrix-grid composites*. *Journal of Composites for Construction* 2009;13(4):243–251, ASCE.
- [6] Faella, C., Martinelli, E., Nigro, E., and Paciello, S. (2010). *Shear capacity of masonry walls externally strengthened by a cement-based composite material: An experimental campaign*. *Construction and Building Materials*, vol. 24, 2010.
- [7] Lourenço, P.B. and Piña-Henriques, J.L. (2006). *Validation of analytical and continuum numerical methods for estimating the compressive strength of masonry*. *Computers and Structures*, vol. 84.

- [8] Binda, L., Fontana, A., and Frigerio, G. (1988). *Mechanical behaviour of brick masonries derived from unit and mortar characteristics*. Proc. 8th Int. Brick and Block Masonry Conf., Dublin, Ireland, 1, 205-216.
- [9] Lourenço, P.B. (1996). *Computational strategies for masonry structures*. Doctoral Thesis, Delft University of Technology. Delft University Press, 1996.
- [10] Francis, A., Horman, C., and Jerrems, L. (1971). *The effect of joint thickness and other factors on the compressive strength of brickworks*. Proc. 2nd Int. Brick and Block Masonry Conf., Stoke-on-Trent, UK, 31-37.
- [11] Calderoni, B., Cordasco, E.A., Guerriero, L., Lenza, P., and Manfredi, G. (2009). *Mechanical Behavior of Post-Mediaeval Tuff Masonry of the Naples Area*. Masonry International, Journal of the International Masonry Society, vol. 21, no. 3.
- [12] Calderoni, B., Cecere, G., Cordasco, E.A., Guerriero, L., Lenza, P., and Manfredi, G. (2010). *Metrological definition and evaluation of some mechanical properties of post-medieval Naepolitan yellow tuff masonry*. Journal of Cultural Heritage, vol. 11, n. 2.
- [13] ElGawady, E., Lestuzzi, P., and Badoux, M. (2004). *A review of conventional seismic retrofitting techniques for URM*. 13th International Brick and Block Masonry Conference, Amsterdam, July 4-7, 2004.
- [14] Triantafillou, T.C. (1998). *Composites: a new possibility for the shear strengthening of concrete, masonry and wood*. Composites Science and Technology 1998;58:1285–1295. Elsevier.
- [15] Croci, G., Ayala, D., Asdia, P., and Palombini, F. (1987). *Analysis on shear walls reinforced with fibres*. IABSE Symp. on Safety and Quality Assurance of Civil Engineering Structures, Tokyo, 1987.
- [16] Triantafillou, T.C., and Fardis, M.N. (1997). *Strengthening of historic masonry structures with composite materials*. Materials and Structures, 1997, 30, 486–496.
- [17] Triantafillou, T.C., and Fardis, M.N. (1993). *Advanced composites for strengthening historic structures*. IABSE Symp. on Structural Preservation of the Architectural Heritage, Rome, 1993, 541–548.

- [18] Schwegler, G. (1994). *Masonry construction strengthened with fiber composites in seismically endangered zones*. Proc. 10th Europ. Conf. on Earthquake Eng., Vienna, Austria, 1994.
- [19] Saadatmanesh, H. (1994). *Fiber composites for new and existing structures*. ACI Structural Journal, 1994, 91(3), 346–354.
- [20] Ehsani, M.R. (1995). *Strengthening of earthquake-damaged masonry structures with composite materials*. In Non-metallic (FRP) Reinforcement for Concrete Structures. Ed. L. Taerwe, 1995, 680–687.
- [21] Roca, P., and Araiza, G. (2010). *Shear response of brick masonry small assemblage strengthened with bonded FRP laminates for in-plane reinforcement*. Construction and Building Materials 2010;24:1372–1384. Elsevier.
- [22] Valluzzi, M.R., Tinazzi, D., and Modena, C. (2002). *Shear behavior of masonry panels strengthened with FRP laminates*. Construction and Building Materials, Elsevier, 2002; 16(7): 409–416.
- [23] ElGawady, M.A., Lestuzzi, P., and Badoux, M. (2005). *In-plane response of URM walls upgraded with FRP*. Journal of Composites for Construction 2005;9(6):524–535. ASCE.
- [24] Avramidou, N., Drdácáký, M.F., and Procházka, P.P. (1999). *Strengthening against damage of brick walls by yarn composites*. Proceedings of the 6th Int. Conf. On Inspection, Appraisal, Repairs and Maintenance of Buildings and Structures, pp. 51-58, Melbourne, December 1999.
- [25] Santa Maria, H., Alcaino, P., and Luders, C. (2006). *Experimental response of masonry walls externally reinforced with carbon fiber fabrics*. In: Proceedings of the 8th US National Conference on Earthquake Engineering; 2006. Paper no. 1402.
- [26] Fam, A., Musiker, D., Kowalsky, M., and Rizkalla, S. (2008). *In-plane testing of damaged masonry wall repaired with FRP*. Adv Compos Lett 2008;11(6):275–81.
- [27] Al-Salloum, Y.A., and Almusallam, T.H. (2005). *Walls strengthened with epoxy-bonded GFRP sheets*. Journal of Composite Materials 2005;(39):1719–1745. SAGE.

- [28] Wang, Q., Chai, Z., Huang, Y., and Zhang, Y. (2006). *Seismic shear capacity of brick masonry wall reinforced by GFRP*. Asian Journal of Civil Engineering (Building and Housing) 2006;7(6):563–580.
- [29] Stratford, T., Pascale, G., Manfroni, O., and Bonfiglioli, B. (2004). *Shear strengthening masonry panels with sheet glass–fiber reinforced polymer*. Journal of Composites for Construction 2004;8(5):434–443. ASCE.
- [30] Marcari, G., Manfredi, G., Prota, A., and Pecce, M. (2007). *In-plane shear performance of masonry panels strengthened with FRP*. Composites - Part B: Engineering, Elsevier, 2007; 38: 887-901.
- [31] Triantafillou, T.C. (1998). *Strengthening of masonry structures using epoxy-bonded FRP laminates*. Journal of Composites for Construction 1998;2(2):96–104. ASCE.
- [32] Luccioni, B., and Rougier, V.C. (2010). *In-plane retrofitting of masonry panels with fibre reinforced composite materials*. Construction and Building Materials. Article in Press. Elsevier.
- [33] Chuang, S., Zhuge, Y., Wong, T., and Peters, L. (2003). *Seismic retrofitting of unreinforced masonry walls by FRP strips*. In: Pacific conference on earthquake engineering; 2003.
- [34] Eshani, M.R., Saadatmanesh, and H., Al-Saidy, A. (1997). *Shear behavior of URM retrofitted with FRP overlays*. Journal of Composites for Construction 1997;1(1):17–25. ASCE.
- [35] Haroun, M.A., Mosallam, A.S., and Allam, K.H. (2003). *In-plane shear behaviour of masonry walls strengthened by FRP laminates*. In: 2nd International Workshop on Structural Composites for Infrastructure Applications, Cairo, 2003.
- [36] Aiello, M.A., and Sciolti, S.M. (2006). *Bond analysis of masonry structures strengthened with CFRP sheets*. Construction and Building Materials 2006;20:90–100. Elsevier.
- [37] Liu, Y., Dawe, J., and McInerney, J. (2005). *Behaviour of GFRP sheets bonded to masonry walls*. In: Proceedings of the international symposium on bond behaviour of FRP in structures (BBFS 2005), International Institute for FRP in Construction (IIFC), 2005. p. 473–80.

- [38] Willis, C.R., Yang, Q., and Seracino, R., Griffith, M.C. (2009). *Bond behaviour of FRP-to-clay brick masonry joints*. Engineering Structures 2009;31:2580–2587. Elsevier.
- [39] Grande, E., Imbimbo, and M., Sacco, E. (2010). *Bond behaviour of CFRP laminates glued on clay bricks: Experimental and numerical study*. Composites: Part B. Article in Press. Elsevier.
- [40] Papanicolaou, C.G., Triantafillou, T.C., Karlos, K., and Papathanasiou. M. (2007). *Textile reinforced mortar (TRM) versus FRP as strengthening material of URM walls: in-plane cyclic loading*. Materials and Structures 2007;40(10):1081–1097. RILEM.
- [41] Papanicolaou, C.G., Triantafillou, T.C., Karlos, K., and Papathanasiou. M. (2008). *Textile reinforced mortar (TRM) versus FRP as strengthening material of URM walls: out-of-plane cyclic loading*. Materials and Structures 2008;41(1):143–157. RILEM.
- [42] Papanicolaou, C.G., Triantafillou, T.C., and Lekka, M. (2011). *Externally bonded grids as strengthening and seismic retrofitting materials of masonry panels*. Construction and Building Materials 2011;25:504–514. Elsevier.
- [43] Faella, C., Martinelli, E., Nigro, E., and Paciello S. (2010). *Shear capacity of masonry walls externally strengthened by a cement-based composite material: An experimental campaign*. Construction and Building Materials 2010;24:84–93. Elsevier.
- [44] Drdácký, M.F., and Lesák, J. (2009). *Retrofitting severely damaged masonry with high performance FRP strips and with anchored PP net reinforced rendering - a comparison*. In ISCARSAH Symposium Mostar - 09 Mostar: Interproject d.o.o. Mostar, 2010. S. 91-97. ISBN 978-9958-9999-0-1.
- [45] Aldea, C.M., Mobasher, B., and Jain, N. (2006). *Cement-based matrix-grid system for masonry rehabilitation*. Textile Reinforced Concrete (TRC) - German/International Experience symposium sponsored by the ACI Committee 549, ACI Special Publications, ACI Special Publications, 2006.
- [47] Lignola, G.P., Prota, A., and Manfredi, G. (2007). *Numerical simulation of in-plane behavior of tuff masonry strengthened with cementitious matrix-grid composites*. Proc., 1st Asia-Pacific Conf. on FRP in Structures APFIS 2007,

- S.T. Smith, ed., International Institute for FRP in Construction (Hong Kong), 255–262.
- [48] Gabor, A., Bennani, A., Jaqueline, E., and Lebon F. (2006). *Modelling approaches of the in-plane shear behaviour of unreinforced and FRP strengthened masonry panels*. Composite Structures 2006;74:277–288. Elsevier.
- [49] Drdácký, M.F. and Lesák, J. (2001). *Tests of brick masonry walls strengthened with polymer grids and subjected to combination of compression and cyclic shear*. Research report ITAM AV CR - CD, ITAM Praha.
- [50] Magenes, G. and Morandi, P. (2008). *Proposal for the evaluation of the q - factor from cyclic test results of masonry walls*. ESECMaSE project, University of Pavia and Eucentre unpublished report.
- [51] Frumento, S., Magenes, G., Morandi, P., Calvi, G.M. (2009). *Interpretation of experimental shear tests on clay brick masonry walls and evaluation of q - factors for seismic design*. Research Report No. 02.09, ESECMaSE project, University of Pavia and Eucentre.
- [52] Augenti, N., Parisi, F., Prota, A., and Manfredi, G. (2011). *In-Plane lateral response of a full-scale masonry subassemblage with and without an Inorganic Matrix-Grid Strengthening System*. J. of Composites for Constructions, ASCE, 2011; 15(4): 578-590.
- [53] Aiello, M.A., Micelli, F., and Valente, D. (2009). *FRP confinement of square masonry columns*. J. of Composites for Construction, ASCE, 2009; 13(2): 148-158.
- [54] CNR-DT 200 R1/2012. *Guide for the Design and Construction of Externally Bonded FRP Systems for Strengthening*. Council of National Research, Rome, 2012.
- [55] Ceroni, F., and Pecce, M. (2006). *Bond tests on concrete and masonry blocks externally bonded with CFRP*. In: Proc. of 3rd Int. Conf. on FRP Composites in Civil Engineering (CICE 2006), Miami, Florida, December 13-15 2006: 17-20.

- [56] Aiello, M.A., and Sciolti, M.S. (2008). *Analysis of bond performance between CFRP sheets and calcarenite ashlars under service and ultimate Conditions*. Masonry International, 2008; 21(1): 15-28.
- [57] Capozucca, R. (2010). *Experimental FRP/SRP–historic masonry delamination*. Composite Structures, Elsevier, 2010; 92(4): 891-903.
- [58] Panizza, M., Garbin, E., Valluzzi, M.R., and Modena, C. (2008). *Bond behaviour of CFRP and GFRP laminates on brick masonry*. In: Proc. of VI Int. Conf. on Structural Analysis of Historical Constructions, Bath (UK), July 2-4 2008, D’Ayala & Fodde eds.: 763-770.
- [59] Seim, W., and Pfeiffer, U. (2011). *Local post-strengthening of masonry structures with fibre-reinforced polymers (FRPs)*. Construction and Building Materials, Elsevier, 2011; 25:3393–3403.
- [60] Mazzotti, C., Ferracuti, B., and Bellini, A. (2012). *Experimental bond testes on masonry panels strengthening by FRP*. In: Proc. of 6th International Conference on FRP Composites in Civil Engineering (CICE 2012), 13-15 June 2012, Rome, Italy, CD ROM.
- [61] Panizza, M., Garbin, E., Valluzzi, M.R., and Modena, C. (2012). *Experimental investigation on bond of FRP/SRP applied to masonry prisms*. In: Proc. of 6th International Conference on FRP Composites in Civil Engineering (CICE 2012), 13-15 June 2012, Rome, Italy, CD ROM.
- [62] Oliveira, D., Basilio, I., Lourenço, P.B. (2011). *Experimental bond behavior of FRP sheets glued on brick masonry*. J. of Composites for Construction, ASCE, 2011; 15(1): 32-41.
- [63] Valluzzi, M.R., Oliveira, D.V., Caratelli, A., Castori, G., Corradi, M., de Felice, G., Garbin, E., Garcia, D., Garmendia, L., Grande, E., Ianniruberto, U., Kwiecień, A., Leone, M., Lignola, G.P., Lourenço, P.B., Malena, M., Micelli, F., Panizza, M., Papanicolaou, C.G., Prota, A., Sacco, E., Triantafillou, T.C., Viskovic, A., Zając, B., and Zuccarino, G. (2012). *Round robin test for composite to brick shear bond characterization*. Materials and Structures, RILEM, 2012; 45: 1761–1791.

- [64] Ceroni, F., Ferracuti, B., Pecce, M., and Savoia, M. (2013). *Assessment of a bond strength model for FRP reinforcement externally bonded over masonry blocks*. Submitted on Construction and Building Materials, Elsevier, 2013.
- [65] Guadagnini, M., Serbescu, A., Palmieri, A., Matthys, S., Bilotta, A., Nigro, E., Mazzotti, C., Sas, G., Taljsten, B., Ceroni, F., Czadersky, C., Olia, S., Szambo, Z., Balazs, G., Barros, J., Costa, I., and Tamuzs, V. (2012). *Bond of FRP Strengthening Systems for Concrete Structures: A Round Robin Test*. In: Proc. of 6th International Conference on Bridge Maintenance, Safety and Management (IABMAS 2012), Stresa, Lake Maggiore, Italy, July 8-12, 2012.
- [66] Aiello, M.A., and Sciolti, M.S. (2003). *Masonry Structures Strengthened with FRP Sheets: Experimental Investigation of Bond between FRP Laminates and Ashlars*. International J. for Restoration of Buildings and Monuments, 2003; 9(6): 639-662.
- [67] Mazzotti, C., Savoia, M., and Ferracuti, B. (2009). *A new single-shear set-up for stable debonding of FRP-concrete joints*. Construction and Building Materials, Elsevier, 2009, 23:1529–1537.
- [68] Bilotta, A., Ceroni, F., Nigro, E., Di Ludovico, M., Pecce, M., and Manfredi, G. (2011). *Bond efficiency of EBR and NSM FRP systems for strengthening of concrete members*. J. of Composites for Construction, ASCE, 2011; 15(5):757-772.
- [69] Ceroni, F., Pecce, M., Manfredi, G., and Marcari, A. (2003) *Experimental bond behavior in masonry elements externally reinforced with FRP laminates*. In: Proc. of Int. Conference on Composites in Constructions (CCC2003), Cosenza, 2003, Italy, Editoriale Bios.
- [70] Ceroni, F., Bilotta, A., Nigro, E., and Pecce, M. (2012). *Bond behaviour of FRP NSM systems in concrete elements*. Composites: Part B, Elsevier, 2012; 43: 99–109.
- [71] Lourenço, P.B. (2004). *Current experimental and numerical issue in masonry research*. Congresso de sismologia e engenharia sismica, Guimarães, 2004 – “Sísmica 2004 - "6º Congresso de Sismologia e Engenharia Sísmica”. Guimarães: Universidade do Minho, 2004, p. 119-136.

- [72] Hordijk, D.A. (1991). *Local Approach to Fatigue of Concrete*. PhD thesis, Delft University of Technology, 1991.
- [73] Hoffmann, G. and Schubert, P. (1994). *Compressive strength of masonry parallel to bed joints*. In: Proc. 10th Int. Brick and Block Masonry Conference, eds. N.G. Shrive and A. Huizer, University of Calgary, Calgary, Alberta, Canada, p. 1453-1462.
- [74] Backes, H.-P. (1985). *On the behavior of masonry under tension in the direction of the bed joints*. (in German). Dissertation, Aachen University of Technology, Aachen, Germany.
- [75] Page, A.W. (1981). *The biaxial compressive strength of brick masonry*. Proc. Intsn. Civ. Engrs., Part 2, 71, p. 893-906.
- [76] Page, A.W. (1983). *The strength of brick masonry under biaxial compression-tension*. Int. J. Masonry Constr., 3(1), p. 26-31.
- [77] Lourenço, P.B., and Rots, J.G. (1997). *A multi-surface interface model for the analysis of masonry structures*. J. Engrg. Mech., 123(7), p. 660-668.
- [78] Lofti H.R., and Shing, P.B. (1994). *Interface model applied to fracture of masonry structures*. J. Struct. Engrg., 120(1), p. 63-80.
- [79] Lemos, J.V. (1998). *Discrete element modeling of the seismic behavior of stone masonry arches*. In: Pande G et al. (ed) Comp. meth. in struc. masonry 4, E&FN Spon, 1998, p. 220–227.
- [80] Baggio, C., and Trovalusci, P. (1998). *Limit analysis for no-tension and frictional three-dimensional discrete systems*. Mech. of Struct. and Machines, 26(3), p.287-304.
- [81] Orduña, A. (2003). *Seismic assessment of ancient masonry structures by rigid blocks limit analysis*. Ph.D. Thesis, University of Minho, Guimarães.
- [82] Lourenço, P.B. (1994). *Analysis of masonry structures with interface elements: Theory and applications*. Report 03-21-22-0-01, Delft University of Technology, Delft.
- [83] Hill, R. (1948). *A theory of the yielding and plastic flow of anisotropic metals*. Proc. Roy. Soc., (London) A, 193, p. 281-288.
- [84] Hoffman, O. (1967). *The brittle strength of orthotropic materials*. J. Composite Mat., 1, p. 200-206.

- [85] Tsai, S.W., and Wu, E.M. (1971). *A general theory of strength of anisotropic materials*. J. Composite Mat., 5, p. 58-80.
- [86] De Borst, R., and Feenstra, P.H. (1990). *Studies in anisotropic plasticity with reference to the Hill criterion*. Int. J. Numer. Methods Engrg., 29, p. 315-336.
- [87] Schellekens, J.C.J., and De Borst, R. (1990). *The use of the Hoffman yield criterion in finite element analysis of anisotropic composites*. Comp. Struct., 37(6), p. 1087-1096.
- [88] Lourenço, P.B. (2000). *Anisotropic softening model for masonry plates and shells*. J. Struct. Engrg., 126(9), p. 1008–1016.
- [89] Sacco, E. (2009). *A nonlinear homogenization procedure for periodic masonry*. European Journal of Mechanics – A/Solid, Volume 28, Issue 2, March-April 2009, p. 209-222.
- [90] Avossa, A.M., Famigliuolo, P., and Malangone P. (2009). *Prestazioni sismiche di edifici in muratura: impiego di un modello “concrete” modificato e analisi di confronto*. XIII Convegno ANIDIS – L’Ingegneria Sismica in Italia, Bologna, 2009.
- [91] Anthoine, A. (1997). *Homogenisation of periodic masonry: Plane stress, generalised plane strain or 3D modelling?* Comm. Num. Meth. Engrg., 13, p. 319–326.
- [92] Lourenço, P.B., Zucchini, A., Milani, G., and Tralli, A. (2006). *Homogenization approaches for structural analysis of masonry buildings*. Structural Analysis of Historical Constructions, New Delhi 2006. P.B. Lourenço, P. Roca, C. Modena, S. Agrawal (Eds.).
- [93] Rots, J.G., and Blaauwendraad, J. (1989). *Crack models for concrete: discrete or smeared? Fixed, multi-directional or rotating?* Heron, Vol. 34, No. 1, 1989.
- [94] Blaauwendraad J. (1985). *Realisations and restrictions - Application of numerical models to concrete structures*. Finite element analysis of reinforced concrete structures, Proc. US-Japan Seminar, (Meyer C., Okamura H. Eds.), ASCE, 557-578 (1985).
- [95] Rashid Y.R. (1968). *Analysis of prestressed concrete pressure vessels*. Nuclear Engng. and Design 7(4),334-344 (1968).

- [96] Magenes, G., and Calvi, G.M. (1997). *In-plane seismic response of brick masonry walls*. Earthquake Engineering & Structural Dynamics, vol. 26, 1091-1112.
- [97] Tian Yi et al. (2006).
- [98] Magenes, G., Calvi, G.M., and Kingsley, G.R. (1995). *Seismic testing of a full-scale, two-story masonry building: test procedure and measured experimental response*. Experimental and Numerical Investigation on a Brick Masonry Building Prototype, Report 3.0, University of Pavia.
- [99] Moon, F.L. (2004). *Seismic Strengthening of Low-Rise Unreinforced masonry structures with flexible diaphragms*. PhD Dissertation, Georgia Institute of Technology, USA.
- [100] Gürel, M.A., Kisa, M., and Çili, F. (2005). *Lateral stiffness of unreinforced masonry circular columns under cracked conditions*.
- [101] Ruiz-García, R.J., and Alcocer, S.M. (1998). *Experimental performance of confined masonry structures retrofitted with welded wire mesh*. Revista de Ingenieria Sismica, nmo. 59, pp.59-79.
- [102] Alcocer, S.M., Arias, J.G., and Flores, L.E. (2004). *Some developments on performance-based seismic design of masonry structures, performance-based seismic design concepts and implementation*. Proceeding of an International Workshop, 233-244.
- [103] Tomažević, M., Lutman, M., and Petkovic, L. (1996). *Seismic behavior of masonry walls: experimental simulation*. Journal of Structural Engineering, no.122, pp.1040-1047.
- [104] Bosiljkov, V., Totoev, Y.Z., and Nichols, J.M. (2005). *Shear modulus and stiffness of brickwork masonry: an experimental perspective*. Structural Engineering and Mechanics Vol. 20, Issue 1, pp. 21-43.
- [105] Anderson, D., and Brzev, S. (2009). *Seismic design guide for masonry buildings*. Canadian Concrete Masonry Producers Association.
- [106] Seible, F., and Kingsley, G.R. (1991). *Modeling of concrete and masonry structures subjected to seismic loading*. In: Donea J. & Jones P.M. (eds.). Experimental and Numerical Methods in Earthquake Engineering. Brussels: ECSC. 1991: 281–318.

- [107] Brencich, A., Gambarotta, and L., Lagomarsino, S. (1998). *A macroelement approach to three-dimensional seismic analysis of masonry buildings*. 11th European Conference on Earthquake Engineering, 1998 Balkema, Rotterdam.
- [108] Cattari, S., Galasco, A., Lagomarsino, S., and Penna, A. (2005). *Analisi non lineare di edifici in muratura con il programma Tremuri*. XIII Convegno ANIDIS – L’Ingegneria Sismica in Italia, Genova, 2005.
- [109] Gilmore, A.T., Cuevas, O.Z., and Garcia, J.R. (2009). *Displacement-based seismic assessment of low-height confined masonry buildings*. Earthquake Spectra, vol.25, no.2, pp.439-464.
- [110] Kappos, A.J., Penelis, G.G., and Drakopoulos, C.G. (2002). *Evaluation of simplified models for lateral load analysis of unreinforced masonry buildings*. Journal of Structural Engineering, vol.128, pp.890-897.
- [111] Salonikios, T., Karakostas, C., Lekidis, V., and Anthoine, A. (2003). *Comparative inelastic pushover analysis of masonry frames*. Engineering Structures, no.25, pp.1515-1523.
- [112] FEMA 273. (1997). *NEHRP guidelines for the seismic rehabilitation of buildings*. Issued by Federal Emergency Management Agency, Washington, D.C..
- [113] Pasticier, L., Amadio, C., and Fragiaco, M. (2007). *Non-linear seismic analysis and vulnerability evaluation of a masonry building by means of the SAP2000 V.10 code*. Earthquake Engineering and Structural Dynamics, no.37, pp. 467-485.
- [114] Belmouden, Y., and Lestuzzi, P. (2007). *An equivalent frame model for seismic analysis of masonry and reinforced concrete buildings*. Construction and Building Materials, vol.23, No.1, pp. 40-53.
- [115] Roca, P., Molins, C., and Mari, A.R. (2005). *Strength capacity of masonry wall structures by the equivalent frame method*. Journal of Structural Engineering, vol.131, pp. 1601-1610.
- [116] Penelis, G.G. (2006). *An efficient approach for pushover analysis of URM structures*. Journal of Earthquake Engineering. Vol.10, no.3, pp. 359-379.

- [117] Magenes, G., and Fontana, A.D. (1998). *Simplified non-linear seismic analysis of masonry buildings*. Proceeding of British Masonry Society, No.8, pp. 190-195.
- [118] Dolce M. (1989). *Models for in-plane loading of masonry walls*. Corso sul consolidamento degli edifici in muratura in zona sismica. Ordine degli Ingegneri, Potenza. (in Italian).
- [119] Oliveira, D.V.C. (2003). *Experimental and numerical analysis of blocky masonry structures under cyclic loading*. PhD Dissertation, University of Minho, Portugal.
- [120] Orduña, A. (2003). *Seismic assessment of ancient masonry structures by rigid blocks limit analysis*. PhD Dissertation, University of Minho, Portugal.
- [121] DIANA Finite Elements Analysis. User's Manual – Release 9.4.4. (2011). *Element Library, Material Library, Analysis Procedures*. TNO Building and Construction Research, Department of Computational Mechanics: A.A. Delft, Netherlands, 2009.
- [122] Augenti, N., and Parisi, F. (2010). *Constitutive models for tuff masonry under uniaxial compression*. Journal of Materials in Civil Engineering, Vol. 22, No. 11, November 1, 2010. ASCE.
- [123] Parisi, F., Lignola, G., Augenti, N., Prota, A., and Manfredi, G. (2011). *Nonlinear behavior of a masonry subassemblage before and after strengthening with inorganic matrix-grid composites*. Journal of Composites for Construction, 15(5), 821–832, ASCE.
- [124] Lourenço, P.B. (2009). *Recent advances in masonry structures: micromodelling and homogenization*. In: Galvanetto U., Aliabadi M.F.H., Editors. London: Imperial College Press; p.251–94.
- [125] NTC 2008. *Norme Tecniche per le Costruzioni*. Decreto Ministeriale del 14/01/2008. In G.U.R.I., 29, 04/02/2008 (in Italian).
- [126] Circolare 617. *Istruzioni per l'applicazione delle "Nuove norme tecniche per le costruzioni di cui al D.M. 14 gennaio 2008*. Ministero dei Lavori Pubblici, Roma, 02/02/2009 (in Italian).
- [127] Galasco, A., Lagomarsino, S. and Penna, A. (2002), *TREMURI Program: Seismic Analyser of 3D Masonry Buildings*. University of Genoa.

- [128] Galasco, A., Lagomarsino, S., and Penna, A. (2006). *On the use of pushover analysis for existing masonry buildings*. Proceedings of the 1st European Conference on Earthquake Engineering and Seismology, Genève, Switzerland, Paper No. 1080.
- [129] Meletti, C., and Montaldo, V. (2007). *Stime di pericolosità sismica per diverse probabilità di superamento in 50 anni: valori di a_g* . Progetto DPC-INGV S1, Deliverable D2, <<http://esse1.mi.ingv.it/d2.html>> (in Italian).
- [130] Eurocode 8. *Design of Structures for Earthquake Resistance – Part 3: Assessment and Retrofitting of Buildings*. Committee for Standardization: Brussels, Belgium, 2005; EN 1998-1.

APPENDIX

In the following pages the plots of the different mechanical parameters evaluated in the parametric analysis are reported. Two types of masonry have been considered: an adobe brick masonry, characterized by a compressive strength of 2.67 MPa and a Young's modulus of 1300 MPa, and a tuff masonry, characterized by a compressive strength of 1.0 MPa and a Young's modulus of 800 MPa. The parametric cases of analyses are carried out with reference to different values aspect ratio h/b considered for the masonry panel, namely 1.0, 1.3 and 2.0. In particular, the following parameters have been taken into account:

$k_{el,t}$ is the tangential stiffness of the non-linear $V - d$ curve;

V_{max} is the peak horizontal force of the non-linear $V - d$ curve;

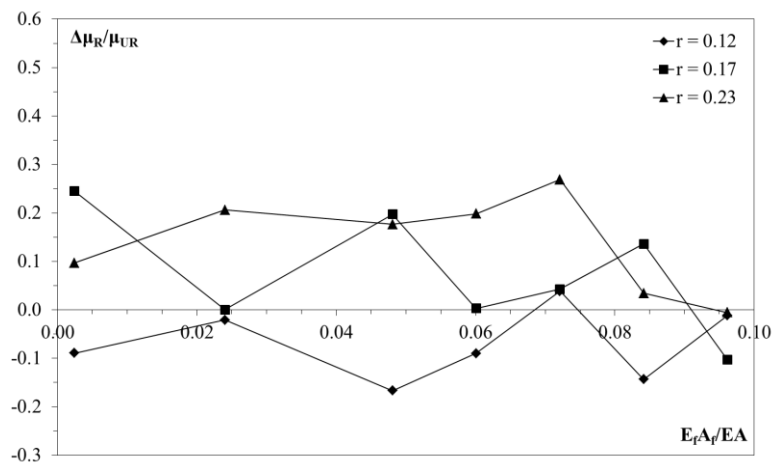
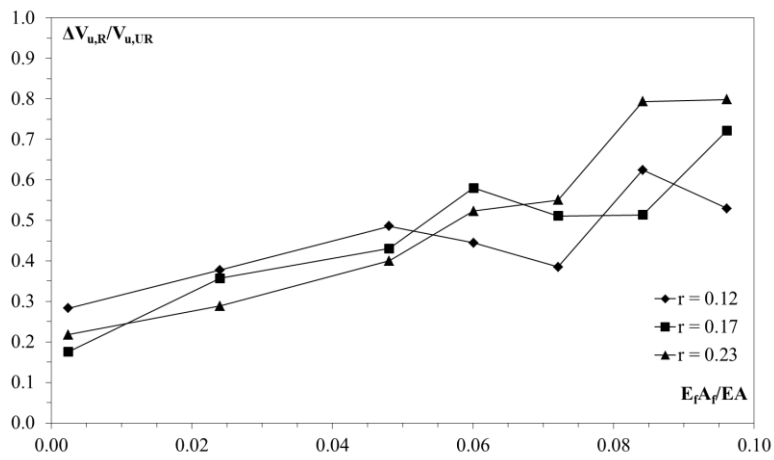
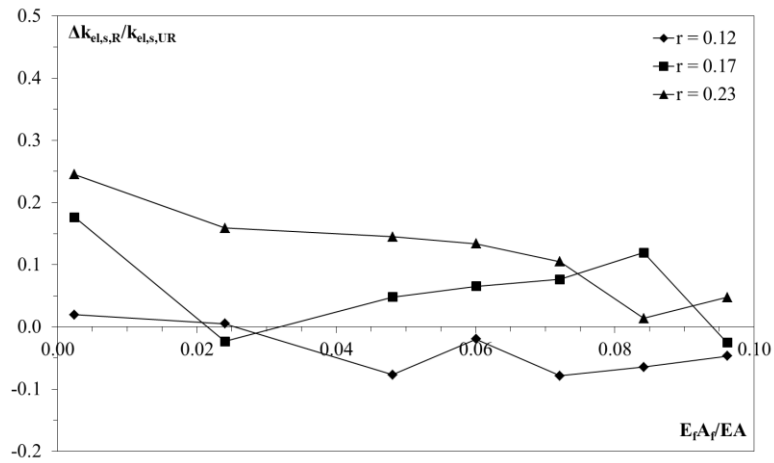
d_r is the maximum drift, calculated as the ultimate displacement d_u (corresponding to 15% reduction of horizontal force) divided by the height of the panel h ;

$k_{el,s}$ is the secant stiffness the non-linear $V - d$ curve at V_{cr} , equal to $0.6 \cdot V_{max}$;

V_u is the yielding value defining the strength of the equivalent bilinear curve, calculated by matching the area under the non-linear $V - d$ curve and the area under the equivalent bilinear curve;

$\mu_{el,s}$ is the ductility of the reinforced wall has been finally evaluated by relating the ultimate horizontal displacement d_u to the elastic horizontal displacement d_e .

In the analyses, the axial stiffness of the composite grid $E_f A_f$, has been varied with respect to the axial stiffness of the plane masonry wall EA . The influence of the compressive strength of the external mortar layers $2t_p f_{cp}$ has been considered and varied with reference to the compressive strength of the wall's masonry $t f_c$, and it is controlled by the parameter $r = 2t_p f_{cp} / t f_c$. In the Figures from A.1 to A.6, the variation of the described parameters is plotted, with respect to the parameter $E_f A_f / EA$. Furthermore, in the Figures from A.7 to A.12, the variation of the same parameters have been plotted also with respect of the parameter $f_{pc} A_i / f_c A$, where A_i is the equivalent area of reinforcement calculated as $A_p + n_f A_f$, considering the homogenization factor $n_f = E_f / E_p$.



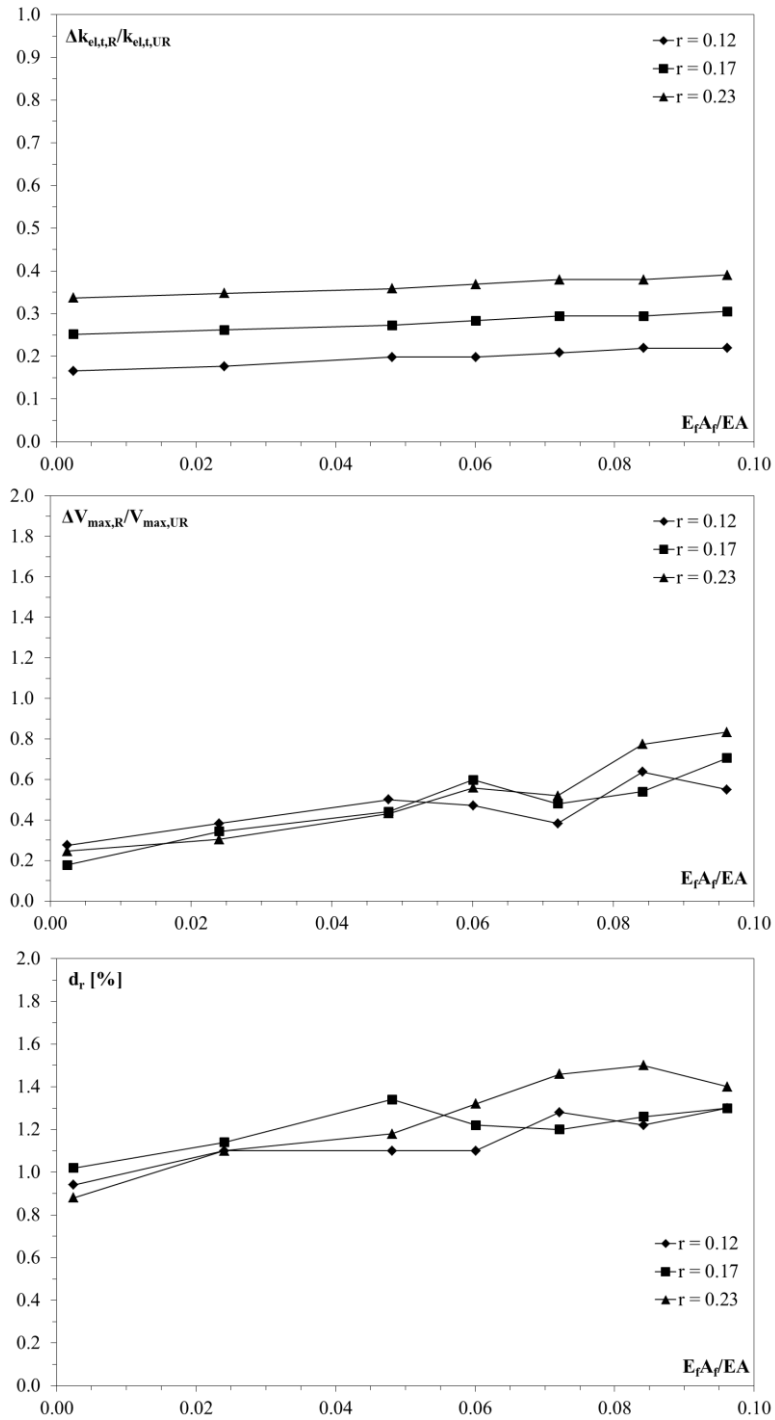
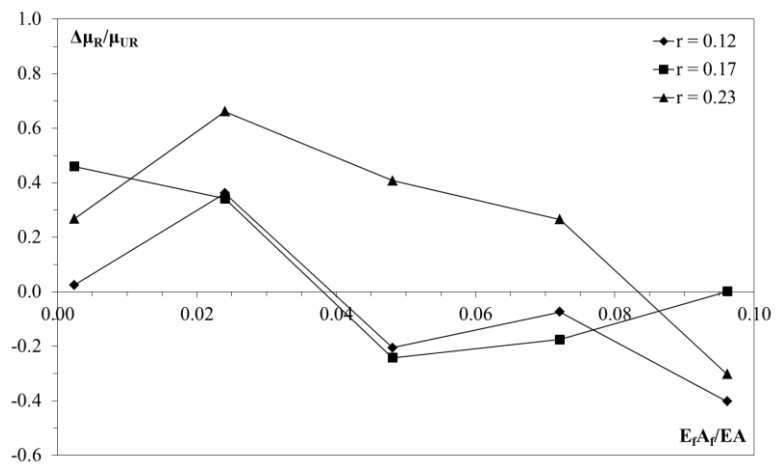
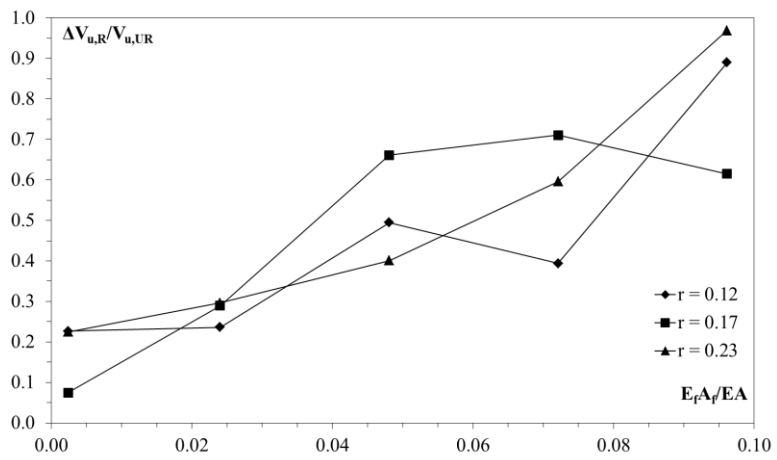
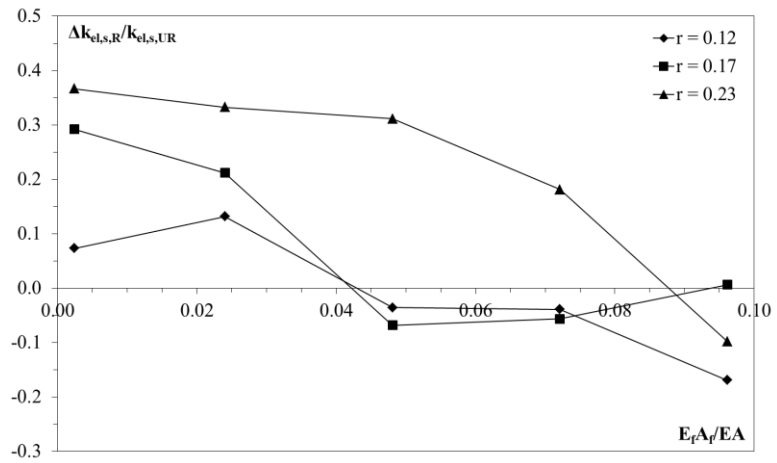


Figure A.1. Adobe brick masonry wall with aspect ratio $h/b = 1.0$: relative variation of $\Delta k_{el,s,R} / k_{el,s,UR}$ (a), $\Delta V_{u,R} / V_{u,UR}$ (b), $\Delta \mu_R / \mu_{UR}$ (c), $\Delta k_{el,s,R} / k_{el,s,UR}$ (d), $\Delta V_{max,R} / V_{max,UR}$ (e), d_r (f) with respect to the axial stiffness $E_r A_f / EA$, for different levels of compressive strength $2t_p \cdot f_{pc} / t \cdot f_c$.



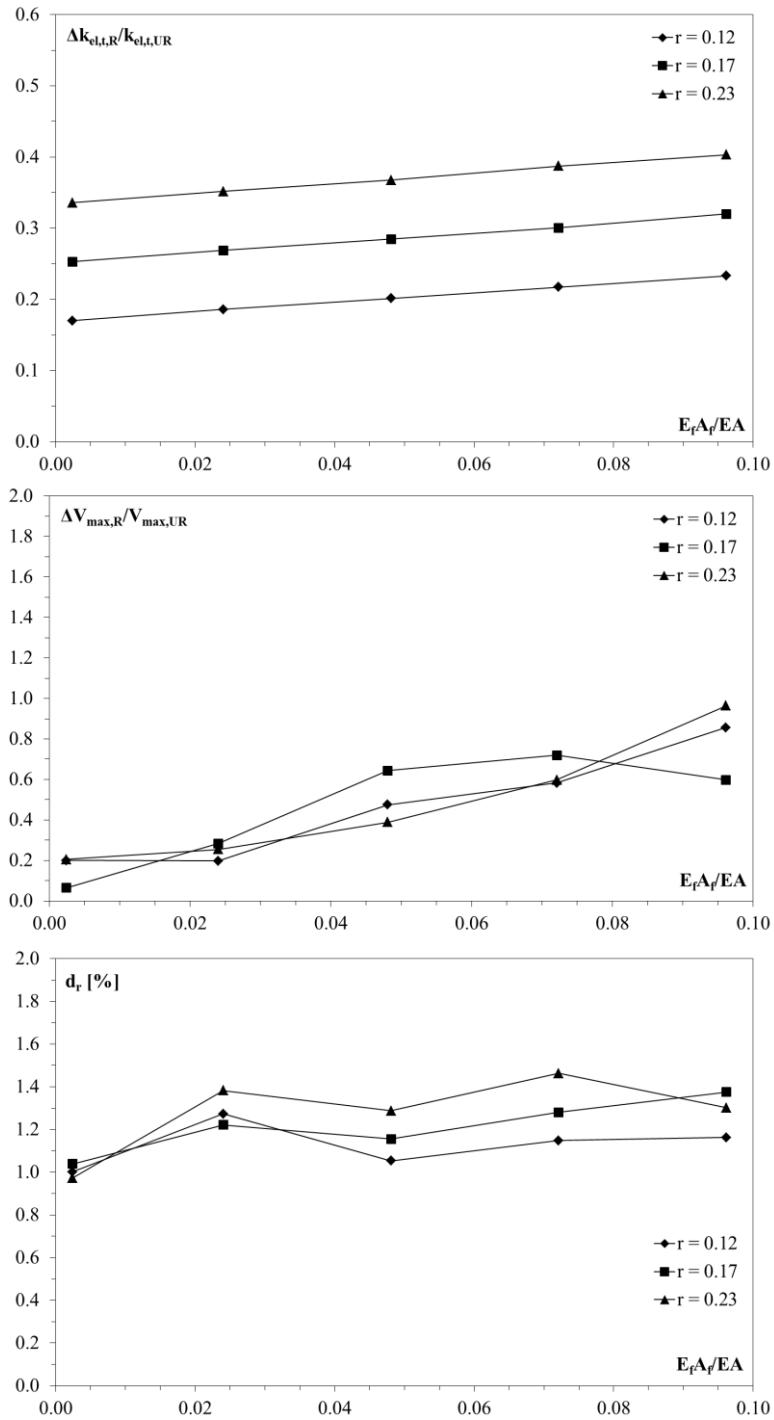
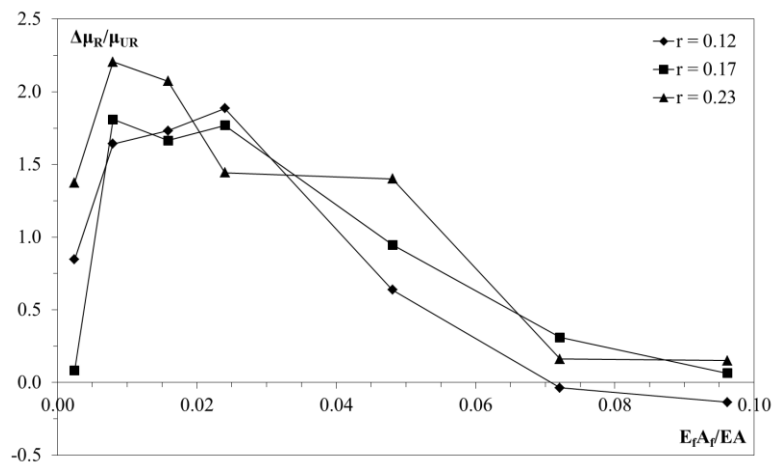
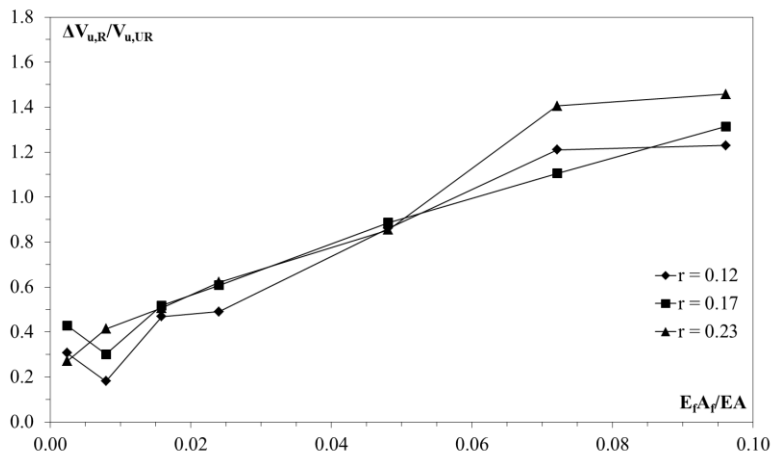
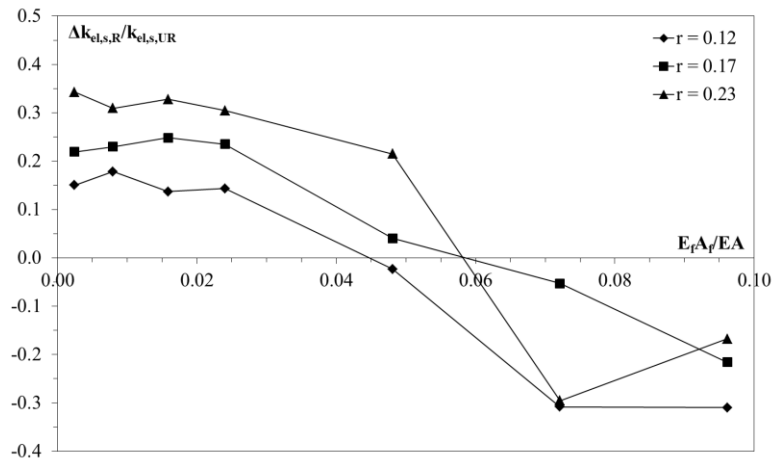


Figure A.2. Adobe brick masonry wall with aspect ratio $h/b = 1.3$: relative variation of $\Delta k_{el,s,R} / k_{el,s,UR}$ (a), $\Delta V_{u,R} / V_{u,UR}$ (b), $\Delta \mu_R / \mu_{UR}$ (c), $\Delta k_{el,s,R} / k_{el,s,UR}$ (d), $\Delta V_{max,R} / V_{max,UR}$ (e), d_r (f) with respect to the axial stiffness $E_r A_f / EA$, for different levels of compressive strength $2t_p \cdot f_{pc} / t \cdot f_c$.



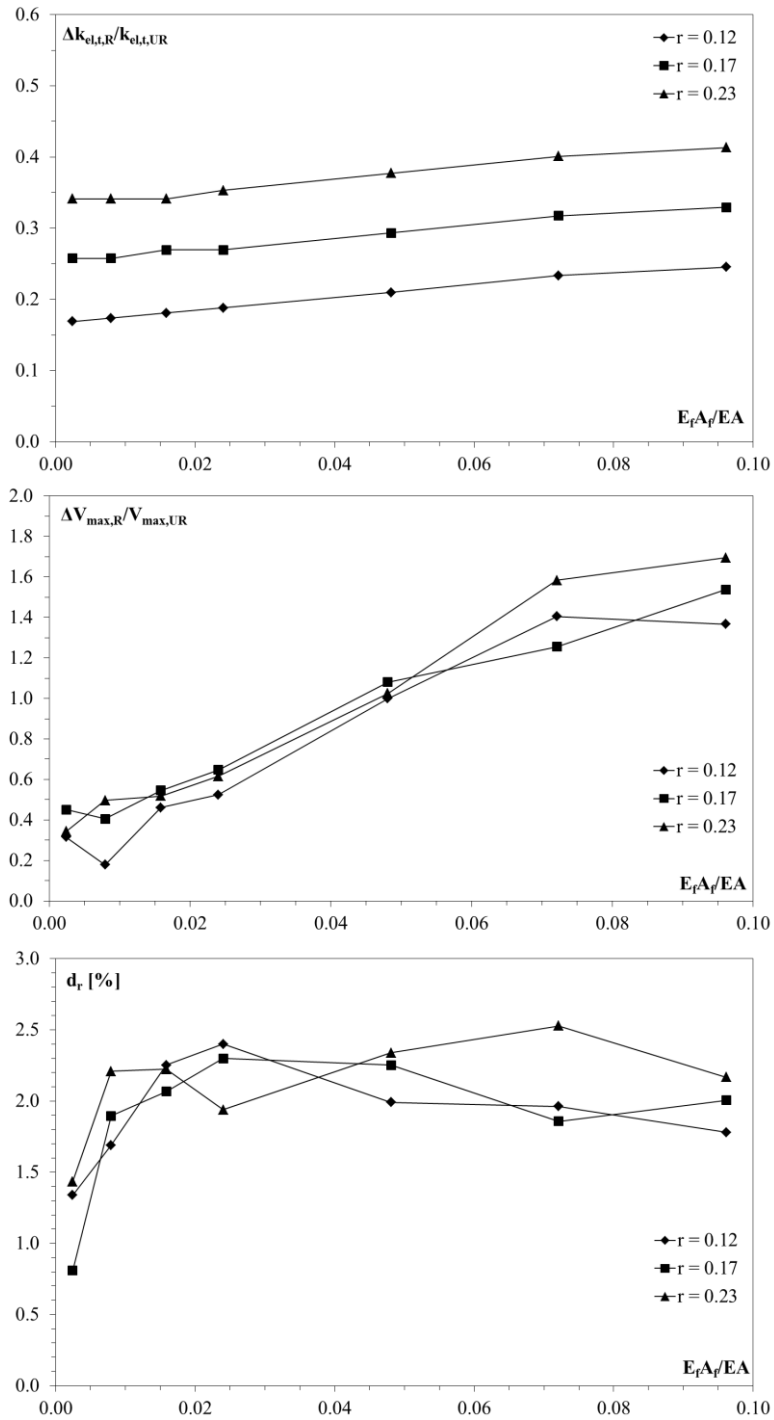
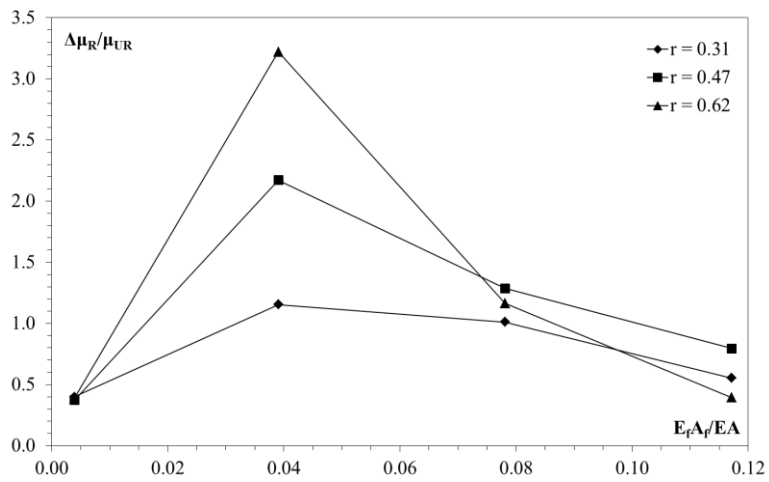
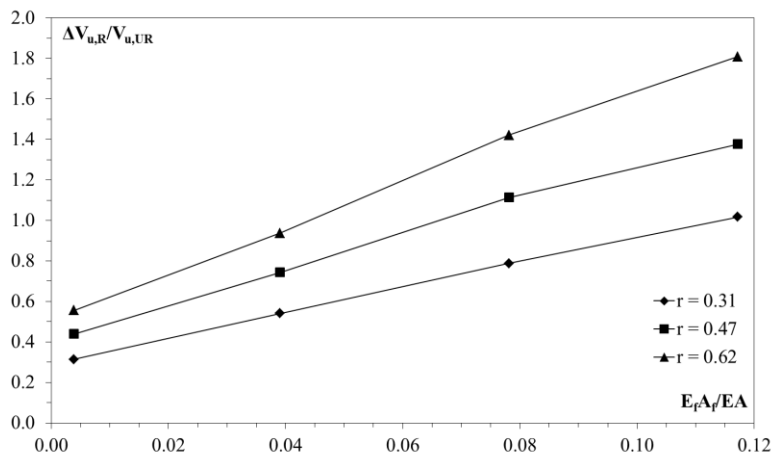
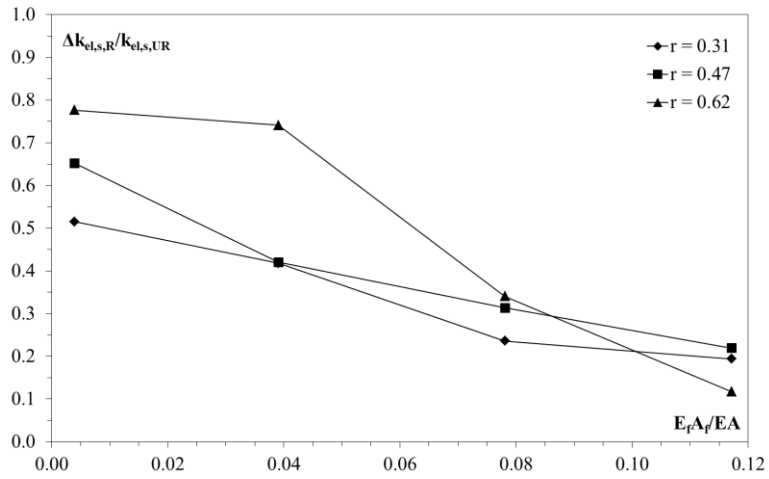


Figure A.3. Adobe brick masonry wall with aspect ratio $h/b = 2.0$: relative variation of $\Delta k_{el,s,R} / k_{el,s,UR}$ (a), $\Delta V_{u,R} / V_{u,UR}$ (b), $\Delta \mu_R / \mu_{UR}$ (c), $\Delta k_{el,s,R} / k_{el,s,UR}$ (d), $\Delta V_{max,R} / V_{max,UR}$ (e), d_r (f) with respect to the axial stiffness $E_f A_f / EA$, for different levels of compressive strength $2t_p \cdot f_{pc} / t \cdot f_c$.



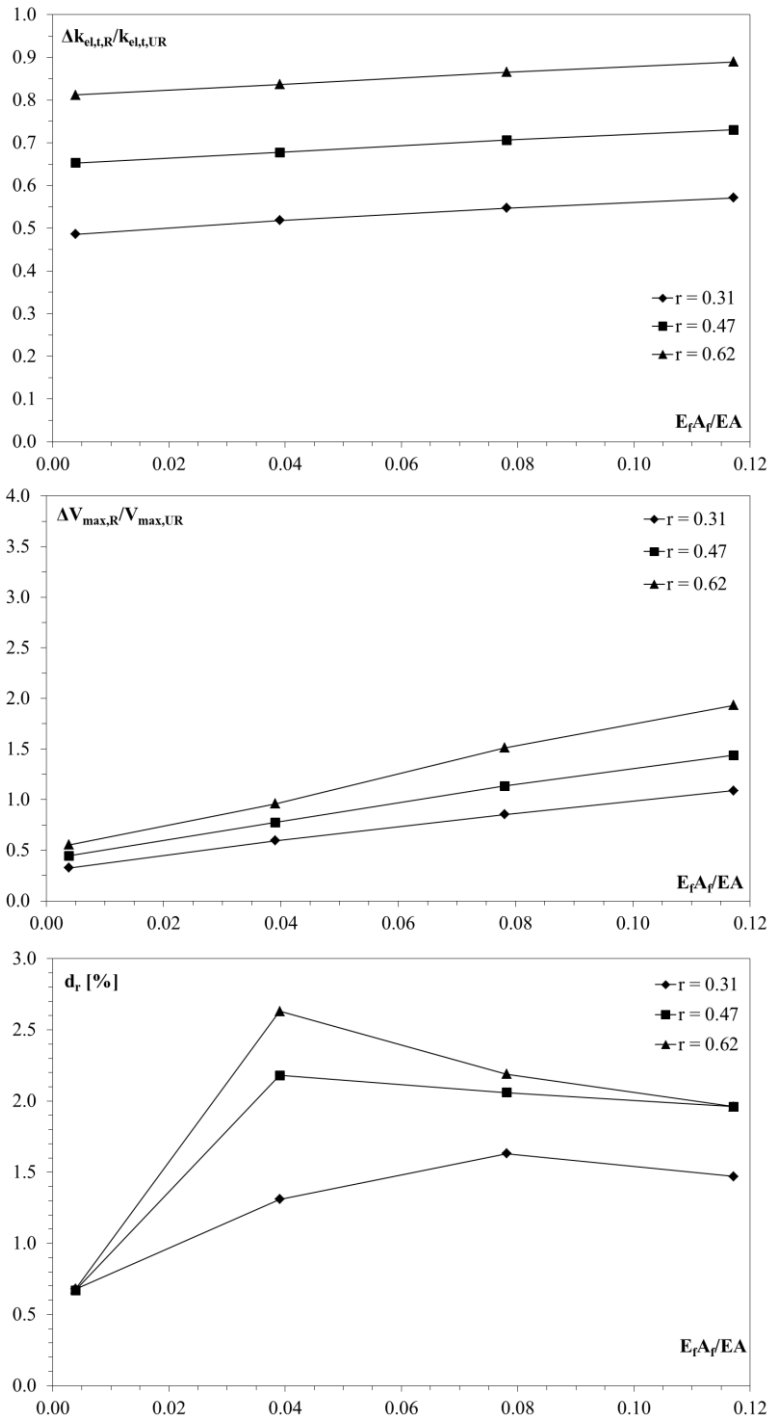
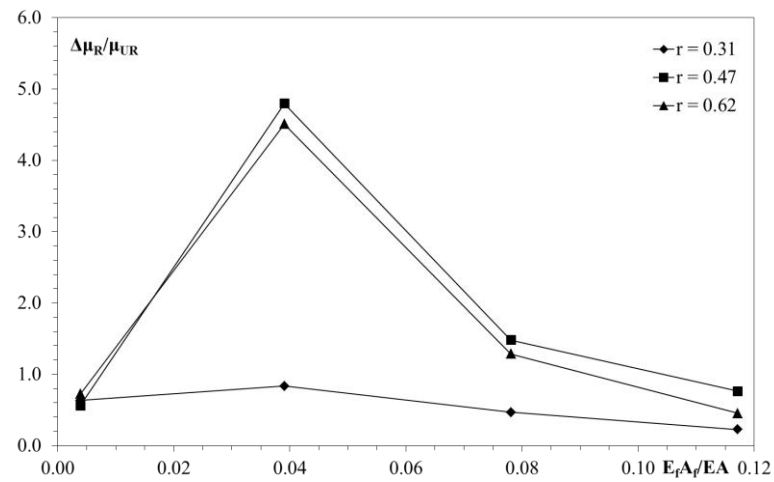
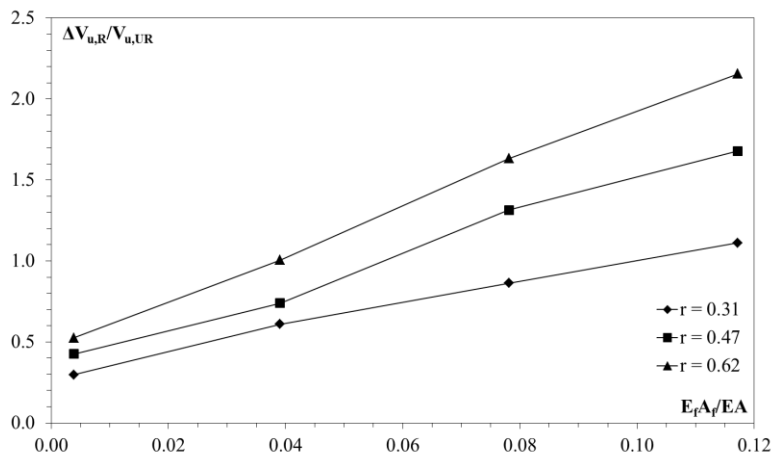
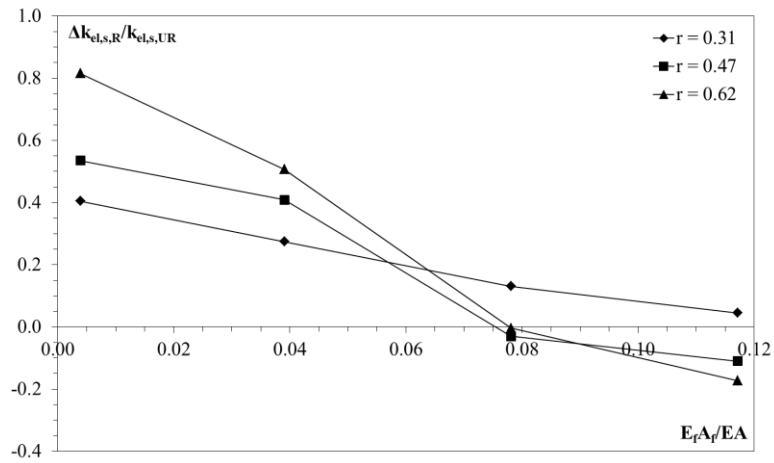


Figure A.4. Tuff block masonry wall with aspect ratio $h/b = 1.0$: relative variation of $\Delta k_{el,s,R} / k_{el,s,U,R}$ (a), $\Delta V_{u,R} / V_{u,U,R}$ (b), $\Delta \mu_R / \mu_{UR}$ (c), $\Delta k_{el,s,R} / k_{el,s,U,R}$ (d), $\Delta V_{max,R} / V_{max,U,R}$ (e), d_r (f) with respect to the axial stiffness $E_r A_f / EA$, for different levels of compressive strength $2t_p \cdot f_{pc} / t \cdot f_c$.



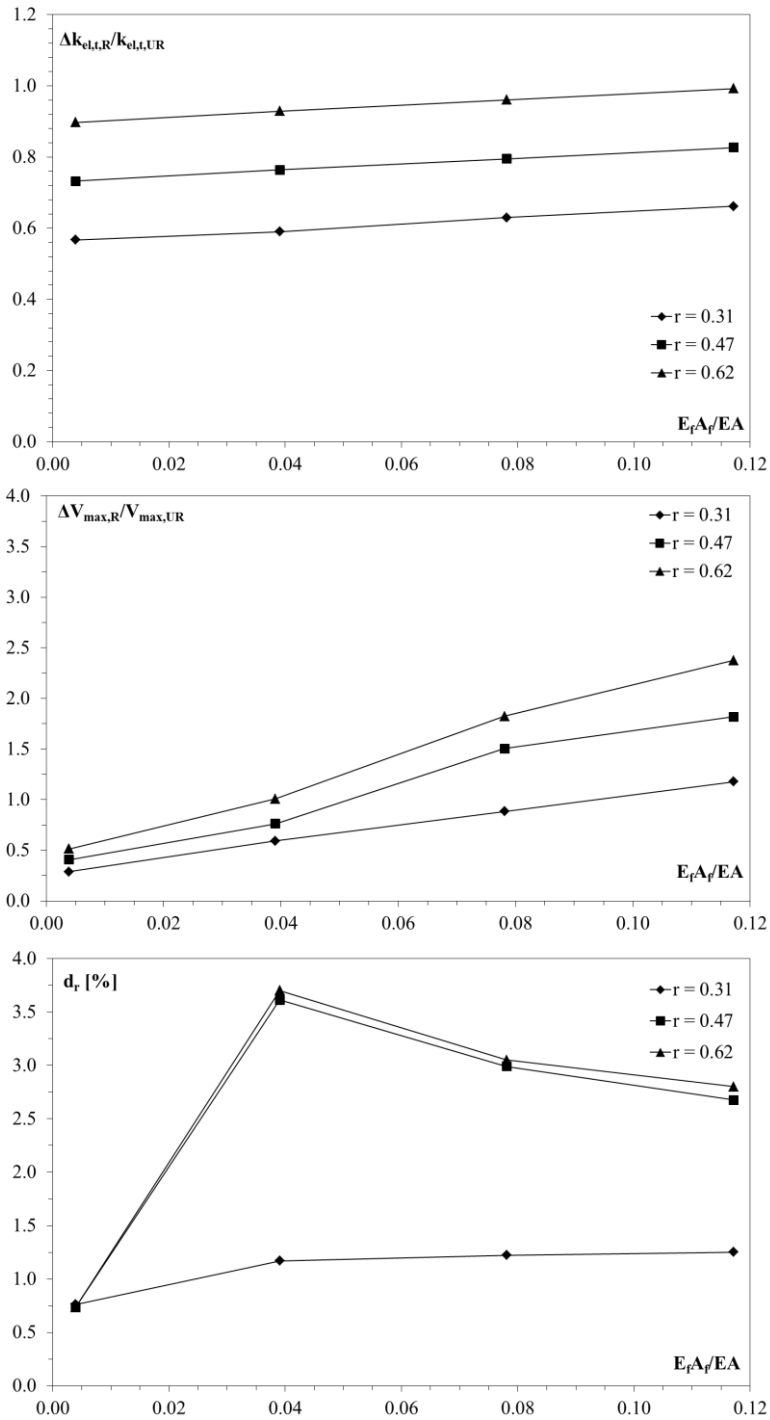
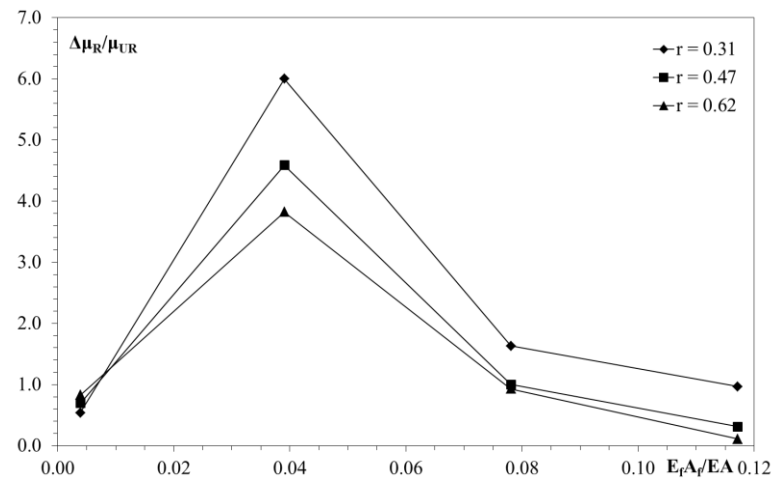
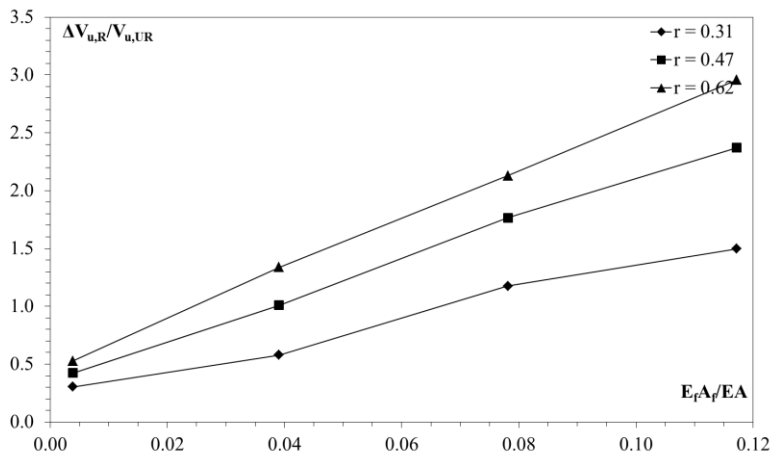
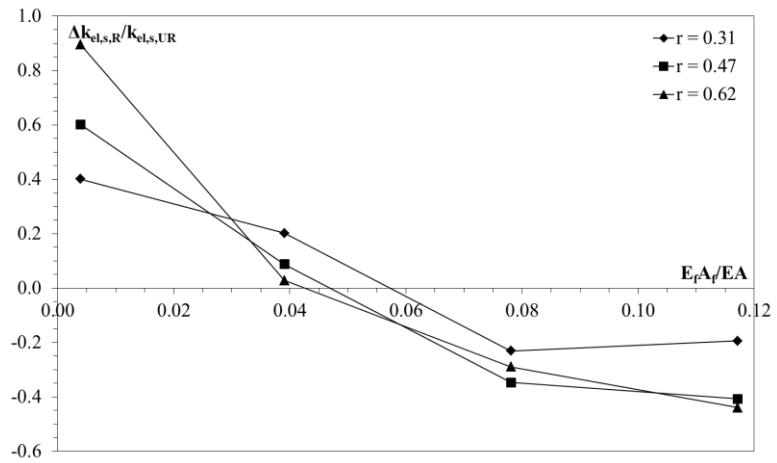


Figure A.5. Tuff block masonry wall with aspect ratio $h/b = 1.3$: relative variation of $\Delta k_{el,s,R} / k_{el,s,U,R}$ (a), $\Delta V_{u,R} / V_{u,U,R}$ (b), $\Delta \mu_R / \mu_{UR}$ (c), $\Delta k_{el,s,R} / k_{el,s,U,R}$ (d), $\Delta V_{max,R} / V_{max,U,R}$ (e), d_r (f) with respect to the axial stiffness $E_f A_f / EA$, for different levels of compressive strength $2t_p \cdot f_{pc} / t \cdot f_c$.



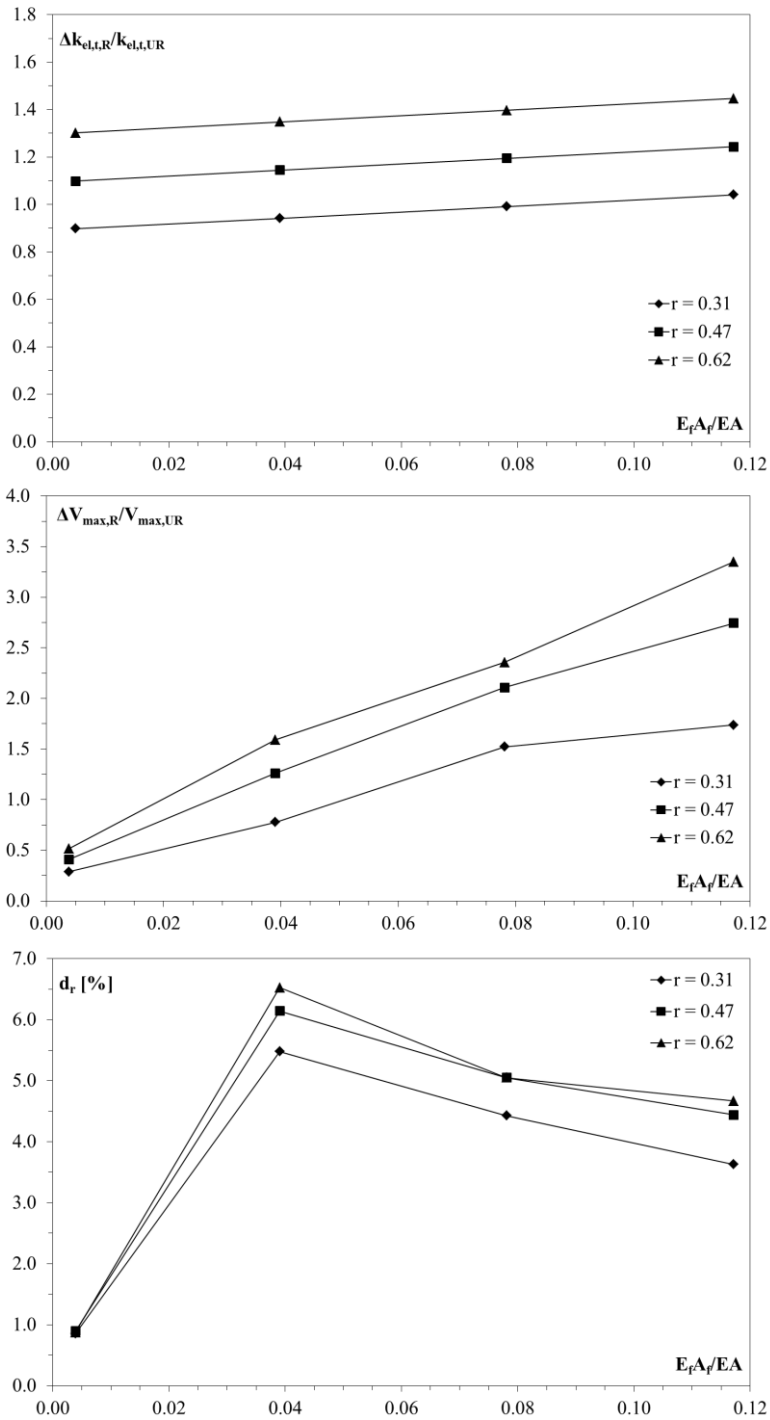
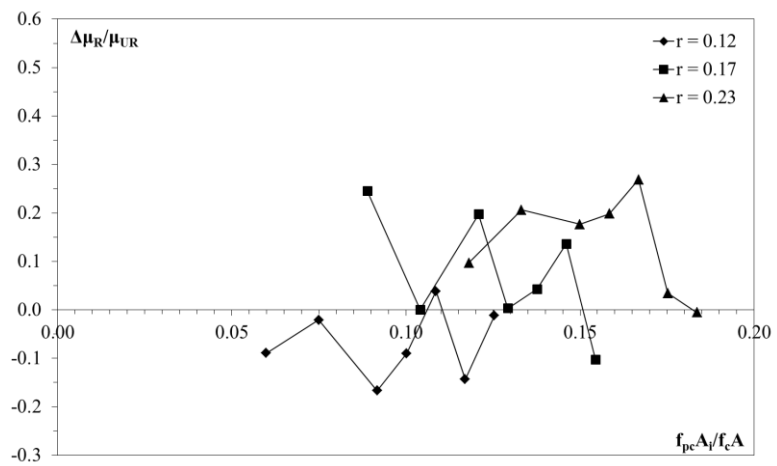
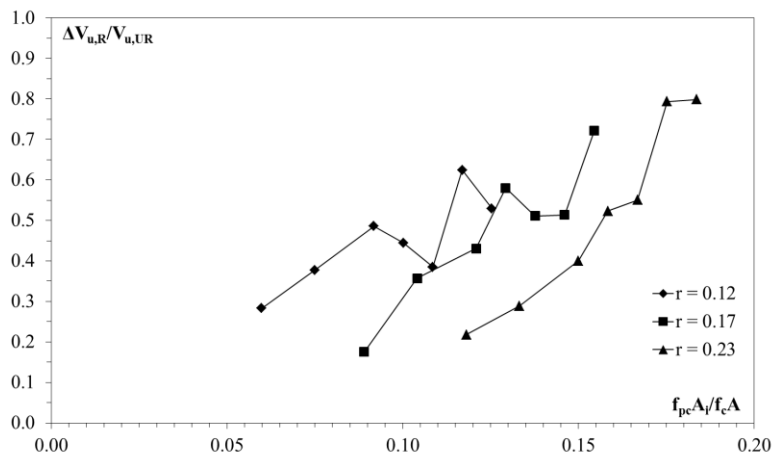
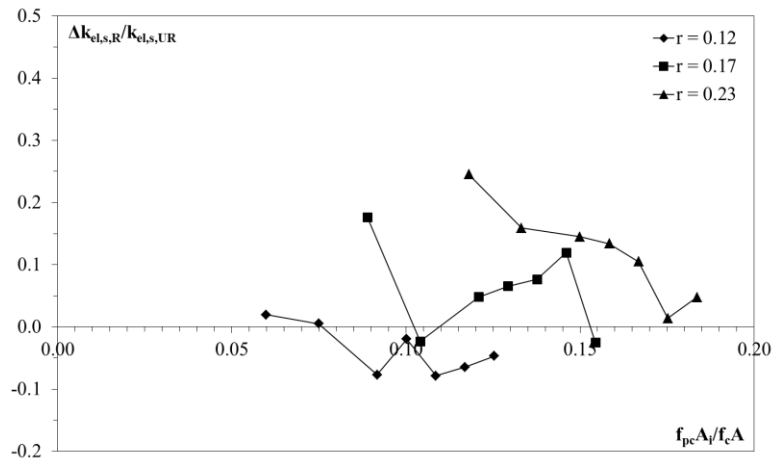


Figure A.6. Tuff block masonry wall with aspect ratio $h/b = 2.0$: relative variation of $\Delta k_{el,s,R} / k_{el,s,U,R}$ (a), $\Delta V_{u,R} / V_{u,U,R}$ (b), $\Delta \mu_R / \mu_{UR}$ (c), $\Delta k_{el,s,R} / k_{el,s,U,R}$ (d), $\Delta V_{max,R} / V_{max,U,R}$ (e), d_r (f) with respect to the axial stiffness $E_r A_f / EA$, for different levels of compressive strength $2t_p \cdot f_{pc} / t \cdot f_c$.



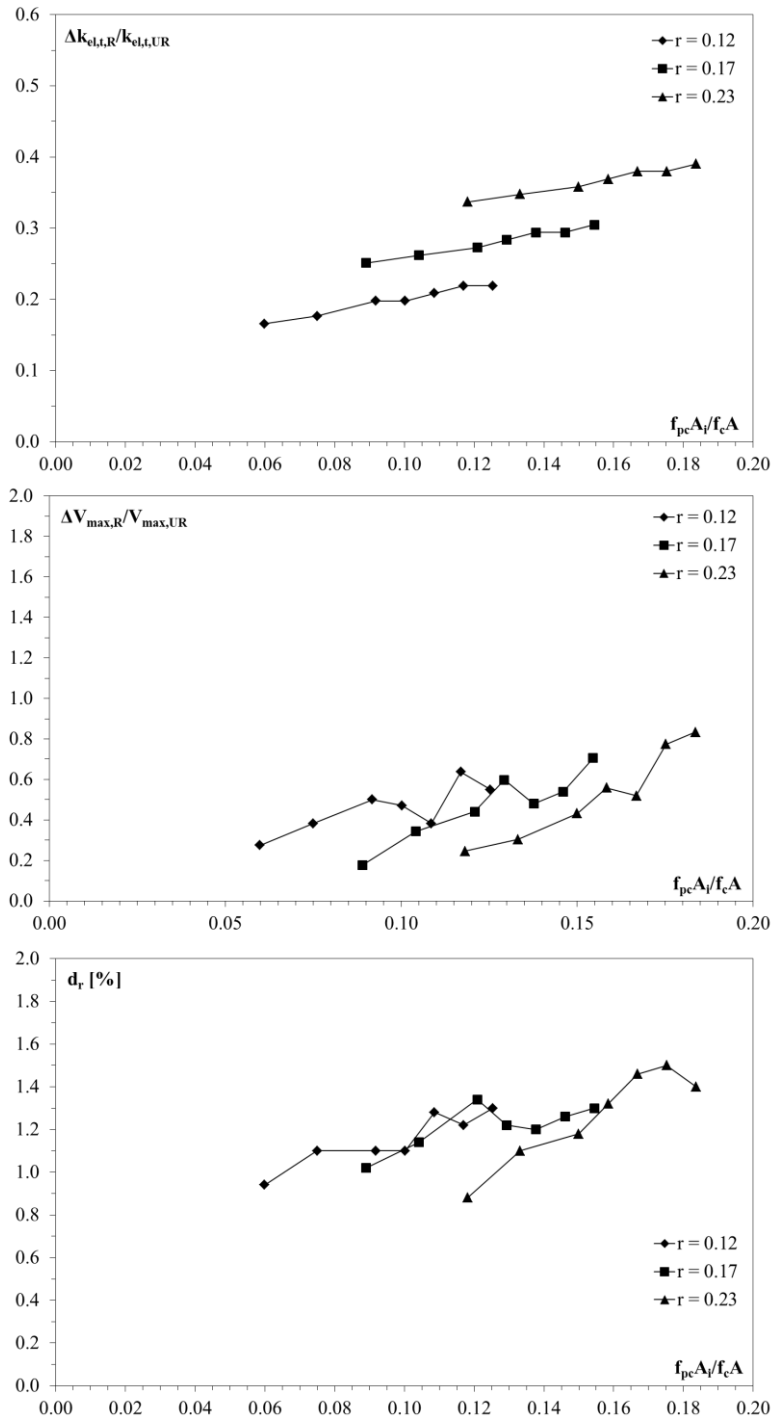
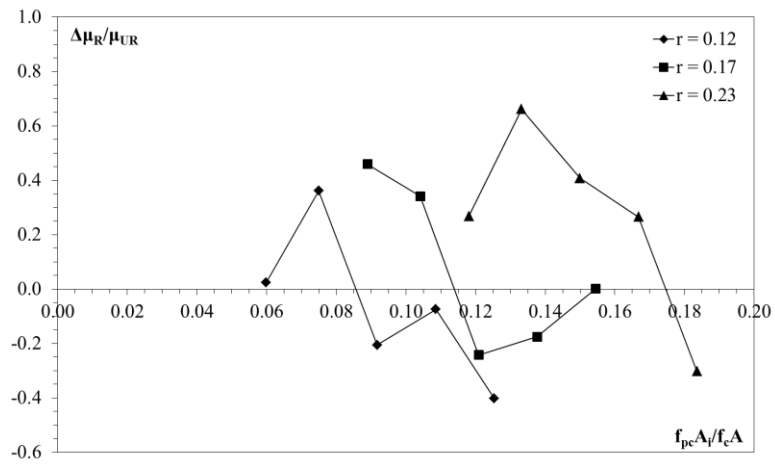
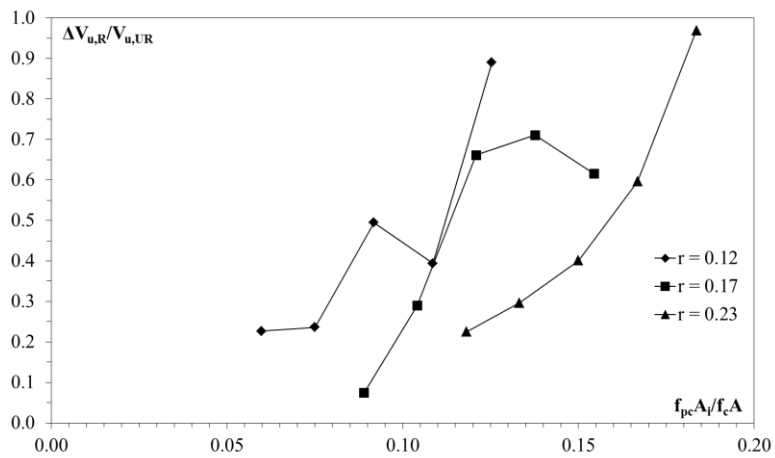
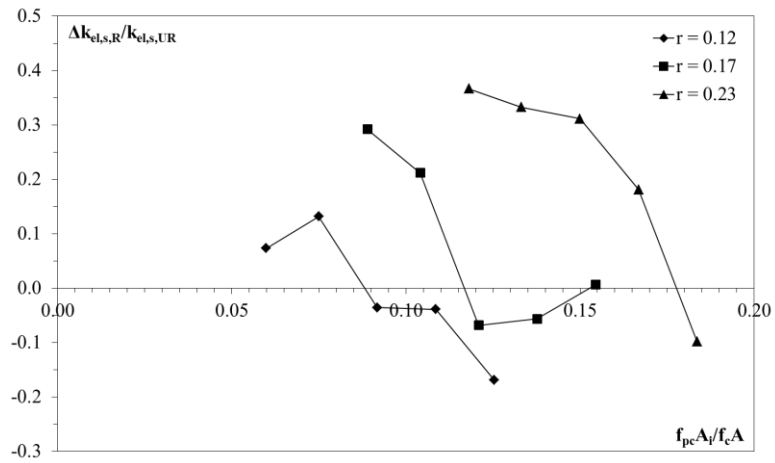


Figure A.7. Adobe brick masonry wall with aspect ratio $h/b = 1.0$: relative variation of $\Delta k_{el,s,R}/k_{el,s,UR}$ (a), $\Delta V_{u,R}/V_{u,UR}$ (b), $\Delta \mu_R/\mu_{UR}$ (c), $\Delta k_{el,s,R}/k_{el,s,UR}$ (d), $\Delta V_{max,R}/V_{max,UR}$ (e), d_r (f) with respect to the relative equivalent strength $f_{pc}A_i/f_cA$ of the reinforcement.



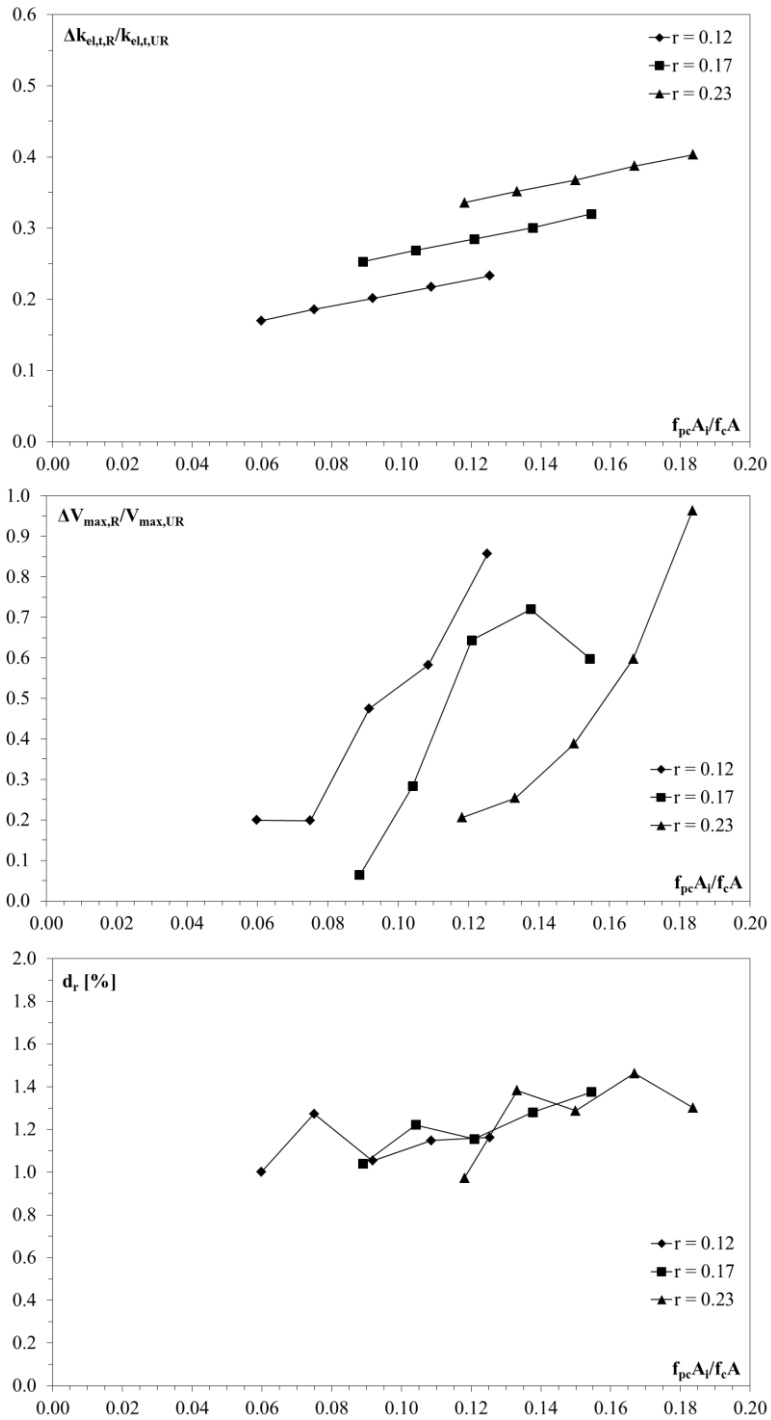
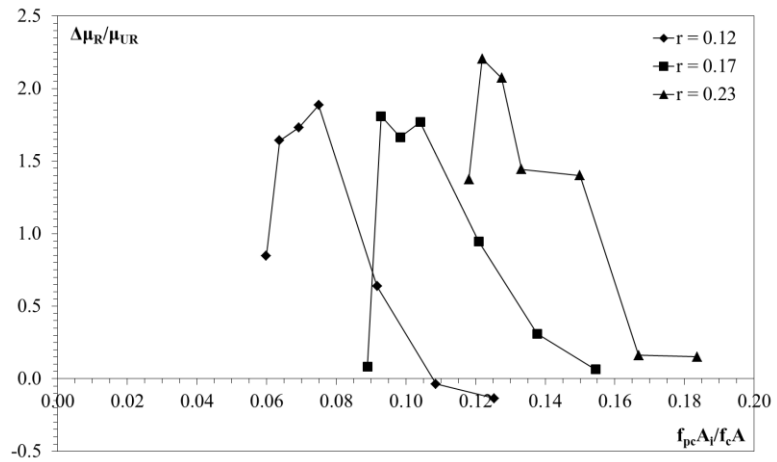
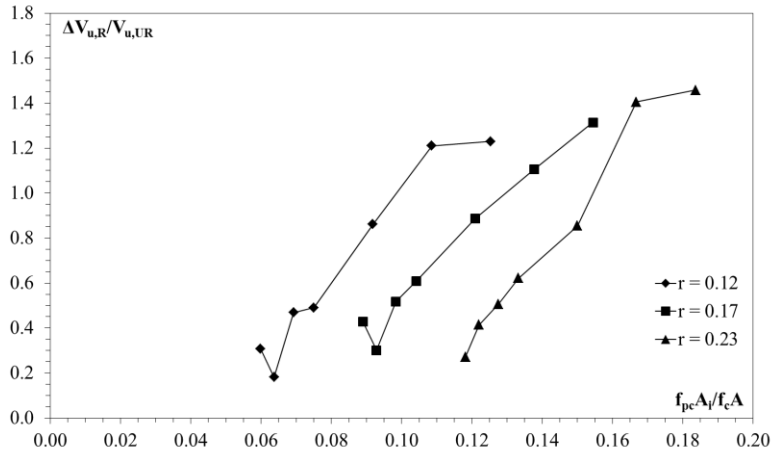
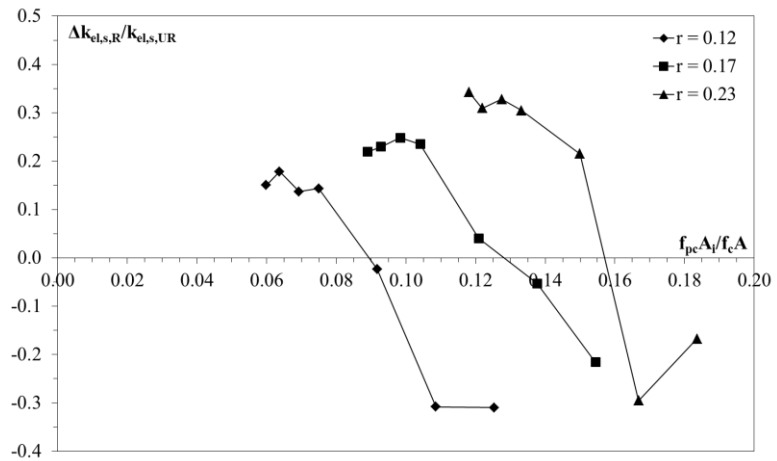


Figure A.8. Adobe brick masonry wall with aspect ratio $h/b = 1.3$: relative variation of $\Delta k_{el,s,R}/k_{el,s,UR}$ (a), $\Delta V_{u,R}/V_{u,UR}$ (b), $\Delta \mu_R/\mu_{UR}$ (c), $\Delta k_{el,s,R}/k_{el,s,UR}$ (d), $\Delta V_{max,R}/V_{max,UR}$ (e), d_r (f) with respect to the relative equivalent strength $f_{pc}A_i/f_cA$ of the reinforcement.



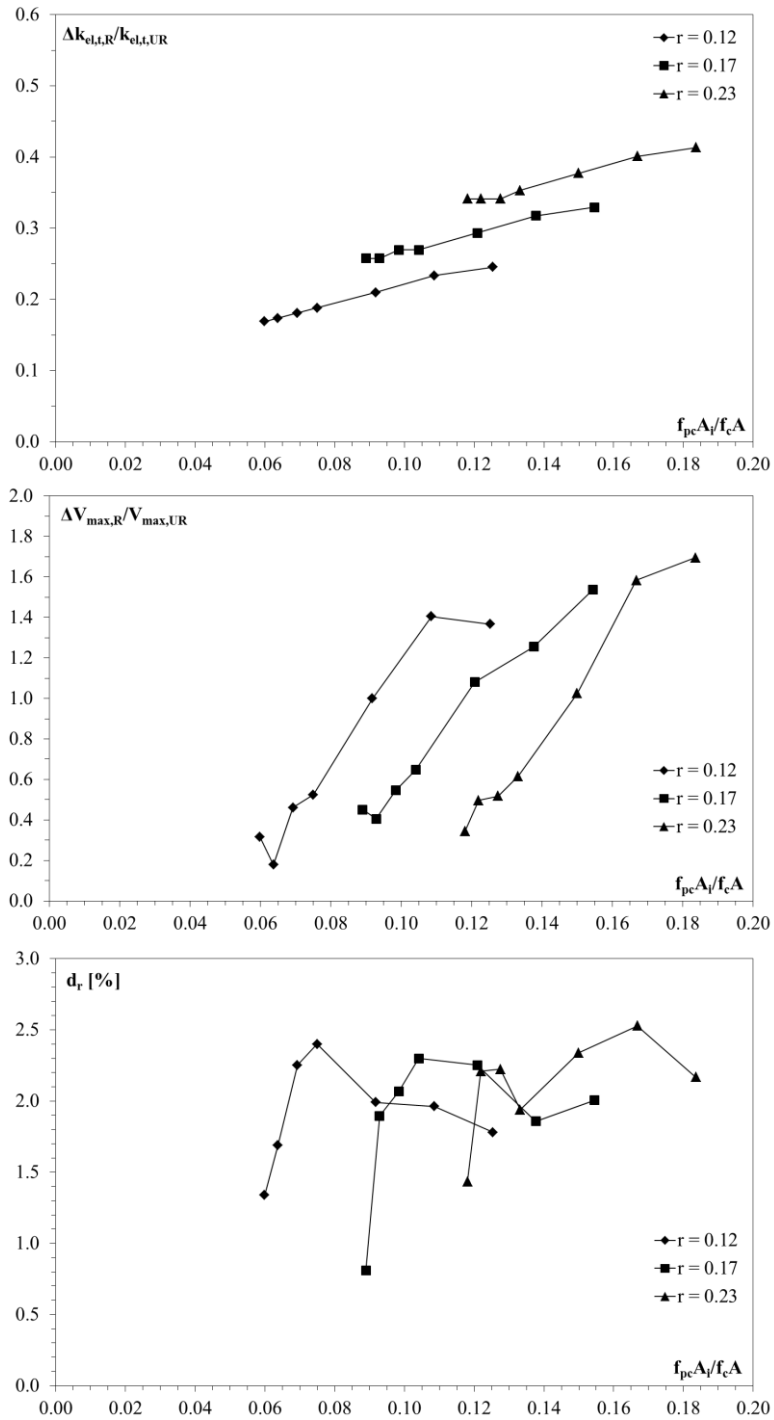
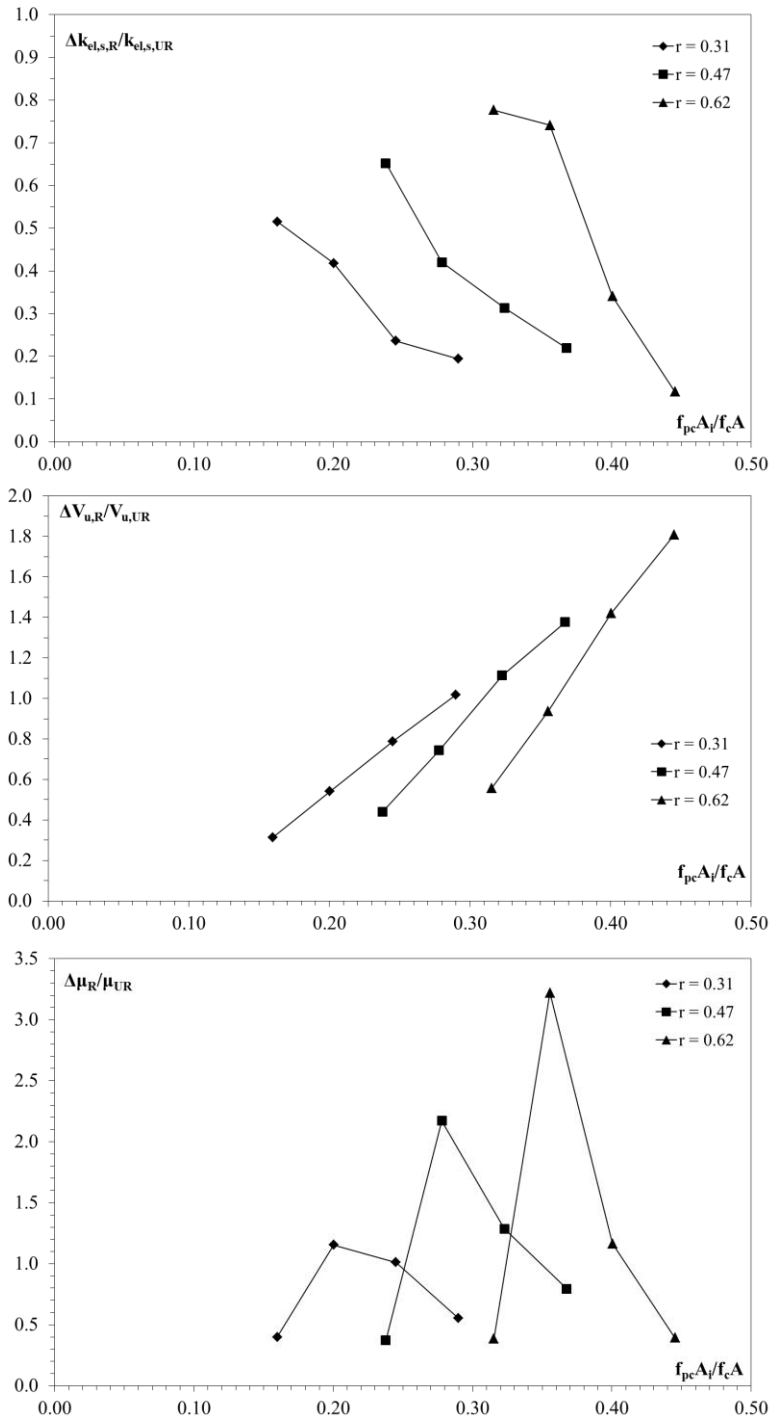


Figure A.9. Adobe brick masonry wall with aspect ratio $h/b = 2.0$: relative variation of $\Delta k_{el,s,R}/k_{el,s,UR}$ (a), $\Delta V_{u,R}/V_{u,UR}$ (b), $\Delta \mu_R/\mu_{UR}$ (c), $\Delta k_{el,s,R}/k_{el,s,UR}$ (d), $\Delta V_{max,R}/V_{max,UR}$ (e), d_r (f) with respect to the relative equivalent strength $f_{pc}A_f/f_cA$ of the reinforcement.



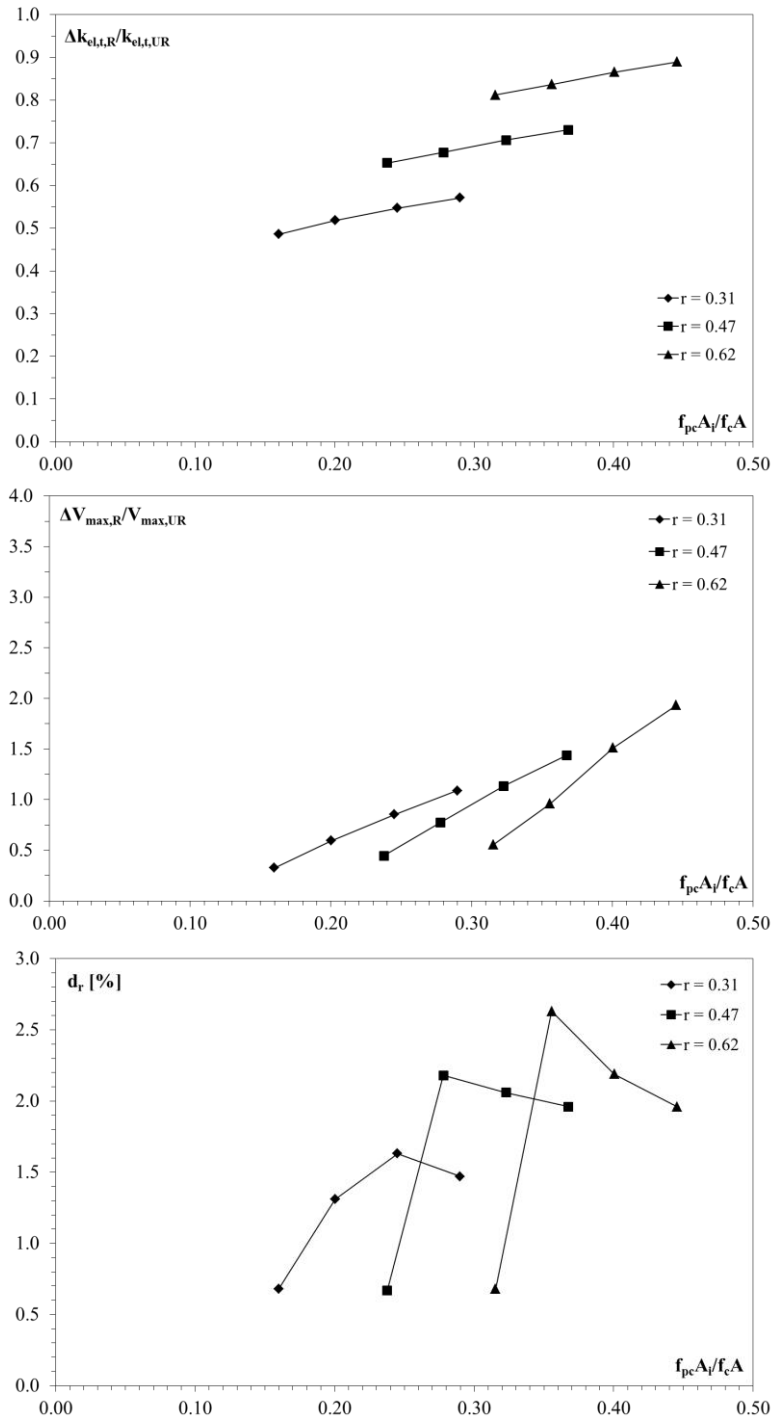
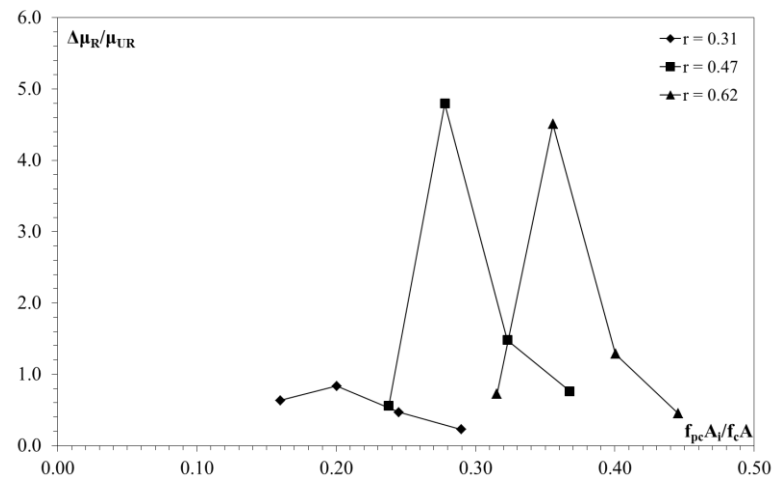
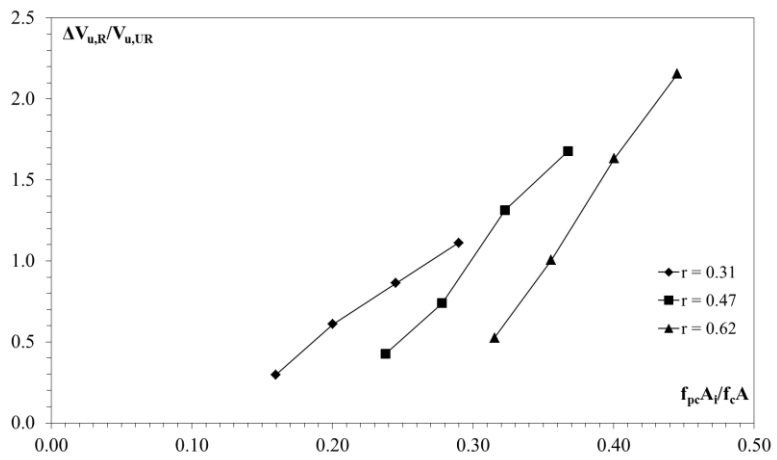
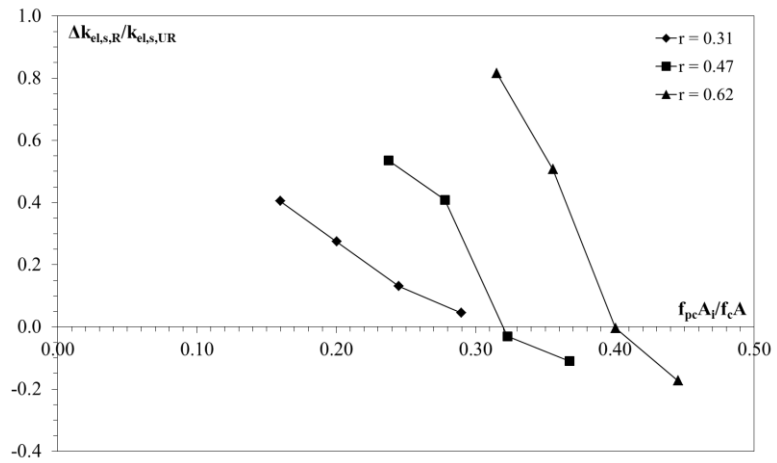


Figure A.10. Tuff block masonry wall with aspect ratio $h/b = 1.0$: relative variation of $\Delta k_{el,s,R}/k_{el,s,UR}$ (a), $\Delta V_{u,R}/V_{u,UR}$ (b), $\Delta \mu_R/\mu_{UR}$ (c), $\Delta k_{el,s,R}/k_{el,s,UR}$ (d), $\Delta V_{max,R}/V_{max,UR}$ (e), d_r (f) with respect to the relative equivalent strength $f_{pc}A_i/f_cA$ of the reinforcement.



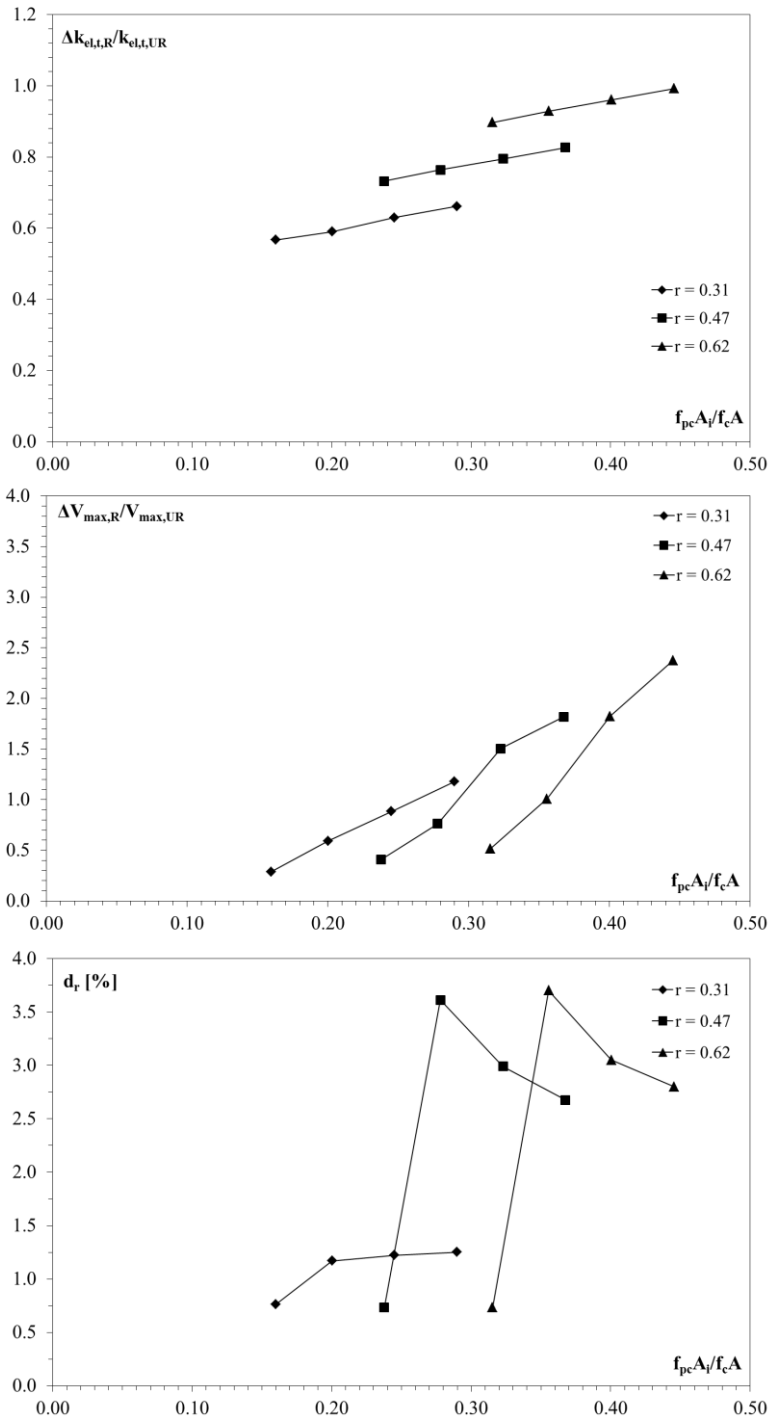
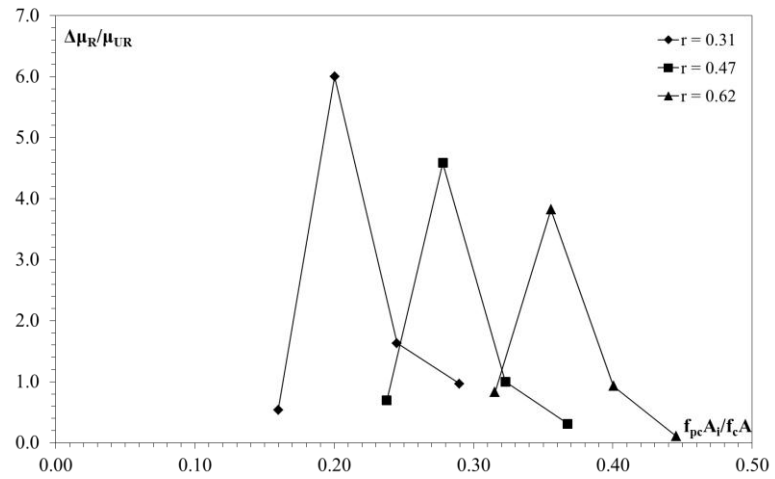
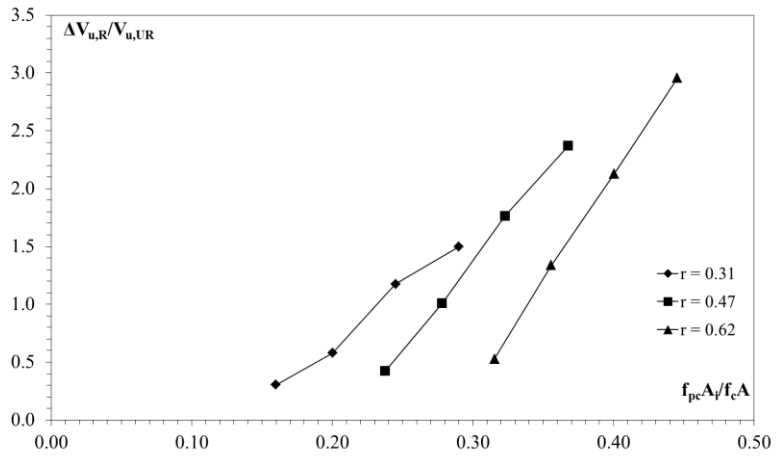
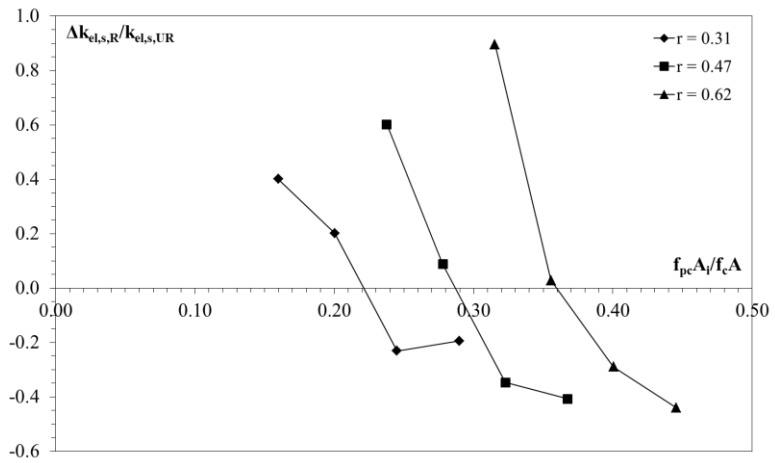


Figure A.11. Tuff block masonry wall with aspect ratio $h/b = 1.3$: relative variation of $\Delta k_{el,s,R}/k_{el,s,U,R}$ (a), $\Delta V_{u,R}/V_{u,U,R}$ (b), $\Delta \mu_R/\mu_{UR}$ (c), $\Delta k_{el,s,R}/k_{el,s,U,R}$ (d), $\Delta V_{max,R}/V_{max,U,R}$ (e), d_r (f) with respect to the relative equivalent strength $f_{pc}A_f/f_cA$ of the reinforcement.



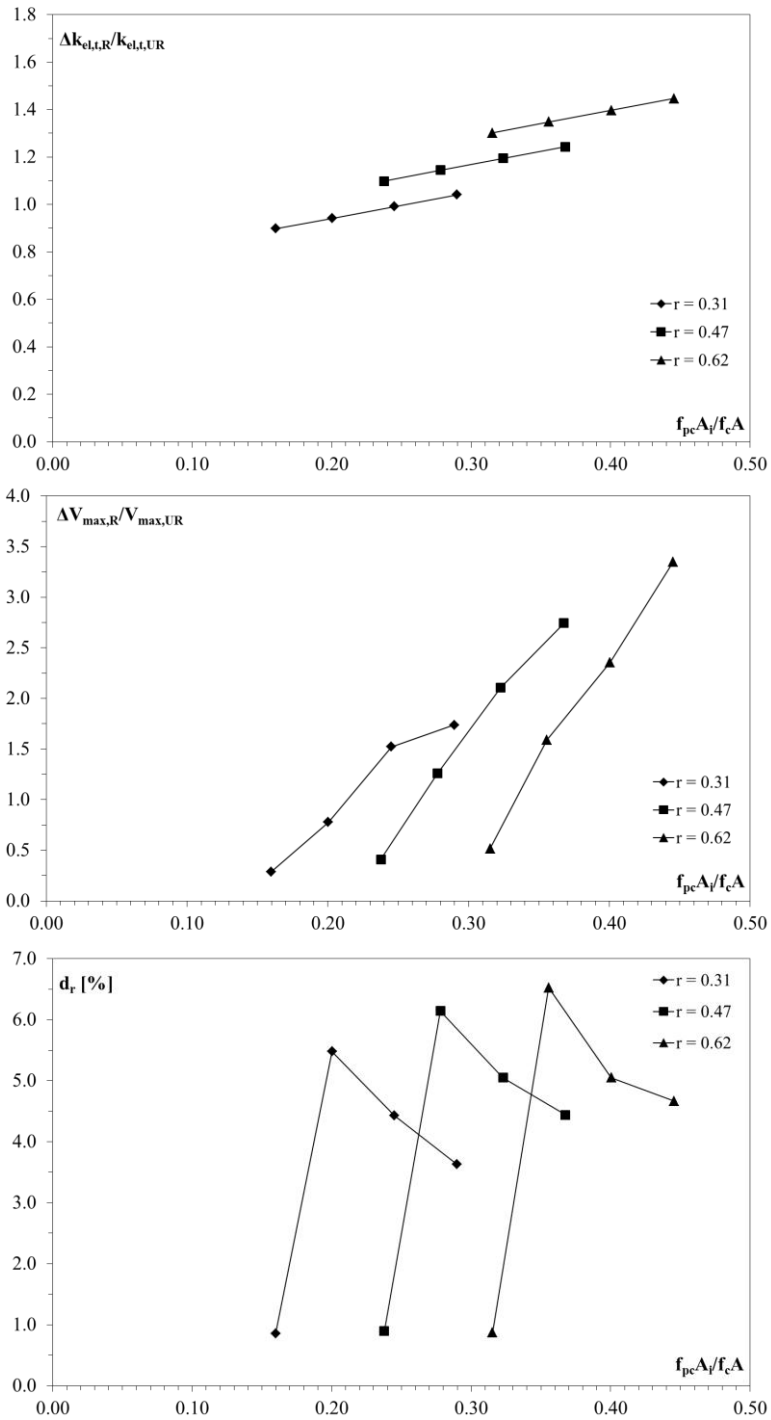


Figure A.12. Tuff block masonry wall with aspect ratio $h/b = 2.0$: relative variation of $\Delta k_{el,s,R}/k_{el,s,UR}$ (a), $\Delta V_{u,R}/V_{u,UR}$ (b), $\Delta \mu_R/\mu_{UR}$ (c), $\Delta k_{el,s,R}/k_{el,s,UR}$ (d), $\Delta V_{max,R}/V_{max,UR}$ (e), d_r (f) with respect to the relative equivalent strength $f_{pc}A_i/f_cA$ of the reinforcement.